REHVA COMMUNITY OF YOUNG PROFESSIONALS

BOOK OF PAPERS

2022

ROTTERDAM, THE NETHERLANDS

HVAC WORLD STUDENT COMPETITION 2022

REHVA STUDENT COMPETITION 2022

Our Sponsors

BOOK OF PAPERS

2022

Rotterdam, The Netherlands

Table of content

Introduction

The Book of papers is presented by RCYP (REHVA Community of Young Professionals). The RCYP aims to facilitate professional activities and knowledge exchange between young professionals (below 35 years) in the fields of indoor climate, HVAC, building physics, and building services. In the current book, the papers written by the participants of the REHVA Student Competition and the ones from the HVAC World Student Competition are presented. The winners of each competition are also shown at the beginning. At the end of the book, the photos of the events can be found.

REHVA Student Competition

Ever since 2005, REHVA has been organizing a yearly international competition to award the best HVAC students in Europe. REHVA member associations nominate one entry per country to the competition after having organized their national level competitions. The submitted works are based on a Master or Bachelor work and can cover any topic in the fields related to REHVA. The Student competitions are organized during the REHVA Annual Meetings and the Students receive a trophy with their names engraved in it, which is then handed over next year to the next winner. The trophy has been traveling long in the past decade, carrying the names of all the proud winners since 2005.

HVAC World Student Competition

In 2013, REHVA founded a World Student competition with several its international partner associations. Ever since 2016, the HVAC World Student Competition has been taking place between students nominated by REHVA (EU), ASHRAE (United States), CAHVAC (China), FAIAR (South America), ISHRAE (India), SAREK (South Korea) and SHASE (Japan). Each association may send one candidate from their region or continent. REHVA's candidate in the HVAC World Student Competition is the winner from REHVA Student Competition. The other MoU partners organise the HVAC World Student Competition according to the same rules around the world with the participation of REHVA in the jury. The first competition was held in 2016 by REHVA in Denmark. REHVA co-finances the participation of the European candidate in these global competitions

REHVA Student Competitions 2022

On Monday 23 May, in Rotterdam, the students of the REHVA Student Competition presented their work to the jury. The yearly competition took place in Ahoy Rotterdam, during the CLIMA Congress 2022.

The jury team members included Manuel Gameiro da Silva (Portugal – OdE), Francis Allard (France – AICVF), Robert Gavriliuc (Romania – AIIR), Pedro Vicente Quiles (Spain – Atecyr), Livio Mazzarella (Italy – AICARR) and Uwe Schultz (Switzerland – Die Planner).

Here is the final result and the subject of their project:

The winner is **Íñigo Martín Melero** for his thesis on "Numerical Modelling of an Ultrasonic Evaporative Precooling Process of the Inlet Air of the Condenser for a Vapour Compression Refrigeration System". Second place goes to **Amila Strikovic**, for her thesis on "Reuse-LCA : Identification of the reduction potential of the environmental impacts of Swiss buildings through material reuse". And the third place goes to **Viktoria Nadas,** for her thesis on "Advanced Design and Control Strategies to Optimize a Deep Borehole Field as Long-Term Thermal Storage".

The 'Best poster' price was awarded to: **Rick Cox**, for his poster on "Forecast Driven Building Energy Flexibility using Battery Electrical Storage System".

The winners were invited to accept their price at the closing ceremony of the CLIMA Congress.

HVAC World Student Competitions 2022

The HVAC World Student Competition 2022 took place online on May 24th, 2022.

The competition was held between the competitors representing ASHRAE (United States), SHASE (Japan), CAHVAC (China), SAREK (South Korea), and ATECYR (Spain).

The first prize was awarded to Íñigo Martín Melero (ATECYR, Spain) with his work on the topic "Numerical Modelling of an Ultrasonic Evaporative Precooling Process of the Inlet Air of the Condenser for a Vapour Compression Refrigeration System". The next two prizes were awarded to Brett Stinson (ASHRAE, USA) and Ms. Mizuho Akimoto (SHASE, Japan), respectively.

The HVAC World Student Competition 2022 was the 3rd time that REHVA's representative won the 1st prize.

About RCYP (REHVA Community of Young Professionals)

The RCYP was founded in 2020 by REHVA and coordinated by Arash Rasooli, the first winner of REHVA and HVAC World Student Competition (2016). REHVA seeks the objective of advancing its programs and services for young engineers, helping them build their professional foundations and career. REHVA organises courses for students and young professionals and promotes their participation in the REHVA network event by discounts. REHVA will support the joint activities defined together with the RCYP members and offer advantages relying on the existing REHVA knowledge sources and services, such as free or discounted access to REHVA guidebooks, events and trainings, publication possibility in the REHVA Journal, specific sessions at REHVA events for the community.

The CLIMA World Congresses are inviting young researchers to submit abstracts. If students team-up and purchase REHVA guidebooks they receive a discount. RCYP is building an online community and information hub tailored to the interest of community members. For any inquiries, feel free to contact us at rcyp@rehva.eu.

Results

REHVA Student Competition 2022

Amila Strikovic

Íñigo Martín Melero

Viktoria Nadas

2

1

3

HVAC World Student Competition 2022

Brett Stinson

Íñigo Martín Melero

Mizuho Akimoto

2

1

3

1ˢᵗ Place
REHVA
Student Competition

**Íñigo Martín Melero
Spain**

1st Place
HVAC
World Student Competition

Numerical Modelling of an Ultrasonic Evaporative Precooling Process of the Inlet Air of the Condenser for a Vapour Compression Refrigeration System.

Íñigo Martín Melero   *inigo.martin@alu.umh.es*   Javier Ruiz Ramírez   *j.ruiz@umh.es*

Avinguda de la Universitat d'Elx, s/n, 03202 Elche, Alicante, Spain.   2021

Abstract—**Pre-cooling of inlet air of the condenser through evaporative cooling effectively improves the performance of the condensers in air conditioning applications. A promising alternative to the conventional evaporative cooling systems (pad, spray) is based on ultrasonic technology. This paper develops the numerical modelling of an ultrasonic mist generator acting as an evaporative cooler. The numerical model was validated against experimental data. A parametric analysis concerning the main variables of the physical process (axial velocity, injection velocity, mass flow rate of injected water) was carried out. The average evaporative cooling efficiency, which reached a maximum of 65.4%, was mostly affected by the dimensionless water-to-air and air-to-air mass flow ratios (m_w/m_{a_T}, m_{a_i}/m_{a_T}). The ranges that lead to the best performance were obtained in the optimisation analysis. Under $5 \times 10^{-4} \le m_w/m_{a_T} \le 0.002$ and $0.035 \le m_{a_i}/m_{a_T} \le 0.05$, there was a more homogenous mist distribution in the outlet and a more effective cooling process.**

Index Terms—**CFD, cooling efficiency, evaporative cooling, ultrasonic nebulizer.**

I. INTRODUCTION

Nowadays, heating and cooling comprises 50% of the final energy demand in Europe [1]. Air conditioning consumption, which already accounts for 20% of the total electric consumption in buildings, will rise due to the economic and demographic development of the countries in zones with warmer climates. A broader access to refrigeration improves economic productivity, with its consequent benefits in human, health and wellbeing development. However, this will have a significant impact on the total energy demand, adding more pressure to the electric grids and increasing the emissions [2]. The development of new technology that require a minimum contribution of fossil fuels is necessary. In this sense, the main efforts should focus on buildings, as they are responsible for the 41% of the final consumption of energy and approximately for the 36% of the CO_2 emissions in the EU. In this path of energetic optimisation, the new buildings under construction since 2020 are of nearly zero consumption (nZEB) [3]. The reduction of the energy consumption of the HVAC systems, in buildings, can be attained through the demand or through the efficiency. Solar cooling is interesting for the chronological coincidence between the available solar radiation and the need of refrigeration. This technology suggests combining the vapour compression systems with thermal or photovoltaic solar panels.

The vapour compression systems powered by photovoltaic energy are very promising in the field of solar energy, specially applied to medium and small units (less than 50 kW). The behaviour of this type of systems can be further enhanced by the improvement of the photovoltaic panels and the efficiency of the heat pump. Lowering the pressure level of the heat pump implies a reduction of the energy consumed by the compressor, leading to a better EER. In addition, the thermal exchange at the condenser is defined by the condensing medium. Most commonly, air is employed to cool the condenser, due to its availability. However, this fluid is not the most effective option because it is deeply affected by the ambient conditions. Water is better, but it implies the use of more complex technology (like cooling towers). There are hybrid systems too, that consist of evaporative precooling of the inlet air. Evaporative cooling is an effective way to cool the fluid, by the means of water evaporation. Therefore, the temperature of an airflow can be reduced at the expense of increasing its humidity. Numerous refrigeration systems are based on this principle, including wet towers.

Two effective methods to obtain evaporative precooling are pad cooling and spray. In pad cooling, the air circulates through a wet surface, reducing its temperature whilst incrementing its humidity. The main disadvantage of this technique is the pressure drop introduced to the HVAC system, with its consequent decreases in air mass flow and heat extraction capacity. On the other hand, spray cooling technology is widely employed and stands out for its simplicity. This evaporative cooling method allows the extraction of large quantities of energy at low temperatures, through sensible and latent heat. The mechanism consists of an injector that atomises water particles that, due to their small size, immediately evaporate into the airflow. This technology is appropriate and justified due to its low cost, simple design and straightforward operation and maintenance. Ref. [4] studied the evaporative precooling through spray in a wind tunnel, employing several horizontal and vertical distributions of sensors. Temperature drops of 4.1 – 7.2 ºC were achieved, with complete evaporation. Nonetheless, the main disadvantage of spray cooling is the energy consumed by the water pump. This is needed to maintain the pressure levels of the injectors.

The application of the ultrasonic technology, on the other side, has been growing and developing as a new and emerging field to study. These systems are formed by transductors capable of producing high frequency vibrations. Ref. [5] concluded that ultrasonics could be interesting in application related to heat or mass transport, as it decreases the internal and external resistance to transport. In this sense, submerging an ultrasonic device with these properties in water leads to atomisation, through the transient vacuum occurred in each oscillation. Applying this to the evaporative cooling spray technique, the water

pump needed in the process can be eliminated, and the particle diameter obtained in the atomisation is smaller.

Furthermore, Computational Fluid Dynamics (CFD) has been employed in the last decades as a very effective tool to analyse and model many physical phenomena. The CFD simulations of injections have acquired a special visibility and meaning in the times of pandemic, allowing the simulation of small droplets expelled while coughing and breathing. CFD enables scientists and designers to understand the atomisation as a physical process, saving up time, effort and experimental tests. Numerous authors have investigated, from a CFD point of view, the evaporative cooling through spray. However, none of them have numerically simulated the combination of ultrasonic technology with spray precooling. There are few references concerning the numerical simulation of ultrasonic mist sprayers, and none of them is related to the spray precooling. The state-of-the-art review shows that ultrasonics is a promising new way to improve the design of evaporative precooling systems. The ultrasonic mist nebulizers eliminate the pressure loss of pad cooling and the pump consumption of spray cooling, enabling an easy operation of the main parameters of the atomiser. There are no previous numerical studies concerning the application of ultrasonic technology to spray evaporative precooling, so exploring this new investigation line is of scientific interest.

The main objective of this paper is to develop the numerical model of an ultrasonic mist generator, applied to cool the condenser inlet air of a vapour compression refrigeration cycle. This numerical model has been validated against the results of several experimental test runs for this purpose. Afterwards, the secondary objectives consisted in carrying out a parametric analysis including the most relevant variables involved in the cooling process. Finally, an energetic optimisation over the total refrigeration efficiency was performed.

II. METHODS AND MATERIALS

A. Experimental facility.

To evaluate the performance and cooling capacity of the mist produced by the ultrasonic generator, a series of tests were conducted in an experimental facility specifically adapted for this purpose. This facility contains the two main components: an ultrasonic mist generator, presented in Figure 1, and a subsonic wind tunnel.
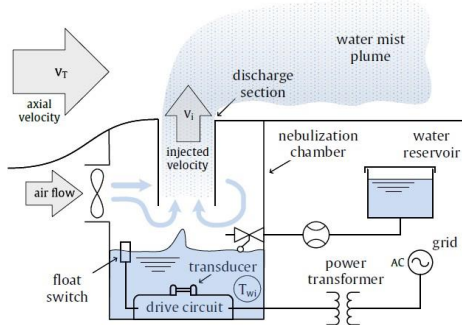

Figure 1. Main components that make the ultrasonic mist generator and layout of the two flows considered in the CFD model.

The ultrasonic mist generator consists of a compact nebulizer device equipped with 10 ultrasonic transductors, submerged in a tank with a constant level of water. Each transductor is capable of transforming the high-frequency electronic signals, typically between 0.8 and 1.65 MHz, to high-frequency mechanical oscillations. The water cannot follow the movements of the ceramic discs, so it detaches in each negative oscillation, producing momentarily a vacuum in which the water cavitates and is atomised.

The subsonic open-circuit wind tunnel shown in Figure 2 was used to carry out the experimental tests of the evaporative cooling through ultrasonics. The nozzle ensures the stability and uniformity of the inlet velocity profiles. The wind tunnel is 5.3 m long and has a transversal section of 0.492×0.712 m². The nozzle dimensions are 1.2×1.7 m² (transversal section) and 1.55 m long.
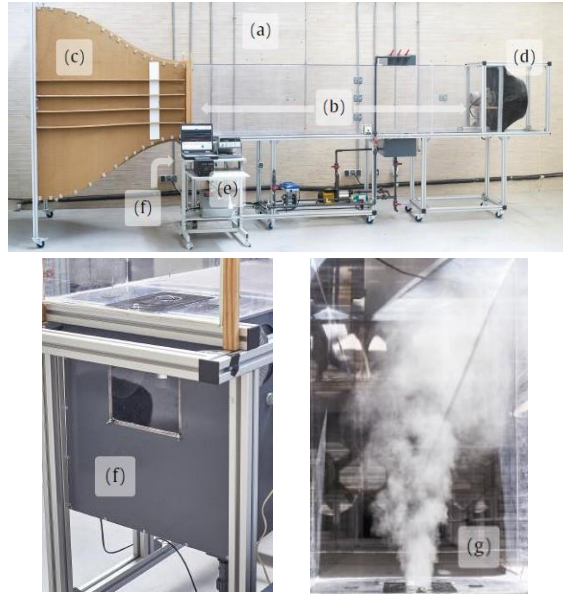

Figure 2. Wind tunnel employed in the experimental tests. (a) wind tunnel; (b) test section; (c) nozzle; (d) diffuser; (e) data acquisition system; (f) ultrasonic mist generator; (g) water mist.

B. Subsonic wind tunnel experiments.

A total of 20 experimental tests were conducted to evaluate the behaviour of the ultrasonic mist generator [6]. The variables registered in the tests and the distribution of the sensors in control section are summarized in Figure 3.
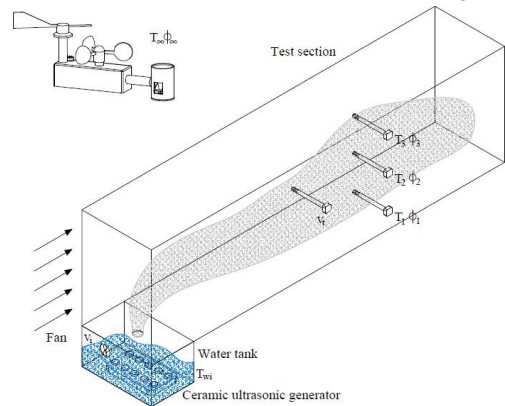

Figure 3. Variables measured in the experimental tests.

The inlet dry temperature (ambient, T_∞) and relative humidity (ambient, ϕ_∞) were measured in a weather station

placed near the wind tunnel. An array of three thermohygometers was employed to measure the vertical distribution of temperature and relative humidity (T_1, T_2, T_3, ϕ_1, ϕ_2, ϕ_3). These sensors were positioned at the control section, 1.5 m downstream from the mist discharge section. A hot wire anemometer, placed 0.435 m upstream from the control section, measured the average velocity of the tunnel airflow, v_T. The injection velocity of the mist at its discharge section, v_i was registered by a vane anemometer located at the atomiser chamber. The injected mass flow of water, $\dot{m}_w$, was calculated using a gravimetric method.

The distribution of the water-droplet size generated in the ultrasonic nebulizer was determined through high-resolution photographs. The photos were taken with a 7360 4912 pixel-resolution camera, and a subsequent image analysis with ImageJ and Fiji software was performed. One of these photos is shown in Figure 4, and Figure 5
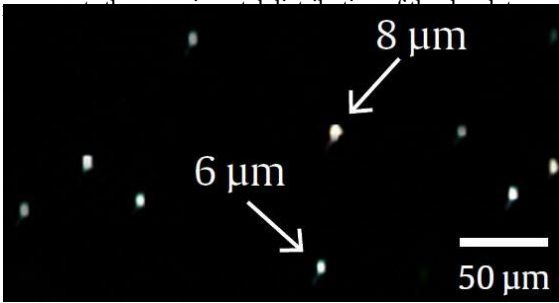

Figure 4. Example of a high-speed photography, with the droplet diameter.
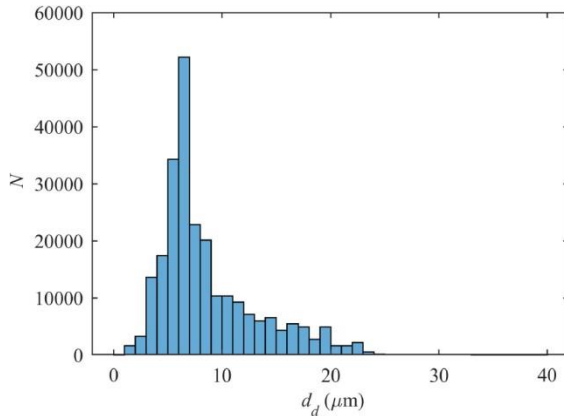

Figure 5. Histogram of the experimental droplet distribution.

The mean droplet diameter under the testing conditions was d = 8.1 µm, and the Sauter diameter was d = 13.2 µm.

C. Mathematical model.

The governing equations are divided between the ones that govern the continuous phase, on one side, and the equations that govern the discrete phase, on the other.

In the continuous phase, the continuity, momentum, energy and species equations can be distinguished (1). The RANS approach was employed, and the inlet air is assumed as steady state, incompressible and turbulent according to the Standard $k - \epsilon$ model. The influence of the discrete phase in the continuous phase is considered through the

mass, momentum and energy source terms of the governing equations.

$$\frac{\partial(\rho v_i)}{\partial x_j} = S_m \qquad \frac{\partial(\rho v_i v_j)}{\partial x_j} = -\frac{\partial p}{\partial x_i} + \frac{\partial \tau_{ij}}{\partial x_j} + \rho g_i + S_{mo}$$

$$\rho v_i \frac{\partial m_j}{\partial x_j} = -\frac{\partial J_{i',i}}{\partial x_j} + S_m \qquad J_{i',i} = -\rho D_{f_{i',m}} \frac{\partial m_j}{\partial x_j} \qquad (1)$$

$$\rho v_i \frac{\partial e}{\partial x_j} = -p\frac{\partial v_i}{\partial x_i} + \frac{\partial}{\partial x_i}\left(k\frac{\partial T}{\partial x_i}\right) + \frac{\partial}{\partial x_i}\left(\sum_{i'=1}^{n} h_{i'}J_{i'}\right) + \phi_v + S_e$$

Here, S_m, S_{mo} and S_e represent the mass, momentum and energy source terms introduced by water droplets, respectively, and $J_{i',i}$ is the diffusion flux of species i´.

The discrete phase equations are written according to a Lagrangian frame of reference. The discrete-phase particle trajectory is obtained with the integration of the force balance in the particle, through Newton's second law (2).

$$\frac{dv_d}{dt} = \frac{18\mu}{\rho_d d_d^2}\frac{C_D Re}{24}(v - v_d) + g\frac{\rho_d - \rho}{\rho_d} \qquad \frac{dr_d}{dt} = v_d$$

$$m_d c_p \frac{dT_d}{dt} = h_C A_d(T - T_d) + \frac{dm_d}{dt}h_{fg} \qquad (2)$$

$$\frac{dm_d}{dt} = h_D A_d M(y_s - y) = h_D A_d M(\rho_s - \rho)$$

$$Nu = \frac{h_C d_d}{k} = 2 + 0{,}6Re_d^{1/2}Pr^{1/2} \qquad Sh = \frac{h_D d_d}{D_f} = 2 + 0{,}6Re_d^{1/2}Sc^{1/2}$$

Here, C_D represents the drag coefficient and the convective and mass transfer coefficients (h_C, h_D) are calculated from the Nusselt and Sherwood number correlations. Refer to [7] for more information regarding the mathematical model.

D. Numerical model.

Regarding the computational domain (shown in Figure 6), air enters uniformly through *Inlet1* (left section) and *Inlet2* (circular section, above the atomisation chamber). In the experimental tests, the air velocity was inside the ranges $0.51 - 2.18$ and $2.99 - 4.15$ m/s for both inlets, respectively. A turbulence of 5% was assumed for both inlet flows.
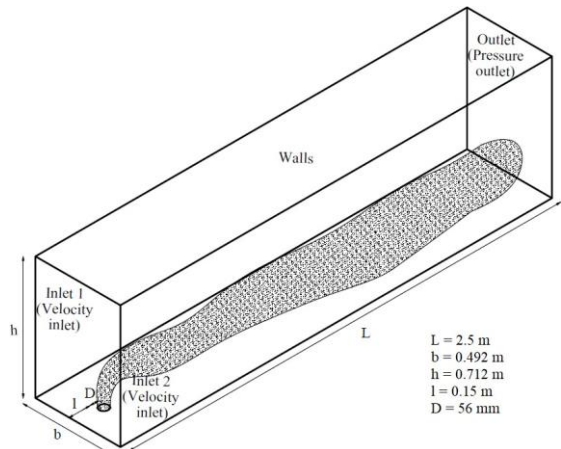

Figure 6. Boundary conditions.

The injection velocity was determined by the discrete phase, and the temperature of the droplets was equal to the

temperature of the water network supply. The pressure at the tunnel exit (*Outlet*) was set equal to the ambient, and the walls were considered as non-slip and adiabatic. The boundary condition of the walls (*Walls*) was escape.

The software ANSYS FLUENT (19.1 version) was used, and a grid independence study of the mesh was carried out. This study was based on the analysis of the Grid Convergence Index (GCI), that measures the percentage deviation of a calculated value with respect to the numerical asymptotic value. Three different meshes were considered, and the GCI parameter was calculated for the predicted temperature and specific humidity at the 3 discrete measurement points. The maximum GCI obtained was 0,06%, for the finest mesh, that shows a nearly negligible dependence of the results with the mesh cell size. The mesh used in the simulations was formed by 1612376 unstructured polyhedral cells. The SIMPLE algorithm was employed to link the continuity and momentum equations through the pressure magnitude. All the calculations were performed through a second-order discretization.

III. DATA PRESENTATION AND DISCUSSION

A. Problem validation.

The general appearance of the cooling process at the tunnel outlet, in one of the test runs selected for the problem validation, is presented in the Figure 7. In addition, Figure 8 shows the comparison of the temperature and humidity distributions in the array of sensors, for that same test run. There is a good agreement between the CFD predicted results and the experimental ones. The numerical model successfully predicts the plume evolution, even though the measurements were done at three discrete and specific points.
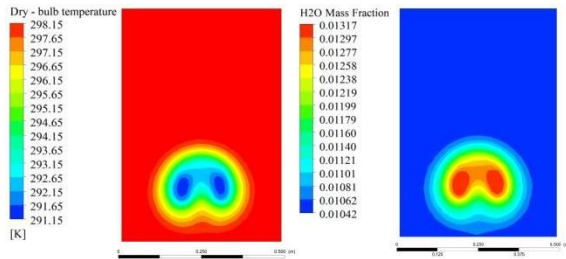

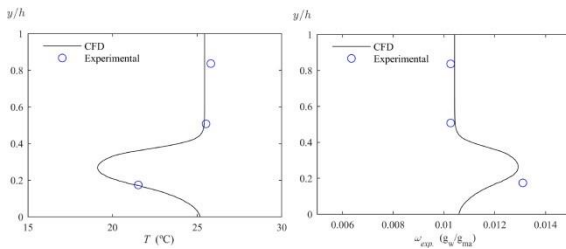Figure 7. General appearance of the cooling process, for a given test run.

Figure 8. Comparison between predicted and experimental results at the array of sensors, for a given test run.

The comparison between the observed and predicted results for dry temperature and water mass fraction in 5 of the tests performed is shown in Figure 9. These results show a good agreement, within a 10% error range for both dry-bulb temperature and water mass fraction, for some

experimental tests and at the 3 discrete measurement points. The mean deviations are $\pm$ 1 ºC and $\pm$ 0.5 g_w / g_{ma}, which is below 5% for both magnitudes. The cause for this deviations is not clear, but they are probably due to limitations in the location of the measuring points, and experimental uncertainties. In the light of the presented results, the model can be considered as validated.
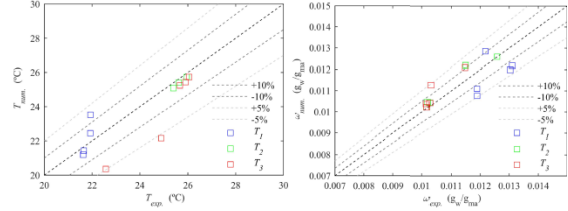

Figure 9. Comparison of the dry-bulb temperature and specific humidity in experimental tests and CFD.

B. Parametric analysis.

After validating the numerical model, a parametric analysis including the most important variables was done. The reason for building a numerical model lies in studying those parameters that cannot be altered experimentally, due to physical limitations or the number of experiments that it would imply. The independent variables modified in this section were v_T, v_i and m_w.

In most practical cases of the inlet precooling in small-to-medium HVAC units, the velocity is range is approximately $0.5 - 2.5$ m/s. Three different levels of v_T were established: 0.5, 1.5 and 2.5 m/s. Another three different levels of v_i were adapted to each case of v_T, all ranging between $2.5 - 6$ m/s. The parameter ranged from $5 \cdot 10^{-5}$ kg/s to $1.2 \cdot 10^{-3}$ kg/s. In total, $3^3 = 27$ simulations were performed. The rest of the variables involved in the analysis were considered constant, and similar to the ones registered in the experimental tests ($T_\infty = 25$ ºC, $\phi_\infty = 0.5$, d = 35 µm).

The first parameter studied in the analysis is the evaporative cooling efficiency $\bar{\eta}^{-X}$, defined as the ratio of the mean temperature difference at a certain section to the wet bulb depression (3).

$$\bar{\eta}^{-x} = \frac{T_\infty - \bar{T}^x}{T_\infty - T_{wb\infty}} \qquad (3)$$

Here, T_∞, $\bar{T}^X$ and $T_{wb\infty}$ are the ambient dry temperature, the average temperature at the transversal section at x location from the tunnel inlet and the ambient wet bulb temperature, respectively.

For a correct characterization of (3), a dimensional analysis involving v_T, v_i and m_w was carried out. The two relevant parameters extracted from this analysis were the water-to-air (axial flow) mass flow ratio, m_w/m_{a_T}, and air-to-air mass flow ratio, m_{a_i}/m_{a_T}. Figure 10 shows the evaporative cooling efficiency at the tunnel outlet, $\bar{\eta}^L$, as a function of m_w/m_{a_T}, for the different m_{a_i}/m_{a_T} simulated. The parameter $\bar{\eta}^L$ reached a maximum of $\bar{\eta}^L = 0.654$, with the lowest v_T velocity (0.5 m/s) and the highest injection air velocity and water mass flowrate, for that level (4 m/s and $m_w = 10^{-4}$ kg/s, respectively).
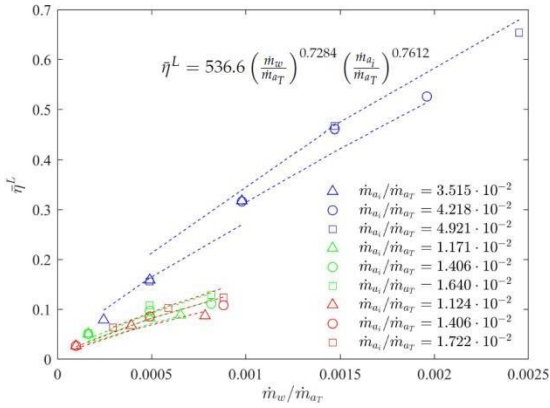
Figure 10. $\bar{\eta}^L$ as a function of $\dot{m}_w/\dot{m}_{a_T}$ and $\dot{m}_{a_i}/\dot{m}_{a_T}$, for all simulated cases.

The general correlation (4) describes the mean evaporative cooling correctly ($R^2 = 0.9835$), for the ranges $0.5 \leq v_T \leq 2.5$ m/s, $2.5 \leq v_i \leq 6$ m/s and $5 \times 10^{-5} \leq m_w \leq 1.2 \times 10^{-3}$ kg/s.

$$\bar{\eta} = 536.6 \left(\frac{\dot{m}_w}{\dot{m}_{a_T}}\right)^{0.7284} \left(\frac{\dot{m}_{a_i}}{\dot{m}_{a_T}}\right)^{0.7612} \qquad (4)$$

Here, m_{a_i}/m_{a_T} and m_w/m_{a_T} are the air-to-air mass flow and the water-to-air mass flow ratio, respectively.

A second parameter that represents the local effects of the cooling process was defined. This parameter, A_T^x, was the percentage area of a section at a certain temperature. Figure 11 depicts how this parameter behaves when evaluated at the tunnel outlet (A_T^L), for three representative cases. In the red and green series ($v_T = 1.5$ m/s and $v_T = 2.5$ m/s, respectively), A_T^L dramatically drops at temperatures similar to T_∞. This means that the cooled area is concentrated in a very small portion of the total outlet area. On the contrary, the blue series ($v_T = 0.5$ m/s) shows a smoother, more homogenous cooling process, that ensures a temperature drop of 4 ºC on at least 60% of the tunnel outlet.
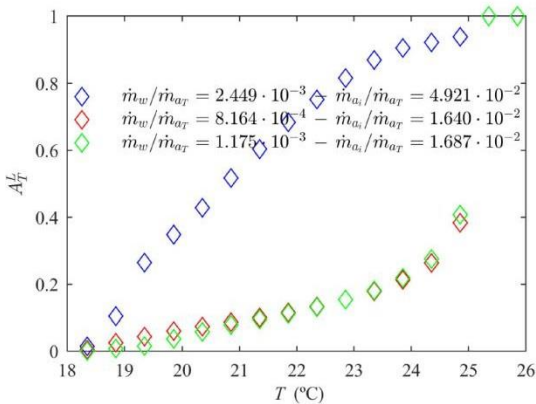

Figure 11. Variation of A_T^L as a function of the air temperature, for three representative cases.

In general, an increment in v_T meant a more concentrated mist distribution (Figure 12), avoiding energy transport to other parts of the domain. This is explained by the contributions of both inlet airflows: axial and injection. In those cases were the axial airflow was dominant with respect to the injection one, the atomised water particles were concentrated in a small area. The cooling process improved with low values of v_T, producing a more uniform mist, where evaporation was favoured (Figure 12a). Therefore, higher values of m_w/m_{a_T} and m_{a_i}/m_{a_T} lead to better cooling efficiencies and lower average outlet temperatures (Figure 12b).
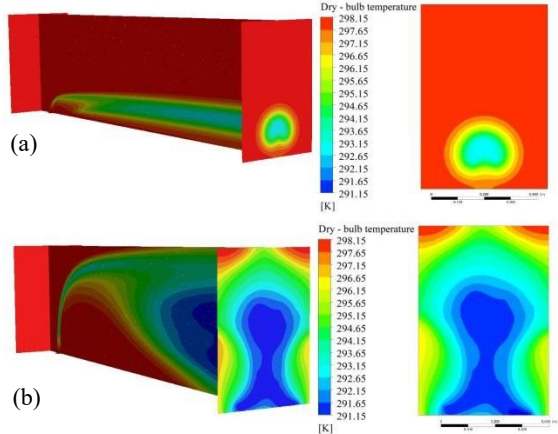

Figure 12. Two simulated cases: (a) $v_T = 2.5$ m/s, $v_i = 4$ m/s and $m_w = 4 \times 10^{-4}$ kg/s (b) $v_T = 2.5$ m/s, $v_i = 5$ m/s and $m_w = 5 \times 10^{-5}$ kg/s.

The last indicator covered in this analysis is the wet length, L_w. L_w is defined as the distance, from the discharge section, where the droplets fully evaporate. In its dimentionless form, L_w/L, the wet length was higher than one in most simulations. Figure 13 presents a case in which full evaporation was attained, and another one in which it was not. Not achieving the full evaporation of the droplets might cause fouling and corrosion to the condenser, so the recommended operation ranges must be limited to those cases where $L_w/L \leq 1$. Therefore, operation outside of the ranges $2.5 \times 10^{-4} \leq m_w/m_{a_T} \leq 10^{-3}$ and $0.035 \leq m_{a_i}/m_{a_T} \leq 0.05$ should be avoided.
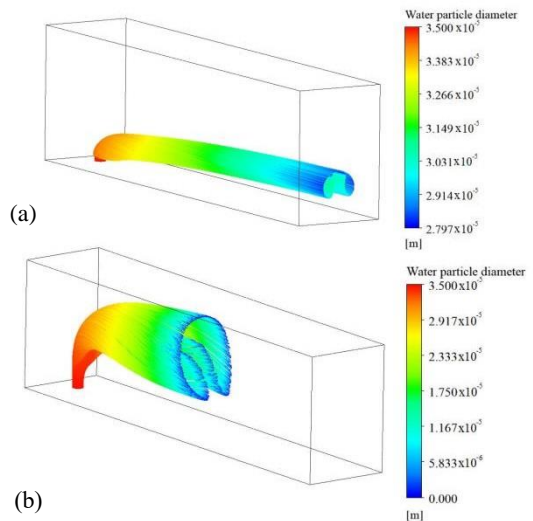

Figure 13. Two simulated cases: (a) $v_T = 2.5$ m/s, $v_i = 5$ m/s and $m_w = 9 \times 10^{-4}$ kg/s (b) $v_T = 0.5$ m/s, $v_i = 3.5$ m/s and $m_w = 10^{-4}$ kg/s.

C. Optimisation.

An increase of m_w improves the cooling capacity, $Q_{cooling}$ (5), and efficiency, η until saturation, but it also implies a higher power consumption in the ultrasonic nebulizer.

$$Q_{cooling} = m_{a_T} c_{p_{ma}} (T_\infty - \overline{T}) \tag{5}$$

Here, m_{a_T}, $c_{p_{ma}}$, T_∞ and $\overline{T}$ are the axial air mass flow, the specific heat at constant pressure of the air, the ambient dry temperature and the average temperature at the tunnel outlet, respectively.

An increase of $\dot{m}_{a_T}$, on the other hand, leads to a lower evaporative efficiency and a higher consumption in the fans. An optimisation is carried out in order to compare the power consumed in the different simulations and find the most efficient combinations, from an energetic point of view.

The parameter that studies the relative contribution of these effects is the overall evaporative coefficient of performance (COP), defined in (6).

$$COP = \frac{Q_{cooling}}{W_{fan_T} + W_{fan_i} + W_{ultrasound}} \tag{6}$$

Here, $Q_{cooling}$, W_{fan_T}, W_{fan_i} and $W_{ultrasound}$ are the cooling capacity, the axial fan consumption, the injection fan consumption and the consumption of the ultrasonics, respectively.

The power consumed by the ultrasonic device was estimated by calculating the number of transducers required to generate a particular $\dot{m}_w$. This value was then linked to the consumption per transducer.

The electric power consumed by each fan was calculated using (7).

$$W_{fan} = \frac{Q \Delta p}{\eta_{fan}} \tag{7}$$

Here, Q, Δp and η_{fan} are the volumetric flow rate of air, the pressure loss and the fan efficiency, respectively.

The variation of the coefficient of performance against m_w/m_{a_T} is presented in Figure 14, for the different m_{a_i}/m_{a_T} levels. In the end, the ultrasonic nebulizer accounted for around 70-90% of the total consumption. The remainder was mainly absorbed by the injection fan, whilst the power to generate the main airflow was almost negligible, compared to the other power consumptions. Therefore, COP values are mainly affected by the variation of m_w/m_{a_T}. An increase of m_w/m_{a_T} decreases COP, due to the ultrasonic power use. The maximum value of this parameter is 7.01, achieved with $m_w/m_{a_T} = 9.8 \times 10^{-4}$ and $m_{a_i}/m_{a_T} = 0.0351$. Operating within the ranges $5 \times 10^{-4} \leq m_w/m_{a_T} \leq 0.002$ and $0.035 \leq m_{a_i}/m_{a_T} \leq 0.05$ guarantees a COP higher than 6. These ranges partially match the operational ranges with the best average cooling efficiencies, so the benefit is two-fold.
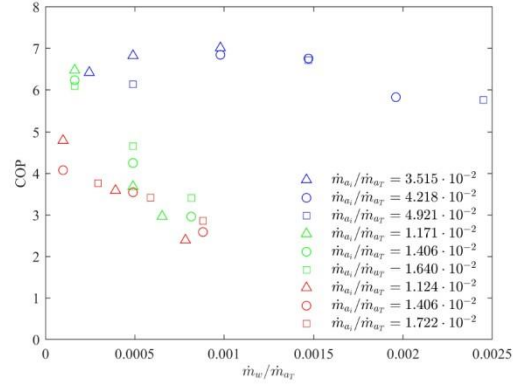

Figure 14. COP as a function of $\dot{m}_w/\dot{m}_{a_r}$ for all simulated cases.

IV. CONCLUSIONS

In this paper, a numerical model of an ultrasonic mist generator for the evaporative precooling of the condenser inlet air was developed. Several experimental tests were conducted in a wind tunnel facility, and the numerical model was validated. A parametric analysis was carried out, including the most relevant physical variables that participate in the cooling process. Finally, an energetic optimisation was performed.

In this preliminary study, considerable temperature drops were attained through the combination of evaporative precooling and ultrasonic technology. However, in most of the numerical simulations, the atomised water droplets escaped without evaporating. This implies that part of the consumption in the ultrasonics is employed in generating water droplets that do not affect the cooling process. In addition, the water injection system favours the concentrated mist shape, which has a lower η and COP.

This is, therefore, the first step in a project that has potential for further improvement and development. A reduction in the power consumption of the ultrasonics must be explored, changing the number of individual transductors employed. The number of injectors, its arrangement and size must be evaluated, in order to achieve a more homogenous cooling with full evaporation. Finally, the variation of the ambient conditions must be studied too.

REFERENCES

1   J. Urchueguía et al, "Common Implementation Roadmap for Renewable Heating and Cooling Technologies", *RHC, Brussels*, 2014.

2   B. Dean et al, "The Future Of Cooling", *IEA Annual Report, Paris*, 2018.

3   European Commission, "Energy Performance of Buildings Directive", *European Union, 2010*.

4   Xia et al, "CFD Analysis of pre-cooling water spray system in natural draft dry cooling towers", *Appl. Therm. Eng., Volume 105*, 2016.

5   Yao, "Research and applications of ultrasound in HVAC field: A review", *Renew. Sustain. Energy Rev., Volume 58*, 2016.

6   Martínez et al, "Experimental study of an ultrasonic mist generator as an evaporative cooler", *Appl. Therm. Eng., Volume 181*, 2020.

[7] Ansys® Fluent, Release 19.2, Help System, Theory Reference, ANSYS.

2nd Place
HVAC World
Student Competition

Brett Stinson
USA

Determining Airflows and Volatile Organic Compound Source Strengths for an Occupied School

Brett Stinson[1], Dr. Elliott Gall[2]

[1,2]Portland State University

1825 SW Broadway, Portland, OR, 97201, U.S.A.

[1]bstinson@pdx.edu, [2]gall@pdx.edu

This work was accepted as an undergraduate honors thesis in 2021.

Abstract—**Volatile organic compounds (VOCs) are a group of air pollutants that can adversely impact human health, engage in chemistry indoors, and meaningfully degrade indoor and outdoor urban air quality. While there exists extensive research on VOC emission rates from indoor sources, fewer studies exist characterizing the magnitudes and type of emissions from humans and human activity. As buildings are constructed to be more airtight, and the materials used are chosen to reduce VOC emissions, it follows that human contributions are poised to become increasingly important indoor sources of VOCs. With data extracted from a three-month campaign conducted at Harriet Tubman Middle School in Portland, Oregon—an institution built near a busy roadway—this study modeled airflows through the school and quantified source strengths for VOCs over the course of one week in May 2019. We developed an approach to estimate outdoor air ventilation rates, occupant density, and supply air flow rates through the school by analyzing the decay, steady-state, and accumulation periods of CO_2 measured in return and supply air. Emission rates for seven compounds with expected sources from human metabolism and activity were calculated, as were source strengths for BTEX compounds (benzene, toluene, xylenes, and ethylbenzene), which are typically associated with traffic-related air pollution (TRAP). Calculated per-person emission rates for VOCs that are associated with human activity or metabolism, e.g., monoterpenes and isoprene, were generally consistent with the few prior estimates in the literature and indicate humans and their activities are an important indoor source of reactive VOCs. Source strengths for BTEX compounds revealed that the majority of their presence was due to supply air, which was expected considering the elevated levels of outdoor TRAP constituents in the near-roadway building. This study provides new data concerning VOC source strengths of indoor and outdoor origin and can enable the modeling of air pollution exposures in schools.**

Index Terms—**air flowrate analysis, indoor air quality, per-person VOC emissions, VOC source apportionment**

Introduction

As humans spend nearly 90% of their time indoors [1], a heightened awareness of sustainable building design, improved indoor air quality, and effective air-filtration has emerged. Volatile organic compounds (VOCs)—which are defined as any compound of carbon (with a few notable exceptions, such as carbon monoxide and carbon dioxide) that participates in atmospheric photochemical reactions— are emitted from thousands of consumer products, as well as from human metabolism [2] and internal combustion engines in vehicles. Long-term indoor exposure to VOCs can cause impaired cognition [3] and detrimental health effects to varying degrees [4]. Because these pollutants have direct health consequences for humans, it is important

to understand exposure concentrations and to investigate the means by which they enter into enclosed spaces. While there are many different VOCs, two important classes that have health consequences indoors are those emitted by humans and human activity and those associated with traffic-related air pollution (TRAP).

Schools are an important environment that contribute to student exposures to air pollution. The present study took place at Harriet Tubman Middle School, an institution built in close proximity to Interstate-5, a heavily trafficked roadway in Portland, Oregon. This seven-lane highway is used by upwards of 120,000 vehicles a day and is located a mere 20-125 meters from the school [5]. Circumstances such as these are far from an anomaly: 40% of urban populations live within 300-500 meters of a major highway or road [6] and 15% of schools, or about 6.4 million children, are less than 250 meters from a highway [7]. Exposure to TRAP has been proven to be a source of health-related issues for humans—particularly for vulnerable populations, such as children [8]. Moreover, an element of racial patterning emerges with regard to TRAP exposure, as schools with a majority African-American student body, such as Harriet Tubman Middle School, are more likely to be located near busy roadways [7].

In Fall 2018—after having been closed since 2012 due to a decrease in enrollment—Harriet Tubman Middle School was reopened with a renovated HVAC system. This system was outfitted with MERV8 and MERV16 high-efficiency particle filters and an activated carbon gas-phase air scrubber. Additionally, the building envelope was redesigned to reduce outdoor air infiltration. A monitoring campaign preceded and accompanied these building improvements, monitoring outdoor air quality at the school site and investigating the air-handling system's air cleaning effectiveness over the course of three, six-week long phases [9]. The majority of the data utilized in the subsequent analysis was taken from measurements made during Phase III, which began in May 2019.

While the primary focus of the campaign was to verify the effectiveness of air cleaning systems in the enhanced HVAC system, the present study expands on this scope, leveraging the high-time resolution and broad analytical window of a deployed proton transfer reaction – time of flight – mass spectrometer and additional time-resolved air monitoring equipment deployed to the air handling systems. Four days during Phase III of the campaign were chosen for further examination: May 27, 2019, a holiday in which the air-handler was operating but the school was mostly vacant, as well as May 28, May 29, and May 31, 2019, weekdays in which the air-handler was operating and the school was fully occupied. May 30, 2019 was ultimately

excluded from the dataset due to the lack of a discernible stable occupancy period.

Airflows through the building were not directly measured, and thus a method for estimating outdoor air ventilation rates and supply air flowrates through the school was developed using an analysis of decay, steady-state, and accumulation periods of CO_2 recorded in return air. CO_2 generation rates were utilized to estimate occupant density; occupant density was then used to calculate per-person VOC emission rates. A source apportionment was performed on a total of 249 compounds, which revealed the rate at which each compound was being emitted from supply air (divided into recirculation and outdoor air sources), the building's occupants, and the building itself. Compounds associated with human metabolism and activity were chosen for further investigation and compared to the limited literature that exists on the subject. Additionally, compounds associated with TRAP— benzene, toluene, xylenes, and ethylbenzene, otherwise known as BTEX compounds—were explored further due to the proximity of the field site to Interstate-5.

In elevated concentrations, VOC exposure has the potential to negatively affect human health, and thus degraded indoor air quality is a phenomenon that must be actively avoided. The goal of this study is to explore how a state-of-the-art air-cleaning system might affect levels of outdoor air pollutants within a building, while also taking into consideration indoor contributions from human metabolism, human activity, and non-human sources.

Methods and Materials

A. Site Description

Harriet Tubman Middle School (2231 N Flint Ave, Portland, OR 97227) is located in Portland, Oregon, USA and in 2019 had an enrollment of 472 students with 33 faculty members, according to Portland Public Schools. Fig. 1 presents a schematic of the institution, emphasizing the renovated air-handler that was installed in Summer 2018 before the school's reopening.

B. Instrumentation and Calibration

VOC sampling was conducted using a proton transfer reaction - time of flight - mass spectrometer (PTR-ToF-MS) instrument. Briefly, this method relies on the reaction of H_3O^+ ions, which fail to react in the presence of clean air but transfer protons to most common VOCs [10]. VOC concentrations were sampled by use of a switching valve, which alternated between return air, outdoor air, and supply air in regular, ten-minute intervals. Additionally, four sensors (Onset MX1102) were used to measure temperature, relative humidity, and CO_2 concentrations. Further details concerning the instrumentation, sampling method, and analysis of data collected during the field campaign can be found in Laguerre et al., 2020 [9].

C. Calculating Flowrates

In order to ultimately determine VOC source strengths, the following mass balance was constructed (1) to determine the mass of a VOC emitted into the building:

$$M = Q_{SA} \int_{t_0}^{t_1} (C_{RA} - C_{SA}) \, dt + V \int_{t_0}^{t_1} dC_{RA} \tag{1}$$

Here, M is the total VOC mass emitted (mg), Q_{SA} is the supply air ventilation rate (m^3/h), C_{RA} and C_{SA} are VOC concentrations recorded at the return and supply air monitoring points (#/cm^3), and V is the building's volume (m^3).

While time-varying concentrations were taken with the PTR-ToF-MS instrument, lack of access to the ducting prohibited direct airflow measurements. Additionally, though Portland Public Schools provided enrollment statistics, occupant density was likely to vary on a daily basis due to student and faculty absences, custodial and cafeteria work, etc. Using CO_2 concentrations in return and supply air, it was possible to take advantage of periods in time where there existed a step-change in occupancy unique to a school environment (e.g., arrival or departure of nearly all students at the beginning or end of the school day) or occupancy remained steady—an example of these varying periods is shown in Fig. 2.

As the building was vacated at the end of each school day, CO_2 concentrations decreased sharply, allowing for a tracer decay test to be implemented—this period is represented by section 1 of Fig. 2. A linear regression was performed as a plot of $\ln \left(\frac{CO_{2,RA} - CO_{2,OA}}{CO_{2,RA,t=0} - CO_{2,OA}} \right)$ vs. time, where $CO_{2,RA}$ is the concentration of CO_2 in return air (ppm), $CO_{2,RA,t=0}$ is the concentration of CO_2 in return air at t = 0 (ppm), and $CO_{2,OA}$ is the concentration of CO_2
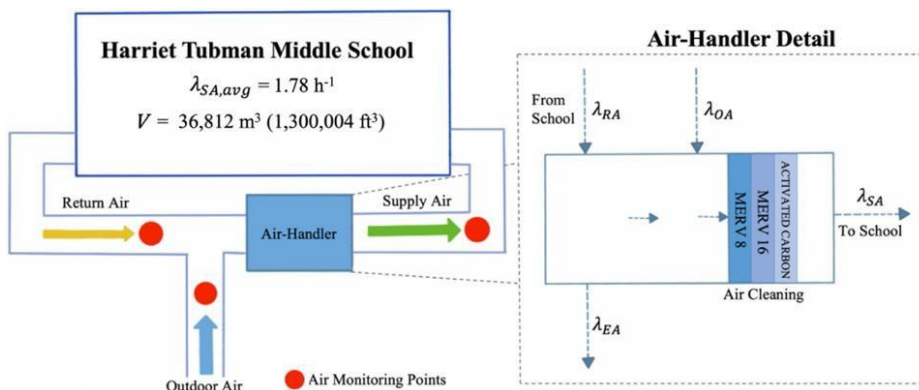

Figure 1. Schematic of Harriet Tubman Middle School and the renovated air-handler installed Summer 2018. The volume of the building is 36,812 m³ (1,300,004 ft³) and the average calculated supply air change rate ($\lambda_{SA,avg}$) through the school is 1.8 h⁻¹. λ_{RA}, λ_{OA}, and λ_{EA} represent the air change rates of return air, outdoor air, and exhaust air, respectively (h⁻¹). The air-cleaning system was outfitted with MERV 8, MERV 16, and activated carbon filters.
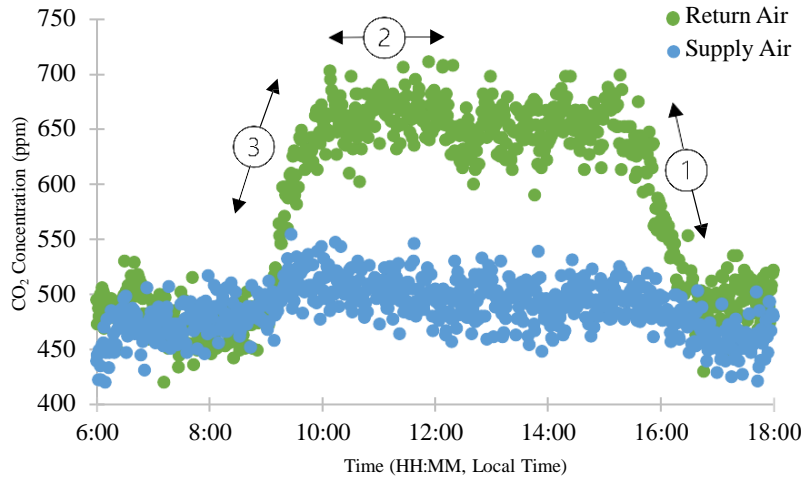
Figure 2. Decay (section 1), steady-state (section 2), and accumulation (section 3) period CO_2 concentrations (ppm) on May 28, 2019, during hours of air-handler operation (06:00-18:00).

outdoors, assumed to be constant at 420 ppm based on long- term monitoring of CO_2 at the site. The resulting slope yielded the outdoor air exchange rate of the school (h^{-1}). CO_2 concentrations in return air reached relatively consistent steady-state levels for a prolonged period of time each occupied day, excluding May 30, 2019 (which was subsequently excluded from the analysis). These stable occupancy periods were determined by visual inspection of CO_2 time-series data for May 28, 29, and 31, 2019, and concentrations of CO_2 were averaged over the stable occupancy period for subsequent calculations. This period is represented by section 2 of Fig. 2. In order to account for a day-to-day variability in occupancy, a refined calculation of the number of people (N) present during the stable occupancy period based on CO_2 generation rates was carried out, using the methods described in Persily, 2017 [11]. Average temperatures over the stable occupancy period and the total number of occupants as reported by Portland Public Schools were utilized to develop a conversion factor, and a per-person CO_2 generation rate of 30.4 g/h/person was calcuated. A steady-state mass-balance

on indoor CO_2 was developed (2), which could be solved for N, knowing λ_{OA} from period 1:

$$EF \times N = (CO_{2,RA} - CO_{2,OA})\lambda_{OA}V \qquad (2)$$

Here, EF is the CO_2 generation rate calculated prior to per-person normalization (g/h), N is the number of people present, $CO_{2,RA}$ is the return air CO_2 concentration averaged over the stable occupancy period, $CO_{2,OA}$ is the outdoor CO_2 concentration, assumed to be 420 ppm, λ_{OA} is the outdoor air exchange rate (h^{-1}), and V is the building's volume (m^3).

When students and faculty entered the building, a sharp rise in return air CO_2 concentration was apparent, which is represented by section 3 of Fig. 2. This accumulation period was used to calculate the supply air flowrate through the school on each occupied day. A correction factor was established to calibrate the CO_2 sensors using return and supply air concentrations in the early morning hours (2:00-4:00). Return air CO_2 concentrations were modeled as shown in (3) and a discretized solution was employed to account for the multiple dependent variables changing in time, $CO_{2,RA}$ and $CO_{2,SA}$ (4).

$$\frac{dCO_{2,RA}}{dt} = \lambda_{SA}CO_{2,RA} - \lambda_{SA}CO_{2,SA} + \frac{EF \cdot N}{V} \qquad (3)$$

$$CO_{2,RA}^{t+\Delta t} = (\lambda_{SA}CO_{2,RA}^{t} - \lambda_{SA}CO_{2,SA}^{t} + \frac{EF \cdot N}{V})\Delta t + \qquad (4)$$

Here, λ_{SA} is the supply air change rate (h^{-1}), and all other terms are as defined previously.

The sum of squared errors was then calculated over a series of timeframes that included the accumulation period and a variable period of the stable occupancy directly following it. The Solver tool in Microsoft Excel was employed with the objective set as the sum of squared errors and the changing variable cell set as λ_{SA}. The goal was to reduce the sum of squared errors, and thus the Solver tool was set to find a minimum, using the GRG non-linear method—the unconstrained variables were left non-negative. The supply air change rate through the school was returned. In order to converge on a number of minutes following the accumulation period to include, the Solver tool in Microsoft Excel was employed several times, with each solution increasing the stable occupancy periods by five minutes until stability with regard to λ_{SA} was realized.

D. *Source Strength Analysis*

In order to determine VOC source strengths, an approach based on mass balance equations was used, similar to that present in the literature [12]. In order to model source strengths due to occupancy alone, we first required the emission rate in the absence of occupants. For this, we used data extracted from May 27, 2019—a day chosen because the school was unoccupied due to the Memorial Day holiday, but because it was a weekday, the air handler operated as normal. Data obtained from this holiday allowed for the isolation of VOC emissions caused by non-occupancy sources, which could be subtracted from total indoor emissions on the occupied day in order to separate for human contributions. It was assumed that the supply air change rate through the school would not be affected significantly by occupancy, and thus the average λ_{SA} value of the three occupied days was utilized for the unoccupied day's calculations.

Further investigating Eq. 1, the first term on the right side represents the net VOC removal (or possibly a source or negative removal, henceforth simply referred to as net

removal) due to airflow through the school, while the second term on the right side accounts for net VOC accumulation inside the school during the analysis period. The terms that include C_{RA} and C_{SA} can be considered time averages over the stable occupancy period, multiplied by its duration. The integral in the net removal expression can be considered the difference between the final and initial return air concentration values, also taken over the stable occupancy period. In order to find emission rates, the mass emitted—whether from indoor sources in total (E_{indoor}), supply air (E_{supply}), or the vacant building itself ($E_{building}$)—is divided by the duration of the stable occupancy period. To arrive at per-person emission rates, the difference between E_{indoor} and $E_{building}$ is divided by N, the number of people present during the stable occupancy period, as calculated previously.

Results and Discussion

A. Airflows

The project's building contractor estimated that the air flowrate through the school was approximately 67,960-101,941 m³/h (40,000-60,000 cfm), a metric used to confirm the accuracy of the average calculated air flow rate from the three-step approach described above, which was 65,893 m³/h (38,783 cfm). As stated previously, Portland Public Schools projected the total number of students and faculty to be 505, which is in close alignment with average calculated occupant density. A summary of these findings is presented in Table 1:

TABLE 1
SUMMARY OF AIR CHANGE RATES AND OCCUPANT DENSITY

Date	Outdoor Air Change Rate (h⁻¹)	Supply Air Change Rate (h⁻¹)	Occupant Density (# of people)
05/28/19	0.85	1.97	448
05/29/19	0.87	1.68	540
05/31/19	1.15	1.71	552
Average	0.96	1.79	513

B. VOC Source Strength Apportionment

While a total of 249 compounds were analyzed, for the purposes of this study, eleven were chosen to be investigated further and reported. The first seven (isoprene, monoterpenes, acetone, formaldehyde, ethanol, methanol, and acetaldehyde) are compounds known to be associated human metabolism or human activity. Isoprene and acetone are byproducts of human metabolism, while monoterpenes are commonly linked to human activities such as the application of personal care products and cleaning. Formaldehyde, which is difficult to quantify using a PTR-ToF-MS instrument [13], can be released from products such as furniture, building materials, and food, and is emitted in small quantities by humans. Ethanol, methanol, and other alcohols are known to be associated with the exhalation of human breath [14], and acetaldehyde is formed in the body due to the breakdown of ethanol. Furthermore, the analysis was conducted on four BTEX compounds (benzene, toluene, xylenes, and ethylbenzene—the latter of the two, as isomeric compounds, could not be distinguished by the PTR-ToF-

MS instrument) that are associated with TRAP. Because these pollutants are not emitted by humans (or may be emitted in very small quantity), their presence indoors in a near-roadway building is likely due to outdoor air ventilation and the infiltration of TRAP through doors, windows, and leaks present in the building. An additional criterion that was kept in mind when selecting VOCs to be investigated was their volatility; the compounds chosen needed to be volatile enough for us to rule out potential interference from the tubing attached to the PTR-MS instrument. The VOCs selected here for in-depth analysis are volatile species, expected to have modest interaction with both the tubing and instrument itself. Prior studies conducted similar analyses with similar instrumentation on the same compounds, ultimately deciding to not explicitly account for tubing and instrument interference [13]—this informed the VOC selection process.

The underlying goal of this study, and often air pollution studies in general, is to apportion air pollutants to their sources in order to understand the relative importance of contributors to a compound in a space. Table 2 provides a source apportionment for the 11 compounds of interest. Emission rates are divided into four categories: E_{indoor}, the total emission rate of the occupied school, E_{supply}, the emission rate as recorded at the supply air monitoring point, immediately after air-cleaning, $E_{building}$, the emission rate of the vacant building, due likely to building materials, cleaning products, etc., and $E_{per-person}$, which is the difference between E_{indoor} and $E_{building}$, normalized by the number of people present.

TABLE 2
VOC SOURCE APPORTIONMENT FOR 11 COMPOUNDS

Compound	E_{indoor} (mg/h)	E_{supply} (mg/h)	$E_{building}$ (mg/h)	$E_{per-person}$ (µg/h/person)
Isoprene	193	61	58	269
Monoterpenes	169	20	28	281
Acetone	930	217	882	1335
Formaldehyde	70	81	51	39
Ethanol	313	255	-73	771
Methanol	531	647	358	347
Acetaldehyde	673	311	379	587
Benzene	9	22	4	10
Toluene	5	12	0	10
Xylenes/ Ethylbenzene	6	1	5	2

Reported in further detail with Fig. 3 is the source apportionment for two select compounds, monoterpenes, which are associated with human activity, and benzene, which is a known TRAP constituent. The source strength for *Occupants* is the difference between the E_{indoor} and $E_{building}$ values from Table 2, where $E_{building}$ is represented by *Building*. *Supply* is the E_{supply} value from Table 2, which is broken into a percentage distribution of *Recirculation*, or return air, and *Outdoor* contributions. Data taken at the supply air monitoring point consists of a combination of return air and outdoor air after being passed through the air-cleaning system (Fig. 1). Average VOC concentrations and ventilation rates in return and outdoor air are used determine the recirculation and outdoor percent contributions to mixed air.
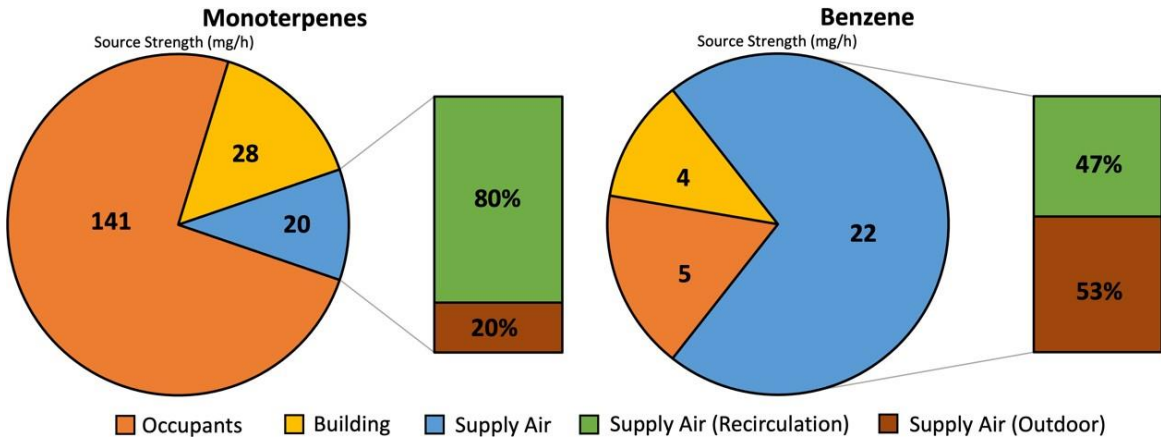
Figure 3. A source apportionment for two select compounds of interest: monoterpenes, which are associated with human activity, and benzene, which is associated with vehicle exhaust

As expected, for VOCs typically associated with human activity such as monoterpenes, occupant contributions account for the highest percentage of apportionment— acetone is a notable exception, for it is present in both vehicle exhaust and human metabolism. In contrast, it is clear that for benzene and toluene (two BTEX compounds), supply air accounts for the highest percentage of apportionment. This suggests that TRAP is entering the school after being pushed through the air-cleaning system, albeit at reduced concentrations than would be present absent the activated carbon scrubber.

C. Per-person VOC Emission Rate Comparison

Three other studies also seeking to quantify per-person VOC emission rates in public places served as an reference for this work [12], [13], [15]. Experimental conditions varied substantially across each study and in the work reported here. First, [12] took place in a university classroom setting, with anywhere between 26 to 67 college-

aged students present during a stable occupancy period. [15] took place at a cinema that held at any one time between 50 and 230 people, and was arranged to distinguish between VOCs emitted by adults and children. Finally, [13] was conducted inside of a university art museum that nearly 300 people cycled through in the course of an evening. In contrast, in 2019 Harriet Tubman Middle School reportedly had 505 students and faculty enrolled or employed at their institution, with approximately 93% of them being children between the ages of 11 and 16. Fig. 4 provides a comparison of per-person emission rates between these four studies for four select compounds associated with human activity: isoprene, monoterpenes, acetaldehyde, and ethanol.

The calculated per-person emission rates were generally consistent with prior studies, with slightly higher emission rates reported for isoprene, monoterpenes, and ethanol than prior studies. VOC emissions from human metabolism, such as isoprene, may have been higher due to eating and
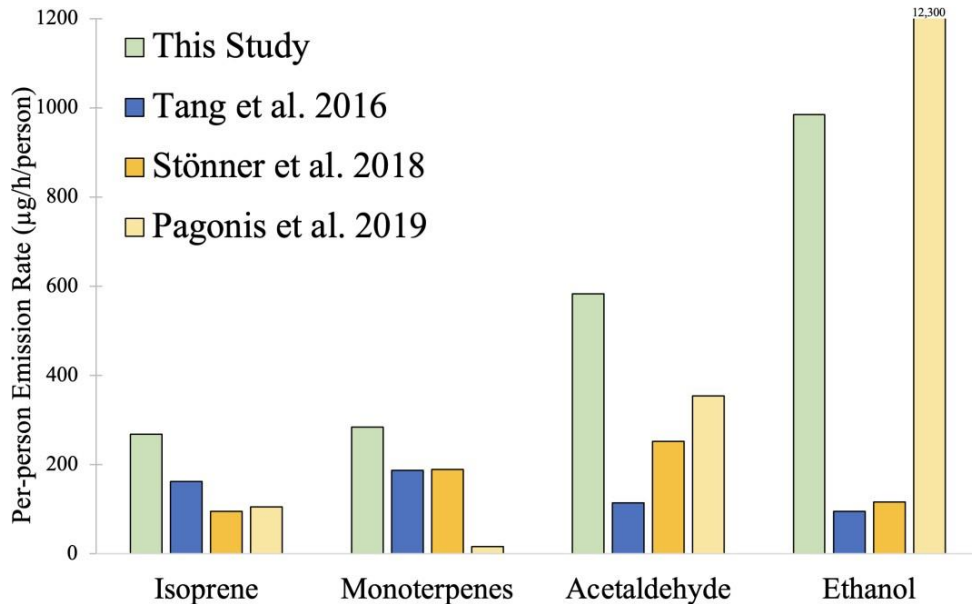

Figure 4. Comparison of per-person emission rates for four select VOCs that are associated with human activity to three studies.

physical exercise activities inside the school, while elevated monoterpenes emissions may have been associated with an increased usage of scented personal care products in the studied middle-school population. Ethanol emissions may have been higher due to hand sanitizer and cleaning products used frequently in the middle school environment.

Conclusion

Advances in building science typically prioritize lowering VOC emissions from materials and improving ventilation infrastructure. Progress being made in these areas, in combination with facilities that are built to be more and more airtight, may lead to the possibility that humans themselves become the primary source of indoor VOCs. While prior experiments have quantified per-person VOC emission rates [12], [13], [15], there exist few studies relative to the diversity of indoor environments and varying demographics that occupy those spaces. Humans emit VOCs at different rates under different conditions, spaces are comprised of different materials, etc., and thus it is worthwhile to explore which conditions lead to which range of source strengths.

While outdoor air brought into an indoor environment is assumed to be clean, this is not always the case—investments in ventilation must take this fact into account. The campaign from which this data was extracted [9] assessed the effectiveness of the renovated HVAC system for TRAP constituents elevated near roadways, and showed that BTEX compounds were being removed from outdoor air before entering the school.

This study provides new data concerning VOC source strengths of indoor and outdoor origin to a building, which can enable the modeling of air pollution exposures in schools. Harriet Tubman Middle School is unique, in that it has the benefit of particle and gas-phase air cleaning systems—source strength results are likely to vary across buildings. Future studies in more buildings are critical for characterizing sources of pollution in environments that house susceptible populations, such as schools.

REFERENCES

1   N. E. Klepeis *et al.*, "The National Human Activity Pattern Survey (NHAPS): a resource for assessing exposure to environmental pollutants," *J. Expo. Anal. Environ. Epidemiol.*, vol. 11, no. 3, pp. 231–52, Jun. 2001, doi: http://dx.doi.org.proxy.lib.pdx.edu/10.1038/sj.jea.7500165.

2   M. Phillips, "Method for the collection and assay of volatile organic compounds in breath," *Anal. Biochem.*, 1997, doi: 10.1006/abio.1997.2069.

3   J. G. Allen, P. MacNaughton, U. Satish, S. Santanam, J. Vallarino, and J. D. Spengler, "Associations of cognitive function scores with carbon dioxide, ventilation, and volatile organic compound exposures in office workers: A controlled exposure study of green and conventional office environments," *Environ. Health Perspect.*, 2016, doi: 10.1289/ehp.1510037.

4   J. M. Logue, T. E. Mckone, M. H. Sherman, and B. C. Singer, "Hazard assessment of chemical air contaminants measured in residences," *Indoor Air*, 2011, doi: 10.1111/j.1600-0668.2010.00683.x.

5   E. T. Gall, "Indoor and outdoor air quality at Harriet Tubman Middle School and the design of mitigation measures: Phase I report," 2018.

6   HEI, "Traffic-Related Air Pollution: A Critical Review of the Literature on Emissions, Exposure, and Health Effects," *Spec. Rep. Institute's Panel Health Eff. Traffic-Relat. Air Pollut. Health Eff. Inst.*, 2010.

7   S. L. Kingsley *et al.*, "Proximity of US schools to major roadways: A nationwide assessment," *J. Expo. Sci. Environ. Epidemiol.*, 2014, doi: 10.1038/jes.2014.5.

8   I. Rivas, X. Querol, J. Wright, and J. Sunyer, "How to protect school children from the neurodevelopmental harms of air pollution by interventions in the school environment in the urban context," *Environ. Int.*, 2018, doi: 10.1016/j.envint.2018.08.063.

9   A. Laguerre, L. A. George, and E. T. Gall, "High-Efficiency Air Cleaning Reduces Indoor Traffic-Related Air Pollution and Alters Indoor Air Chemistry in a Near-Roadway School," *Environ. Sci. Technol.*, 2020, doi: 10.1021/acs.est.0c02792.

[10]   W. Lindinger, A. Hansel, and A. Jordan, "Proton-transfer-reaction mass spectrometry (PTR-MS): on-line monitoring of volatile organic compounds at pptv levels," *Chem. Soc. Rev.*, vol. 27, no. 5, pp. 347–354, 1998, doi: 10.1039/a827347z.

[11]   A. K. Persily and L. De Jonge, "Carbon dioxide generation and building occupants." 2017.

[12]   X. Tang, P. K. Misztal, W. W. Nazaroff, and A. H. Goldstein, "Volatile organic compound emissions from humans indoors," *Environ. Sci. Technol.*, 2016, doi: 10.1021/acs.est.6b04415.

[13]   D. Pagonis *et al.*, "Time-Resolved Measurements of Indoor Chemical Emissions, Deposition, and Reactions in a University Art Museum," *Environ. Sci. Technol.*, 2019, doi: 10.1021/acs.est.9b00276.

[14]   J. D. Fenske and S. E. Paulson, "Human breath emissions of VOCs," *J. Air Waste Manag. Assoc.*, 1999, doi: 10.1080/10473289.1999.10463831.

[15]   C. Stönner, A. Edtbauer, and J. Williams, "Real-world volatile organic compound emission rates from seated adults and children for use in indoor air studies," *Indoor Air*, 2018, doi: 10.1111/ina.12405.

2nd Place
REHVA
Student Competition

Amila Strikovic
France

Reuse-LCA:
Identification of the reduction potential of the environmental
impacts of Swiss Buildings through material reuse

Reuse-LCA :
Identification of the reduction potential of the environmental impacts of Swiss buildings through material reuse.

Amila Strikovic - strikovicamila@gmail.com[1], Kyriaki Goulouti – LESBAT (Avenue des Sports, 1400 Yverdon-les-Bains, Suisse)[2], Carmen Müller – INSA Strasbourg - carmen.vasile-muller@insa-strasbourg.fr[3]

Abstract - Since Switzerland engaged to halve its CO_2 emissions by 2035 compared to 2000 and become carbon neutral by 2050, it is essential to act on one of the most polluting sector, which is the buildings by focusing on the most effective strategies to reduce the impacts during the manufacturing and demolition of the building. It is in this context that my master thesis project is inscribed, with the aim of calculating the life cycle analysis (LCA) of different buildings integrating reused materials, reuse still not being widely used and applied, by using 3 new LCA methodologies. Subsequently, the Reuse-LCA project will be extend to other buildings with different reuse strategies in order to have a large sample, and thus make these data and calculation methods available to all construction trades through the SIA 2032 standard.

Index Terms – Reuse, LCA, Building, Materials

Introduction

Industrialization has brought economic prosperity; additionally, it has resulted in urbanization, material prosperity, leading to the consequent depletion of the environmental resources and the degradation of the world's ecosystems. Specifically, the building sector is responsible for more than a third of all solid waste and greenhouse gas emissions in Europe [1]. In Switzerland, while 30% of the GHG emissions are due to construction of building materials, which represents approximately 650 kg CO_{2-ea}/m^2 [2]. Until now, measures have been taken, in order to consume less energy during the operational. However, the construction and demolition of building represents still an important share in the

environmental impact. Thus, in the context of the 2050 environmental strategy, it is necessary according to the Swiss policy to focus on the circular economy in the building sector, in the Swiss' path to carbon neutrality.

One of the oldest and relatively widespread techniques, which has regained its value during the past years, primarily because of the significant benefits, linked to the environment's preservation, is the reuse of the materials. Different definitions exist, concerning the reuse of materials. Generally, this term refers to the recovery of building components during the demolition, refurbishment or transformation phase of a building and their application in another building. Different strategies of reuse exist that allow keeping as much as possible material in a second life cycle and therefore preserving the environment. **Error! Reference source not found.**, presents the principle of **reuse, repurpose**, which includes the **upcycling** and **downcycling** methods. Through **upstream reuse**, the components are reused from **other sites**, the **same site** or even **market reuse**. The materials recovery is facilitated through the **downstream reuse**. Finally, **adaptive reuse** is a sort of maximized building transformation: all or most of the building systems are retained.

FIGURE 1: DIFFERENT STRATEGIES OF REUSE
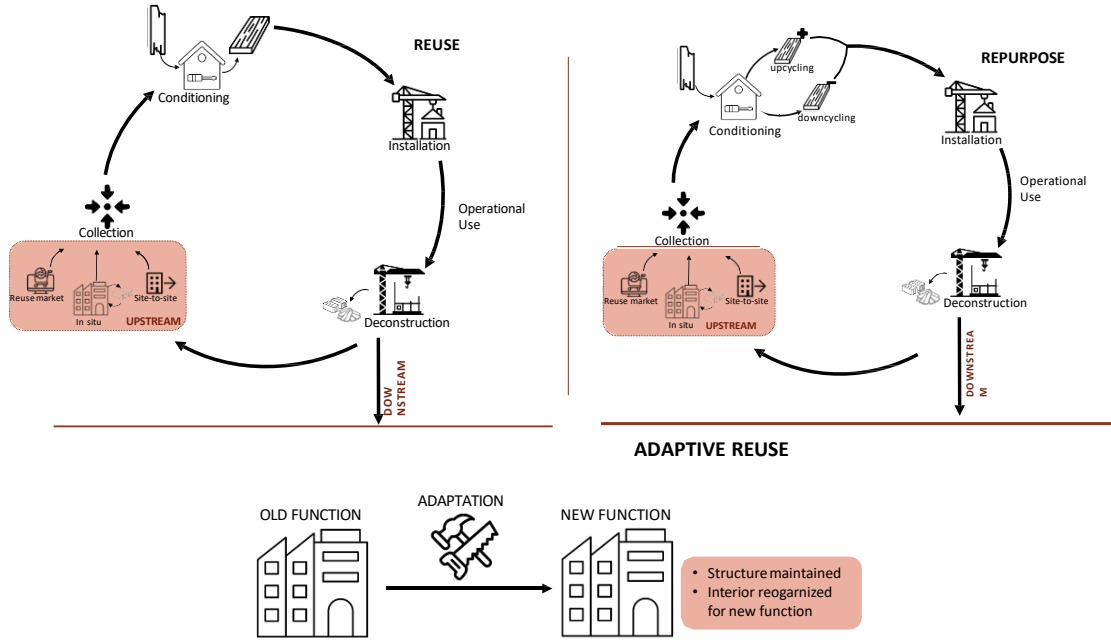
I. AIM OF THE PAPER

This master thesis project is part of the Reuse-LCA project, which aims to raise awareness of the subject of reuse and its importance in the alarming environmental context. The general objective of this master project is *the analysis of the environmental impacts of the reused building materials*. For this reason, two case studies were chosen, i.e. the 'ELYS', a building located in Basel and the 'TOUR FIRMENICH', located in Geneva, see **Error! Reference source not found.**. These case studies are real building projects that include reused and new materials, while the reuse strategy for each case study has already been defined by the architects, during the design phase of the buildings. Thus, the *environmental impacts of the reused materials* will be defined, through the environmental analysis of specific building components of these case studies that include reused materials. The results of these studies can be used to create a database where future studies from the research project and other studies from a systematic review can be found

FIGURE 2: *WORKPLAN FOR THE ANALYSIS OF THE TWO BUILDING CASE STUDIES*
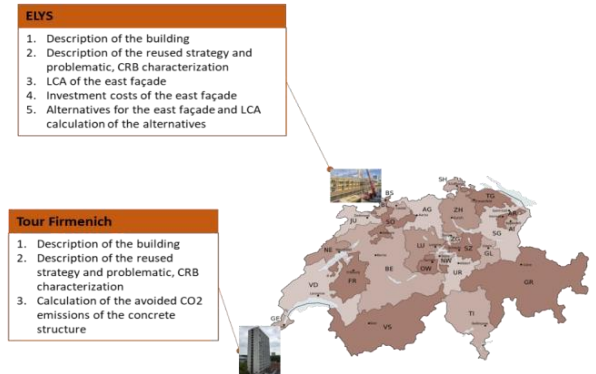
II. METHODOLOGY

In order to evaluate the environmental impacts and gains of the reused building materials, the Life Cycle Assessment (LCA) was used. In the building sector in Switzerland, the SIA 2032 Swiss standard sets all the rules for the LCA [3]. The different stages of the building life cycle for new and reused materials, with black and green, respectively are presented in **Error! Reference source not found.**. The environmental impact of a building is divided in the different stages occurring along the life cycle of the building, i.e., construction stage that includes the manufacturing/end-of-life of the materials, as well as the construction/deconstruction of the building and the operation stage of the building. The basic building LCA is calculated using the equation defined in the SIA 2032, in which two impact indicators are used in this

project, the NRE Non-Renewable Energy, the GHG (Greenhous Gas) emissions.

The reuse of the building components starts at the end of the use phase of the building, before its deconstruction and thus through the material reuse, the emissions and energy consumption of stages C1 to C4 can be saved. Thus, the basic LCA methodology defined according to the SIA 2032 was not suitable to buildings project with reused materials. Therefore, the architect K.Pfäffli has established tree alternative methods, which roles are to adapt the current methodology [4]. They will be presented hereafter in order to discuss how the environmental impacts of the reused materials can be allocated.

First calculation method:

The environmental impact of the reused materials is calculated using the equation below:

$$LCA_{tot} = \sum LCA_{Manufacturing} \times residual\ value\ (\%) + \sum LCA_{replacement} + \sum LCA_{disposal} \times residual\ value (\%) \quad (4)$$

$$\sum LCA_{replacement} = \sum (LCA_{Manufacturing} + LCA_{Disposal}) * k \quad (5)$$

$$k = \frac{RSP}{SL} - 1 \times residual\ value (\%) \quad (6)$$

According to these first method "amortization period", the environmental impact of a reused material (i.e. impacts from A1-A3 to C1-C4 and B4 in **Error! Reference source not found.**) has been partially amortized, during its first life cycle, meaning that only a "residual value" of the impact is considered in the further cycle. This residual value corresponds to a fraction of the years that the materials was installed in the first cycle.

Second calculation method:

According to the method "additional impacts", no impacts for the stages A1-A3 or C1-C4 are considered, as they were amortized in their first life cycle. However, this method takes into account the additional costs that arise from reuse, as for example the disassembly, the material treatment, etc. This method is divided in two variants: variant 2a takes into account all the additional environmental impacts, while variant 2b only the additional impacts that correspond to the impacts considered for the new materials (in green, **Error! Reference source not found.**).

FIGURE 3: LIFE CYCLE ASSESSMENT TO SIA 2032:2020
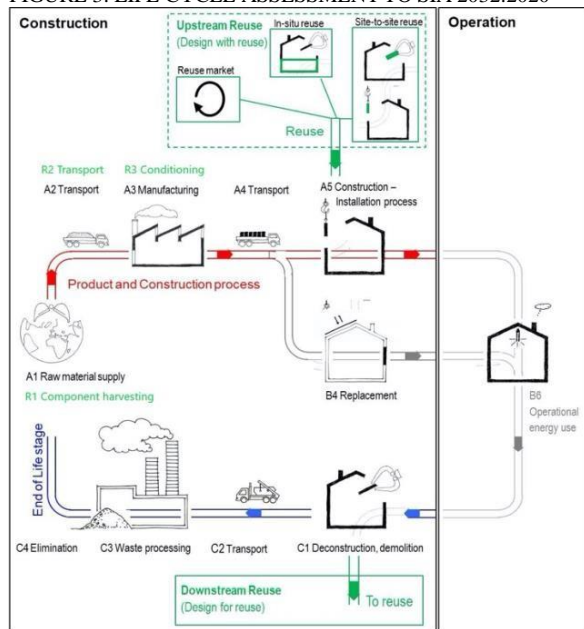
The following equation is therefore used for the environmental impact:

$$LCA_{tot} = \sum LCA_{disassemble/assembly} + \sum LCA_{transport} + \sum LCA_{treatment} + \sum LCA_{replacement}$$

$$LCA_{dismantling-assembly-treatment} = \sum P_{el} \times T_{op} \times LCA_{elec.mix}$$

$$LCA_{transport} = \sum D_{site} \times M_{material} \times LCA_{lorr}$$

Where:

P_{el}	Power consumption	[kW]
T_{op}	Operating time of the device	[h]
$LCA_{elec.mix}$	LCA of consumed electricity mix	[per kWh]
D_{site}	Distances from first construction site to intermediate site, distance from intermediate site to final site	km
$M_{material}$	Masse of the reused transported material	t

Third calculation method:

In the third, all the materials are considered as new materials. Thus, the LCA calculation follows the SIA 2032 basic methodology. Two alternative methods are also conceived, differentiating the in-site and site-to-site reuse. According to variant 3a, all the reused materials reclaimed on site are excluded from the balance, while variant 3b considers all the materials.

The environmental impacts of the manufacturing, deconstruction and related to the energy were calculated using the KBOB database. The nominal service life of the materials was given by SIA depending on the CRB characterization.

III. BUILDING CASE STUDIES AND RESULTS

The studies of the pilot buildings presented hereafter, each presenting different reuse strategy, will give a first overview on the environmental impact of the reused materials using the methodologies presented in paragraph **Error! Reference source not found.**, which will be completed by other case studies.

a. First building case study: 'la Tour Firmenich'

FIGURE 4: VIEW OF 'LA TOUR FIRMENICH'

This 16 floors building located in Geneva, with an energy reference area of 7885 m², is subject to a refurbishment and transformation. The structure of the building is made out of concrete, which is totally maintained, i.e. concrete columns, floors, walls, and some of the interior walls, while all the finishing (claddings, insulation and windows) is going to be replaced. Thus, the strategy of adaptive reuse was applied in this building. After an inventory of the building materials, it was calculated that reused materials, mainly composed of concrete represented 97% of the total mass of the building with 1,366 tonnes. It can be supposed that the concrete elements will present the greatest reuse potential. Three of the methodologies presented in the paragraph **Error! Reference source not found.** were used for the LCA calculation: methodology 1 (scenario 1), methodology 3a (scenario 2) and methodology 3b (scenario 3).

Figure 5 presents the results of the environmental impacts according to the three methods. It shows that through adaptive reuse, approximately 75% and 65% of the GHG emissions and NRE respectively, are saved. The slight difference in the impacts (2%) between the 1st method and the 2nd is that the reused concrete is not yet amortized in the first one. These results confirms the supposition of the reused potential mentioned in the paragraph before.

FIGURE 5: *ENVIRONMENTAL COMPARISON OF THE THREE METHODOLOGIES*
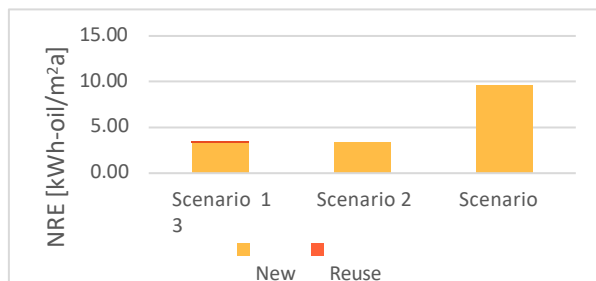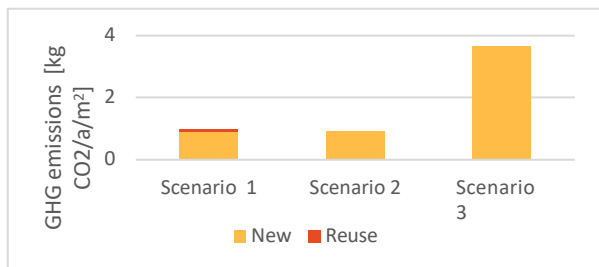
a. Second case study: ELYS

This building composed of three floors is also a renovation project, which will accommodate different cultural facilities (sports hall, cultural centres, music rooms, etc.). Owing the large size of the building, the basis of the study was the south wall of the building, with a surface area of 515 m² (see Figure 6). This wall is divided into prefabricated wooden modules made of essentially reused materials, using site-to-site and in-situ reuse. In the reused materials, we can count the 40% of the wood for the structure, the insulation, the windows and the metal sheets, representing in total 50% of the façade's mass.
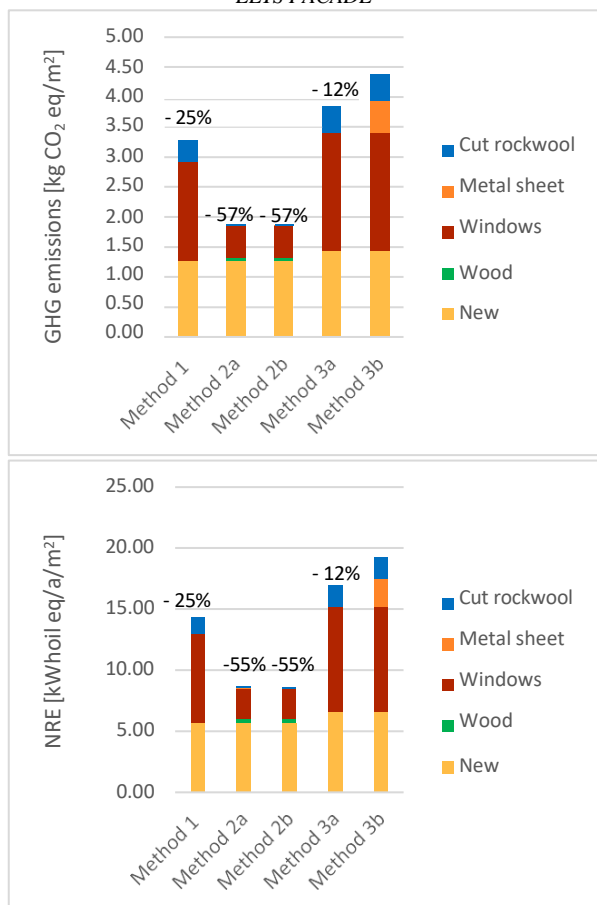

FIGURE 6: SHOT OF THE SOUTH WALL OF THE BUILDING ELYS

The three methodologies for the LCA calculation of the reused materials, already presented in paragraph **Error! Reference source not found.** will be used in order to evaluate the environmental impacts and gains of the reused materials.

The results of the different approaches are presented in Figure 7, for the GHG emissions and NRE indicators. The comparison are based on the third scenario, which presents the highest environmental impacts, since all the materials are considered as new. The impacts can be reduced by about 25% for the 1st method, to significantly more than half for method 2. This makes the potential of reuse obvious. The additional savings through in-situ reuse of the metal sheet is presented by the method 3a, which are about 12%. It should be noted that method 2a and 2b present similar result, which is explained by the fact that assumptions are almost the same. Even though, windows represent 10% of the total mass, it accounts a large share of the indicators, as their unit impact is very important. The cut rockwool is responsible for 11% and 1% of the impacts for the 1st and 2nd method respectively; this gap is explained by the fat that no treatment was required. Wood presents the minor share on the impacts, as it is a bio-based material originally.

FIGURE 7: COMPARISON OF THE METHODOLOGIES FOR ELYS FACADE

that the structure was made of 100% reused wood. It was shown that even though, the impacts are reduced to approximately 10% with the 100% reused scenario, the investment costs is 20% more expensive. The scenario "as built" will be privileged to the other scenario.

CONCLUSION

In order to reduce the environmental impacts of the sector buildings especially during the construction of the building, implementation of reuse strategies is necessary, and its effectiveness has been proven through these 2 case studies. However, it is necessary to complete these results with others. While reuse give promising results, its application is still not widespread in the construction field. Today's architects and technicians do not have enough knowledge and experience on reused materials. Therefore, it time and expenses for designing a building with reused materials. This is accented by the fact that the buildings are not designed so that the materials can be easily dismantled. These extra costs is still the major obstacle to reuse strategy. Thus, the goal of this study and more generally, the project "Reuse LCA" is to raise awareness and put these strategies forward in order to facilitate the implementation of reused materials in the building sector.

ACKNOWLEDGMENT

REFERENCES

[1] -, «European Comission,» April 2008. [En ligne]. Available: https://ec.europa.eu/growth/sectors/construction_ en.

[2] S. Lasvaux, «Reuse-LCA Full Proposal 301120,» 2020.

[3] C. T. SIA, *SIA 2032: l'énergie grise - Etablissement du bilan écologiaue pour la construction de bâtiments,* 2020.

[4] K. Pfäffli, «Graue Energie und Treibhausgasemissionen von wieder- verwendeten Bauteilen Methodik und Berechnung in Varianten am Fallbeispiel Gebäude K118 in Winterthur,» 2020.

IV.   DISCUSSION

This section discusses on the different methodologies used for the Elys calculation. As mentioned in paragraph 4, the 1st and 2nd methodologies gave very different results, which is explained by the assumptions they make for the calculation. Both of them can be questioned: on one hand, the 1st methodology penalises the reused materials with a short, amortised period, which can be as performant as new materials. On the other hand, the 2nd method is considered as the most consistent methodology for the calculation of the reused components in the Swiss context since the manufacturing and disposal impact were already considered in their first life. However, problems linked to the availability of the necessary data of the reused materials, hinders the wide use of the method.

The reuse strategy on the building Elys was confronted with another strategy: changing the reused insulation by bio-based insulation: cellulose wadding and flax insulation. After an analysis according to three criteria, i.e. environmental impact, financial cost, heat losses, presented in Figure 8 it can be concluded that the bio-based scenarios presents promising results and could be considered for this project. Even though, the scenario "as built" is still more globally advantageous, the cellulose-wadding scenario presents results that are closer than the flax insulation scenario. The last scenario considered

3rd Place
HVAC World
Student Competition

Mizuho Akimoto
Japan

Effects of Bedroom Ventilation and Thermal Environment on Sleep Quality

Mizuho Akimoto Waseda
University, Tokyo, Japan

Abstract— This research comprises a collection of studies mainly focusing on the relationship between sleeping environments and sleep. The objective was to investigate the effects of the ventilation and the thermal environment in the bedroom on sleep quality. Four different methods, a literature review, air distribution measurements in the bedrooms, an online questionnaire survey, and field measurements with human subjects, were used to examine various aspects. First, results indicated that poor bedroom ventilation consistently has a negative impact on sleep quality and next-day performance. Second, focusing on air inhaled by a person, a carbon dioxide (CO_2) sensor located in the bedroom near the head of the person at a 0.5 m distance as found to indicate realistic CO_2 exposure during the nighttime. Third, concerning the changes in lifestyles and work styles associated with COVID-19, the conversion of the bedroom into a workplace was shown to be potentially problematic, even though increased ventilation in the bedroom is expected to affect sleep positively. Finally, with regard to the occurrence of awakenings during sleep, it was observed that the ventilation of bedrooms in hot and humid regions such as Japan requires simultaneous dehumidification.

Index Terms— Sleeping environment, Air change rate, Carbon dioxide, COVID-19, Human heat load

I. INTRODUCTION

On average, humans spend more than 20 years (approximately one-third of our lives) in bedrooms. Good sleep is essential for health and daytime functioning; 7–9 hours of sleep is recommended every night for people aged 18 to 64 years. To date, most research on sleep has focused on labs and characterizing sleep, but little work has been performed on the effects of bedroom indoor environmental quality (IEQ). IEQ research has mainly focused on offices, schools, and dwellings. However, even in the latter case, research is less abundant than that for other environments, and there is limited evidence regarding the conditions in bedrooms. Considering that people are exposed to the same environment for approximately 7–9 hours per day and cannot control bedroom conditions during sleep, it is imperative to secure a high quality bedroom environment for good sleep.

Noise, light, temperature, and air quality have an essential role in sleep [1]. In particular, only a limited number of studies has examined the effects of air quality and ventilation on sleep. Considering that poor indoor air quality (IAQ) impairs physical and cognitive well-being [2], it is worth investigating the effects of not only the thermal environment but also bedroom ventilation on sleep quality.

Fig. 1 shows the framework of the research. The objective of this study was to investigate the effects of ventilation and thermal environment in the bedroom on sleep quality. Four different methods, specifically a literature review, air distribution measurements in the

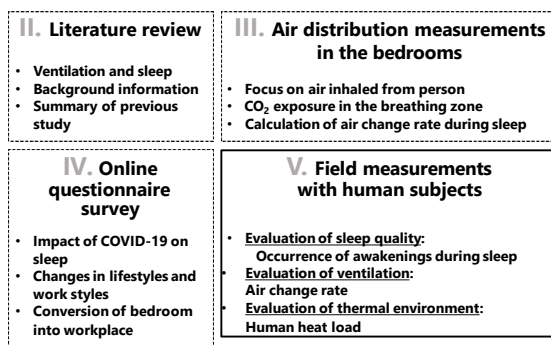| II. Literature review	III. Air distribution measurements in the bedrooms
• Ventilation and sleep • Background information • Summary of previous study	• Focus on air inhaled from person • CO_2 exposure in the breathing zone • Calculation of air change rate during sleep
IV. Online questionnaire survey	V. Field measurements with human subjects

• Impact of COVID-19 on sleep
• Changes in lifestyles and work styles
• Conversion of bedroom into workplace
	• **Evaluation of sleep quality:**
	   Occurrence of awakenings during sleep
	• **Evaluation of ventilation:**
	   Air change rate
	• **Evaluation of thermal environment:**
	   Human heat load

Figure 1. Framework of the research

bedrooms, an online questionnaire survey, and field measurements with human subjects, were used to examine various aspects.

II. LITERATURE REVIEW

This section reviews seven studies reported in six publications [3–8] that examined whether providing clean air to a sleeping person will result in improved sleep quality. This section provides information on the expected effects of bedroom ventilation and IAQ on sleep.

Materials/Methods

Seven published studies on bedroom ventilation, IAQ, and sleep quality were selected from the research by Sekhar et al. [9], who reviewed 46 previous studies reporting field measurements of carbon dioxide (CO_2) concentrations and the air change rate (ACR) in bedrooms. Because only two references addressed the ACR, the reported mean CO_2 concentration was used as a ventilation index, as shown in Fig. 2. It should be noted that these were not always intervention studies but rather observed a comparison between the higher and lower ventilation conditions indicated by lower/higher CO_2. Overlaps between the yellow and blue circles indicate that the difference between the high and low conditions in reported CO_2 levels was less than that in other studies. The location, sample size, ventilation system, venue, season, and sleep quality assessment method were selected from each study.

Results and Discussions

Fig. 2 shows that overall, poor bedroom ventilation, as indicated by increased levels of CO_2, has adverse effects on several aspects of sleep and can also result in poor cognitive performance the next day. Table I shows the tentative relationship between CO_2 levels and sleep. Different effects were observed at different IAQ levels, but generally, no negative effects were observed at and above the ventilation rates at which the CO_2 concentration in the bedroom was 835 ppm. Thus, it is recommended that the lowest rate of

Figure 2. Summary of the available studies examining the effect of bedroom ventilation (IAQ) on sleep quality
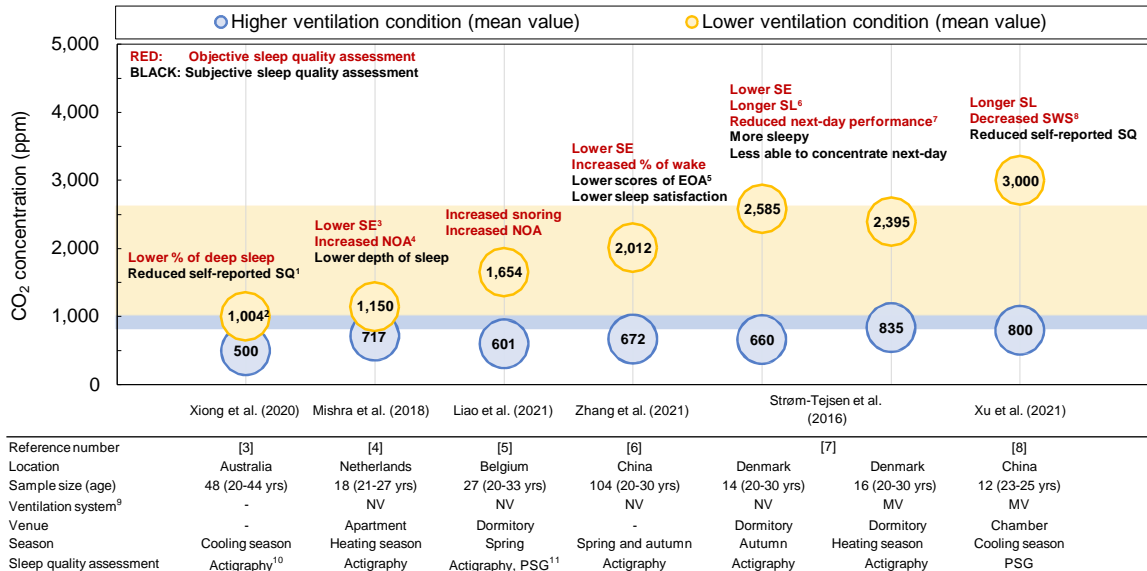
1 - SQ: sleep quality, 2 - the mean CO_2 concentration with a single occupant is adopted., 3 - SE: sleep efficiency, 4 - NOA: number of awakenings, 5 - EOA: ease of awakenings, 6 - SL: sleep onset latency, 7 - next-day performance: next-day performance of a logical thinking task, 8 - SWS: slow wave sleep, 9 - NV: natural ventilation, MV: mechanical ventilation, 10 - Actigraphy: a wrist-worn sleep tracker, 11 - PSG: Polysomnography

bedroom ventilation should be maintained at this level, ensuring that the bedroom CO_2 concentration is no higher than 835 ppm. Above this level, negative effects are more likely to occur, and significant effects have already been observed when the CO_2 concentration is as low as 1,004 ppm. Between 1,005 and 2,585 ppm, different effects on sleep quality were observed, whereas above 2,585 ppm, negative effects on next-day performance were also demonstrated. Based on these findings, a simple recommendation is to keep the bedroom CO_2 below 800 ppm and avoid higher levels because levels up to 2,600 ppm are likely to disturb sleep and those above this will decrease next-day performance.

Conclusions

The limited number of studies published to date has consistently shown that poor bedroom ventilation has negative consequences for sleep quality and next-day performance. Considering that poor bedroom ventilation has been reported not only in temperate but also in tropical climates and considering the sparse standards and guidelines for the ventilation of bedrooms [9], it would be prudent to intensify research in this area, extending it to studies on the thermal effects on sleep quality and their interaction with IAQ and other parameters.

III. AIR DISTRIBUTION MEASUREMENTS IN BEDROOMS

Whereas some studies have shown that providing outdoor air directly to the breathing zone of a sleeping person results in better sleep quality, most of the published literature has focused on the ventilation rate in the entire bedroom. To avoid higher exposure to CO_2 at night, it is vital to focus on the actual ACR using CO_2 measurements in the breathing zone during sleep. The main objective of this section was to investigate the spatial distribution of the CO_2 concentration close to the breathing zone of a sleeping person in bedrooms with natural ventilation (NV) and mechanical ventilation (MV).

TABLE I.
TENTATIVE RELATIONSHIP BETWEEN CO_2 LEVELS AND SLEEP

CO_2 levels		Tentative relationship
< 835 ppm		Undisturbed sleep quality range
835	– 1,004 ppm	Possibly disturbed sleep quality
1,005	– 2,585 ppm	Disturbed sleep quality range
> 2,585 ppm		Disturbed sleep quality range with possible reduced next-day cognitive performance

Materials/Methods

Field measurements were conducted in two residential buildings during the heating season in Denmark. The test site of the NV was a 2-story semi-detached house. The trickle vent on the bedroom window was kept open to provide NV during measurements. The test site of the bedroom with a balanced MV was an apartment with a mechanical inlet in each room. In the apartment, there was a mechanical outlet in the bathroom and kitchen hood exhaust based on NV, which always worked during the measurements. Fig. 3 shows the details of the test sites and CO_2 sensor (HOBO MX1102 CO_2 logger with an accuracy of ±50 ppm) locations. Notably, three sensors were kept at a 0.5 m distance vertically and horizontally around the subject's head to ensure the effects of sensor positioning around the immediate breathing zone of the sleeping person in the bedroom.

One adult occupied each bedroom during the experiment and slept throughout the night with the door closed. The person left the bedroom after waking up in the morning. The air temperature, relative humidity, and CO_2 level in the bedroom were recorded at 1-minute intervals. The ACR was estimated based on the CO_2 decay measured in the morning after a person left the room. All parameters were measured at night and in the morning during decay.
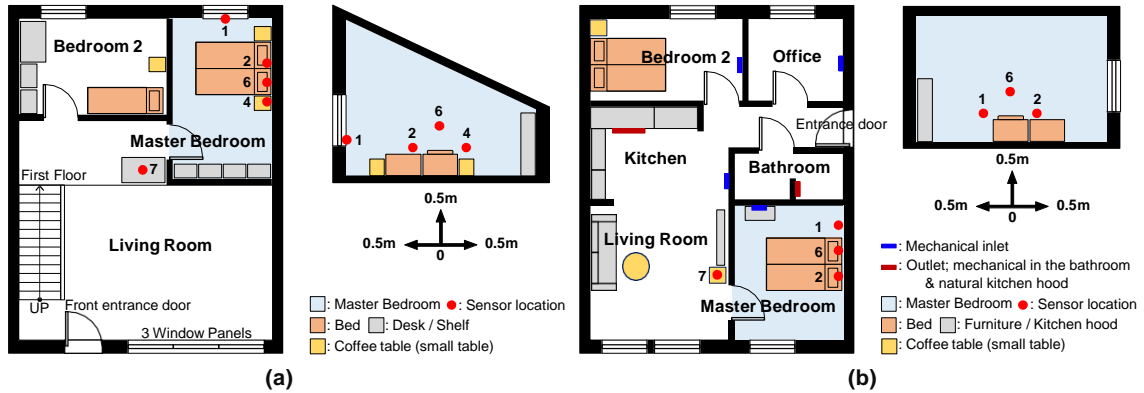
Figure 3.   Details of the test sites and CO_2 sensor's locations – (a): semidetached house (NV), (b): apartment (MV)
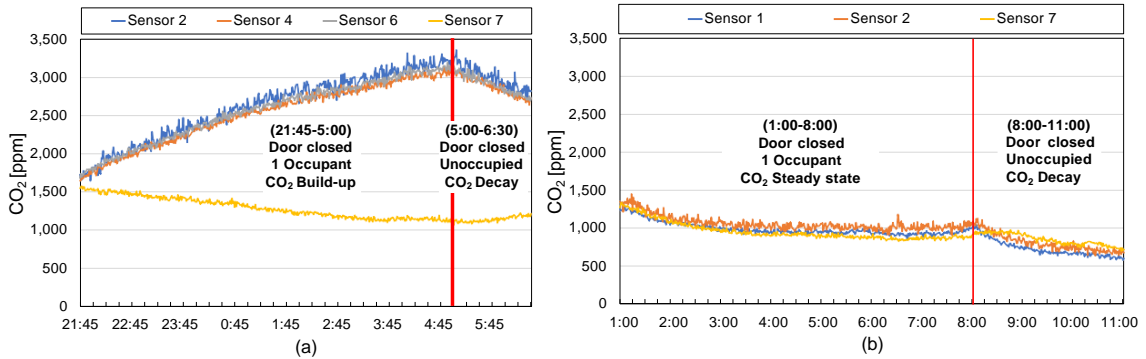

Figure 4.   Results of the CO_2 measurements – (a): semidetached house (NV), (b): apartment (MV)

Results and Discussions

The results of CO_2 measurements close to the breathing zone and outside the bedroom are shown in Fig. 4. The data from sensor 6 in the MV (b) condition were excluded because of sensor problems. In the case of NV (a), it was observed that the CO_2 build-up started at approximately 1,500 ppm and lasted for over 7 h until the subject woke up and exited the bedroom. The breathing zone sensors 2, 4, and 6 reached between 3,000 and 3,200 ppm, and the sensor located outside the bedroom did not show any build-up, suggesting that there was no exfiltration of CO_2 through the bedroom door. These results suggest that sleeping with fully opened trickle vents still might not provide the necessary dilution to reduce exposure to CO_2 during the night. People should consider sleeping with an open bedroom door in addition to an open trickle vent, which might help CO_2 exfiltration from the bedroom.

The CO_2 level in the bedroom with MV (b) started at approximately 1,300 ppm, gradually decreased, and reached a steady state at 1,000 ppm. The CO_2 levels were at a steady state throughout the night. It can also be seen that the bedroom air was well mixed by MV. All three sensors recorded the same CO_2 value even though sensor 7 was located 0.6 m high outside the bedroom and next to the door. These results indicate that bedroom air passed through the gap below the door and the keyhole on the door because of the positive pressure created by the mechanical inlet in the bedroom.

The average CO_2 levels measured at night and the ACRs computed from each CO_2 decay profile for each sensor in each experiment are presented in Table II. Considering that

TABLE II.   THE AVERAGE CO_2 LEVELS AND THE COMPUTED ACR – (A): SEMIDETACHED HOUSE (NV), (B): APARTMENT (MV)

(a)	Average CO_2 level [ppm]	ACR [/h]	(b)	Average CO_2 level [ppm]	ACR [/h]
Sensor 2 (horizontal)	2,613	0.08	Sensor 1 (horizontal)	991	0.38
Sensor 4 (horizontal)	2,519	0.08	Sensor 2 (horizontal)	1,062	0.30
Sensor 6 (vertical)	2,564	0.12	-	-	-
Sensor 7 (outside)	1,307	(No Decay)	Sensor 7 (outside)	956	0.16

the CO_2 sensors had an accuracy of ±50 ppm, it can be concluded that there was no difference in the sensor locations in the immediate breathing zone. The slightly more significant differences between the two horizontal sensors were attributed to the direction of the sleeping subject's head.

As shown In Table II, the ACR in the bedroom with NV was approximately four times lower than that in the bedroom with MV. This explains the higher CO_2 level with NV than with MV. The ACR with MV (b) and sensor 7 showed values half those of sensors 1 and 2, which indicates that there is critical contrast between the CO_2 value in the bedrooms and those outside the bedroom. In both bedrooms, the air temperature was in the range of 22.0–23.7°C. The relative humidity in the NV bedroom was between 55 and 72%, and in the case with MV, it was between 36 and 44%.

Conclusions

This section provides clear evidence that a mechanical inlet provides adequate ventilation in a bedroom, and a bedroom equipped with trickle ventilation on the window is exposed to higher CO_2, even when the trickle vent on the bedroom window is kept open. Furthermore, the sensor located outside the bedroom could indicate the air exfiltration of the bedroom, and it is suggested that the CO_2 sensor should be located in the bedroom and outside the bedroom to provide the actual CO_2 exposure during nighttime and assess air distribution in the bedroom.

IV. ONLINE QUESTIONNAIRE SURVEY

As more evidence emerges about the airborne spread of SARS-CoV-2 via the inhalation of infectious aerosols, the importance of indoor ventilation has been highlighted and addressed by international health authorities and professional societies. The public now has increased awareness of the benefits of increasing indoor ventilation to reduce the risk of infections and dilute contaminants during regular daily operations. Currently, there is no information about the implementation of such measures and their associated benefits during the pandemic, especially considering that sleep quality is possibly linked to a poor bedroom environment (indicated as the measured CO_2 concentration). The bedroom environment before and during the pandemic and its potential influence on sleep quality are worthy of investigation. Therefore, the objective of this section was to examine the immediate impact of the COVID-19 pandemic on bedroom environment changes and its consequences on occupants' sleep quality.

Materials/Methods

There were two instances of lockdown caused by the spread of COVID-19 in Denmark in the periods of March 2020 and December 2020–April 2021. Liao et al. [10] surveyed the types of bedroom ventilation in Danish dwellings before the pandemic (from January to February 2020) and the associated subjective sleep quality among members of the Danish population in the capital region of Denmark. We sent an email requesting a re-survey to those who responded to the previous questionnaire [10], and an additional online questionnaire survey during the pandemic (from March to April 2021) in Denmark was conducted. It should be noted that the additional survey was conducted not during the period immediately after the lockdown but 1 year later. The study comprised a structured questionnaire packet that inquired about demographic information, anthropometric data, regular sleep patterns, the bedroom environment, subjective sleep quality assessed using the Pittsburgh Sleep Quality Index (PSQI), health conditions, and additional factors that might affect sleep quality. In this section, six representative questions and their answers are presented.

Results and Discussions

Table III shows the number of valid responses. The most recent response was considered if the same person responded more than once. It should be noted that 517 people (median age, 33 years; 54.5% males) responded to the survey before the COVID-19 pandemic, and 182 people (median age, 27.0 years; 49.5% males) responded to the survey during the pandemic.

TABLE III. NUMBER OF VALID ANSWERS

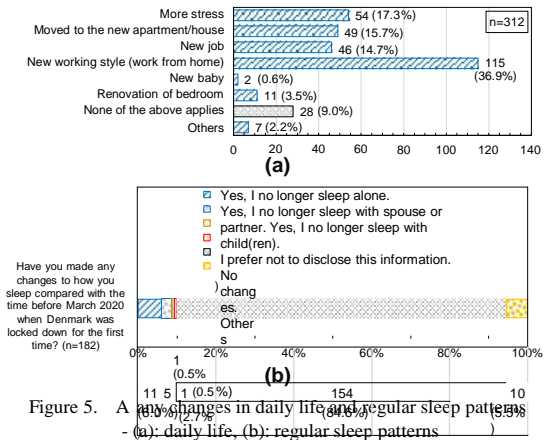|			
	Total number of sent email	478	100%
1)	All Answer	195	41%
2)	Who accept the consent	192	40%
3)	Duplicated Answers	10	2%
2)-3)	Valid Answers	182	38%

Figure 5. A any changes in daily life and regular sleep patterns - (a): daily life, (b): regular sleep patterns
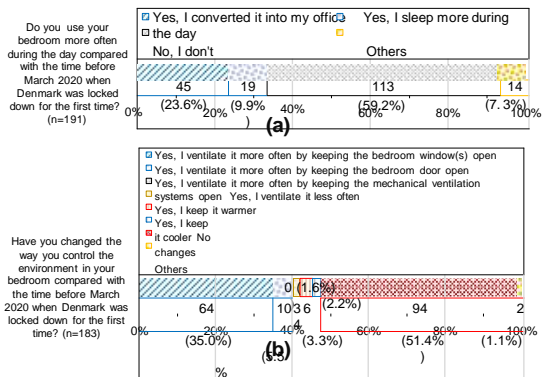

Figure 6. A any changes in bedroom environment - (a): how often use the bedroom, (b): how to control the bedroom environment conditions

In Fig. 5, it can be seen that approximately 17% of people felt more stress and 36% started working from home. However, approximately 85% of individuals did not change their regular sleep patterns. Compared with the time before March 2020, when Denmark was locked down for the first time, more stress and new working styles were observed, whereas no changes were observed in sleep patterns.

Fig. 6 shows that 23% of respondents converted their bedroom into an office and 10% slept more during the daytime, and thus, approximately 33% of people spent more time in the bedroom. Approximately 40% of people started to ventilate their bedrooms more often. Bedrooms tended to be converted into offices and ventilated more often during the day. Results shown in Fig. 7 indicated that people tended to get up later and go to bed later, and approximately 30% of respondents felt that their sleep quality was reduced. The PSQI analysis of subjective sleep assessment will be incorporated in further studies.

Conclusions

An online questionnaire survey was conducted in Denmark, before and during the pandemic. The survey analysis is ongoing, but it should be noted that 40.4% began to ventilate their bedrooms by keeping the window/door open, which should have positive effects on sleep. Further, 33.0% thought that the COVID-19 pandemic had affected their sleep quality and reduced it. It can also be seen that people were significantly affected by stress, new working styles, new babies, new jobs, and other aspects. Moreover, 23% converted their bedroom into an office, but converting it to a working environment would create an issue. When the resting environment becomes a person's work environment, this can create psychological problems at several levels. More stress, the shifting of sleep hours, and an increased reporting incidence of poorer sleep quality were observed.

V. Field measurements with human subjects

This section provides a comprehensive assessment of bedroom ventilation and the effect of the thermal environment on sleep quality. In bedrooms, the ventilation characteristics and thermal environment change simultaneously and mainly depend on the behavior of the occupants. For example, people might close windows/indoor vents or turn off ventilation to adjust to the thermal environment, resulting in insufficient outdoor air inflow and poor ventilation. Hence, a field survey was conducted to investigate how the control of the bedroom thermal environment affects IAQ and sleep quality.

Materials/Methods

This study was conducted from August to September, 2021, in the Greater Tokyo area of Japan. The participants in the study took measurements in their bedrooms and completed questionnaires on five consecutive weekdays. Data from 98 nights of measurements in the bedrooms of 20 healthy individuals (12 males and eight females) were collected. Table IV shows the anthropometric data of all subjects. The PSQI score was 2.3 ± 1.0 (mean $\pm$ S.D.), indicating that the participants had regular sleep habits.

Bedroom environmental data, including temperature, relative humidity, air velocity, sound level, illuminance, and CO_2 concentration, were continuously monitored. Participants' skin temperature, sleep quality, and bedroom environment were recorded during sleep. The subjective responses to a sleep quality questionnaire were also assessed.

The human heat load, which comprehensively considers six thermal factors (temperature, relative humidity, radiant temperature, air velocity, metabolic rate, and clothing value), was introduced to evaluate the thermal environment. Positive (warm) and negative (cold) heat loads were observed. It is known that a human heat load further from the thermal neutral zone results in an increased occurrence of awakenings [11]. The ACR was estimated based on the CO_2 decay measured in the morning after the person left the room or with the steady-state level during sleep.

Results and Discussions

Fig. 8 shows the relationship between the human heat load and the occurrence of awakenings during sleep, and Fig. 9 shows a comparison of the relative humidity between the less ventilated and more ventilated bedrooms with the
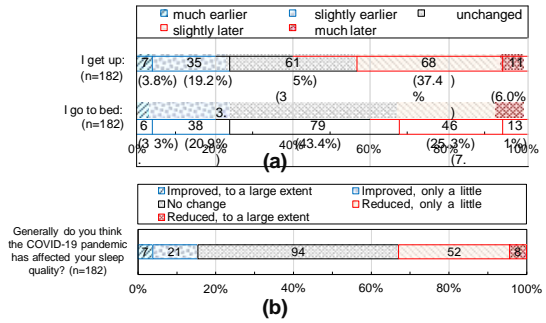

Figure 7. A any changes in sleep - (a): sleep time, (b): sleep quality

TABLE IV. Anthropometric data of all subjects

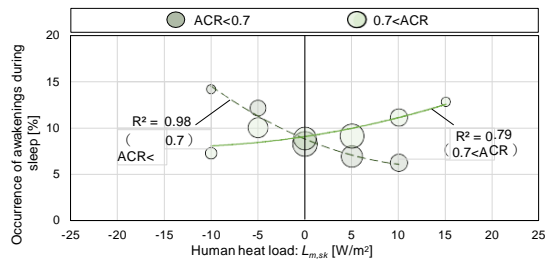|	Age [yrs-old]	Height [m]	Weight [kg]	PSQI [-]
Male (N=12)	23.5 ± 2.6	171.4 ± 4.2	64.3 ± 10.8	2.1 ± 1.1
Female (N=8)	26.9 ± 11.4	160.0 ± 6.7	52.1 ± 6.5	2.6 ± 0.5
All data (N=20)	24.9 ± 7.7	166.8 ± 7.7	59.4 ± 11.1	2.3 ± 1.0

Mean±SD

Figure 8. Relationship between human heat load and the occurrence of awakenings during sleep
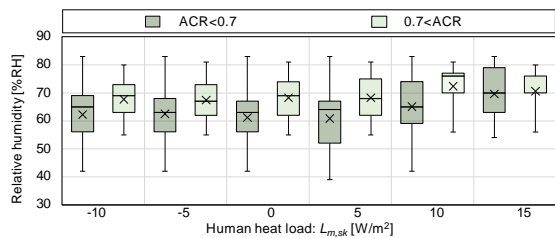

Figure 9. Comparison of relative humidity between less ventilated bedrooms and more ventilated bedrooms

same heat load. All valid data were divided into two groups with the median value of the ACR, specifically 0.7 h^{-1}, to compare the bedroom environment in the more ventilated bedrooms (0.7<ACR) with that in the less ventilated bedrooms (ACR<0.7).

Fig. 8 indicates that increased ventilation increased the positive load, probably caused by moist air from the outdoors increasing awakenings during sleep. With lower ventilation and a negative load, awakening during sleep also increased. A negative heat load suggests a cooler environment and the use of an air conditioner (AC). With a low ventilation rate, the use of AC has increased because people try to conserve cool air. As a result, they overcool their bedroom, which leads to awakenings during sleep.

There are also awakenings with higher ventilation and negative heat loads, but they are less frequent than those with low ventilation because overcooling is expected less.

A positive heat load indicates a warmer environment. Most likely, people open the window but do not use the AC. They open the window to reduce overheating, but at the same time, this causes the infiltration of moist air indoors and results in awakenings during sleep. Even when windows are closed, there is some overheating and awakening, and thus, other factors could cause this reduction. They might still use AC, but this is insufficient.

Conclusions

Field measurements in bedrooms were conducted during the hot and humid summer seasons in Japan. In this section, a comparison of the bedroom environment in the more and less ventilated bedrooms is presented to examine how ventilation affects the bedroom environment. The results show that there is a possibility that not only ventilation, but also humidity in the bedroom, have an effect on sleep. Concerning the susceptibility to awakenings during sleep, it was indicated that ventilation of bedrooms in hot and humid regions, such as Japan, requires simultaneous dehumidification. These results require further analysis in future studies.

VI. Further implication

At present, our recommendations employ CO_2 as a marker for the outdoor air ventilation rate in the bedroom. The caveat of this approach is that CO_2 might not sufficiently account for other pollutants present indoors, including those brought outdoors. However, it should be emphasized that human bio-effluents are likely to be a major source of pollution in bedrooms, and under these conditions, CO_2 is a reasonably good marker of ventilation sufficiency. Nevertheless, in the future, the effects of different sources of air pollution in bedrooms on sleep and interactions with thermal and acoustic conditions in bedrooms should be investigated.

In addition, many bedrooms achieved adequate ventilation through window and door opening and infiltration. This can increase external noise, moisture, and insect infiltration and result in bedroom temperatures that are too low in cold climates or too high in hot climates. Additionally, research is required to develop bedroom ventilation solutions not only for newly constructed buildings but also as retrofit solutions for existing buildings to ensure that the bedroom IAQ does not disturb sleep and is of sufficient quality to minimize health and other risks.

VII. Conclusions

The objective of this study was to investigate the effects of the bedroom environment on sleep quality, focusing mainly on the ventilation and thermal environment in the bedroom. Four different methods were used to examine various aspects. The main conclusions are as follows:

1. A literature review survey reported that poor bedroom ventilation has a negative impact on sleep quality and next-day performance. It was also concluded that the available research is limited.

2. Air distribution measurements in the bedroom showed clear evidence that a mechanical inlet provides adequate ventilation in the bedroom, as indicated by the steady-state CO_2 levels at 1,000 ppm. A bedroom equipped with trickle ventilation on the window is exposed to higher CO_2 even when the trickle vent on the bedroom window is kept open.

3. Considering the accuracy of the CO_2 sensors (±50 ppm), there was no difference in the CO_2 levels measured vertically and horizontally from the head of the sleeping person. To assess the air distribution in the bedroom, a CO_2 sensor was placed near the door outside the bedroom.

4. An online questionnaire survey was conducted to investigate the immediate impact of the COVID-19 pandemic on bedroom environment changes and their consequences for occupants' sleep quality among members of the Danish population in the capital region of Denmark. Whereas increased ventilation in the bedroom is expected to positively affect sleep, the study shows that converting the bedroom into a workplace could be problematic in itself.

5. Field measurements in the bedrooms were conducted during the hot and humid summer seasons in Japan. The results indicate that there is a possibility that not only ventilation, but also humidity in the bedroom, affect sleep. This indicates that the ventilation of bedrooms in hot and humid regions such as Japan requires simultaneous dehumidification.

References

1   Z.A. Caddick, K. Gregory, L. Arsintescu, E.E. Flynn-Evans, "A review of the environmental parameters necessary for an optimal sleep environment," *Build. Environ.*, vol. 132, 2018, pp11–20.

2   B. Du, M.C. Tandoc, M.L. Mack, J.A. Siegel, "Indoor CO2 concentrations and cognitive function: A critical review," *Indoor Air.*, vol. 30, 2020, pp1067–1082.

3   J. Xiong, L. Lan, Z. Lian, R. De dear, "Associations of bedroom temperature and ventilation with sleep quality," *Sci. Technol. Built Environ.*, vol. 26, 2020, pp1274–1284.

4   A.K. Mishra, A.M. van Ruitenbeek, M.G.L.C. Loomans, H.S.M. Kort, "Window/door opening-mediated bedroom ventilation and its impact on sleep quality of healthy, young adults," *Indoor Air.*, vol. 28, 2018, pp339–351.

5   C. Liao, M. Delghust, P. Wargocki, J. Laverge, "Effects of window opening on the bedroom environment and resulting sleep quality," Sci. Technol. Built Environ., vol. 27, 2021, pp995–1015.

6   X. Zhang, G. Luo, J. Xie, J. Liu, "Associations of bedroom air temperature and CO2 concentration with subjective perceptions and sleep quality during transition seasons," *Indoor Air.*, vol.31, 2021, pp 1004-1017.

7   P. Strøm - Tejsen, D. Zukowska, P. Wargocki, D.P. Wyon, "The effects of bedroom air quality on sleep and next - day performance," *Indoor Air.*, vol. 26, 2016, pp679‑686.

8   X. Xu, Z. Lian, J. Shen, T. Cao, J. Zhu, X. Lin et al., "Experimental study on sleep quality affected by carbon dioxide concentration," *Indoor Air.*, vol. 31, 2021, pp440–453.

9   C. Sekhar, M. Akimoto, X. Fan, M. Bivolarova, C. Liao, L. Lan et al., "Bedroom ventilation: Review of existing evidence and current standards," *Build. Environ.*, vol. 184, 2020, pp107229.

10 C. Liao, M. Akimoto, M.P. Bivolarova, C. Sekhar, J. Laverge, X. Fan et al., "A survey of bedroom ventilation types and the subjective sleep quality associated with them in Danish housing," *Sci. Total Environ.*, vol. 798, 2021, pp149209.

11 Y. Akiyama, E. Miyake, R. Matsuzaki, M. Ogata, K. Tsuzuki, S. Tanabe, "Effect of thermal environment on sleep quality in actual bedroom in summer by sleep stages analysis," *J. Environ. Eng., AIJ*, vol. 83 No.745, 2018, pp277–284. (*in Japanese*)

3rd Place
REHVA
Student Competition

Viktoria Nadas
Finland

Advanced Design and Control Strategies to Optimize a Deep Borehole Field as Long-Term Thermal Storage

Viktoria Nadas[1,2], Markku J. Virtanen[1], and Mika Vuolle[2]

[1] Aalto University, Otakaari 4, 02150 Espoo, Finland [firstname.lastname@aalto.fi]
[2] Equa Simulation Finland Oy, Kivenlahdenkatu 1, 02320 Espoo, Finland [firstname.lastname@equa.fi]
The Master's Thesis upon which this article is based was accepted at Aalto University in May 2020.

Abstract–**Building performance and sustainability requirements defined by the EU have been continuously tightening. This includes high energy efficiency, low CO₂-emissions, a long-term decrease in the fossil fuels in thermal energy production. In the HVAC design world, focus has been shifting towards compact energy systems, local thermal energy sources for heating and cooling: namely ground as energy source and seasonal thermal storage. In respect of the ground, long-term temperature monitoring, control and versatile control schemes are needed. Borehole fields combined with heat pumps supported with PV electricity and energy-collecting building envelope foretell a new era in building consumption and energy management, with a dazzle of transforming the building into a prosumer. Designing such an energy collective must be completed with a sophisticated simulation tool that is programmable, has scientific base of its calculations, output options and long-term calculations. Simulations also serve as behavior estimation, scenario testing, testbed, comparison base and a review for additional changes. After an "educational" period, the simultaneous complex simulation and comparison to previous years results, an automated Digital Twin may be established to achieve additional energy savings, energy usage predictions and small-scale trading with interconnected, nearby buildings.**

Index Terms–**borehole field, long-term temperature balance, control, simulation**

Introduction

Geothermal energy as a comprehensive concept has been serving buildings[1] for several decades now. Due to the known building temperature profiles and the relatively stable ground temperature in the ground, this type of energy source is mostly suitable to non-residential buildings, such as offices, higher education and a particular university building complex in Espoo, Finland. The complex is a new construction (operating since January 2019), serves in ca. 39 000 m² and is built according to Finnish building requirements. The energy source is the earth itself beneath, with 74 boreholes (depth over 310 meters) drilled into it. The plant is based on 9 heat pumps, 2 large water tanks (hot and cold) and an extensive control mechanism. As the building operates according to multiple schedules, setpoint collections and temperature profiles (higher education, gym, student restaurant, grocery store, metro station: open all days, no teaching in summertime, other services available throughout the year), the collection of summer heat provides a self-explanatory possibility to return the heat extracted in heating season into the ground.

The thesis work focused on the long-term temperature balance of the ground, based on simulated annual building energy consumption. The simulation software used was IDA ICE 4.8, with a specifically developed extension element to simulate advanced control mechanisms and to conclude ground thermal changes. Additional simulations were completed with an established connection to multiple nearby buildings to emulate a low-temperature local network to gain proof on the "local" concept.

Since the complex was designed and built for long-term usage, the temperature balance below was a central point of prior research by the design team (Wise Group). The published research, simulated with different tools (Earth Energy Designer, ComSol) has shown that the central core area of the borehole field would reach after 20 years a significant, approximately 6-7 °C of temperature drop. The extracted nor returned heat amount is not known. In the location given and with the calculated heat extraction, this rate of cooling could lead to irreversible heat diminishing and terminate the designated usage of the borehole field.

As during the thesis study the actual measured values were not relevant (flush through: first operational year with constant ventilation) nor available, the study was completed with pre-simulated consumption time series, using the same energy rate in long-term simulations as well. This is based on annually repeated weather file as well, which produces rather practical but not definitely realistic results. Additional difficulties in comparing were the measured energy amounts intervals (monthly) that included domestic hot water energy as well, and the lack of the measured data of the borehole field (temperatures and mass flows). Since the complex includes multiple different profile building partitions, such as a shopping center, directly connected metro station, a large student cafeteria and a spectacular sized atrium, it was difficult to find the assumed inclusion and the boundaries of energy consumption.

I. METHODS

A. Simulation tool and working process

Due to the limited availability of sufficient applicable design information, the study needed a tailored working process (Fig.1) to obtain a realistic energy consumption time series.

The simulation tool is a crucial part of this study: the requirements concerning a dynamic tool include multiple, interdependent requirements. These are, among others different level modeling space, transparent, detailed and connectable construction parts and machinery components, adjustable timesteps for iterations and output results, variables logging, user-defined simulation types and periods, parallel process calculations and an objectively short calculation time. IDA ICE version 4.8 with additional development was a suitable choice for the task.
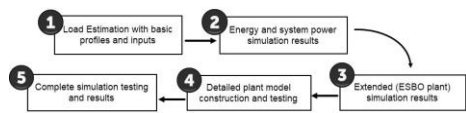
Figure 1. Simulation process to obtain the hourly energy time series of one year.

The initiative energy simulation was based on a simplified building geometry and produced building profile, utilizing the Load Estimator function of IDA ICE (Fig.1, step 1). No actual building geometry (IFC) was available; however the simplified geometry had the same main characteristics as the project building: same heated surface and ground-connected area, same window-to-wall ratio, construction element values (U-values), HVAC machinery, setpoints and main mass flows, system powers (step 2). Since the borehole field serves the heat pumps and the direct cooling panel loop, the preliminary ESBO design of the plant joined with the borehole (step 3) needs a reliable mass flow and temperature, as time series. The plant however was modeled (step 4) according to the submitted automation plans[2], considering all seasonal modes, connections, response delays, conditions, rules and temperature limits. This combination (simplified geometry and accurate plant model with borehole field) was run together and resulted (step 5) in a pertinent hourly energy consumption result. running together in the early phase model.
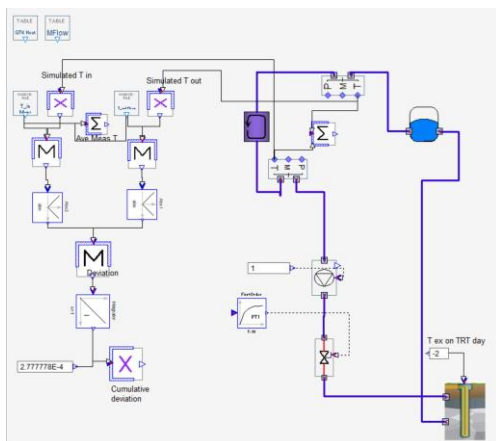

Figure 2. TRT simulation and result comparison model.

The next step (Fig.2) was to introduce a simulation model on Thermal Response Test (TRT). TRT[3] is and should be the first step in every geoenergy-related project: Geological Survey of Finland (GTK) has provided[4] the results of two of their conducted field TRT from their planning phase. Knowledge about the local geological properties is a binding condition: to estimate the available thermal capacity and recognize additional, environment–related risks. The main purpose of these tests is to evaluate the thermal profile of the ground, to prevent it from under- or oversizing. The test focuses on the thermal conductivity (k-value) and tries to estimate the test borehole resistance (Rb-value).

Both GTK and the thesis study has obtained values for Rb and k, which helps to 1) compare the TRT returning temperatures 2) evaluate the calculation methods 3) accurately predict the ground's heat transfer ability. During the study, two additional parameter-fitting (Fig.3) calculation was concluded (optimization and cumulative error[5]), to obtain specific other values (density, cp and lambda) to ensure the similarity of the simulated and assumed ground in long-term simulations.
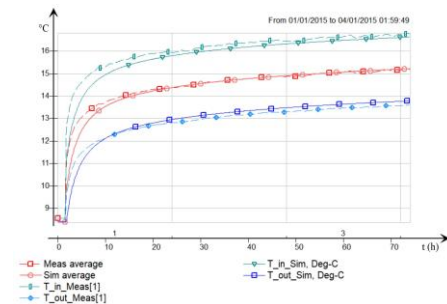

Figure.3. Parameter-fitting between simulated and measured results.

All models were based on the heat extraction-return-sublayers heat conduction ground heat balance: the study aimed to define a minimum ratio that does not cool (and preferably not heat either) the ground. This balance itself creates the long-term/seasonal storage in the ground.

After successfully obtaining the TRT-based ground values, the model used for TRT simulation was ready to run long-term. The default 25-year long simulation was stable and provided space for additional field control variations.

B. Control description

After setting the environment for the multiyear simulations and concluding the first results, the idea of sectorizing the design uniform mass flow field grew intuitively. The original design does not differentiate between the sectors or sections of the borehole field, i.e. the mass flow is uniform (0.6 L/s) throughout the field, decrease in the flow concerns uniformly all wells. As

mentioned earlier, the field's long-term thermal balance was unclear and therefore, appeared as a valid research question. During the study the idea of three sectors emerged, in a cylindrical layout (Fig 3). The original design also included three, adjoining sectors but finally, was not installed: the boreholes created one single entity of heat source. The newly suggested, concentrical three sectoral control idea has created an inner core (9 boreholes), an intermediate sector (22 boreholes) and an outer sector (43 boreholes), see Fig.4 and Table 1.
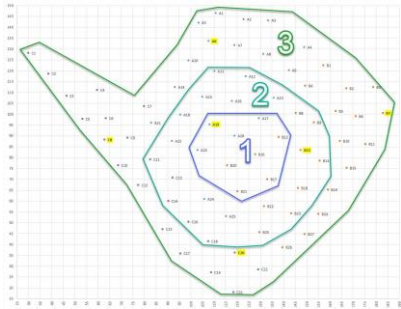
Figure 4. Suggested sectors layout.

The field has no additional influencing heat transfer-inducing installations, such as groundwater flows, aquifers, large district heat/cold pipelines nearby: the outer sector is in direct conduction with the external areas. Controlled heat extraction starting from the central core, until reaching a certain ground temperature provides a safe, computable cooling rate in heating season that can be directly utilized in the intermediate and cooling season. The nominal well mass flow remains 0.6 L/s, however the sectors establish differently sized areas. With this way, the field has limited cooling extent, preventing the middle core from over-exploitation, and allowing enough time to recover.

TABLE 1. SECTORAL DIVISION.

	Sector 1	Sector 2	Sector 3
Boreholes (pcs)	9	22	43
Mass flow (L/s)	5.4	13.2	25.8
Thermal energy (dT = 1.5K) (MWh)	77	1034	1314

C. Control variations description

Once the restructured ground heat element (GHX_MANY) was ready, the loop (Fig.5) was set to simulate those several different control methods that occurred during the study; listed in the followings:

1)half-volume ground with half-length borehole wells. This example served as a basic comparison to the existing energy demand: how a considerably smaller volume will be able to serve and with that extent of temperature drop in the ground?

2)sequenced order of the sectors (illustrated in Fig.5): the central core (S1) is expected to deliver first the demanded energy. After reaching its maximum capacity and heat

transferred, the next sector will be activated – without stopping the first one. The same principle goes on to reach the third sector (S3): it will cease the operation first when the heating demand decreases, consequently, the inner core is expected to show the largest temperature fluctuations.

3)temperature-limit on the returning brine of S1: at the times when the borehole temperature exceeds the set limit, the circulation stops. This control strategy helps to ensure free cooling to a greater extent. The expected behavior of the inner sector S1 is to be less active than previously, and to shift the loads towards S2 as mainly active field and S3 acting as a buffer.

4)thermal accumulation and sectoral shut-off: S1 is not in use for free cooling either, instead it is at rest before the heating season starts again (summertime). Free cooling is provided from S2 primarily, and S1 is expected to deliver more heat than in the plain sequencer control at the start of heating season.

5) return of rejected heat: a demonstration case where 10 % of the annually rejected heat (total rejected: ca. 90-120 MWh) is feeding back, together with the previous temperature limit-based control. A slight heating trend is expected.
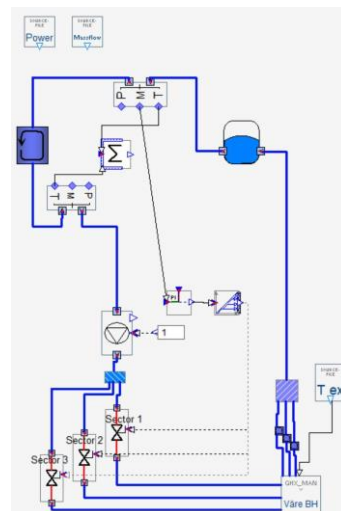

Figure 5. The loop used in 25 year-long multisector simulations.

All control schemes were tested under 2 different set of temperature setpoints (and, logically different energy consumption time series), a default and a modified one (Table 2). Additionally, the comparisons were run long-term (25 years), aiming to show the ground temperature change throughout the field.

TABLE 2. INDOOR TEMPERATURE SETPOINTS.

	Heating	Cooling
Default	21.5 °C	22.5 °C
Altered	20.5 °C	23.0 °C

II. RESULT PRESENTATION AND DISCUSSION

Finalized results of the single-entity borehole field, as-built with the default heating (21.5 °C) and cooling (22.5 °C) with 84 % cooling to heating (or return) rate show an approximated 0.66 °C average temperature drop over 25 years. This first result shows the significant differences between the simulation tools and calculation methods. More energy-saving setpoints (heating 20.5°C and cooling 23 °C) lead to lower return ratio (62 %), which in long terms also leads to a larger temperature drop (-1.82 °C). This result means that the extraction may be larger, as long as the return rate is high. The additional control simulation results are listed in Table 3: they show varying rates, a few of them are practically identical. The temperature level did not change more than max. ±2.0 °C/25 years in any case. In the light of the results, we may divide the results into 3 categories: A) heat accumulative, B) heat balanced and C) heat lost.

Simulations that show A) heat accumulation (temperature change max (±0.7°C/25 years), suggest potential heat collection possibility in the core sector, achieving it with sequential (2.0) or seasonal mass flow limitation (4.0, 4.1) and high return ratios. Particularly the shut-off of S1 case allows the borehole field to regain heat if necessary.

The B) heat balanced cases (current design 0.0, sequential with temperature limit 3.0 and both partial returned heat cases 5.0, 5.1) give directions if there is no need to heat nor cool the ground: these strategies provide long-term heat balance with both temperature setpoint cases. The depth of the field clearly lacks the ground's temperature gradient which could compensate for the extracted heat towards the building, in both half-volume cases.

The remaining cases of C) heat loss show that the field must be large enough to balance the heat extraction (1.0, 1.1) and that the lower return ratio is not sufficient, regardless of the control scheme (0.1, 2.1, 3.1).

Due to the annually varying heating and cooling loads, the mass flows/temporary termination of mass flows in the sectors are individual cases, which give a possibility to build up a temperature gradient in different sectors of the field. The temperature trend lines describe the average fluid temperatures, balancing out the differences between the sectors temperature gradients. Figure 6 illustrates this phenomenon, capturing Case 2.0 (sequence sectoral control, default temperatures), where S1 and S2 temperatures (red and green) are rather similar to each other, but S3 (purple line) is always offset of S1 and S2.

TABLE 3. CONTROL STRATEGIES 25 YEARS SIMULATION RESULTS.

| Case	Control strategy	Heating SP	Cooling SP	Output / Return	dT_ ground/ 25y	Category	Effect
0.0	Equal mass flow, as built, single-entity field	21.5 °C	22.5 °C	84 %	-0.66 °C	B	dropping
0.1	... with altered setpoints	20.5 °C	23.0 °C	62 %	-1.85 °C	C	dropping
1.0	Half volume homogenous field	21.5 °C	22.5 °C	84 %	-1.33 °C	C	dropping
1.1	... with altered setpoints	20.5 °C	23.0 °C	62 %	-3.65 °C	C	dropping
2.0	Sequenced operation of the sectors	21.5 °C	22.5 °C	84 %	+0.89 °C	A	rising
2.1	... with altered setpoints	20.5 °C	23.0 °C	62 %	-1.79 °C	C	dropping
3.0	Sequential, temperature-limited operation	21.5 °C	22.5 °C	84 %	+0.29 °C	B	rising
3.1	... with altered setpoints	20.5 °C	23.0 °C	62 %	-0.91 °C	C	dropping
4.0	Seasonal shut-off of Sector 1	21.5 °C	22.5 °C	84 %	+0.73 °C	A	rising
4.1	... with altered setpoints	20.5 °C	23.0 °C	62 %	+0.91 °C	A	rising
5.0	Returned rejected heat with sequencer	21.5 °C	22.5 °C	84 %	+0.22 °C	B	rising
5.1							ping
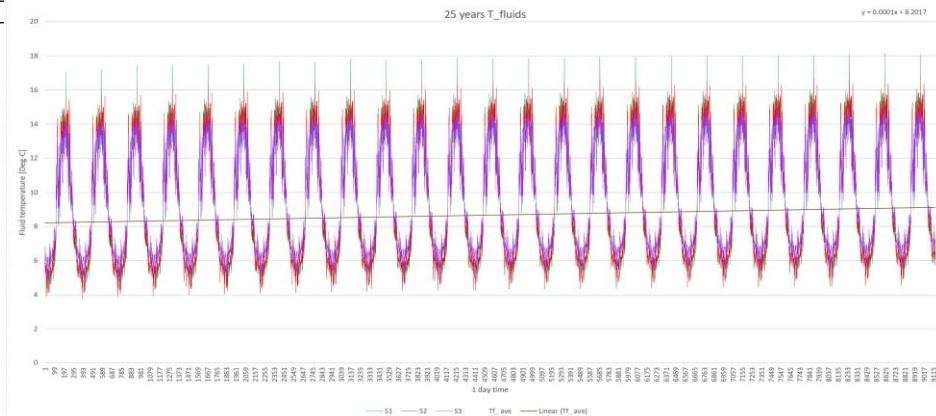
Figure.6. 25 years simulation, sectoral operation, default temperature setpoints. Logged sector temperatures and their averaged linear calculation.

The actual simulation results about the borehole field verify that the borehole field is able to serve both as an effective daily source and long-term (seasonal) thermal storage with the current design, without the risk of overexploitation. Due to its large volume the field has most likely enough capacity to supply heating and cooling to other consumers as well, such as local networks or buildings–in that case, additional control strategies would be vital to develop.

Despite the different, preliminary simulation results (EED, ComSol) showing an ambiguous ground thermal behavior, the borehole field together with the building was commissioned, constructed and it is operating. It provides an excellent possibility to re-simulate again, and to calibrate the known heat transfer processes– now with the assistance of more complex and flexible software. The need of a control mechanism emerged while reviewing the prior ground simulation results. The tests concluded on the field are of exemplary significance: they intend to introduce the possibilities built in deep borehole fields and within a suitable software environment.

The convenience of control strategies is expected to materialize in later phases of both field operations, continuous optimization and Digital Twin applications: it will provide valuable inputs for analyses, long-term decision-making process, trading outcomes, just to name a few.

To continue the research concerning this particular and involving other borehole fields, a few subjects are worthy of attention:
1) validation between the New Campus Complex borehole field model and the measurements, including the energy consumption measurements.
2) testing of additional heat return rates combined with control schemes (dual sector, further heat/cooling accumulation) to define a safe heat return ratio.
3) Large-scale production of financial analyses with additional demand variations (extended service, short-term thermal battery integration), to optimize and to mature a borehole field design process.

III.   CONCLUSION

Geoenergy or ground heat source, combined with heat pumps and a transfer fluid can serve buildings thermal needs (both heating and cooling) for long terms, without cooling down the Earth, i.e. without the danger of eliminating the heat source. Ideally, the extraction and return of heat together with natural ground heating processes are balanced, controlled and supervised. In Nordic conditions, an estimated 84 % of heat returned ensures the ground temperatures in long-term. The ground after heating season is capable of providing direct cooling into the room units, without the immediate need of chiller usage. Additional tasks, such as installing renewable electricity (on-site PV generation), envelope-generated heat collection, rejected heat return all assist to decrease the backup district heat exchanger connection size, consumption and increase overall efficiency.

It is crucial to note that a task as such (design, monitoring and revision operation of a borehole field) is not possible without a wide-scale platform software that considers all influencing factors and provides a user-friendly environment to complete, utilize and develop the model for several different purposes (e.g. Digital Twin, energy trading, optimal maintenance, thermal accumulation) in the future.

ACKNOWLEDGEMENT

REFERENCES

1   HELANDER, J., TANHOLA, M., 2017. "Toimintakaavio Energiajärjestelmä, Aalto-yliopisto Uusi Rakennus", Espoo: Wise Group.
2   GEHLIN, S., 2002, "Thermal Response Test - Method Development and Evaluation", *Doctoral Thesis 2002:39*.
3   REUSS, M., 2015, Chapter 6 – "The use of borehole thermal energy storage (BTES) systems", *Advances in Thermal Energy Storage Systems*. Woodhead Publishing. pp. 117-147.
4   LEPPÄHARJU, N. et al, 2015, "Uuden Rakennuksen geoenergia", GTK.
5   ERIKSSON, J & TILLBERG, M., 2019, "Validation of a simulation model of a plant equipped with ground source heat pumps". *REHVA Journal 6/19*, pp. 28-31.
6   GEHLIN, S., 2016, Chapter 11 – "Borehole thermal energy storage", S.J. REES ed., Advances in Ground-Source Heat Pump Systems. *Woodhead Publishing*. pp. 295-327.
7   HESARAKI, A. et al, 2015, "Seasonal thermal energy storage with heat pumps and low temperatures in building projects−A comparative review" in *Renewable and Sustainable Energy Reviews 43*, pp. 1199-1213.
8   MAZOTTI, W. et al, 2018, "Deep Boreholes for Ground-Source Heat Pump: Final report".
9   WELSCH, B. et al, 2018, "Environmental and economic assessment of borehole thermal energy storage in district heating systems".

HVAC World
Student Competition
Other Participants' Contribution

Chenxi GUI Yi WU	China
HyeonJin Ji	Korea

Research on the Vertical Meteorological Patterns and Parameter Generation for HVAC Design and Building Energy Simulation

Chenxi Gui [1], Da Yan [1,*], Wu Yi [1]

Abstract—**An increasing number of tall buildings have been constructed over the last 20 years with growing economic development and populations. In 2017, there were 144 new buildings worldwide that were 200 meters or greater in height; 50% of these buildings were in China. Due to the vertical gradient impact of meteorological parameters, the energy performance of tall buildings differ from general buildings. Few studies exist on vertical meteorological changes using measured data at different heights. Most studies on dynamic energy simulation simulate meteorological parameters using models. This study explores vertical meteorological patterns using hourly dry bulb temperature, humidity, and wind speed data from 2007 to 2017 for a 325-meter meteorological tower in Beijing and analyzes the influence of vertical meteorological patterns on the building load. Moreover, this research gives suggestions on the correction of outdoor air design conditions and TMY for different heights, and proposes a method for verification based on measured data.**

Index Terms—**Meteorological tower, tall buildings, vertical meteorological patterns, weather parameters, outdoor air design conditions, TMY**

Introduction

An increasing number of tall buildings have been constructed over the last 20 years with growing economic development and populations. The Council on Tall Buildings and Urban Habitat (CTBUH) defines tall buildings as those with a height greater than 50 meters or consisting of more than 14 stories [1]. The national standard in China, GB 50352-2005 Uniform Standard for Design of Civil Buildings, classifies buildings according to the number of floors or heights above the ground. It specifies that buildings greater than 100 metres in height are considered super tall buildings [2].

According to the CTBUH [3], in 2017, there were 144 newly-constructed buildings worldwide that were 200 meters or greater in height; 72 of these buildings were in China, accounting for 50% of the global total. The numbers of buildings that are over 150, 200, and 300 m in height all rank first among countries in the world. In Beijing, the number of tall buildings has grown rapidly. As of January 2020, there were 67 buildings greater than 100 m in height, approximately 97% of which were less than 300 m, and two new buildings that were over 300 m in height.

With an increasing number of tall buildings, numerous simulation studies on tall buildings have been conducted to support building design or evaluate energy performance. Building energy performance is affected by a variety of factors, including meteorological conditions, building envelope, indoor environmental parameters, occupant behavior, equipment and system type, and operational management [4]. Of these inputs, meteorological conditions need to be reconsidered for tall building simulations. Typically, only one set of meteorological parameters are inputted (e.g., typical meteorological year weather data) when the energy performance of one single building is simulated. These parameters are used to simulate the performance of all floors of a building without adjustments to the meteorological parameters [5]. However, in tall buildings that are 300 m or above in height, the meteorological parameters cannot not be ignored. There are previous studies on the vertical variations of meteorological parameters and their influences on simulated building performance results. Tong et al. [6] analyzed natural ventilation potential at different heights for high-rise buildings in major cities across six climate zones in the US, considering the diurnal cycle of the atmospheric boundary layer. They found that building height greatly influenced the vertical pattern of natural ventilation. Jung et al. Moti Segal et al. [7] analyzed the weather pattern of some US cities using the radiosonde measured data to better calculate building loads. Song et al. [8, 9] used radiosonde measured data to calculate the heating and cooling loads of supertall buildings in Osan, Korea.

In general, most studies on the load characteristics of tall buildings are based on theoretical formulas or meteorological models to obtain meteorological data at different heights. With the development of meteorological observation methods and computing technology in recent years, the quantity and quality of measured meteorological data has greatly improved. Such data better reflects vertical meteorological variations under actual conditions. As such, if this data is used in building simulations, they have the capacity to improve the accuracy of simulated thermal loads for tall buildings.

I. METHODS

A. Overall technical approach

In this study, we used a 10 year dataset of measurements from a 325 m meteorological tower in Beijing to investigate: (1) the vertical meteorological profile in Beijing, revealing the vertical patterns of meteorological parameters such as variations in dry bulb temperature, absolute humidity and wind speed at different heights and times under actual conditions; (2) the influence of the vertical meteorological profile on building cooling and heating loads; and (3) gives suggestions on the correction of outdoor air design conditions and TMY for different heights, and proposes a method for verification, shown as Fig. 1.

B. Data source

This study used 10-years measured data (2007 to 2017) of a meteorological tower (herein referred as "the Tower") in Beijing. The data utilized includes outdoor dry-bulb temperature, absolute humidity, and wind speed measured
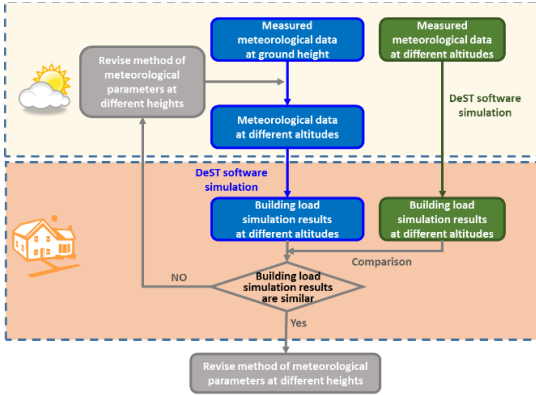
Figure 1. Verification of Revised method of meteorological parameters at different height.

at various heights. It is 325-meter high and the base is 49 meter above sea level [10]. The tower is located in an open space with minimal wind-shielding from its surrounds. It has 15 observation platforms. Other meteorological parameters used in the simulation were derived from the fifth-generation reanalysis meteorological data dataset (ERA5), including atmospheric pressure, solar radiation, ground temperature, and effective sky temperature. The ERA5 is a reanalysis dataset of the European Center for Medium-Term Weather Forecasting (ECMWF) [11]. We downloaded hourly instantaneous weather variables at 39°54'N, 116°23'E from 2007 to 2017. It included surface pressure, total cloud cover, skin temperature, and the hourly accumulated data of surface solar radiation downwards and the total sky direct solar radiation at the surface. The total cloud cover and skin temperature were used to generate the hourly effective sky temperature [12].

C. The tall building model

We used the Designer's Simulation Toolkit (DeST) software [13] to develop an energy model of tall buildings and run simulations to investigate the influence of the vertical variations of weather parameters on cooling and heating loads. The simulation model was developed based on a tall office building with a height of approximately 250 m in Beijing. The total building floor area is 106 000 m², and the area of a typical floor is 2200 m² with approximately 80% of this (1790 m²) being air-conditioned. A three-dimensional (3D) sketch and a typical floor plan are shown in Fig. 2. The detailed input parameters were determined according to the actual building, as shown in Table 1. The schedule of air-conditioning was determined based on working hours; this was from 7:00 to 21:00. The thermal parameters of the envelope were established in accordance with the latest national standard in China, the GB50189-2015 Design Standards for Energy Efficiency of Public Buildings [14], as shown in Table 2.

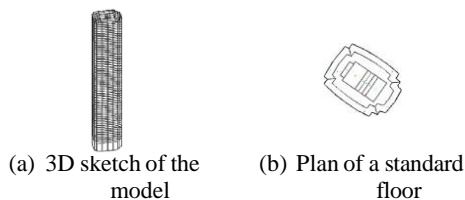(a) 3D sketch of the model   (b) Plan of a standard floor

Figure 2. Tall building model.

As DeST uses a user-defined constant convective heat transfer coefficient to calculate exterior surface heat balance, we selected the annual average wind speed (V) at the height of the standard floor to calculate the convective coefficient (h_c) using Equations (1) and (2) [15]:

$$h_C = 5.82 + 3.95V \qquad \text{if } V \leq 5\text{m/s} \qquad (1)$$

$$h_c = 7.14V^{0.78} \qquad \text{if } V > 5\text{m/s} \qquad (2)$$

II. Vertical profiles of meteorological parameters

A. Dry-bulb temperature

The hourly outdoor air dry-bulb temperature varies significantly with height. The frequency distribution of the dry-bulb temperature at various heights showed two peaks. For the 8 m high observatory platform, the peaks were within 2 and 3 °C and 24 and 25 °C. For the 140 m platform, the peaks were within 0 and 1 °C and 23 and 24 °C. For the 320 m platform, the peaks were within -1 and 0 °C and 22 and 23 °C. As height increases, the peak temperature decreases. The daily curve at different heights is shown as Fig.3. The difference between the dry-bulb temperature measured at the 8 m high platform and the 320 m high platform was approximately 4 °C at 16:00. The daily range of the 8 m platform was higher than that of the 320 m platform. For winter days and summer days, the dry-bulb temperature tends to decrease as vertical height increases, with changes exhibiting a near-linear pattern, consistent with previous research findings [16, 17]. Changes were clearer at 12:00 and 18:00 than 6:00 and 24:00. Quantitative analysis of the vertical temperature drop was performed by piecewise fitting using the data of two adjacent observatory platforms. Based on the statistics of 86 360 hours of temperature data between 2007 to 2017, the temperature gradient was 0.9 °C per 100 m. And at
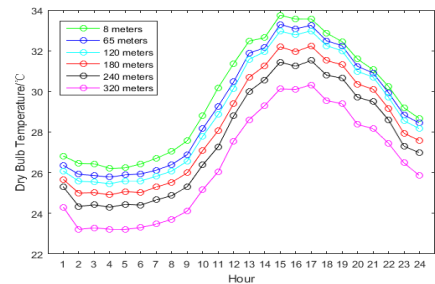
(a) 11th August, 2015
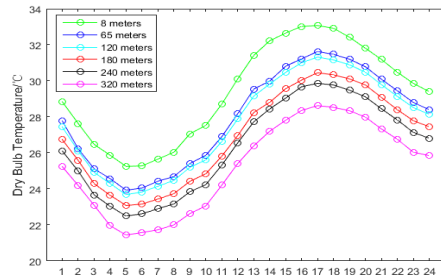
(b) 22nd February, 2015

Figure 3. Dry-bulb temperature curves from 24-hour observations on two days.

different heights, there was variance in the daily temperature range (i.e., maximum to minimum temperature). With an increase in vertical height, the daily temperature range decreases. The average daily range of temperature at 320 m was approximately 2.50 °C less than at 8 m.

B. Absolute humidity

To analyze the vertical gradient of humidity independently, we chose to analyze absolute humidity which is not influenced by dry-bulb temperature. The absolute humidity was calculated based on the measured relative humidity and the dry-bulb temperature. Fig. 4. shows that the absolute humidity frequency distribution curves at different heights were similar, where the most frequent values were between 0.7 and 0.9 g /kg of dry air,

with no obvious change in the absolute humidity at different heights. The average did not vary considerably with height, with the main trend being humid in summer and dry in winter; typical of the climate in Beijing. The average absolute humidity was approximately 1.5 and 15 g/kg of dry air in winter and summer, respectively.

C. Wind speed

The hourly measured wind speed at each altitude, from 8 (ground) to 300 m, showed that the wind speed increases significantly with height, also shown as Fig. 5. As height increases, the peak wind speed increases. The peak at the 8 m platform was between 1.2–1.4 m/s, while at the 240 m platform the range was 3.2–3.4 m/s. The average wind speed tends to increase with vertical height, as well as the standard deviation. As the height increases, the changing

TABLE I.
INDOOR ENVIRONMENTAL PARAMETERS

| | Summer | | Winter | | Fresh air volume |
	Setpoint temperature（°C）	Relative humidity（%）	Setpoint temperature（°C）	Relative humidity（%）	（mt/h·person）
Lobby	25	55	16	—	16
Office	25	55	20	40	40

TABLE II.
THERMAL PARAMETERS OF BUILDING ENVELOPE

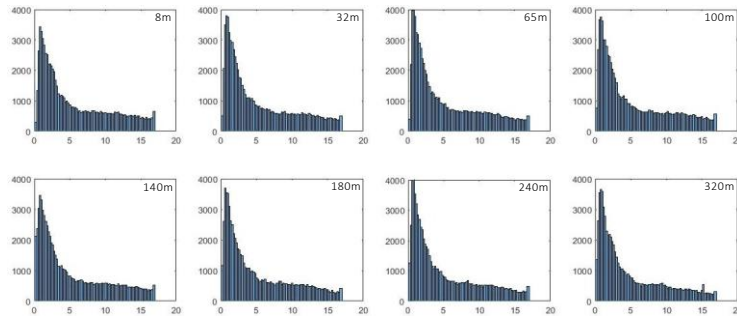|	
Roof U-factor	0.453 W/m²·K
Non-transparent wall U-factor	0.498 W/m²·K
Transparent curtain wall U-factor and Solar Shading Coefficient (SC)	1.9 W/m²·K SC：0.402 (non-North)/0.69(North)

Figure 4. Frequency distribution of outdoor air absolute humidity at different heights
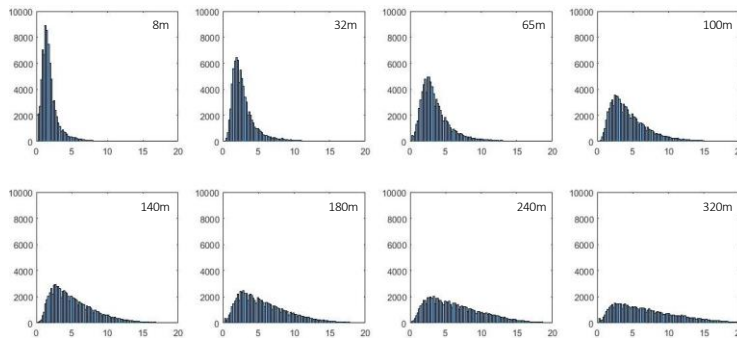(vertical axis – count, horizontal axis – air absolute humidity in g/kg of dry air).

Figure 5. Frequency distribution of hourly wind speed (m/s) at different heights.

rate of wind speed also decreases, which is consistent with some previous research findings [18, 19]. Using the piecewise fitting from the data of two adjacent platforms based on the statistics of 86 360 hours of temperature data, the wind speed was found to increase by 2 m/s per 100 m in most cases.

III. Load result comparison at different heights

A. The influence of temperature daily range differences on building load

Based on the above analysis results of the hourly temperature and day-to-day variation of the temperature at the vertical height and the typical annual data of the ground height, the annual hourly temperature value at each height was generated, and building energy simulation software DeST was used to do the simulation.

Based on the analysis of the measured data, the temperature range with the highest frequency is reduced by 0.8 ~ 1.0 ° C per 100 meters, so the hourly temperature value of each height constructed throughout the year is reduced by 0.9 ° C per 100 meters. For the daily variation, let the ratio of the daily range at a certain height to the daily range difference in ground height be x, then for the i day with the daily average temperature ti, the temperature daily difference is Δti, where the temperature at j meters is tij. At the height h, take the daily difference as Δti * x, 0 <x <1, then the temperature at time j is ti + (tij–ti) * x. Based on the analysis of the actual daily variation, corresponds to heights at 300m, 240m, 180m, 120m, 60m, give the value at x as 0.85, 0.88, 0.91, 0.94, and 0.97.In order to compare the effect of temperature drop of vertical height and the decrease of day-to-day difference on building load results, two sets of calculation examples are set. The meteorological parameter input of Case 1 only considers the vertical temperature drop, and the meteorological parameter input of Case 2 also considers the effect of altitude temperature drop and diminishing daily range. At the height of 300 meters, the annual heating load difference between Case 2 and Case 1 is 1.19%, and the annual cooling load difference is 1.27%. On the whole, the impact of temperature drop on load is much greater than the impact of temperature daily variation.

B. The influence of wind speed differences on building load

Based on the dry bulb temperature, relative humidity, and wind speed data, this section uses building energy simulation software DeST to simulate and calculate the results in two scenarios. The first scenario considers the difference in convective heat transfer coefficient of the outer surface of the envelope structure caused by the difference in wind speed in height, and the second scenario does not consider the the difference in wind speed. In scenario 2, the convective heat transfer coefficient of the outer surface of the envelope is taken as 19W/(m2·K). Comparing the simulation calculation results under the two scenarios, the maximum difference between the 2015 annual heating load result is 6.88% and the annual cooling load result is 1.75%. For peak load, peak heating load differ by a maximum of 2.8%, and peak cooling load results differ by a maximum of 0.5%.

C. Overall building thermal loads

Overall building thermal loads were calculated based on the simulation results of each floor using weather data at the corresponding height. Weather data at each height was not always available; therefore, we compared several scenarios of measurement heights and analyzed how they influenced the overall building heating and cooling loads, as shown in Table 3. The first scenario only has one measurement height at the ground level; therefore, the simulation results with the weather input at the ground level are representative of all the floors of the building. The second scenario has weather measurements at two heights; the ground and the top floor (roof) levels. The simulation results with the weather input at each measurement height represent half of the floors of the building. In general, for a building with weather measurements at n heights in addition to the ground and the top/roof (n ≥1), building load is calculated using Equation (3):

$$Load_{al} = \frac{1}{2(n+1)} Load_{to} + \frac{1}{2(n+1)} Load_{gnd} + \frac{1}{n+1} \sum_{k=1}^{n} Load_k \quad (3)$$

where $Load_{top}$ is the simulated load using the weather data at the top floor/roof; $Load_{groud}$ is the simulated load using the weather data at the ground level; and $Load_k$ is the simulated load using the weather data measured at the kth height. The simulation results of a 320 m building are shown in Table 4. The load ratio was defined as the ratio of the simulated loads of each scenario to the simulation loads of the 9-point measurement scenario shown in the last column of Table 4.

It is clearly that a greater number of measurement heights improve the accuracy of the results. If only weather data at the ground level is used, the heating load ratio is 61.90%, which means an underestimation of 38.1%. Two height measurements can improve the heating load ratio to 94.52%. Therefore, it is crucial to undertake weather measurements at two heights at the minimum if it is not possible to do more.

For the cooling load simulation, weather measurements at the ground and top floor levels were adequate. However, using only the ground level weather data in simulation will lead to an overestimate of 12.44% for the annual cooling load.

IV. The Generation and Verification of Vertical Meteorological Patterns

A. Outdoor air design conditions

Based on the analysis of the changes in the measured data of the 325m meteorological tower in Beijing, and the sensitivity analysis of various meteorological parameters to the building simulation results, this section presents a every 100 meters of altitude; it is not necessary to correct the absolute humidity; for the wind speed, the wind speed is corrected by 2m/s with every 100 meters of altitude increasing.

In this study, outdoor air design conditions at a height of 8m were generated based on the measured data at 8m (the

TABLE III.
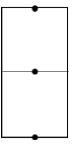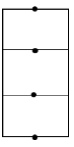THE SIMULATED LOADS AT DIFFERENT WEATHER MEASUREMENT SCENARIOS.
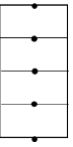
Weather measurement scenarios							
Number of measurement heights	1 (Ground level)	2 (Ground and top floor levels)	3	4	5	7	9
Annual cooling load (kWh/m²)	229290.0	204623.4	207084.2	203425.7	202183.4	204140.6	203929.2
Cooling load ratio	112.4%	100.3%	101.6%	99.8%	99.3%	100.1%	100.0%
Annual heating load (kWh/m²)	14594.4	22284.1	22034.1	23301.8	23399.8	23330.3	23575.5
Heating load ratio	61.9%	94.5%	93.5%	98.8%	99.6%	99.0%	100.0%

TABLE IV.
COMPARISON OF THE GRIDDED OUTDOOR AIR DESIGN CONDITIONS AND THE RESULTS OF THE MEASURED DATA

Heights	Heating DB(℃)		Winter cooling DB(℃)		Summer cooling DB(℃)	
	Measured	Grid	Measured	Grid	Measured	Grid
15m	-5.27	-5.35	-8.16	-8.19	26.84	26.91
65m	-5.89	-5.80	-8.71	-8.64	26.29	26.46
120m	-6.11	-6.30	-9.18	-9.13	25.89	25.96
180m	-6.72	-6.84	-9.63	-9.67	25.26	25.42
240m	-7.23	-7.38	-9.75	-10.21	25.08	24.88
320m	-8.06	-8.10	-10.55	-10.93	24.26	24.16

Load simulation result range based on 2007-2017 measured meteorological data
Average of Load simulation result range based on 2007-2017 measured meteorological data
Simulation results for gridded TMY
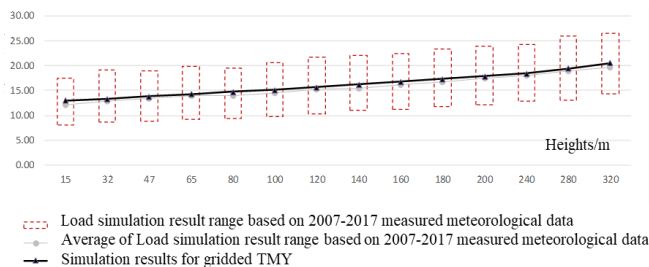
Figure 6.   The simulation result of annual heating load (kW·h/m²)

Load simulation result range based on 2007-2017 measured meteorological data
Average of Load simulation result range based on 2007-2017 measured meteorological data
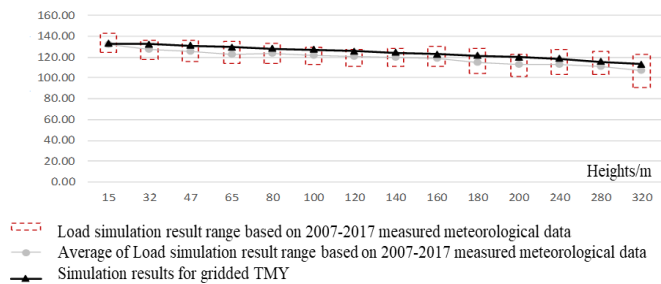Simulation results for gridded TMY

Figure 7.   The simulation result of annual cooling load (kW·h/m²)

lowest platform) of the tower, and the vertical grid outdoor air design conditions were obtained through simplified correction methods. Through the comparison with the outdoor air design conditions generated directly by the measured data of various heights, the vertical grid outdoor air design conditions of this study are verified.

Table 4 shows several temperature parameter value results of several heights, the grid outdoor air design conditions of this study based on the simplified correction method are basically consistent with the results obtained by direct statistics based on measured data.

B. TMY

Similarly, TMY at a height of 8m were generated based on the measured data at 8m of the tower, and the vertical grid TMY were obtained through simplified correction methods. Through the comparison with the TMY generated directly by the measured data of various heights, the vertical grid TMY of this study are verified based on simulation.

The simulation results of gridded TMY in this study are basically consistent with the average level of TMY obtained by measured data at each heights, shown as Fig.6 and Fig.7. The difference in annual heating load between the gridded TMY and the TMY based on measured data at 200 meters is the largest, with a difference of 6.08%, and the smallest difference is 0.82% at 15 meters. The differences in annual cooling load is 7.92% at 15 meters, while the minimum is 2.19%.

V. Conclusions

This study analyzed the vertical meteorological gradients in Beijing based on 10 year of hourly outdoor air dry-bulb temperature, relative humidity, and wind speed measured at 15 observation platforms at a 325 m meteorological tower in Beijing. Results show the hourly dry-bulb temperature decreases significantly with increasing altitude by about 0.9 °C per 100 m. The daily temperature difference decreases with increasing altitude. However, the absolute humidity, almost remains the same at every level. As altitude increases, the wind speed increases significantly by approximately 2 m/s per 100 m; however, the rate of change in wind speed decreases.

To investigate the impact of vertical weather gradients on the building cooling and heating loads, we conducted building performance simulation of a tall building using DeST. The results demonstrates that the impact of vertical meteorological gradients should be considered for a 300 m tall building. The difference in the building cooling and heating loads across different heights were mainly due to vertical temperature differences. Although the effect of wind speed differences on thermal loads was lower than that of dry-bulb temperature, it cannot be negated. The peak heating load also increases significantly with height mainly due to differences in hourly temperature and wind speed.

Moreover, a simplified correction method for outdoor air design conditions and TMY used for high-rise building design and simulation are given, and also, proposes a method for verification based on the measured data. The results show that the vertical gridded parameters obtained in this study are consistent with the meteorological parameters obtained from the measured data.

Acknowledgement

References

[1] (CTBUH), T.C.o.T.B.a.U.H. CTBUH Height Criteria for Measuring & Defining Tall Buildings https://www.ctbuh.org/resource/height.

2 Development, M.o.H.a.U.-R., GB 50352-2005 Uniform standard for design of civil buildings (in Chinese). 2019, China Architecture & Building Press.

3 (CTBUH), T.C.o.T.B.a.U.H. The Skyscraper Center- Global Tall Building Database of the CYBUH https://www.skyscrapercenter.com/.

4 Yoshino, H., T. Hong, and N. Nord, IEA EBC annex 53: Total energy use in buildings—Analysis and evaluation methods. Energy and Buildings, 2017. 152: p. 124-136.

5 Herrera, M., et al., A review of current and future weather data for building simulation. Building Services Engineering Research and Technology, 2017. 38(5): p. 602-627.

6 Tong, Z., Y. Chen, and A. Malkawi, Estimating natural ventilation potential for high-rise buildings considering boundary layer meteorology. Applied Energy, 2017. 193: p. 276-286.

7 Segal, M., R. Turner, and D.T. a, Using radiosonde meteorological data to better assess air conditioning loads in tall buildings. Energy and Buildings, 2000. 31(3): p. 243-250.

8 Song, D. and Y.S. Kim. Heating and cooling load analysis of supertall building considering the vertical micro climate change. in CTBUH 2011 World Conference. 2011. Seoul, KOREA.

9 Song, D. and Y.S. Kim, Effects of vertical meteorological changes on heating and cooling loads of super tall buildings. International Journal of High-Rise Buildings, 2012. 1: p. 81-85.

10 Peng, Z., Statistical Analysis of Observation Data of 325m Meteorological Tower in Beijing (in Chinese). 2005, Institute of Atmospheric Physics, Chinese Academy of Sciences.

11 (ECMWF), T.E.C.f.M.-R.W.F. ECMWF ERA5 Reanalysis https://www.ecmwf.int/en/forecasts/datasets/reanalysis-datasets/era5.

12 Liu, S. and Y. Huang, Discussion on effective sky temperature (in Chinese). ACTA ENERGIAE SOLARIS SINIGA, 1983. 4(1): p. 63-68.

13 Yan, D., et al., DeST — An integrated building simulation toolkit Part I: Fundamentals. Building Simulation, 2008. 1(2): p. 95-110.

14 Development, M.o.H.a.U.-R., GB 50189-2015 Design Standards for Energy Efficiency of Public Buildings. 2015, China Architecture & Building Press. p. 89p:A4.

15 Liu, T., Air conditioning design for super high-rise buildings (in Chinese). 2004: China Construction Industry Press.

16 Lutgens, F.K., et al., The Atmosphere: An Introduction to Meteorology. 1982: Prentice Hall.

17 Foken, T., Micrometeorology. 2008, Berlin: Springer.

18 Hsua, S.A., E.A. Meindlb, and D.B. Gilhousen, Determining the Power-Law Wind-Profile Exponent under Near-Neutral Stability Conditions at Sea. Journal of Applied Meteorology, 1994. 33(6): p. 757-765.

19 Simmonds, P., ASHRAE Design Guide for Tall, Supertall, and Megatall Building Systems. 2015, ASHRAE: Atlanta, GA, USA.

Artificial Neural Network Based Optimized Control of Chilled and Condenser Water Temperatures Set point

Hyeon jin Ji[1], Young Jun Lee[1], Jin Hwa Jung[2], Young Tae Chae[2] and Kwang Ho Lee[1*]

1. Department of Architecture, College of Engineering, Korea University, Seoul, South Korea
2. Department of Architectural Engineering, Cheong Ju University, Cheong Ju, South Korea

* Correspondence: wlguswls2@korea.ac.kr, kwhlee@korea.ac.kr.

Abstract— **In this study, the artificial neural network (ANN) based real-time predictive control and optimization algorithm for a chiller-based cooling system was developed and applied to an actual building to analyze the cooling energy-saving effect through in-situ application and actual measurement. For this purpose, we set the cooling tower's condenser water outlet temperature and the chiller's chilled water outlet temperature as the system control variables. To evaluate the algorithm performance, we compared and analyzed the electric consumption and the COP when the chilled and condenser water temperatures were controlled conventionally and controlled based on ANN. As a result, the ANN model's accuracy was high with a Cv(RMSE) of 4.9%. In addition, the ANN-based control algorithm's energy saving analysis showed that the average energy-saving rate for chiller was 24.7%, and the total average energy-saving effect for chiller and cooling towers was 7.4%. The results confirmed that the proposed MPC algorithm could contribute to improved HVAC energy efficiency in commercial buildings.**

Index Terms— **ANN(Artificial Neural Network), MPC(Model Predictive Control), Cooling Energy, In-situ Application**

1. Introduction

Research on reducing the energy consumption of buildings is actively underway, having developed various algorithms for improving the performance of HVAC systems. A number of studies related to the optimization of the performance of the HVAC system itself and the comparison of system performance through the development of various algorithms, the development of predictive control algorithms through building simulation programs, and the prediction of system performance according to the operating conditions were identified through the literature review [1].

However, research to predict the cooling energy consumption of HVAC by applying the developed control algorithm to an HVAC system operating in an actual building and verifying the effects of the algorithm by utilizing actual data is limited. HVAC systems involve a number of devices with different characteristics, such as chillers, cooling towers, pumps, AHUs, and boilers, and changes in control set-points of any one of these components can affect the energy consumption of other devices and the internal environment of the building. In order to predict quantitative energy consumption, it is necessary to operate an HVAC and verify its performance by applying the developed algorithm to an actual building. In addition, although cooling towers and chillers take up a large portion of a building's cooling energy consumption, the predictive and control research using various operating conditions and variables related to cooling towers and chillers is insufficient [1].

We analyzed the control variables to find a method for optimizing the control of setpoints, and based on this, we developed MPC based HVAC System real-time prediction control and optimization algorithm. In addition, to accurately the predict energy and further reduce energy consumption by utilizing the performance information of operating variables, the developed algorithm was applied to an actual building to analyze cooling energy savings using actual monitored data [1]. The overall flowchart of this study is shown in Fig. 1 Training data were collected by randomly changing the system control variables, chilled water, and condenser water temperatures in the summer of 2018, and the ANN model was developed with the acquired training data. Subsequently, in the summer of 2019, data was collected after applying the conventional control and ANN-based control algorithm every other day to the target building. Finally, the cooling energy savings effect in each cooling load region was analyzed by comparing the power consumption and COP of the conventional control method and the ANN-based control method [1].
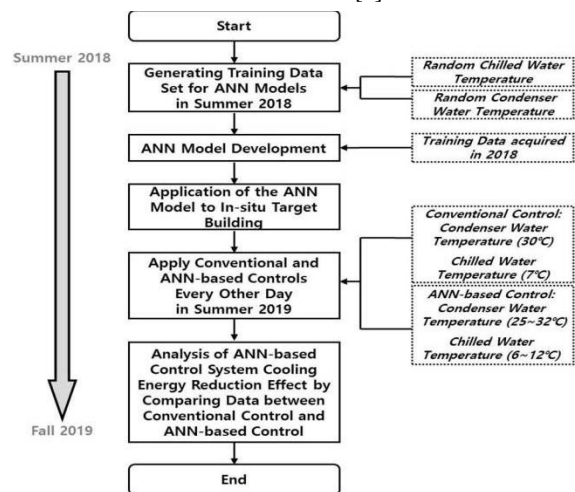

Figure 1 Overall Flow Chart of the Study [1]

2. Method

2.1 Description of the target building

A 10-story office building with a Building Energy Management System (BEMS), for which it is easy to apply and collect algorithms for deriving more accurate results in predicting and controlling MPC-based HVAC real-time energy consumption was selected as the target building. Fig. 2 shows the target building selected. It is located in Gwanak-gu, Seoul, Korea, and the areas utilized in this study – A podium (2nd basement to 3rd floor), A-wing (3rd to 8th floors), and B-wing (3rd to 10th floors), has a floor area of 42,565 m2. The building's HVAC system consists of two absorption chillers, one turbo chiller, one cooling tower, two chilled water pumps, and two condenser water pumps. Neither the building's occupancy rate nor the cooling load was high during the measurement period, so two absorption chillers were not operated and only one turbo chiller was operated. Consequently, absorption chillers were excluded from the analysis [1].

In addition, 18 AHUs and 3 OHUs are installed on the podium, A-wing, and B-wing to handle indoor heat loads. The building equipment specifications for the building to be analyzed are shown in Table 1, and most of the energy consumption data of the building, such as HVAC systems, heat source systems, and lighting systems, could be collected through their BEMS [1].

Figure 2 "S" Company Cooperation R&D Center Aerial View [1]

Table 1 HVAC System Equipment Specifications [1]

Equipment	Spec
Turbo chiller	Cooling capacity: 450 USRT(1,582 kW), COP 5.7, Condenser water inlet temperature: 32℃/ outlet temperature: 37℃, Chilled water flow rate: 2,826 LPM(170 m³/h), Condenser water flow rate: 5,400 LPM(324 m³/h)
Chilled Water Pump	Chilled water flow rate 2,826 LPM(170 m³/h), head 23m, motor 18.5kW
Condenser Water Pump	Condenser water flow rate 5,398 LPM(324 m³/h), head 31m, motor 45kW
Cooling Tower	Cooling capacity 500 CRT(2,267 kWh), Condenser water inlet temperature: 37℃/ outlet temperature: 32℃, Condenser water flow rate: 5,398 LPM(324 m³/h), motor 30kW X 5EA
AHU (Air Handling Unit) OHU (Outdoor Air Handling Unit)	Cooling capacity: 110 kW ~ 446 kW(Total 4,338kW) Chilled water flow rate: 7,817 LPM(469 m³/h), Chilled water inlet temperature 6℃/outlet temperature 14℃

3. A predictive model based on Machine Learning

3.1 Data description

ANN model development was carried out using actual data from the HVAC system of the target building. The data collection period was from June 19, 2018, to July 13, 2018, and we collected 41,850 data per minute, excluding weekends. In addition, for application to the developed ANN, deletion of data during the downtime of the cooling plant system and the exclusion of abnormal data (null) values were performed to preprocess using per minute 19,582 data. Finally, 19,582 data per minute was acquired, and 1306 usable data were acquired by averaging per 15 min, which is an energy consumption evaluation standard unit [1].

3.2 Development of the predictive model

The predicted performance of energy consumption was analyzed by comparing 1 to 5 hidden layers at 15-minute intervals. Performance improved as the number of hidden layers increased; 4 hidden layers produced the best performance, a Cv(RMSE) of 4.9%. Table 2, shows the results of the optimal setting conditions for the hyperparameters, and Fig. 3 is a graph comparing the results of actual building energy consumption measurements with the results predicted by ANN. The CV(RMSE) value is considered to be a reliable value when it is below 30% of the hourly data standard based on ASHRAE Guideline 14, indicating that predictive performance shows excellent reliability with a Cv(RMSE) of 4.9% [1].

Table 2 Optimal Setting Conditions for ANN Model [1]

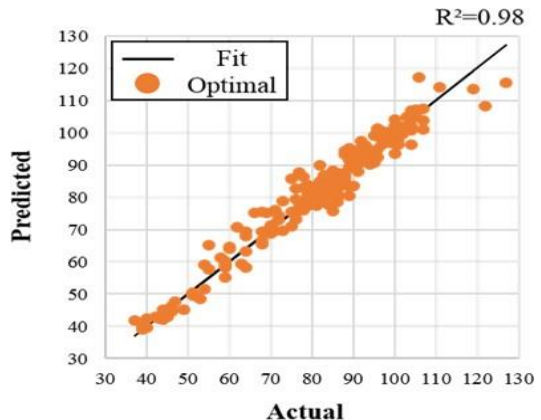| Type	Setting Condition
Hidden layer	4
Weight initialization	Xavier normalization
Updater	Adam (learning rate=0.001)
Activation function	ReLU
Loss function	MSE (Mean Square Error)
Normalization	Z-transformation

Figure 3 Comparison between Measured and Predicted Building Energy Consumption by the Optimized ANN Model [1]

3.3 Local optimization

The minimized building energy consumption point among the operating ranges of chilled water and condenser water temperatures according to each load region was sought using the completed ANN model through the optimization process. The range of the control variable was 6 °C–12 °C for chilled water temperature and 25 °C–32 °C for condenser water temperature. When each temperature was changed by 1 °C, the temperature point at which the building energy consumption was minimized according to the expected load section was calculated and supplied to the BEMS under the set conditions of the next time-step [1].

4. Overview of the In-situ of the optimization algorithm

4.1 Overview of the In-situ data collection

This study aims to reduce energy consumption and improve the efficiency of the chiller and cooling tower operation through optimal control of AI-based chilled water and condenser water temperatures. For this, the developed ANN-based optimization algorithm was applied to the target building, and through optimization processing, the data necessary for analysis were extracted. The data collection period for data verification applied to the HVAC system was from July 8 to September 6, 2019, and the acquired data were collected in 1-minute increments [1]. For empirical evaluation of the reduction of building energy consumption through chilled water and condenser water temperature control, data related to the turbo chiller and cooling tower of the target building were analyzed. Table 3 is the in-situ data information related to the operation data input and output and energy consumption required for this study. From the items related to the HVAC system, input/output data and energy consumption information related to the turbo chiller and cooling tower were extracted [1].

Table 3 In-situ Data Information [1]

Measured Data	Data to be Calculated
Outdoor air temperature	Wet-bulb temperature
Outdoor humidity	Chilled water temperature difference
Chilled water outlet temperature	Cooling load
Chilled water inlet temperature	Condenser water temperature difference
Chilled water flow rate	
Bypass flow rate	**Control Variables Set-point Data**
Condenser water inlet temperature	Condenser water set-point temperature
Condenser water outlet temperature	Chilled water set-point temperature
Terminal differential pressure of wing A	Control Variables Set-point Data
Terminal differential pressure of wing B	
Cooling tower electric consumption	
Chiller electric consumption	

4.2 The calculation formula for hourly cooling load and COP

Since COP is an essential element in data analysis, the COP data for this study were obtained using a calculation formula. To establish the COP calculation formula, the chiller's COP calculation concept was used. Eq. (1) is a chiller's COP calculation concept and calculation formula through a P (Pressure) - h (Enthalpy) diagram [1].

$$COP(\varepsilon) = \frac{\text{Heat absorbed by refrigerant from evaporator}(\frac{kcal}{h})}{\text{Heat amount of work supplied by the compressor}(\frac{kca}{lh})} \quad (1)$$

$$= \frac{\text{Refrigeration effect}}{\text{Compression workload}} = \frac{q_e}{AW} = \frac{(h_a - h_c)}{(h_b - h_a)}$$

Where,

q_e : The amount of heat absorbed by 1 kg of refrigerant in the evaporator. $(\frac{kcal}{kg})$

$h_c = h_d$: Refrigerant enthalpy at the inlet of the evaporator $(\frac{kcal}{kg})$

AW : the amount of work in a compressor $(\frac{\text{kcal}}{\text{kg}})$

h_a :
Refrigerant enthalpy at compressor inlet $(\frac{\text{kcal}}{\text{kg}})$

h_b
: Refrigerant enthalpy at compressor outlet $(\frac{\text{kcal}}{\text{kg}})$

Finally, Eq. (2) of the calculated chiller COP and Equation 6 of the system COP are as follows [1]:

$$\text{Chiller COP} : \frac{\text{Cooling Load}}{\text{Turbo Chiller Electric Energy Consumption}} \quad (2)$$

System COP
$$: \frac{\text{Cooling Load}}{\text{Total Electric Consumption of (Cooling Tower 1 + Cooling Tower 2 + Turbo Chiller)}}$$

5. Result analysis

To verify the ANN model applied to the actual building, electric energy consumption and COP were analyzed using the acquired data. As a method for verifying the effectiveness of ANN, the electric consumption and COP of the cooling tower and the chiller when the ANN model was applied to the building and when the building was conventionally controlled (fixed chilled and condenser water temperatures) were compared. As independent variables, cooling load and outdoor air wet-bulb temperature, which greatly affect system performance, were selected [1].

5.1 Chiller electric consumption and COP

Fig. 4 is a graph of the electric consumption of the chiller according to the chiller cooling load region. It can be seen that the chiller electric consumption increases as the cooling load increases. Additionally, in the cooling load region of about 1300 kWh or more, the electric consumption of the ANN-based control and conventional control were similar to each other. The reason for showing this result is that the load section is close to 450RT (1.580 kW), which is the rated capacity of the turbo chiller, and it

is considered that the ANN-based control and conventional control are controlled under similar conditions [1].
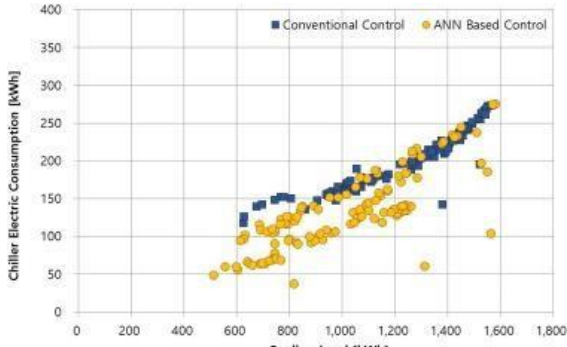

Figure 4 Chiller Electric Consumption According to Cooling Load [1]

Fig. 5 is a graph showing the COP of the chiller according to the load. It can be confirmed that the two control methods are similarly controlled in sections with a load of 1250 kWh or higher. It can also be observed that the ANN-based control is divided into cases where the COP is improved and cases where the COP overlaps when compared to the conventional control in the section where the outdoor air wet-bulb temperature is 25 °C or higher [1].

On the other hand, when the ANN-based control was applied in the time period where the outdoor air wet-bulb temperature was below 25 °C and the load was lower than 1250kWh, the chiller COP data was improved. In particular, the COP of the chiller was significantly improved when the ANN-based control was applied in a load section between 600 and 800 kWh [1].
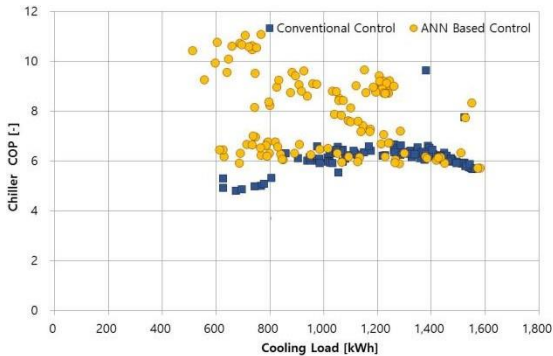
Figure 5 Chiller COP according to Cooling Load [1]

5.2 Chiller energy savings variations according to cooling load

Based on the previous data analysis, we analyzed the profile of reducing the cooling energy consumption of the ANN-based chiller operation. Fig. 6 is the chiller average electric energy consumption graph for each load section, and Fig. 7 is the chiller average COP graph for each load section. In the cooling load region above 1300kWh, the ANN-based control and conventional control showed similar performance due to similar control behavior with a high load; hence, a load range from 600kWh to 1300kWh was selected for analysis. In the condition of the lowest cooling load region, 600kWh to 700kWh, the ANN

algorithm shows an electric energy savings rate of about 38.2% and a COP increase rate of about 41.6% when compared to when the ANN algorithm is not applied, the most outstanding improvement shown [1].
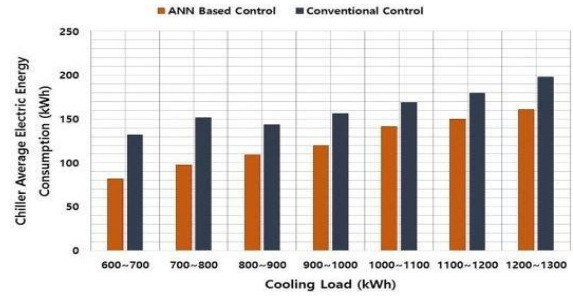

Figure 6 Chiller Average Electric Energy Consumption According to Different Cooling Load Regions [1]
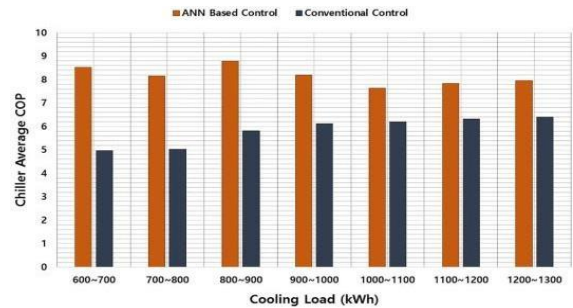

Figure 7 Chiller Average COP According to Different Cooling Load Regions [1]

5.3 System electric consumption and COP

Fig. 8 is a graph showing the system electric consumption according to the cooling load. The system electric consumption in this study indicates the sum of the electric consumption of the cooling tower and the chiller, excluding the constant pump electric consumption in most of the time period due to the constant flow system. As shown in the graph, as the cooling load increases, the electric consumption of the system also increases proportionally. The reason for these results is that since the cooling tower electric consumption to be analyzed takes up 36% of the total cooling energy, the ANN control algorithm reduces the electric consumption of the chiller at the expense of increasing the cooling tower electric consumption. In the end, this is because the system was controlled in the direction of minimizing the total system electric consumption [1].
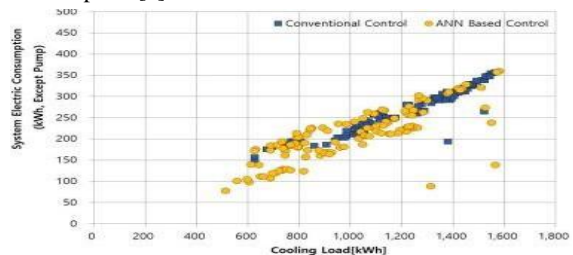

Figure 8 System Electric Consumption According to Cooling Load [1]

Fig. 9 is a graph showing the system COP according to the cooling load. The overall graph pattern shows that when the ANN-based control is applied, COP is divided into improved data and similar data compared to the conventional control. The ANN-based control data showed a similar COP to the conventional control, and the improvement of the system COP was lower than that of the chiller COP when the ANN-based control was applied. The reason for this is considered to be due to, as mentioned above, the ANN control algorithm working to minimize the overall system electric consumption by reducing the electric consumption of the chiller at the cost of increasing the electric consumption of the cooling tower [1].
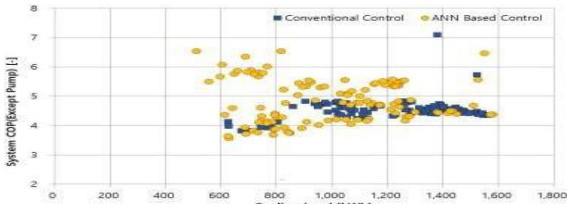
Figure 9 System COP According to Cooling Load [1]

5.4 System energy savings according to cooling load

Based on the data analysis of the system, the effect of reducing the cooling energy consumption of the ANN model according to the cooling load was analyzed. Fig. 10 is a system average electric energy consumption graph for each cooling load region with and without the ANN-based control, and Fig. 11 is a system average COP graph for each cooling load region with and without the ANN-based control [1].

When the ANN-based control is applied, it can be seen that the electric energy consumption of the system is reduced and that the COP is improved in all the cooling load regions. The average energy savings rate of the ANN-based control was 5.7%, and the COP increase rate was 4.6% when compared with the conventional control at cooling loads between 800 kWh and 1100 kWh, which showed the lowest energy savings effect among all the cooling load regions [1].
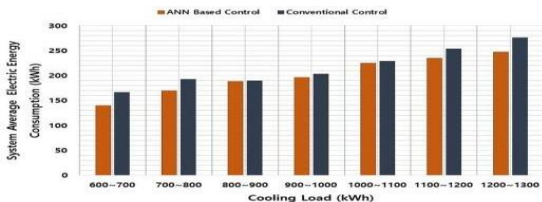

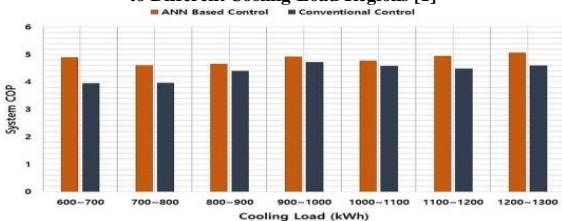**Figure 10 System Average Electric Energy Consumption According to Different Cooling Load Regions [1]**

Figure 11 System Average COP According to Different Cooling Load Regions [1]

6. Conclusion

In this study, an ANN-based predictive control algorithm was developed and applied to an actual building of the "S" company located in Seoul, Korea. The in-situ evaluation of the cooling energy savings effect was performed using actual operation data after applying the ANN-based predictive control algorithm in the HVAC system.

The accuracy of the final ANN model was Cv(RMSE) 4.9%, which ensured reliable performance. In addition, to verify the energy reduction effect when applied to a real building, the electric consumption and COP of the chiller and cooling tower were compared and analyzed with and without applying the ANN control method.

A cooling load region of about 1300 kWh or more showed similar results with and without ANN control implementation, while a cooling load region of 1300 kWh or less showed significant electric consumption reduction when ANN is applied. The average energy savings rate of the chiller was 24.7%, and the average COP increase rate was 28.2%.

Moreover, the total system electricity, indicating the sum of the electric consumption of the cooling tower and the chiller, was analyzed. The system analysis results showed a pattern similar to that of the chiller analysis, but the energy savings effect was lower than that of the chiller alone. The reason for this is thought to be due to the ANN control algorithm operating in the direction of minimizing the total system electric consumption by lowering the electric consumption of the chiller at the expense of increasing the electric consumption of the cooling tower. Finally, it was confirmed that the average energy savings rate of the total system is 7.4% and that the average COP increase rate is 9.4% [1].

REFERENCES

[1] W. H. Kang, Y. B. Yoon, J. H. Lee, K. W. Song, Y. T. Chae and K. H. Lee, "In-situ Application of an ANN Algorithm for Optimized Chilled and Condenser Water Temperatures Set-point During Cooling Operation," Energy and Buildings, Vol. 233, 110666, February 2021

REHVA
Student Competition
Other Participants' Contribution

Milica Prugić	Serbia
Marie Anne Resmond	France
Pedro Navarro Cobacho	Spain
Moritz Bienz Kevin Bucheli	Switzerland
Raul-Lucian Nistor	Romania
Martin Sokol	Slovakia
Gabriele Risoli	Italy
Rick Cox	The Netherlands
Cătălin Constantin Oprescu Bogdan Țarălungă	Romania

Automation of the Conference Room by Applying Struxure Ware Environment

Milica Prugić; dr Velimir Čongradac (Supervisor)

University of Novi Sad; Faculty of Technical Sciences; Trg Dositeja Obradovića 6, Novi Sad

prugicm@gmail.com; velimir@uns.ac.rs

2021.

Abstract— The problem that is approached in this thesis is the design of an automatic heating and cooling system, lighting, media devices, as well as the control system of the conference room within the business premises, which will improve business and provide energy and save money. This thesis represents the system for monitoring, measuring, and controlling the automatic control system of the conference room. The operation of the system is presented within the Schneider software for the control and programming of microcontroller devices.

Index Terms—**Building automation, controling, cooling, heating, management**

Introduction

The level of automation in residential and commercial buildings is constantly growing. This phenomenon occurs not only because of the greater need for easier management and comfort but also because of the many advantages that the automation of buildings and their premises brings in terms of savings and energy management.

Smart buildings and automated business premises are becoming a trend of the new generation of building construction. That enables smart building control to meet users' necessities. Business premises represent large energy consumers, and for that reason, the control and automation of the building's energy management system are of great importance. By implementing them, it is possible to achieve savings in energy and money. Also, improving energy efficiency contributes to environmental protection.

I. ENERGY CONSUMPTION IN OFFICE BUILDINGS

The construction sector is the largest consumer of final energy, followed by transport and industry. About 41% of final energy consumption in the EU belongs to buildings. It is also responsible for 36% of EU CO2 emissions [1]. For this reason, the construction industry has the task of designing such systems that will save energy, provide a forecast of future energy consumption, promote its conservation and monitor its constant consumption [2]. The following diagram shows the usual electricity consumption in buildings. The largest consumer in office buildings is lighting with 39% including exterior decorative and interior lighting, which is followed by 15%

of energy consumption for cooling, then 10% of consumption caused by computers, 9% ventilation, 5% space heating, 4% office equipment, 1% water heating and 13% other consumers.[1]

Figure 1.1 Average electrical energy consumption in office buildings [3]

By installing the cheapest sensors, controllers and upgrading the *BAS*, energy consumption in buildings can be reduced by as much as 20-30%. The price of advanced sensors and controllers on the market is slowly declining. They are relatively easy to install during a building reconstruction project or when building a new building.

II. MODEL OF THE CONFERENCE ROOM

This subchapter shows the sensors used as well as the controller used to create the conference room model. These are the presence sensor, the magnetic window opening sensor, the temperature sensors, CO2 sensor and the *SmartX AS-B-36* controller.

The presence sensor used is *Argus Presence*, manufactured by *Schneider Electric*. Inside this sensor, there is also a device for measuring natural light, which, depending on the brightness in the room, measured in lux, will provide information for reduced brightness and turn on the lighting in the presence of a person. In addition to the fact that we will achieve savings, the productivity of employees is also increasing because the lighting is constantly optimal.

Figure 2.1 Presence sensor ARGUS MTN550-1119 [5]

Figure 2.2 Magnetic sensor for detecting window openings [6]

In the conference room model discussed in this paper, a magnetic sensor is used to stop the heating and cooling system and acts as a switch. The working principle of the magnetic sensor is normally closed. When the windows are closed, a logic 1 is sent to the controller. When opening the window, the sensor gives a logic 0.

Using this magnetic sensor will automatically stop the heating system in winter and the cooling system in summer, and thus achieve great savings in both energy and money.

Two temperature sensors will be installed in the conference room model - one sensor inside the room, manufactured by *Schneider Electric*. We will use it to operate a two-pipe fan-coil system, while the other will be installed outdoor and used to measure the outside temperature that we will use in the hot or cold water system. The manufacturer of the external temperature sensor is *Phoenix BB*.

Figure 2.3 Indoor temperature sensor AP9335T [5]   *Figure 2.4 Outdoor temperature sensor STS-1 [5]*

Sensor for measuring CO_2 levels in air, manufactured by SystemAir, will be used for regulation of opening VAV damper. Variable Air Volume systems are used for distribution of air indoors, which can have variable capacity, but constant temperature. The main benefit of using VAV systems is energy saving, furthermore they offer increase of comfort in thermal zones.

SmartX AS-B server is a powerful device with a built-in power supply and I/O modules. The server can act as a standalone server using built-in I/O modules. It can be used to monitor and manage devices as well. In small installations, the built-in *SmartX AS-B* server functions like a standalone server, while in medium and large installations, the functionality is spread across multiple *SmartX* servers that communicate via the *TCP/IP* protocol.

Figure 2.5 Schnaider Electric AS-B-36 [5]   *Figure 2.6 SystemAir CO2 sensor*

III. SYSTEM MANAGEMENT LOGIC

To implement the idea of automation of the conference room, we used the *EcoStruxure Building Operation*

environment, within which we used *WorkStation* and the software tools it offers, such as *Fuction Block Editor* and *Graphic Editor*. The next part of the paper describes the logic of operation and system management.

A. Operation of a Two-pipe Fan-coil System

Inside the conference room, a two-pipe fan-coil system is placed on the ceiling of the room. It is used for heating or cooling. For the system to work, it needs to receive a signal from the main switch - a timer. The timer determines the operating time of the entire system and is set to give a logic 1 in the period from 7 am to 5 pm.

Magnetic sensors mounted on 3 windows can suspend the heating and cooling system when the windows are open. Another device that regulates the operation of the fan-coil is the presence sensor. If the sensor detects someone in the room, it will automatically turn on the heating or cooling system. On the other hand, if the sensor detects no one in the room, with a delay of 10s, the system will enter the saving mode. This will be achieved by lowering the setpoint temperature on the thermostat to 15 °C if heating is selected on the mode selector switch, or increasing it to 26 °C if cooling is selected. This can be bypassed using the bypass button, which will delay the entering save mode, for the 30s. This button is used if the employee expects another member to enter the room soon. This way there will not be necessary to change the operating mode three times in a short period.

The fan located in the fan coil has 3 speeds. Depending on the absolute difference between the temperature on the thermostat and the temperature using the temperature sensor, the fan-coil will increase the optimal fan speed. In some cases, just starting the fan-coil unit fan is not necessary for the reason that by opening the three-way valve on the hot or cold water supply, 20% of the energy will be emitted by radiation. If the absolute temperature difference is 2 °C, the fan will be switched off and the three-way valve will open. This will be able to compensate for the required temperature difference without convection. The first fan speed will be switched on if the difference is between 2 °C and 4 °C, the second 4 °C and 6 °C and the third if the absolute difference is greater than 6°C.

Another thing that is managed is opening of the VAV damper. VAV system is connected to the fan-coil and by using the CO2 sensor, the opening of the VAV damper which regulates the flow of fresh air and the air from the room, will be controlled. Furthermore, if the level of CO2 is higher than desired 600ppm, the higher will be percentage of the flow of the fresh air and vice versa. Following this, the percentage of open state of the VAV damper will be:

➢ 100% if CO2 level is above 1000ppm
➢ 80% if CO2 level is between 1000-900ppm
➢ 60% if CO2 level is between 900-800ppm
➢ 40% if CO2 level is between 800-7000ppm
➢ 20% if CO2 level is between 700-600ppm
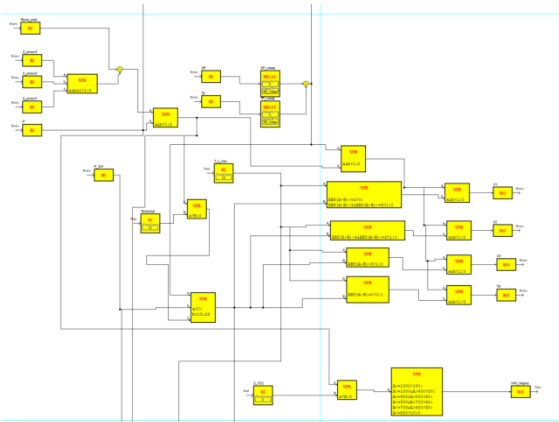➢ 10% if CO2 level is below 600ppm

Figure 3.1 Function block diagram of fan-coil system control logic

B. Control of Lightning, Curtains, and Projector

The lighting is activated if the lighting switch is activated and if the presence sensor detects people in the room. If the presence sensor detects the room is empty, the lighting will turn off automatically after 10s. The lighting is additionally adjusted with a dimmer and lux meter. Namely, if the lux meter detects lighting less than 300lux, the lighting will be activated, otherwise, it will turn off.
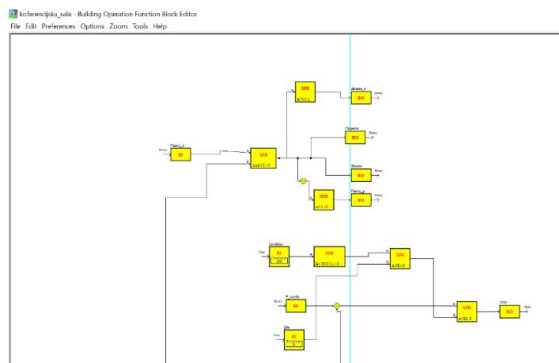
Figure 3.2 Function block diagram of lightning, projector and curtains control logic

The dimmer will dim the lighting depending on how much light is needed to reach 300 lux in the room.

When presenting a certain content in the conference room by lowering the screen with an *IR* controller, that has a built-in electric motor and an *IR* receiver, the curtains will be automatically drawn and the projector, which also has an *IR* receiver, will be turned on. The lighting will be adjusted manually depending on the wishes of those present in the hall.

C. Water Preparation

The water temperature in the system is maintained by the heating subsystem and the water cooling subsystem. The water temperature in the system is regulated by a *PID* controller depending on the current water temperature and the set point water temperature. The set point temperature

in the heating mode is obtained based on the absolute difference between the set point temperature in the room and the outside temperature. Based on this, it follows that the set point water temperature for the heating mode will be:

- 40 °C - for a difference equal to or less than 10 °C
- 45 °C - for a difference greater than 10 °C and equal to or less than 20 °C
- 50 °C - for a difference greater than 20 °C and equal to or less than 30 °C
- 55 °C - for a difference greater than 30 °C and equal to or less than 40 °C
- 60 °C with a difference greater than 40 °C

In cooling mode, the setpoint water temperature will be:

- 15 °C - for a difference equal to or less than 5 °C
- 13 °C - for a difference greater than 5 °C and equal to or less than 10 °C
- 10 °C - for a difference greater than 10 °C and equal to or less than 15 °C
- 7 °C - for a difference greater than 15 °C and equal to or less than 20 °C
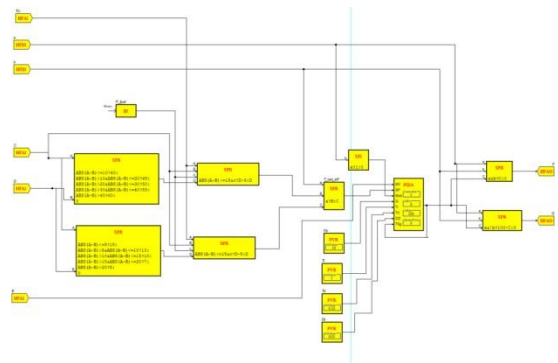- 5 °C - for a difference greater than 20 °C

Figure 3.3 Function block diagram of a water treatment management logic

In the same way as the regulation of the set point temperature using the thermostat in the previous chapter is explained, it will automatically decrease to 15 °C in the heating mode or increase to 26 °C in the cooling mode.

It is worth mentioning that that people just by sitting or doing office work, can emit from 105W to 150W of thermal energy. In special instances, with reference to this fact the set point temperature can be additionally regulated. If heating mode is activated and the expected number of people is higher than the usual, the set point temperature of water can be reduced. The level of reducing set point temperature can be defined by experimental method where we need to take into account the power of our heating and cooling devices, difference between outside and indoor temperature, as well as thermal envelope of the building. On the other hand, a slight opposite action would be done if cooling mode is on. Respectively, if number of people is expected to be lower than usual, we can increase the set point temperature, and in that way achieve savings without threatening comfort in thermal zone.

At the output of the *PID* controller, an analog value is obtained that should control the opening of the mixing valve of hot or cold water with return water that has already handed over its cooling or thermal energy to the room.
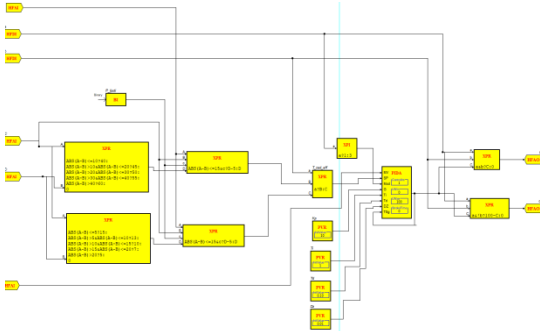

Figure 3.3 Visual presentation of water treatment management logic

IV. SUPERVISORY CONTROL AND DATA ACQUISITION

Three figures of the interface in SCADA system were implemented.

The first figure of the interface, called Homepage, shows a real-time state of the conference room. This figure shows 3 magnetic window sensors, lighting, presence sensor, and fan-coil system operation. If the windows are closed, the squares showing the window will be gray, while when the window is opened, they will turn orange, and the heating or cooling, or fan-coil, will be switched off automatically. A similar sequence of events will occur with the presence of a sensor and lighting. If the presence sensor is active, the square showing two people will be orange, otherwise, it will be gray, and the operating mode will enter the saving mode. Also, if the lighting is less than desired, and if the presence sensor is active, the lighting will be activated, and the square will be orange, otherwise, it will not work and will change color to gray. If the fan-coil unit is in operation, the box showing the fan will be orange, and the fan will rotate to the right, but if it is off it will be gray, and the fan will be stopped.

Figure 4.1 shows the state of the system in which the presence sensor is active, as well as the lighting, while one window is closed, and two are open, thus the fan-coil unit is stopped.

The second figure of the interface shows the control of the fan-coil unit parameters, lighting, three-way valve, saving mode, and heating or cooling mode. On the left side, there is a rectangle in the frame when the current temperature in the room is displayed and the desired temperature is set on the thermostat, in this case, it is 22 °C. The heating or cooling system is shown in the middle of the picture. If the main switch is active and receives a signal from the timer, the circle above which the system is written will be orange, otherwise, it will be white. To its right is a circle showing the operating mode. If the heating is on, as shown in the picture below, the circle will be red with the letter *H* in the middle. If the heating is off, it will

be blue with the mark *C*. If we click on the middle of the field with the graph of current temperature values and the graph of historical values of room temperature, the desired graph will open automatically. The last rectangle in the middle shows the current level of CO_2 in the room. The right side shows the saving mode, the active fan speed, the opening of the three-way valve, and the current lighting in the room. Namely, if the save mode is activated, the circle will be orange, otherwise, it will be white. 3 circles are shown within the rectangle showing the fan speed, where each circle represents one speed. Accordingly, which fast is active, its circle will be colored orange. The circle marked *TV* will be orange if the three-way valve is open. The last item shows us the current brightness in the room in lux. In the figure 4.2, the brightness is 100 lux out of the desired 300 lux, which means the lighting system will start automatically.

Figure 4.1 Graphical presentation of Homepage of the SCADA system interface
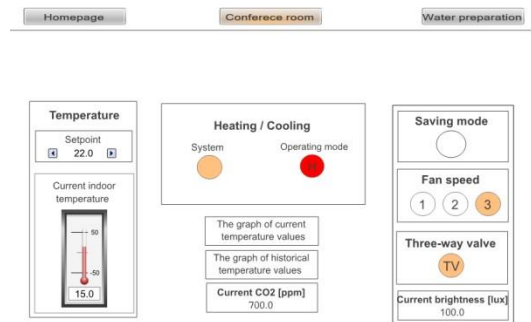

Figure 5 Graphical presentation of Conference room of the SCADA system interface

The third figure of the *SCADA* system interface shows the water preparation system for heating or cooling. This figure shows the water temperature, outside temperature, heating/cooling mode, mixing valve openness, and *PID* controller parameters based on which the required water

temperature is calculated to heat or cool the room. On the left side, there is a set value of water temperature, below this value, there is a graphical display of the thermometer showing the current water temperature, and below it a thermometer showing the outside temperature. In the middle is a circle showing the activity of the main switch, where if it receives a signal from the timer it will be orange, otherwise, it will be white. To its right is a circle showing the operating mode. If the heating is on, as shown in the picture below, the circle will be red with the letter *H* in the middle, in the case of cooling, it will be blue with the *C* mark. A display of the open state of the mixing valve, during heating or cooling, is shown in the middle which can vary from 0 to 100%. On the right side are the parameters of the *PID* controller.
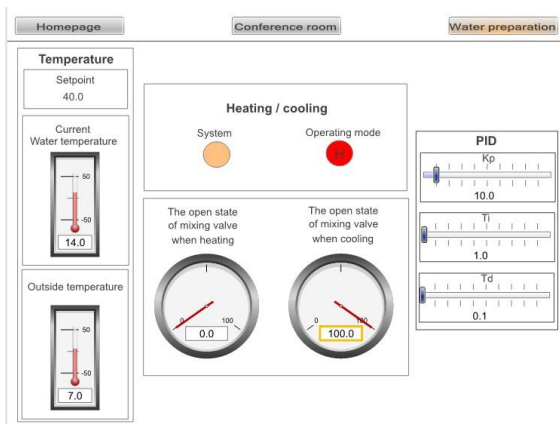

Figure 4.2 Graphical presentation of the Water preparation of the SCADA system interface

V. CONCLUSION

Building construction automation is constantly in progress. The goal of all buildings is to become more economical, safer, more comfortable, and energy-efficient, which is what the introduction of automatic control brings. Aspects that automation covers are *HVAC*, lighting, plumbing, *IoT* devices, electrical devices, etc. by using the most flexible and customizable software from the best automation companies, great savings can be achieved.

The building construction automation system can be connected to various functional systems inside, and in that way, it is possible to react to the problem significantly faster. Automated premises have many advantages over non-automated ones, such as energy savings, safety, reduced costs, and supervision and management. Shortly, automation technology will become more accessible and reliable, and the integration of automation itself will become more widespread.

Based on the analysis of energy consumption in business facilities, introduction to communication protocols, and taking into account the selected devices used in the design of the conference room automation project within the business premises, it is concluded that the application of automatic heating, cooling, and lighting would be justified, efficient and cost-effective.

REFERENCES

1 **D.W.U. Perera, N.O. Skeie** „Modeling adn Simulation of Multi-Room Buildings'' Faculty of Technology, University College of Southest Norway, Postboks 203, N-3901, Norway

2 **Keith Moss** „Energy Management in Buildings" 2nd Edition 2006

3 https://www.prescriptivedata.io/content/chart-of-the-day/average-office-building-electricity-consumption Accessed: September 10, 2021.

4 **Jennifer King and Christopher Perry** „Smart Buildings: Using Smart Technology to Save Energy in Existing Buildings'' American Council for an Energy-Efficient Economy, February 2017

5 https://www.se.com/ww/en/product Accessed September 16, 2021.

6 https://www.absoluteautomation.com/products/seco-larm-sl-sm200qw-normally-closed-proximity-door-switch-5-pk Accessed: September 16, 2021.

Artificial neural network simulation of energetic performance for sorption thermal energy storage reactors

Marie-Anne RESMOND, Carla DELMARRE

Department of Civil Engineering and Urbanism, INSA, Lyon, France (CETHIL Laboratory)
E-mail: marie.anne.resmond@gmail.com; carla.dlmarre@gmail.com
Under the supervision of Professor F. KUZNIK, CETHIL Laboratory, f.kuznik@insa-lyon.fr
Academic year 2019-2020

Abstract— **This research project is based on the modelling of a sorption thermal energy storage system (STES). Due to the high storage densities and very low heat losses, sorption has become a popular topic of research, particularly in the application of seasonal storage [1]. The storage material studied was a Zeolite (alumi-nosilicate), the most common and most researched type of sorbent for sorption heat storage, due in part to its low cost [2]. Such systems have traditionally been designed using complex physical models requiring powerful software and machines to produce results. In this study an artificial neural network (ANN) was implemented to model a heat storage, leading to drastically lower computational costs. The neural network was trained using experimental results to model reality as best possible. Moreover, combined with TRNSYS, the ANN model can be used to study the effect of a sorption thermal energy storage reactor on the heating demand of a building. By using a recurrent neural network (RNN) and the Deep Learning Toolbox in MATLAB, good accuracy was obtained, and the predicted results are close to the experimental results. The mean squared error in the data set used in this study is around 2.4 degrees Celsius for the prediction of the difference in temperature entering and leaving the reactor. Given that the variation of temperature ranges from 0 to 40 degrees Celsius during the hydration of the storage material, which represents the worst-case scenario, the model gave accurate results to within 6%.**

Index Terms— **Artificial neural network model; deep learning, ettringite; sorption thermal energy storage; zeolite**

Introduction

The future energy performance of buildings is one of the key factors in achieving the 40% reduction in the greenhouse gas emissions as part of the EU Climate & Energy objectives [2]. Thermal Energy Storage (TES) systems can be applied in conjunction with renewable energy deployment to permit a more efficient energy usage. For instance, abundant solar energy in summer could be stored and used to fulfil heating requirements in winter. Furthermore, the efficient design of inexpensive energy storage systems could mitigate the inherent intermittency of renewable energy sources.

Currently, three types of thermal energy storage systems exist: sensible heat storage, latent heat storage and thermochemical storage [3]. This study focuses on the latter which occurs through a completely reversible chemical reaction. Energy can be absorbed and released through the breaking (endothermic) and reforming (exothermic) of

molecular bonds, respectively. The energy storage capacity depends on the reaction enthalpy as well as the storage density of the material [4].

Thermochemical energy storage takes place either in the form of chemical reactions or sorption systems [3]. Sorption systems in TCES, the object of this study, require adsorption for solid materials or absorption for liquids. Such systems, which have been largely researched in the over the last 10 years [1, 4, 8-10, 11-13], are most commonly comprised of zeolites due in part to their low cost [2]. The system requires the porous surface of the solid to be bound by a gas on its inner surface. Heat is then transferred into the material during the desorption step and released during the adsorption. The process is cyclic and can be used for long-term energy storage. For instance, heat in the summer can be stored and released during the winter.

Whilst the first two means of storage have been widely exploited and many resources can be found on them, the initial phase of the latter has not yet led to substantial concrete results and as such it is still in its experimental phase. Nonetheless, this method of energy storage could theoretically be more productive thanks to a higher relative theoretical energy density and a capacity to store energy for long periods of time without heat dissipation [5].

Detailed physical models of TES have been developed and reported in the literature [9,10]. Usually based on the analysis of heat transfer, mass transfer, and reaction kinetics in the reactor, they are complex and require large computational efforts, making it difficult to use them for yearly simulations. One possible strategy to overcome this difficulty is the use of regression methods based on machine learning, such as that of artificial neural networks (ANN), which are considerably less demanding in terms of computation. Furthermore, once a neural network has learnt the behaviour of a STES reactor, predictions on any additional data sets become almost instantaneous. Afterwards, by using software like TRNSYS, a material can be modelled to study its impact in a building as a STES reactor.

Recently, Scapino et al. [9] modelled a potassium carbonate (K_2CO_3) TES using an ANN. The network was trained using dataset from a simulation using a physics-based model, showing a considerable reduction in computation time whilst maintaining acceptable discrepancies with respect to the physics-based model. The objective of this research work was, therefore, to develop an ANN to assess the performance of a zeolite TES. Real experimental data, instead of simulation data, were used for

the training and validation of the ANN. Such a model could be sued to assess the performance of a given heat storage system from experimental data, as well as to develop a control system for the reactor.

A. Zeolite, the storage material

The focus of this research was a sorption material, zeolite (physical sorption), which has been widely studied for inter-seasonal heat storage.

Analysis of the energy chain of zeolite shows that approximately 70% of absorbed energy is converted into useful heat released upon discharge. However, approximately half of the total heat is also directly lost at the outlet of the adsorbent bed. The overall system efficiency is, therefore, 36% [7].
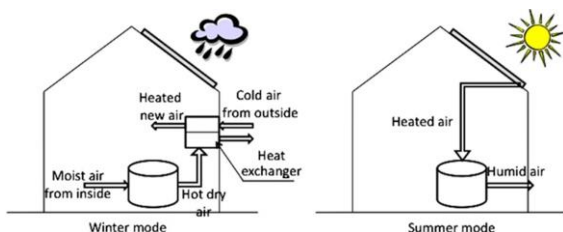
B. The reactor

Figure 1. A possible concept for the charging (left) and discharging (right) modes of solar thermal energy storage by sorption materials for a single-family house [5].

Two cycles can be defined in the figure 1: The charging cycle and the discharging cycle.
• The charging cycle consists of dehydrating the storage material by supplying heat. Hot, dry air could be sourced, for example, from industrial waste heat or the solar panel of an individual home. During this cycle, water would be evacuated from the storage material as a result of the dehydration.
• The discharging cycle consists of introducing water vapour (coming from outside or inside with a relative humidity of above 60%) to hydrate the storage material. The hydration of the zeolite releases hot, dry air which could be used to heat a building. This air could also pass through a heat exchanger to warm up the cold, outside air before being released in a room.
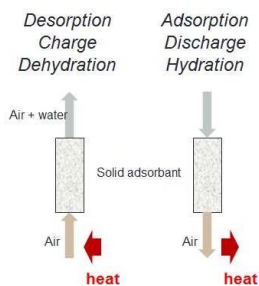

Figure 2. The charging cycle and the discharging cycle

A reactor containing zeolite has been observed to operate under the following range of operating conditions [12]:
• charging temperature from 120 °C to 180 °C,

• inlet humidity during charge of 30% at 20 °C,
• inlet humidity during discharge from 50% to 70% at 20 °C,
• inlet fluid velocity from 0.01 m/s to 0.03 m/s and below.

C. Neural Networks, the model of the reactor

Artificial neural networks (ANN) are a form of machine learning inspired by the way the brain works, learning from experience. An ANN is composed of different layers; an input layer with the training information input into the network, hidden layers showing the inter-influence among different elements, and an output layer. All these layers can contain different numbers of neurons [9].

Neural networks have different architectures which fall under three main categories: multilayer feedforward neural networks, recurrent neural networks (RNN) and multilayer recurrent neural networks. The focus of this study was an RNN which allow the time dependency of a problem to be accounted for by using long short-term memory (LSTM). In an RNN, information can flow both ways, from the inputs to the outputs or vice versa. Whilst traditional neural networks assume that every input and output is independent of one another, RNNs allow the results of previous simulations to be remembered, and this memory is necessary when modelling certain problems. Standard RNNs consist of a chain of repeating modules, with a very simple structure.
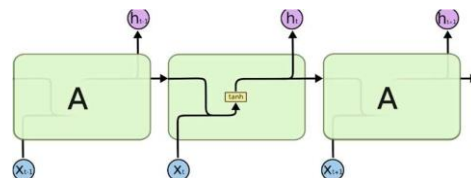

Figure 3.   Standard RNN cell [14]

Within this architecture, cell type can also be varied. The most common variation, LSTM networks, allows certain difficulties such as the exploding gradient and the vanishing gradient that can arise during RNN training to be overcome. The LSTMs also feature a chain structure, but the repeating module is more complicated; instead of having a single neural network layer, there are four, each interacting in differing ways. This construction allows for information to be removed or added to the cell state by regulating it through gates (sigmoid neural network layer and a pointwise multiplication operation). An LSTM has three of these gates, to protect and control the cell state.
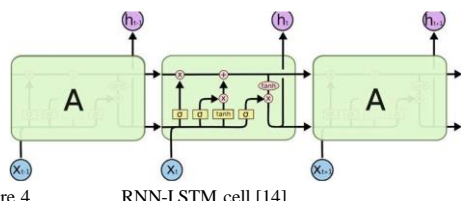

Figure 4.   RNN-LSTM cell [14]

Methods

A. RNN - Learning and validation

Firstly, an RNN was trained and validated using the same experimental data covering both cycles. The data used were taken from a series of experiments on a zeolite heat storage system [11] covering the two cycles of zeolite: dehydration (charging phase) and hydration (discharging phase).

A total of 6 different hydration experiments and 3 dehydration experiments were used for the training. This corresponds to a total of 15700 data entries. For the validation of the model 5500 data entries, corresponding to 3 hydration and 1 dehydration experiment, were used.

The data were separated into training and validation sets and used with a second RNN, providing an accurate measure of the accuracy of the model.

When testing with the validation data set, a verification method to evaluate the accuracy is used. There are different verification methods, such as the performance indicator RMSE (Eq. 1) that was being used for this study:

$$RMSE = \left(\sum_{i=1}^{n} \frac{(\hat{y}_i - y_i)^2}{n} \right)^{\frac{1}{2}} \quad (1)$$

Where $\hat{y}_1, \hat{y}_2 ... \hat{y}_n$ are the predicted values; $y_1, y_2, ... y$ the observed values, and n the number of observations.

The RMSE is the square root of the variance of the residuals. RMSE is an absolute measure of fit and the lower its value is, the more accurate the model. This indicator allows for verification of the work state of the neural network, evaluating the accuracy and comparing with multiple training cycles to arrive at the best values for the parameters' values.

B. Parameters

To find the most accurate model, the different parameters of an RNN (e.g. number of hidden layers, number of epochs and the number of batches) are generally tested to find the best combination to get the most accurate results. The number of epochs corresponds to the number of times that the entire training set will undergo both the forward and backward pass. The batch size corresponds to the number of training data from the experimental data that are used in one forward/backward pass. Therefore, the smaller this number is, the longer the training of the neural network will take as a smaller amount of data will suffice for each forward/backward pass. The number of hidden layers corresponds to the size of the network and the number of neurons that are used for learning. The bigger this number is, the bigger the neural network will be and the longer it will take to train.

C. Data processing

A significant amount of data processing had to be performed before training the neural network. As listed in Tables 1 & 2, the parameters selected from the data as inputs were the humidity measured at the entry of the reactor (r_e), the temperature of airflow at the entry of the reactor (T_{in}), and the rate of airflow inside the reactor. The parameter selected as the output was the variation of the temperature between the entry of the reactor and the output temperature ($\Delta T = T_{out} - T_{in}$). Those parameters were used for both hydration and dehydration in order to construct a neural network capable of predicting both phases.

TABLE I.
HYDRATION DATA [12]

Experiment	Minimum T_{in} (°C)	Maximum T_{in} (°C)	Minimum r_e	Maximum r_e	Minimum airflow (m³/h)	Maximum airflow (m³/h)	Minimum ΔT	Maximum ΔT	Number of data	Training (T) / Validation (V)
1	19.7	20.4	0.0067	0.0073	127.9	189.8	-0.2	38.4	784	T
2	19.4	20.5	0.0074	0.0089	49.09	90.2	-0.4	37.7	2671	V
3	19.5	20.6	0.0074	0.0089	56.2	95.9	-0.5	37.8	2671	T
4	17.5	20.2	0.0046	0.0050	91.5	99.8	-5.8	37.2	2272	V
5	17.3	20.3	0.0046	0.0050	85.3	92.6	-7.6	37.2	2272	T
6	16.9	20.1	0.0038	0.0047	72.5	99.2	-0.5	26.5	2695	T
7	17.1	20.2	0.0038	0.0047	17.2	92.7	-0.5	26.6	2695	T
8	18.8	20.0	0.0025	0.0030	55.1	65.8	-0.1	36.7	2083	T
9	18.9	20.18	0.0025	0.0030	52.5	62.4	-0.5	36.6	2083	V

TABLE II.
DEHYDRATION DATA [12]

Experiment	Minimum T_{in} (°C)	Maximum T_{in} (°C)	Minimum r_e	Maximum r_e	Minimum airflow (m³/h)	Maximum airflow (m³/h)	Minimum ΔT	Maximum ΔT	Number of data	Training (T) / Validation (V)
1	19.3	122.0	0.005	0.010	76.7	99.8	-96.2	-0.2	544	V
2	19.4	124.3	0.005	0.010	69.0	87.7	-103.0	-0.4	544	T
3	18.9	123.1	0.005	0.005	75.7	101.5	-100.0	0.6	980	T
4	189	126.6	0.005	0.005	66.8	86.1	-107.3	-0.8	980	T

D. Cycle modelling:

The data for every experiment used during the training process had to be in the same document, however, the neural network must know that each entry corresponds to different experiments in order to learn properly. Therefore, during the data processing, all experiments were numbered. All the data from the first experiment will be prefixed with the number 1, and so on. Thanks to a data processing code, the neural network can separate each experiment as a cycle. The experiments were organised randomly.

Data Presentation and Discussion

A. Parameters

The parameters have been indicated below in the following manner: (mini-batch size, number of max epochs, number of hidden layers). For each simulation the RMSE of each cycle is given, and the mean of all the cycles in a simulation are compared.
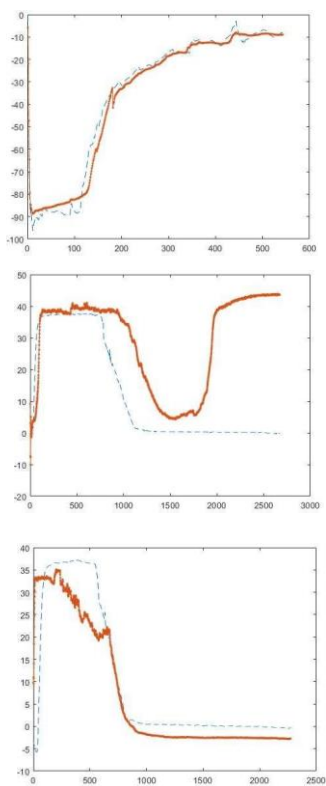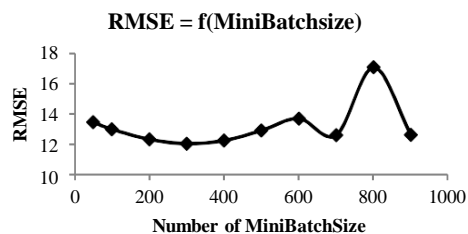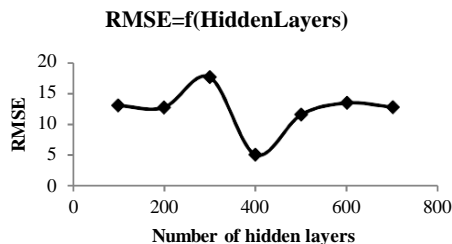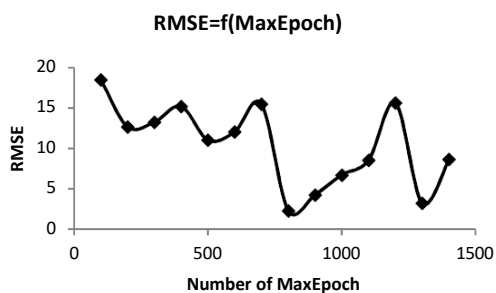
Figure 6. Graphics showing the evolution of the chosen RNN parameter when the other two have a value of 200.

Figure 6 represents the RMSE depending on the variation of the parameters. It indicates that a small mini batch size will give better results than a bigger one. Indeed, a smaller number of data go through one forward/backward pass, therefore the RNN will learn better as it processes fewer data. However, since all the data still passed through the RNN the simulation took longer. The curve representing the number of epochs generated an odd shape. It shows that there is an optimal number of epochs (800 or 1300) that is not necessarily the biggest one. Finally, the number of hidden layers' curve also indicates an optimum number (400) that is not the highest one. It also suggests that an even number of hidden layers works better than an uneven number.

From these curves, it was deduced that for this data set, the minimum batch size to use was between 100 and 300, that the number of hidden layers should be 400, and that the number of epochs should be 800 or 1300. Indeed, the results gave the lowest RMSE for each simulation (Figure 6). Note that the calculation times substantially increase when the number of epochs or the number of hidden layers increases. For our data set that the simulations ran with, the maximum calculation time did not exceed 3 hours.

B. Validation of the model with the same training and verification data set:

With parameters of the RNN being (200, 800, 400), the mean RMSE, when the training and validation tests are the same, is 1.6. This result indicates that the network correctly predicted the outcome of the data set that was used to create the network.

Figure 5 Comparison of predicted values (orange) with experimental values (blue) giving an RMSE of respectively (t to b) 3.88, 24.08 and 8.05– (Time in seconds on the x-axis, temperature delta on the y-axis)

A first simulation (200, 200, 200) was launched and gave an RMSE of approximately 12. The shapes of the predicted results matched the experimental results. It was then decided to model the influence of each parameter whilst the other 2 parameters were fixed at 200 (Figure 5).

TABLE III.
RMSE VALUES OF PREDICTIONS [11]

Experiment	1	2	3	4	5	6	7	8	9	Mean RMSE
RMSE value	1,66	1,32	0,90	2,10	2,02	2,02	1,11	0,99	2,31	**1,60**

above method using RNNs. The model would still be considered accurate when admitting this precision.

C. Complete cycles of dehydration and hydration model:

Many simulations computing different sets of parameters have been run. The (200, 1300, 400) gave the most accurate results for our data set (Figure 7).
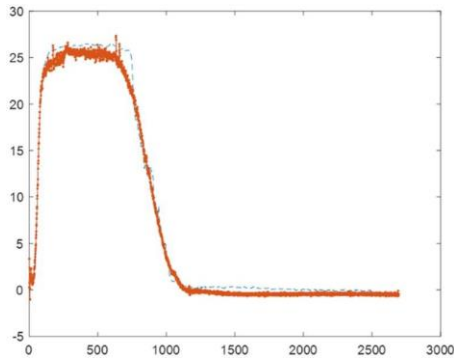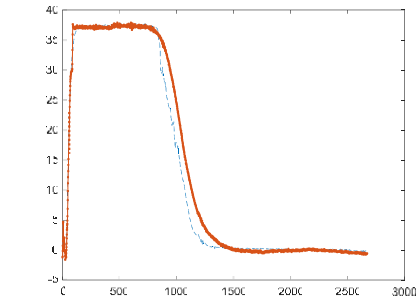

Figure 7. Outcome of the prediction – Best (top) and worst (bottom) predictions for dehydration (Time in seconds on the x-axis, temperature delta on the y-axis)
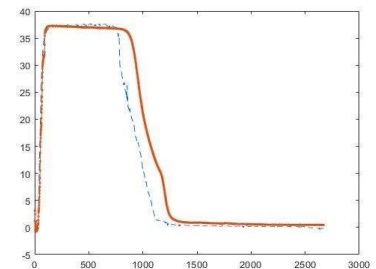
TABLE IV.
RMSE VALUES OF PREDICTIONS [11]

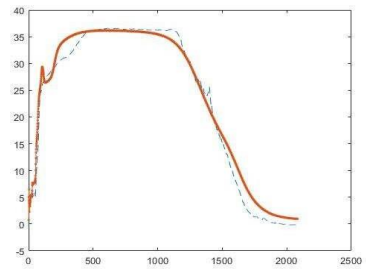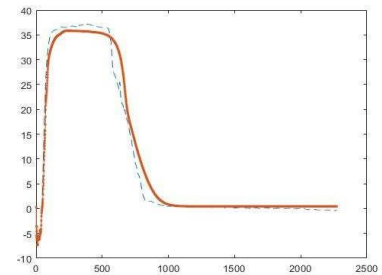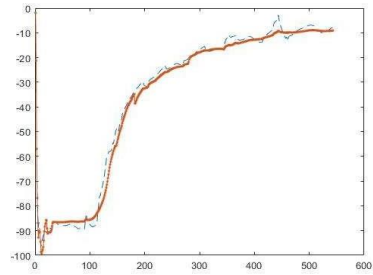| EXPERIMENT	1	2	3	4	MEAN RMSE
RMSE VALUE	2,91	2,11	2,59	1,87	**2,37**

Figure 8. Outcome of the prediction – Best (top) and worst (bottom) predictions for hydration (Time in seconds on the x-axis, temperature delta on the y-axis)

As seen in Figures 7 and 8, the prediction curve closely follows the shape of the experimental curve but is slightly offset. The mean RMSE being around 1.6, it validates the

Figure 9 Outcome of the prediction with the neural network (200, 1300, 400) - (Time in seconds on the x-axis, temperature delta on the y-axis) – top is hydration, the 3 others are dehydration

The mean RMSE of the simulation was 2.35. The predictions generated by the RNN were accurate but not perfect. For example, on the last curve, the prediction curve closely follows the experimental curve but is very offset for the duration of the temperature drop. The other prediction curves, the 3 top ones, are more acceptable. Comparing Figure 9 to Figure 7 and Figure 8, it can be assessed that the prediction is less accurate when the neural network has never been trained on the data. The RMSE is not the same for all the hydration simulations. This result could perhaps be further improved using better-adapted parameters.

Conclusions

An RNN model adapting to zeolite-based thermal energy storage has been constructed. For the quoted experimental data, the RNN model gave accurate results on the prediction of the temperature of the airflow leaving the reactor on complete cycles of both dehydration and hydration of zeolite.

The calculation time for the RNN model is substantially lower than that of a physics-based model (less than 2-3 hours to compute more than 15700 data entries when it would require hours or days for a powerful computer). Moreover, once the RNN model is trained, predictions on any additional data sets is almost instantaneous (less than a minute for more than 7500 data entries).

However, in the predictions given by an RNN there remains a gap between the curves of the experimental results and those of the predicted results. The predictions could still be improved in their accuracy, especially when a sharp change in the curve occurs.

The results from the RNN are promising. It can be noted that the predictions for the dehydration cycles are often more accurate than those for the hydration cycles, which could be due to the fact that the variation of the output parameter is twice as large in the case of dehydration. This being said, there is less experimental data available for the dehydration cycles. Furthermore, the experiments covered only full hydration and dehydration cycles, as it was the only experimental data available. However, this is not the reality of the TCES reactors, which will combine incomplete dehydration and hydration cycles all year round. It would, therefore, be more realistic to model the reactor's behaviour using cycles including both hydration and dehydration in an experiment to see if an RNN accurately models such cases.

REFERENCES

1   Johannes, K., Kuznik, F., Hubert, J.-L., Durier, F., Obrecht, C., 2015. Design and characterisation of a high powered energy dense zeolite thermal energy storage system for buildings. Appl. Energy 159, 80–86. https://doi.org/10.1016/j.apenergy.2015.08.109

2   Kuznik F., Opel O., Osterland T., Ruck W.K.L., 2021. 19 - Thermal energy storage for space heating and domestic hot water in individual residential buildings, Advances in Thermal Energy Storage Systems (Second Edition), Woodhead Publishing, Pages 567-594, ISBN 9780128198858, https://doi.org/10.1016/B978-0-12-819885-8.00019-X.

[3] Cabeza, L. F., Martorell, I., Miró, L., Fernández, A.I., Barreneche, C., 2015. 1 - Introduction to thermal energy storage (TES) systems, in: Cabeza, Luisa F. (Ed.), Advances in Thermal Energy Storage Systems, Woodhead Publishing Series in Energy. Woodhead Publishing, pp. 1–28. https://doi.org/10.1533/9781782420965.1

4   Sunku Prasad, J., Muthukumar, P., Desai, F., Basu, D.N., Rahman, M.M., 2019. A critical review of high-temperature reversible thermochemical energy storage systems. Appl. Energy 254, 113733. https://doi.org/10.1016/j.apenergy.2019.113733

5   Chen, B., Kuznik, F., Horgnies, M., Johannes, K., Morin, V., Gengembre, E., 2019. Physicochemical properties of ettringite/meta-ettringite for thermal energy storage: Review. Sol. Energy Mater. Sol. Cells 193, 320–334. https://doi.org/10.1016/j.solmat.2018.12.013

[6] Li, T.X., Wu, S., Yan, T., Wang, R.Z., Zhu, J., 2017. Experimental investigation on a dual-mode thermochemical sorption energy storage system. Energy 140, 383–394. https://doi.org/10.1016/j.energy.2017.08.073

7   Kuznik, F., Gondre, D., Johannes, K., Obrecht, C., David, D., 2019. Numerical modelling and investigations on a full-scale zeolite 13X open heat storage for buildings. Renew. Energy 132, 761–772. https://doi.org/10.1016/j.renene.2018.07.118

8   Hongois, S., Kuznik, F., Stevens, P., Roux, J.-J., 2011. Development and characterisation of a new MgSO4−zeolite composite for long-term thermal energy storage. Sol. Energy Mater. Sol. Cells 95, 1831–1837. https://doi.org/10.1016/j.solmat.2011.01.050

[9] Scapino, L., Zondag, H.A., Diriken, J., Rindt, C.C.M., Van Bael, J., Sciacovelli, A., 2019. Modeling the performance of a sorption thermal energy storage reactor using artificial neural networks. Appl. Energy 253, 113525. https://doi.org/10.1016/j.apenergy.2019.113525

10   Korhammer, K., Druske, M.-M., Fopah-Lele, A., Rammelberg, H.U., Wegscheider, N., Opel, O., Osterland, T., Ruck, W., 2016. Sorption and thermal characterization of composite materials based on chlorides for thermal energy storage. Appl. Energy 162, 1462–1472. https://doi.org/10.1016/j.apenergy.2015.08.037

11   Kuznik, F., Gondre, D., Johannes, K., Obrecht, C., David, D., 2020. Sensitivity analysis of a zeolite energy storage model: Impact of parameters on heat storage density and discharge power density. Renew. Energy 149, 468–478. https://doi.org/10.1016/j.renene.2019.12.035

[12] Fujii, S., Horie, N., Nakaibayashi, K., Kanematsu, Y., Kikuchi, Y., Nakagaki, T., 2019. Design of zeolite boiler in thermochemical energy storage and transport system utilizing unused heat from sugar mill. Appl. Energy 238, 561–571. https://doi.org/10.1016/j.apenergy.2019.01.104

13   Takasu, H., Hoshino, H., Tamura, Y., Kato, Y., 2019. Performance evaluation of thermochemical energy storage system based on lithium orthosilicate and zeolite. Appl. Energy 240, 1–5. https://doi.org/10.1016/j.apenergy.2019.02.054

14   Olah, C., 2015. Understanding LSTM Networks -- colah's blog [WWW Document]. URL http://colah.github.io/posts/2015-08-Understanding-LSTMs/ (accessed 1.23.20).

Study of the influence of different construction aspects on the thermal performance of the inverted cooling tower.

Pedro Navarro Cobacho, Antonio Sánchez
Kaiser Atecyr's applicant

• *Abstract*— In this work, the influence of different constructive aspects on the thermal performance of a new inverted cooling tower prototype was studied, without this affecting its drift. For the characterization of the thermal performance, the Merkel number was used. While for the measurements of drift, the method of hydrosensitive paper. Thanks to the results of this work, it has been concluded that the spray characteristics and the manifold position has been found to be the most important parameters affecting the tower performance. Therefore, in view of the results, the combination of a higher pressure level in the spray and a larger exchange surface (lower manifold) will result in the best configuration. The fill has influence on all manifolds operation, since all the cooling takes place in the parallel flow arrangement for almost all of them (similar for 0.8 meters and none fill, and 26% better for 1.6 meters of fill). Finally,

the drift results are practically zero and are well below the limits imposed by several international standards (up to 300 times lower). Which allows us to conclude that the inverted tower fulfills the main objective with which it was conceived.

Index Terms—Cooling tower, Evaporative cooling, Thermal performance, Poppe, Drift.

I. INTRODUCTION

Evaporative heat rejection systems, such as cooling towers, are widely used in power generation, cooling cycles or industrial processes. The main problem with the use of this equipment is related to drift (emission of droplets into the atmosphere). This is undesirable for several reasons, but mainly because it can cause the emission of chemical products and microorganisms into the atmosphere, among which the Legionella bacterium stands out, due to the operating conditions of the cooling towers.

In this work, the influence of the fill length and the nozzles arrangement (position and hydraulic characteristics) on the thermodynamic characteristics of a new inverted cooling tower prototype was studied, without this affecting the promising drift results reported in previous works [1]. This would be the main novelty of the work, since the cooling tower studied reported practically zero levels of emission of particles into the atmosphere (0.00015% of circulating water).

The main difference with a conventional mechanical-draft, wet cooling tower relies on the arrangement of the water and air flows. In this novel device (201730077, ttps://patentimages.storage.googleapis.com/e5/e5/cc/ed73 725 8f5703c/ES2608912B2.pdf), water flows upwards from the nozzles to the fan until the inertia and drag forces balance and then downwards to and through the fill, to finally be collected in the tower basin (Fig. 1). The air intake takes place at the top of the tower (inlet section, where the axial fan is placed forcing the air in) and is driven

Figure 1. Experimental facility located in ELDI building, Technical University of Cartagena (Spain).

downwards to the exit area which is located at the bottom.

As the outlet area of the cooling tower is several times higher than the inlet area, the air velocity is significantly reduced compared to commercial cooling towers. As a consequence, the water droplets carried out by the air stream that have not evaporated are easy to collect, limiting the system's environmental impact (drift emissions). Besides, the low inertia and the position of the exit area also contribute to lower the environmental impact since the few escaping water droplets will probably be evaporated or deposited on the ground nearby the tower.

II. METHODOLOGY

A. Test facility

The experimental tests were performed in the novel forced, mechanical-draft wet cooling tower previously described, Fig. 1. This facility is located on the roof of the ELDI building, at the Technical University of Cartagena (Cartagena, Spain). It was designed to reject a heat rate of 20 kW in nominal conditions.

The total height of the tower is 3.5 m. The upper inlet area is square-shaped (0,64x0,64 m^2). An axial fan (Sodeca HPX-63-4T-2) is placed at the upper section of the tower, driving the air downwards. The outlet section is rectangular-shaped, 3,5 x 0,7 m^2 erected at ground level.

The hydraulic circuit is composed of a network of polypropylene pipes. The flow circulates through a centrifugal pump (Pentax CBT400) from the basin to the level of spraying nozzles. The distribution system consists of three spray nozzle manifolds consisting of nine hollow cones, horizontally arranged. The nozzle manifolds are placed at 0.7 m, 1.2 m and 1.7 m down from the fan. The hydraulic characteristics of the spray nozzle manifolds are different. In the lower manifolds, Spraying Systems model LAP-PP40 nozzles (18 units) spraying upwards are used. In

the upper manifold, Spraying Systems AX model nozzles (9 units) are used spraying downwards, due to their proximity to the fan (Fig. 2). In this way, the influence of the flow arrangement and the hydraulic characteristics can be investigated.

The trickle type fill is set between the water nozzles and the tower basin, and the thermal load consists of a conventional boiler of 45 kW nominal power (Gabarrón CPE45). The flow rates of water and air can be changed by two variable frequency drives connected to the pump and the fan, respectively. Besides, the water mass flow rate can be manually changed by a balancing valve. Drift eliminators (Munters CelDek 7090) are located in the tower outlet section.

The variables required to experimentally characterize the thermal performance were monitored by the sensors shown in Fig.3. Air velocity, temperature and relative humidity were measured in the inlet and outlet sections of the cooling tower, as well as, water flow, and inlet and outlet water temperatures.

Also, the results of the thermal performance assessed in [2] showed that it was necessary to know if heat and mass transfer occur both in the counterflow and parallel arrangements in the inverted cooling tower. Hence, to measure the temperature in the highest height reached by the water (where the arrangement of the flows changes) two water collection channels were installed in the tower. These are located at different heights to ensure that the measurement obtained corresponds to the abovementioned temperature.

The tower data was recorded by a Distech Eclypse model acquisition unit, while the environmental conditions (ambient air temperature, air relative humidity, wind speed and wind direction) were measured with a meteorological station placed just beside the experimental facility (Davis Vantage Pro2).

B. Thermal performance tests

The well-known Merkel number is accepted in the literature to measure the performance of a wet cooling tower. This dimensionless number measures the degree of difficulty of the mass transfer processes taken place in the cooling tower exchange area. In [2] the combination of the Merkel [3] and Poppe [4,5] methods of analysis and the counterflow, parallel and counterflow/parallel flow arrangements were discussed, for a total of 5 different approaches.

According to the results obtained, in this work the method that uses the Poppe theory and combines counterflow and parallel flow arrangements will be used to evaluate the thermal performance. The major equations for the heat and mass transfer in an evaporative device have been adapted from Poppe and Rögener [4], and Kloppers and Kröger [5] and they are derived from the mass balance for the control volume shown in Fig.4, which considers the flow as a one dimensional problem ((1), (2), (3)).

$$\frac{d\omega}{dT_w} = \frac{c_{p_w}\frac{\dot{m}_w}{\dot{m}_a}(\omega_{sw}-\omega)}{h_{sw}-h+(Le-1)[h_{sw}-h-(\omega_{sw}-\omega)h_v]-(\omega_{sw}-\omega)c_{pw}\cdot T_w} \quad (1)$$

$$\frac{dh}{dT_w} = c_{p_w}\frac{\dot{m}_w}{\dot{m}_a}\left(1+\frac{c_{pw}\cdot T_w(\omega_{sw}-\omega)}{h_{sw}-h+(Le-1)[h_{sw}-h-(\omega_{sw}-\omega)h_v]-(\omega_{sw}-\omega)c_{pw}\cdot T_w}\right) \quad (2)$$

$$\frac{dMe_p}{dT_w} = \frac{c_{pw}}{h_{sw}-h+(Le-1)[h_{sw}-h-(\omega_{sw}-\omega)h_v]-(\omega_{sw}-\omega)c_{pw}\cdot T_w} \quad (3)$$
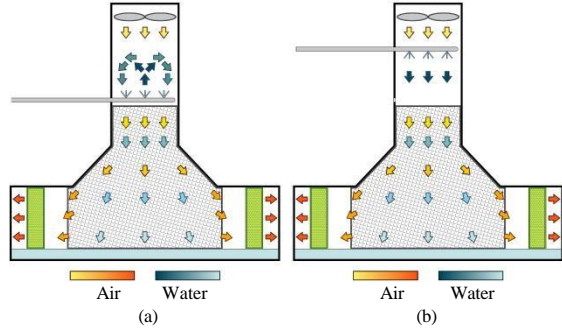

Figure 2. Schematic of the new prototype of wet cooling tower highlighting the counterflow-parallel flow arrangements and the main parts of the tower. (a) Counterflow-parallel. (b) Parallel.
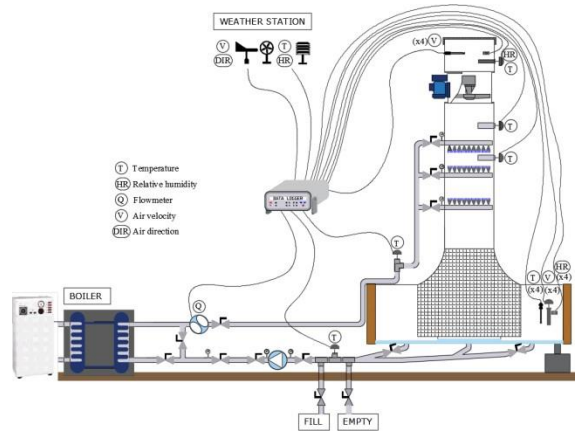

Figure 3. Schematic of the novel mechanical forced draft wet cooling tower.
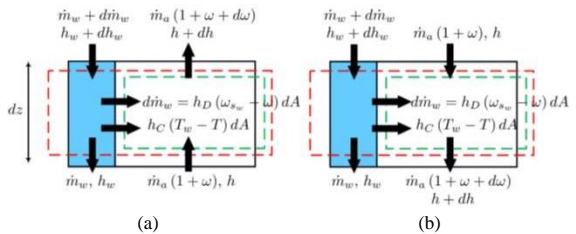

Figure 4. Control volume in the exchange area of a wet cooling tower. (a) Counterflow and (b) parallel flow arrangements.

The above set of coupled ordinary differential equations is usually regarded as the Poppe model. They can be solved simultaneously to provide the air humidity, the air enthalpy, the water temperature, the water mass flow rate and the Me profiles in the cooling tower.

The main advantage is that no simplification is made in the process, and it allows the air outlet conditions to be predicted. The above described governing equations can be solved by the fourth-order Runge-Kutta method. Refer to Ref. [5,6] for additional information concerning the calculation procedure.

The two elements with the greatest influence on the thermal efficiency of the tower are the fill and the distribution system (nozzles). The design of the improved inverted tower has 3 levels of spray nozzle manifolds, so the influence of the relative position of the injection, the

water-air flow arrangement and the hydraulic characteristics of the nozzle on the thermal performance can be studied.

The thermal performance of the cooling tower was experimentally investigated for three fill lengths (1.6 m, 0.8 m, and None trickle fill, Fig.5) and all the available nozzle manifolds (lower, intermediate and upper manifolds). Concerning the experimental procedure, five sets of experiments for each nozzle manifold and fill length, for a total of 45 tests. Five different airflow rates were obtained by modifying the value of the variable frequency drive into five levels (ranging from 10-50 Hz in 10 Hz intervals). The lowest frequency level of the fan is selected by ensuring that water droplets are not carried out by the air stream to the inlet section of the cooling tower. Accordingly, if the 10 Hz value is not enough, it is increased until there is no drift in the upper part of the tower.

The water flow rate was fixed at around 1.3 kg/s (nominal conditions, 50 Hz in the variable frequency drive) with the aim to obtain different water-to-air mass flow ratios. The operational range of water-to-air mass flow ratios for this work is about 0.2–1. The thermal load used was 30kW for all tests.

The standards UNE 13741 [7] and CTI [8] were taken as a reference to evaluate the stationary conditions of the tests.

C. Drift tests

To experimentally measure the emissions from the tower, the Sensitive Paper (SP) method was used, because it is capable of providing the drop size distribution data, and it is economical and easy to apply. Its principle of operation relies on the detection of the droplets by inertial impact onto a chemically treated surface. Impacting drops leave a blue clear stain on the yellow paper background, which is proportional to the droplet´s original speed, diameter, and angle of attack. As described in [1], the stages to calculate the drift emissions using the SP method are:

At stage 1, by means of papers carrier (five PVC plates with four papers on each plate), twenty sensitive papers were exposed to the air stream in each of the tower outlet surfaces, Fig.6. Each outlet area was divided into twenty equal quadrants covering the same portion of the surface and the papers were placed at the center of each quadrant. The papers used in the experiments were sized 76 × 52 mm.

The coated side of the papers was exposed to the air stream against the flow direction during an exposure time of 4 min (240 s). Normally, this time is set as a trade-off between over-occupancy of drops and paper edges becoming green due to the moist airflow. In the case of the inverted cooling tower, and due to the low level of drift emissions, the over-occupancy of droplets was not a problem, and the exposure time was set according to the second criterion. After the expiry of the exposure time, the PVC plates were withdrawn back.

At stage 2, a high-resolution scanner was used to digitize the sensitive papers. The software DRIFT© was used to extract the recorded information from the scanned papers. This software was developed by the group of scientists who conducted this research and it is based on the digital software platform described in [9].

The software operates as follows. First, all the stains present in the paper are detected by using the well-known Canny edge detector. Next, the stains are filtered and classified. The idea behind this procedure is to consider
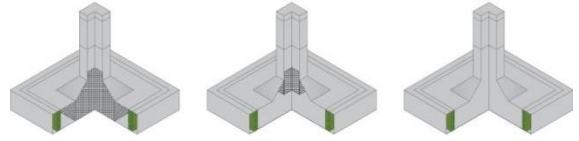

Figure 5. Arrangement of the fill for the different lengths tested: (a) Length of 1.6 metres, (b) Length of 0.8 metres, (c) None fill
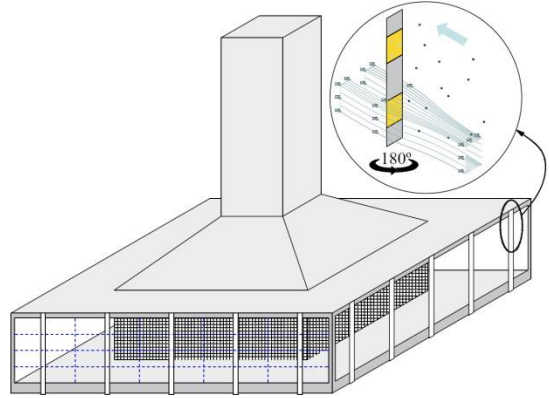

Figure 6. Positions of measurement in the cooling tower exit area.

only the stains coming from real drops and discard those otherwise (i.e. paper background stains, fibres, etc.). Performing the filtering and the classification involve gathering information concerning physical features of the stains, such as the roundness or the Hu moments, and using it to describe them. To design the classification algorithm, a training data set of 3000 samples (stains) was extracted from the papers and was classified manually. The resulting classifier (decision tree) was able to filter and classify the stains that have their origin in real drops with a success rate of 95%. As a result, the software provides the number of real drops count per diameter size. A correction factor accounting for the drop-stain relationship is applied during this stage.

At stage 3, the drop size distribution data and the amount of drift are calculated. Drift emissions are obtained by using the set of (4), (5), (6). The drifted mass flow by unit of surface, $\dot{m}_d$, refers to the mass flow exiting the tower at the portion of the surface covered by each one of the exposed papers. It is calculated according to (4) and, at this step, water droplets are considered to be perfect spheres of diameter d_d. These results include the efficiency correction factor (ε) to account for the drops originally present in the air stream which have not ended up impacting on the paper due to their inertia. The total drifted mass flow, $\dot{m}_s$, is the total mass flow of water droplets exiting the tower. It is calculated by multiplying the mass flow by unit of surface to the area covered by the paper. In the case that the papers are equally distributed at the exit section of the cooling tower (each paper covering the same area), $\dot{m}_s$ can be calculated as in (5). Finally, the drift emissions, D, are computed as a fraction of the circulated water flow $\dot{m}_w$, (6).

$$\dot{m}_{d,j} = \frac{\rho_w\,\pi}{6\,A_P t_{exp}} \sum_{i=1}^{N} d^3_{,id}\varepsilon_i^{-1} \qquad (4)$$

$$\dot{m}_s = \frac{A_T}{n_p} \sum_{j=1}^{n_p} \dot{m}_{d,j} \qquad (5)$$

$$D = \frac{\dot{m}_S}{\dot{m}_w} \qquad (6)$$

A drift test was performed for each of the available combinations (different fill lengths and different nozzles positions). Therefore, 6 tests (2 fill lengths and 3 nozzles positions) were carried out under nominal pump and fan conditions (50 Hz).

III. RESULTS AND DISCUSSION

A. Thermal performance

The experimental results obtained for the variation of the Merkel number with the water-to-air mass flow ratio, for the novel design of cooling tower, are presented in Fig.7. The results have been calculated using the Poppe method for the calculation of the Merkel number. It should be noted that for the intermediate and lower manifolds, the Merkel number has been calculated taking into account the contribution in each of the cooling areas (counterflow and parallel). While in the case of spraying from the upper manifold, all the cooling takes place in parallel arrangement.

As an example, Table I shows the average values of the most relevant ambient and operating conditions during the 5 tests carried out for the intermediate manifold and 1.6m fill length. In [12] the results of the 45 tests described in Section II.C are shown. The water temperature at the different locations (inlet, intermediate and outlet) is also included in Table I. It is important to mention that there were not always measurements for the intermediate temperature, T_{wi}, which is measured in the water channels described in the Section II.A (top right area of the tower depicted in Fig.3). A visual inspection of the water collection channels was carried out during the tests, showing no water being collected in cases where the fan frequency was very high.

Table I also shows the predicted results for the calculated Merkel number for each flow arrangement, the total Merkel number ($Me_{CF+PF} = Me_{CF} + Me_{PF}$). The experimental uncertainty has been calculated according to [10], with the type B evaluation for standard uncertainty and a coverage factor of k = 2 (level of confidence of 95%) for the expanded uncertainty. Averaged values of 3.53%, and 11.73% were obtained for $\dot{m}_w/\dot{m}_a$ and Me, respectively.

As can be seen, Me decreases while the water-to-air mass flow ratio increases for all fill length and nozzle arrangement investigated. It can also be observed that for the same value of water-to-air mass flow ratio, the Merkel number is different for the different cases analyzed. As it can be seen, the sequence of manifold positions in terms of better thermal efficiency is upper, intermediate and lower.

The cooling occurs mostly in parallel arrangement for high fan frequencies, as well as for low frequencies. The cooling is mixed (counterflow and parallel) for intermediate frequency levels. For those cases where the fan frequency is very high, the highest height reached by the water (where the arrangement of the flows changes) is very close to the location where the nozzles are placed. Therefore, it can be said that the counterflow cooling in this case is practically zero and therefore, all the cooling occurs in parallel. As the frequency of the fan decreases, water is collected in the channels, and it is possible to identify the amount of counterflow and parallel cooling. Finally, for the lowest fan frequency level tested, the water reaches the
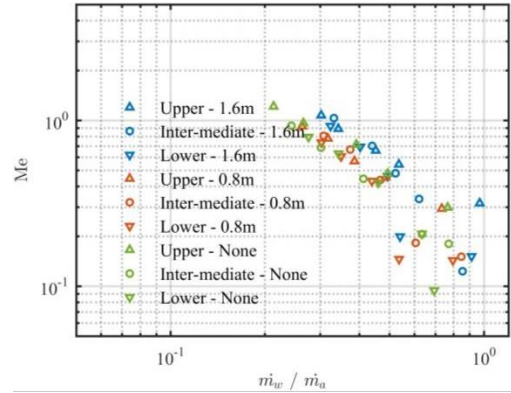

Figure 7. Experimental results for the Me number as a function $\dot{m}_w/\dot{m}_a$.

channels without modifying its temperature, probably because the short time required to reach the top height. This is justified because for low air flow, the cooling capacity decreases (term h_D). Therefore, for these cases the counterflow cooling is zero and all cooling occurs in parallel. Fig. 9 graphically attempts to explain this behavior.

In the case of the lower manifold, the change of trend (mixed flow to parallel) takes place for the highest tested $\dot{m}_w/\dot{m}_a (\approx 0.62)$ while in the intermediate manifold the shift occurs for ≈ 0.83. This fact is justified due to the greater distance available for heat and mass exchange between both spray positions and the fan (Fig. 8).

Fig.8 shows the comparison between the three fill lengths and three the available manifolds. If it is studied which manifold of nozzles is more optimal, for the lower ratios, the trend is that the manifolds that spray upwards (intermediate and lower) have a better thermal performance. In addition, between both manifolds, the intermediate manifold is always above the lower manifold for the three fill lengths. However, another factor that most influences is the type of nozzles. In this sense, for high ratios, the best performance is presented by the upper manifold. This is justified by the uniformity of the flows and the type of nozzles used, which emits a greater number of smaller droplets, which increases the a_V term. If the results are studied globally, the sequence would be upper, intermediate and lower. Results show an average difference between Lower and Upper manifolds of around of 37% and around of 26% for Inter-mediate and Upper manifolds. While, in the case of Lower and Inter-mediate manifolds are around of 15%.

However, if the difference between the cases is studied as a function of the $\dot{m}_w/\dot{m}_a$, It is observed that the differences are not always the same, unlike what happened with the fill length. For low ratios, it is observed that the performance tends to converge at the same point for the three manifolds, the sequence being seen as Inter-mediate $\approx$ Lower > Upper. While for high ratios, it is clearly observed that the sequence is Upper > Inter-mediate > Lower (although for the case of 1.6 m of fill the point tends to be the same).

Results show an average difference between 1.6 and 0.8 m of fill length of around of 26%. This is due to the little difference between the two amounts of fill (a volume of 32.58 dm³ for 1.6 meters and 3.70 dm³ for 0.8 meters). For this reason, in the case of 0.8 m and without fill, the results

TABLE I.

AVERAGED VALUES IN THE THERMAL EXPERIMENTAL TEST RUNS CONDUCTED

Manifolds	Fill	$T\infty$ (ºC)	$\phi\infty$ (%)	$\dot{m}_a$ (kg s⁻¹)	$\dot{m}_w$ (kg s⁻¹)	$\dot{m}_w/\dot{m}_a$	T_{w1} (ºC)	T_{wi} (ºC)	T_{w3} (ºC)	Me_{CF}	Me_{PF}	Me_{CF+PF}	$\dfrac{Me_{CF}}{Me_{CF+PF}}$
Inter-mediate	1.6 m	28.47	71.78	3.9575	1.3151	0.3323	33.39	-	28.13	1.0320	0.0000	1.0320	0.00
Inter-mediate	1.6 m	26.39	76.40	2.9776	1.3109	0.4403	34.40	-	29.22	0.7017	0.0000	0.7017	0.00
Inter-mediate	1.6 m	27.36	62.97	2.5029	1.3088	0.5229	36.02	31.33	30.67	0.0726	0.4070	0.4796	0.85
Inter-mediate	1.6 m	27.23	75.30	2.1145	1.3145	0.6217	40.34	36.74	34.94	0.1309	0.2048	0.3357	0.61
Inter-mediate	1.6 m	30.24	62.23	1.5501	1.3260	0.8555	49.85	49.85	45.47	0.1230	0.0000	0.1230	0.00

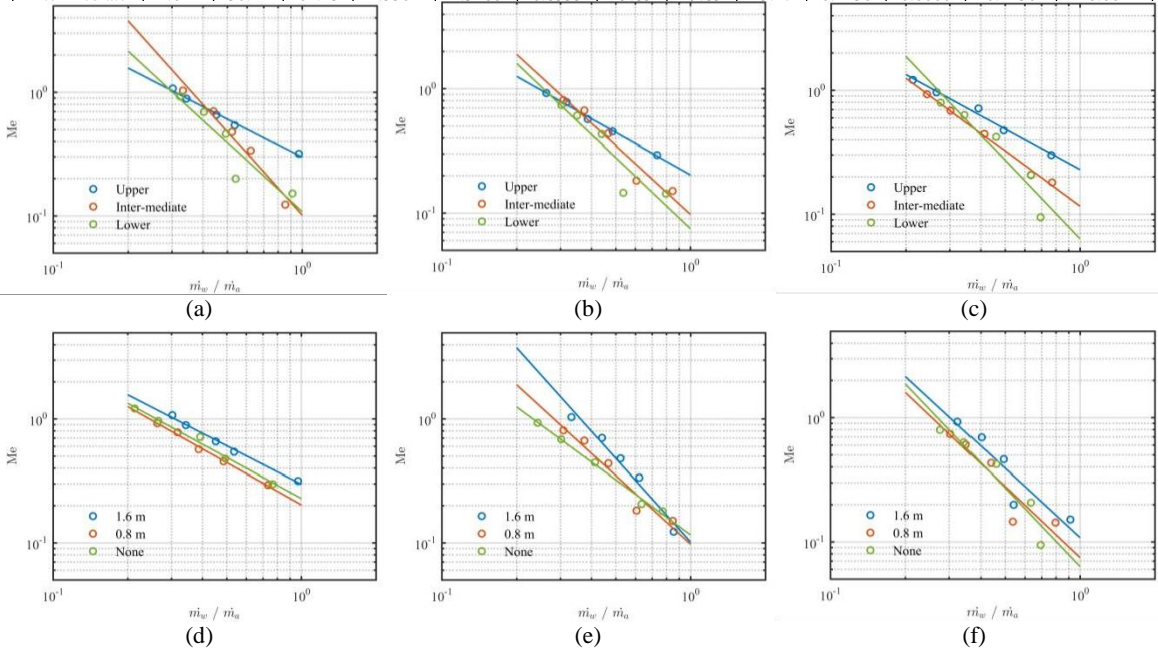(a) (b) (c)

(d) (e) (f)

Figure 8. Cooling tower characteristic versus water-to-air mass flow ratio for the correlations of the three fill lengths and three the available nozzle manifolds. Comparison between different fill length: (a) 1.6 m, (b) 0.8 m, (c) None; and different nozzle manifolds: (d) Upper, (e) Inter-mediate, (f) Lower.

1.48 $\dot{m}_a$ (kg/s) 4.21   1.69 $\dot{m}_a$ (kg/s) 4.55   1.77 $\dot{m}_a$ (kg/s) 5.38
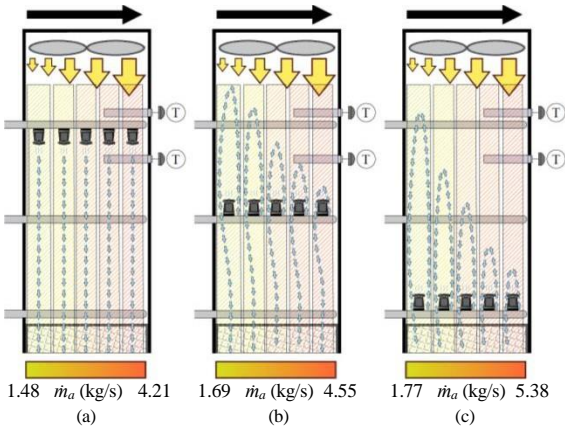
(a) (b) (c)

Figure 9. Channel location and flow arrangement.

are very similar. In the upper manifold it is above even. This is justified by two reasons, the experimental uncertainty (since the differences between the Merkel numbers for these cases are very small) and by a compromise between the two factors that are modified by varying the fill. On the one hand, the exchange surface (increasing the fill increases the contact surface between the two fluids, which improves performance) and other hand, the loss of load (if we add fill to the tower, the air consumption drops around 10% compared to the case without fill, what makes the thermal performance worse).

Finally, to correlate the values of the Merkel number of a tower, it is common to use the ratio of water-to-air mass flow ratio as an independent variable, described by an equation of the form $Me = c(\dot{m}_w/\dot{m}_a)^{-n}$, as described in [1,5,11]. These are represented by a solid line in the Fig.9.

To evaluate the goodness of the correlation, the values of the experimental water outlet temperature and the calculated one can be compared with the correlations. The maximum mean deviation obtained is 2.34% (lower manifold and 0.8 m fill). This indicates that the correlation proposed by [11] together with the Poppe model is sufficiently approximate for the prediction of the outlet water temperature with the model. As for the air outlet temperature, Poppe model is also quite reliable for its calculation. The average maximum difference is 8.36% (lower manifold and none fill). Which is an absolute difference of 2.64ºC.

B. Drift

The main conclusion deduced from the drift results obtained is related to the characteristic diameter, since this

is close to the experimental uncertainty (25μm), as described in [1,9,12]. Therefore, after analyzing the data as described in [1,12], the results obtained are shown in Fig.10. It is important to mention that the results of the upper manifold with a length of 0.8 m were affected and therefore their values are distorted with respect to the others.

As can be seen, drift emissions were found to be up to 300 times lower than the limits imposed by several international standards: 0.00015-0.00022% of the circulating water compared to 0.05% (Royal Decree RD 865/2003 [13] in Spain) and 0.02% (Australian Standard AS/NZS 3666 [14] in Australia), respectively.

If the influence of the fill length is analyzed, it is observed that the drift decreases as the filling length increases. This seems evident, since, if the fill increases, the number of obstacles that the drops have to be dragged by the air current increases.

For the different levels of nozzles, a linearity between the drift results is also observed. The drift level increases in the following order: upper manifold, inter-mediate manifold, and lower manifold. This is logically justified by the proximity of the nozzles manifold level to the outlet section. The drops are sprayed closer to the air outlet section and have a shorter path inside the tower.

Finally, no significant differences were observed in the characteristic diameter of the drops. This is 21 μm. Which is below the uncertainty of the method that is 25 μm [1,12]. What justifies even more the affirmation that the inverted tower presents practically zero drift and what has been measured in the tests is due to the background error of the papers.

IV. Conclusions

This study has enabled investigating the effect of the spray configuration and length fill on the thermal performance and drift of a novel inverted cooling tower. The main conclusions are summarized below:

The spray characteristics and the manifold position has been found to be the most important parameters affecting the tower performance. The upper manifold is, in the light of the obtained results, the best configuration for all mass flow ratios in which the tower works. However, the combination of a higher pressure level in the spray and a larger exchange surface (lower manifold) will result in the best configuration.

The fill has influence on all manifolds operation, since all the cooling takes place in the parallel flow arrangement for almost all of them. The performance for the 1.6 m length of fill is 26% better than for the other two lengths tested. However, in the case of 0.8 m, the amount of fill introduced is so small compared to 1.6 m (approximately 9 times less), that the pressure drop becomes important. And that's why the results are similar or better when we remove it.

The drift results are practically zero and are well below the limits imposed by several international standards. Which allows us to conclude that the inverted tower fulfills the main objective with which it was conceived.

Finally, as future lines of work, the nozzles could be optimized in terms of required pump power consumption and spray characteristics to cover a larger exchange area.
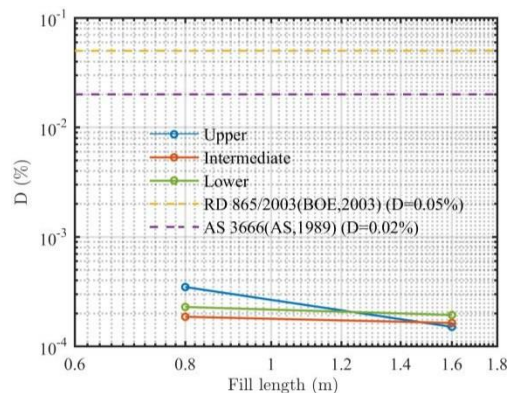

Figure 10. Drift levels as a function of nozzles manifold and fill length

Which would increase the a_v term and, consequently, the Merkel number.

References

1 Ruiz, J., Navarro, P., Hernández, M., Lucas, M., & Kaiser, A. S. Thermal performance and emissions analysis of a new cooling tower prototype. Applied Thermal Engineering, 2022, pp 118065.

2 Ruiz, J., Hernández, M., Navarro, P., Lucas, M., & Kaiser, A. S. Experimental study on the thermal performance of a new prototype of cooling tower. 15th International Conference on Heat Transfer, Fluid Mechanics and Thermodynamics (HEFAT 2021). Virtual Conference, 2021.

3 Merkel F., Verdunstungskühlung, VDI Zeitschriff Deutscher Ingenieure, Berlin, Alemania, 1925, pp 123–128.

4 Poppe M., and Rögener H., Berechnung von Rückkühlwerken, VDI wärmeatlas, 1991, pp. Mi 1.

5 Kloppers, J.C., and Kröger D.G., A critical investigation into the heat and mass transfer analysis of counterflow wet-cooling towers, International Journal of Heat and Mass Transfer, Vol. 48 (3), 2005, pp. 765-777.

6 Rubio-Castro, E., Serna-González, M., J. M. Ponce-Ortega, M., Morales-Cabrera, M. A., Optimization of mechanical draft counter flow wet-cooling towers using a rigorous model, Applied Thermal Engineering, Vol. 31, 2011, pp. 3615 –3628.

7 UNE, Thermal performance acceptance testing of mechanical draught series wet cooling towers, UNE, 2004.

8 CTI, Code Tower, Standard Specifications. Acceptance Test Code for Water Cooling Towers, Cooling Technology Institute, 2000.

9 Ruiz J., Kaiser A., Ballesta M., Gil A., Lucas M. Experimental measurement of cooling tower emissions using image processing of sensitive papers, Atmos. Environ, Vol. 69, 2013, pp. 170-181.

10 J. C. for Guides in Metrology (JCGM), Evaluation of measurement data. Guide to the expression of uncertainty in measurement, 2008.

11 Ashrae, HVAC systems and equipment. Chapter 36: Cooling towers, 2004.

12 Navarro, P. Experimental characterization of droplet emission from an improved inverted cooling tower (in Spanish). Final Project, Polytechnic University of Cartagena

13 BOE, RD 865/2003. Hygienic-sanitary criteria for the prevention and control of legionellosis., Spanish Ministry of Health and Consume, 2003.

14 AS, AS-4180.1. Drift loss from cooling towers; Laboratory measurement. Part 1: Chloride balance method., Standards Australia., 1994.

Testing of the climate-friendly tracer gas HFO-1234yf to determine air exchange rate and ventilation effectiveness in occupied spaces with Covid-19 boundary conditions (2021)

First authors: Bienz Moritz, Bucheli Kevin
Second authors: Huber Heinrich, Walser Stefan

Abstract— **The usage of tracer gas methods under realistic environmental conditions to draw conclusions regarding the ventilation effectiveness under Covid-19 conditions were examined. Two differently ventilated classrooms were subject to the study. In addition to the well-established sulphur hexafluoride (SF6), 2,3,3,3-tetrafluoropropene (HFO-1234yf) was used as a tracer gas, and its possible range of applications was examined. Both constant dosing methods and the pulse dosing method were used. The latter, in addition to determining the air exchange rate, also proved to be very suitable for investigating all kinds of air flow phenomena. The investigations further show that HFO-1234yf, with its low environmental impact, is a suitable tracer gas. And finally, the inevitable advantages of displacement ventilation for pollutant removal compared to mixing ventilation become apparent.**

Index Terms—**Covid-19, HFO-1234yf, Tracer gas, Ventilation effectiveness.**

I. INTRODUCTION

Tracer gases are already used for a variety of applications, one of which being air flow determination in closed environments. In the current situation surrounding the coronavirus pandemic, possibilities for determining flow patterns in rooms and the associated determination of ventilation effectiveness are especially significant. Since the widely used tracer gas sulphur hexafluoride (SF6) has a high global warming potential (GWP), alternatives are sought after. The gas 2,3,3,3-tetrafluoropropene (HFO-1234yf) with a GWP of <1 represents one of these possible alternatives, which comes close to the requirements for the ideal tracer gas as stated in Figure 1. Therefore, the possibilities of using this new tracer gas were investigated in our bachelor thesis. [1]
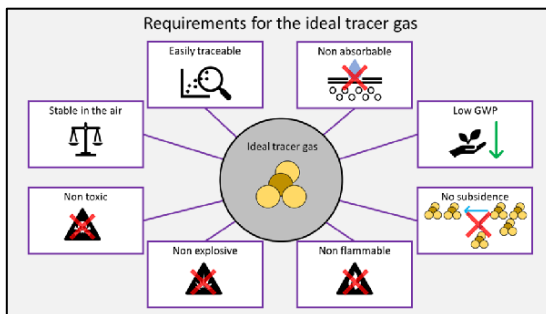

Figure 1.   Requirements for the perfect tracer gas

The aims of these studies were to compare the still unproven tracer gas HFO-1234yf with the well-established SF6. For this purpose, the known measurement methods of constant and pulse dosing were used and their significance regarding the spread of pollutants in the air and the currently ever-present coronavirus was investigated. Statements are also made on the ventilation effectiveness as defined in [2] of various ventilation systems and how they could be improved.

II. METHODS

A. Approach

Measuring was done with three different test objects and under different general conditions. The first experiment was carried out under laboratory conditions without a mechanical ventilation system. This was primarily intended to verify the identical behaviour of the two tracer gases used, SF6 and HFO-1234yf.

The next two tests were carried out in different classrooms equipped with different ventilation systems. One being a concept with displacement ventilation, the other using a mixing ventilation. Both tracer gases were also used in these tests to investigate their comparability under realistic conditions. All tracer gas measurements were visually verified by fog tests.

To prevent measurement errors and inaccuracies as well as to find the most suitable analytical methods, three different measuring instruments with three types of analytical methods were used:

- Fourier-transform infrared spectroscopy – FTIR (single-point)
- Nondispersive infrared spectroscopy – NDIR (single-point)
- Photoacoustic spectroscopy (multi-point)

The advantages of multipoint sampling are the simultaneous analysis of several measuring points of a room as well as the time saving since the measurement setup for several measuring points is only necessary once. However, the measurement intervals, with a minimum of one minute, take longer than those of the other two analysis methods used, which allow for measurement intervals of a few seconds.

The dosing methods used are described in detail further below.

B. Comparison of HFO-1234yf with SF6

The theoretical comparison of the two gases HFO-1234yf and SF6 reveals no fundamental hindrances to the use of HFO-1234yf as a tracer gas. The behaviour in the air is stable and the gas is virtually harmless. Only the risk of flammability needs to be considered.

TABLE I.
COMPARISON OF HFO-1234YF WITH SF6

Description	HFO-1234yf	Sulfur Hexafluoride
Chemical Name	2,3,3,3-Tetrafluorpropen	Sulfur Hexafluoride
Chemical Formula	$C_3H_2F_4$	SF_6
Molecule Structure		
Global warming potential (over a period of 100 years)	<1	26087
Hazard Pictograms	GHS02; GHS04	GHS04
Hazard Warnings	H220; H280	H280
MAK- Value	200 ppm; 950 mg/m³	1000 ppm; 6000 mg/m³
Molar Mass	114.04g/mol	146g/mol
Explosion limit	6.2-12.3%	-
Specific conditions 20°C and 101.3 kPa		
Relative density to air	3.9	5.3
Water solubility	0.2 g/l	0.041 g/l
Autoignition temperature	405 °C	-
Specific conditions 25°C and 100 kPa		
Specific heat capacity c_p	0.9050 kJ/(kg*K)	0.6580 kJ/(kg*K)
Thermal conductivity eg. air 26.2 mW/(m*K)	13.5 mW/(m*K)	13.65 mW/(m*K)

C. Constant dosing methods (Step-up and Decay)

In the following tests, two different constant dosing methods were used which, due to their measurement procedure, can be used in a complementary manner and can mutually verify and supplement the measurement results. The basic framework conditions for the implementation of the two methods are taken from the standard SN EN ISO 12469:2017.

Decay

During decay measurement, the tracer gas is constantly dosed into the room being tested. The concentration in the room increases until a state of equilibrium is reached between the tracer gas flowing in and the tracer gas being extracted. In rooms with higher ventilation efficiency, the equilibrium state is at a lower concentration than in rooms with low ventilation efficiency. As soon as this point has been reached, the tracer gas supply is stopped. The tracer gas present in the room is now removed by the mechanically induced or naturally occurring air exchange and the concentration in the room decreases. The following figure 2 illustrates a typical measurement setup with the dosage in the supply air and the expected curve of the tracer gas concentration in the room beside it.
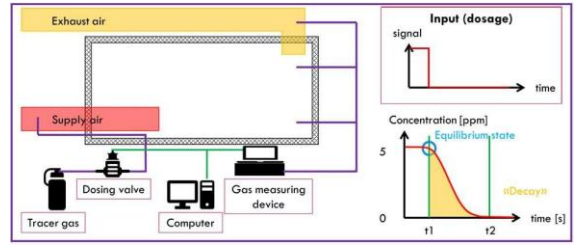

Figure 2.   Constant dosing - Decay

This behaviour can be mathematically explained with formula (1) according to the standard SIA382/1, 2014 [3]. By transforming this formula, the airflow rate of the mechanical or natural ventilation can be calculated.

$$C_{RÆL,t} = C_{RÆL,0} * e^{-\frac{q_{v,ZUL}}{7_R} * t} \qquad (1)$$

$C_{RÆL,t}$ Indoor air concentration at time t in ppm
$C_{RÆL,0}$ Indoor air concentration at time t=0 in ppm
$q_{v,ZUL}$ Supply air volume flow in m³/h
V_R Volume of the room in m³
t Time t in h

Step-up

The second constant dosing method now looks at the dosing behaviour of tracer gas in the room. The measurement is like the decay measurement described before. However, the dosing process in the room is measured, not the decay. The starting point of this measurement therefore represents the situation in the room with no tracer gas concentration present. By subsequently adding tracer gas at a constant rate, the concentration increases until it reaches the equilibrium state between the tracer gas flowing in and the tracer gas being extracted, as mentioned previously. The following figure 3 again illustrates the measurement setup with the dosage in the supply air and the expected curve of the tracer gas concentration in the room beside it.
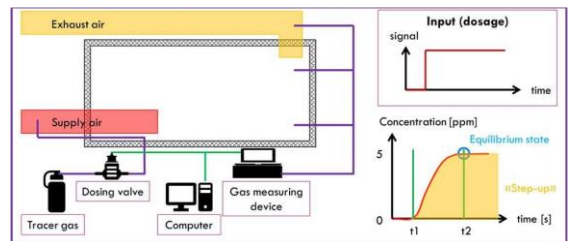

Figure 3.   Constant dosing - Step up

This behaviour can be mathematically explained with formula (2) according to the standard SIA382/1, 2014 [3]. By transforming this formula, it is again possible to calculate the airflow rate of the mechanical or natural ventilation.

$$C_{IDÆ,t} = C_{IDÆ,\infty} * (1 - e^{-\frac{g_{v,ZUL}}{7_R}*t}) \qquad (2)$$

$C_{IDÆ,t}$ Indoor air concentration at time t in ppm
$C_{IDÆ,\infty}$ Indoor air concentration at equilibrium in ppm
$q_{v,ZUL}$ Supply air volume flow in m³/h
V_R Volume of the room in m³
t Time t in h

D. Pulsed emission dosing method

In principle, the pulsed emission dosing method is also a method with decreasing concentration. The main difference to the decay method is the fact that only a short burst of tracer gas is injected and thus no equilibrium is reached at the beginning of measurement. This offers the advantage that a very small amount of tracer gas is already sufficient for measuring. A limitation is, however, that the measurements by the analysing devices must be carried out in very short intervals of a few seconds to obtain reliable results and not to miss the pulse completely in a worst-case scenario. The measurement setup is like that of the constant dosing methods and is illustrated in figure 4.

A key advantage of this dosing method is the possibility to simulate pulse emission sources at different locations in the room and then analyse how quickly and in what residual concentration a pulse arrives at another location in the room. The findings gained can be applied to potential risks of infection with airborne pathogens.
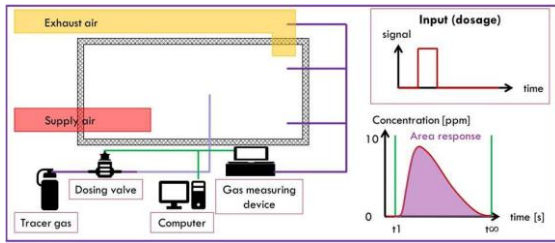

Figure 4. Pulsdosierung

To calculate the air flow rate, a quotient between the tracer gas added at the beginning and the measured tracer gas over the entire measurement period is calculated according to the pulse method of the standard SN EN ISO 12569.2017 [4].

$$q_{v,ZUL} = \frac{V_{gas}(t_1)}{\int_{t_1}^{\infty} C_E(t)*dt} \qquad (3)$$

t Time t in h
t_1 Starting time of measurement in h
$q_{v,ZUL}$ Supply air volume flow in m³/h
$V_{gas}(t_1)$ Volume of indicator gas supplied at the beginning of the measurement in m³/h
$C_E(t)$ Concentration in the exhaust air in m³/m³

III. DATA PRESENTATION AND DISCUSSION

A. Experiment 1 – Climate chamber

The first experiment was carried out in the climate chamber of the Lucerne University of Applied Sciences and Arts. The walls of the chamber can be tempered in variably, which allows the simulation of a bedroom with a poorly insulated exterior wall during winter. The ventilation system of the climate chamber was not in operation at the time of the measurement, which simulates a typical situation in an older building with window ventilation.

The tracer gas measurements showed the indoor air circulation that occurs due to the temperature differences, which was verified visually in Figure 5 by fog tests. The two tracer gases used, HFO-1234yf and SF6, showed identical behaviour, which formed the basis for the subsequent measurement experiments and represents the first step towards confirming the applicability of HFO-1234yf as tracer gas in our test environment.

During this first measuring experiment, only the Gasera One, which works according to the principle of photoacoustic spectroscopy, was available. The measuring intervals of around one minute per measuring point were therefore set by the equipment and have showed to be too large. The results of the pulsed emission dosing method could only be used to a limited extent.
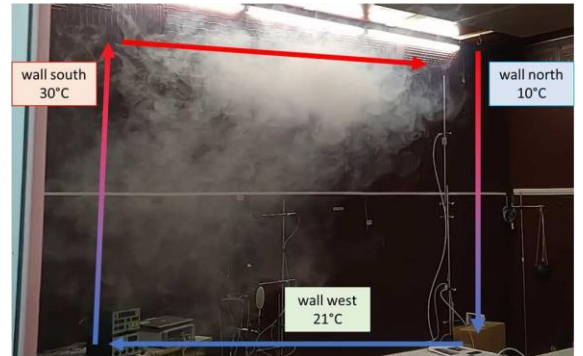

Figure 5. Indoor air circulation in the climate chamber

B. Experiment 2 - Classroom in a training facility

The second experiment took place in a training facility in Lucerne. The analysed classroom has a mechanical ventilation system that works according to the principle of mixed ventilation with supply air outlets mounted in the ceiling. The exhaust air is collected centrally above the lecturer, also on the ceiling. To analyse a situation as close to reality as possible, the room was equipped with dummies, in addition to the four people present, which act as heat sources and influence the air circulation accordingly.

The tracer gas measurements revealed a massively lower ventilation effectiveness than would be expected in the case of perfect mixed ventilation. The measurements resulted in an airflow rate of 450 m3/h, which corresponds to only about half of the supplied airflow rate of 800 m3/h. The existing arrangement of the supply air outlets favours a short-circuit airflow, which prevents efficient mixing of the room air. The linear ceiling diffusers installed ensure that a large part of the supply air adheres to the ceiling due to the coandă effect and does not reach the occupied zone of the

room. Since the exhaust air is arranged exactly along the direction of the airflow and is also located on the ceiling, a large proportion of the supply air is discharged directly. The airflow is shown in the following figure 6.
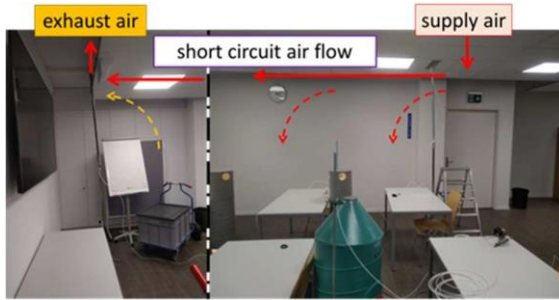

Figure 6. Short circuit airflow in the classroom

An improvement of the situation could already be achieved by rotating the linear ceiling diffusers, which would allow an increased mixing of the supply air with the indoor air. Another possibility is to choose a different air inlet armature all together.

C. Experiment 3 – Small lecture hall of a university

The third experiment took place in a small lecture hall at a university and allowed a measurement setup to be operated over several days. In addition to the two people present, the room was again equipped with dummies serving as additional heat sources. Furthermore, three different analysis devices could be used in this experiment, which allowed an efficient evaluation of the pulsed emission dosing method.

The lecture hall is equipped with a mechanical ventilation system that provides the supply air via diffusers installed in the grandstand. The exhaust air is extracted at the ceiling in the area of the lecturer. As in the two previous experiments, the measuring points were distributed throughout the room. The set-up over four days is displayed in Figure 7.
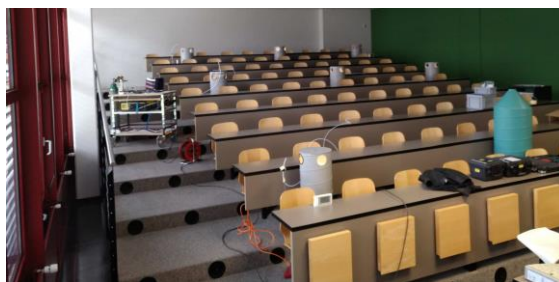

Figure 7. Measurement setup of the small lecture hall

The first finding during the measurements was a malfunction of the ventilation system, which meant that the recirculation flap did not close as set by the control unit. Part of the exhaust air was thus unintentionally mixed back into the supply air. The malfunction was detected by the Gasera One, which works according to the principle of photoacoustic spectrometry and allows the simultaneous measurement of several measuring points using multipoint sampling.

By using three different measuring instruments, they could be tested for their suitability for the different dosing methods. It turned out that the previously very valuable Gasera One with its multipoint sampling is not suitable for the analysis of the pulse method due to the technically required long measuring intervals of about one minute. As can be seen in Figure 8, it misses the actual pulse depending on the exact time of the measurement. An area calculation of the pulse is therefore not possible. The faster measurement methods (FTIR & NDIR) allow for a measurement interval of only a few seconds, which makes it possible to detect the pulses. Thus, it is not only possible to determine the time span that a pulse takes from the point of emission to the point of reception, but also to determine the dilution or, depending on the measuring arrangement, the airflow rate via the calculation of the area.
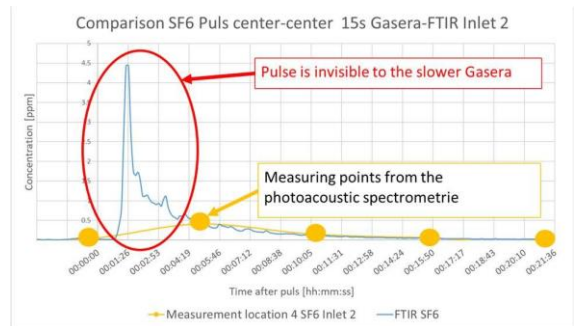

Figure 8. Comparison of FTIR (singlepoint) and photoacoustic spectroscopy (multipoint)

The large airflow rate of 5,000 m3/h and the advantageous arrangement of the supply and extract air outlets create an almost perfect plug flow in parts of the lecture hall, as can be seen in Figure 8, a sectional view of the lecture hall. The pollutants emitted are directly displaced upwards to the exhaust air intake. Only in the last rows of seats does the air, and thus the pollutants contained in it, remain longer. The average dwell time of the air in the front rows is around 3 minutes compared to 9 minutes in the last three rows.

This indoor air movement could be detected equally with the pulsed emission dosing method as well as with the constant dosing methods. The airflow rate can also be determined in the same way by both methods. The use of pulse dosing is therefore advantageous, as the amount of tracer gas required is several times lower.
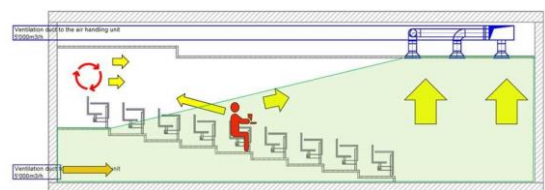

Figure 9. Schematic illustration of the plug flow

IV. CONCLUSIONS

A. Comparability HFO-1234yf and SF6

The measurements have shown that the two tracer gases HFO-1234yf and SF6 are comparable with only a few minor restrictions. The measurement results obtained correspond with such small deviations that they can be explained by the measurement inaccuracy of the analysing instruments. Larger deviations, which could falsify the measurements, were found regarding the absorption behaviour of HFO-1234yf during gas drying of one of the measuring instruments. Similar behaviour could already be observed with coated rotary heat exchangers in tests conducted by the Lucerne University of Applied Sciences and Arts outside of this study. Beyond these observations, no deviations in the behaviour of the two gases could be found.

B. Conclusions regarding Covid-19

Regarding the risk of infection in the room, the findings of the measurements carried out using the pulsed emission dosing method could be used. These have shown that the risk of spreading pollutants and thus also virus particles stable in the air can be minimalised if the air is introduced into the room in an optimal way. The optimum from the analysed tests is an air introduction near the floor with subsequent removal of the room air upwards towards the exhaust air openings near the ceiling, which can be described as a plug flow. However, as soon as there are areas that are not captured by this plug flow, the transition to mixed ventilation begins. Mixed ventilation that works according to the dilution principle, as well as the previously mentioned uncovered zones of a plug or displacement flow, inevitably entail a longer residence time of pollutants in the air. The efficiency of dilution in mixed ventilation decreases as soon as a short circuit airflow occurs, as it did in measurement experiment 2. The investigations are limited to those virus particles that are carried in the air like aerosols and are carried along with the air flow. The behaviour of droplets was not investigated during these experiments.

C. Conclusions regarding indoor air flows

In addition to these key statements, the experiments made it possible to gain further insights into the ventilation systems and the measurement procedure. For example, the occurrence of the indoor air circulation, which is caused by different surface temperatures and leads to a rapid homogenisation of the indoor air, can be quantitatively measured, and interpreted by the tracer gas measurements. Furthermore, the measurement tests revealed a wide variety of malfunctions in the ventilation systems of the examined rooms. These range from short-circuit flows caused by suboptimal arranged air outlets through to control errors.

D. Measuring methods

Regarding the measurement methods, photoacoustic spectroscopy, due to the possibility of multipoint sampling, can show its advantages in an initial evaluation of the room as well as in the constant dosing methods. However, the intervals of this measurement method are set apart too far for an efficient analysis of the pulsed emission dosing method. The short pulses are often not detected exact enough, which falsifies the measurements. The Fourier-transform infrared spectroscopy (FTIR) or nondispersive infrared spectroscopy (NDIR) prove to be more suitable. However, these methods have the disadvantage of not being able to perform multipoint sampling. This means that several analysers operated parallelly are required, which makes the measurement setup and data evaluation more complex. This means that at least two analysers would already be required to determine the ventilation effectiveness using constant dosing methods.

E. Final statement

In conclusion, it can be said that although tracer gas measurements are gaining in importance due to the coronavirus pandemic, the informative value of these measurements go far beyond. A broader application in the HVAC industry, especially in refurbishment or fault analysis, is therefore desirable.

REFERENCES

1   Bienz M, Bucheli K, (2021): Erprobung des klimafreundlichen Tracergases HFO-1234yf zur Bestimmung der Luftwechselrate und der Lüftungseffektivität in belegten Räumen unter Covid-19 Randbedingungen. Bachelorthesis, Hochschule Luzern – Technik & Architektur, Horw/Lucerne, 2021. (in german)

2   Willigert Raatsschen (1988): Was ist Lüftungseffektivität. 1-3 Teil: KI Klima – Kälte – Heizung. (in german)

3   SIA 382/1 (2014): Lüftungs- und Klimaanlagen – Allgemeine Grundlagen und Anforderungen. (in german)

4   SN EN ISO 12569, Thermal performance of buildings and materials – Determination of specific airflow rate in buildings – Tracer gas dilution method, European Committee for standardization, Brussels, 2012.

THE AFFILIATIONS OF THE AUTHORS

Lucerne School of Engineering and Architecture

Technikumstrasse 21

CH- 6048 Horw

+41 41 349 33 11

technik-architektur@hslu.ch

E-MAIL CONTACTS

Students:
Moritz Bienz: moritzrene.bienz@hslu.ch
Kevin Bucheli: kevin.bucheli@hotmail.com

Supervisor:
Heinrich Huber: heinrich.huber@hslu.ch
Stefan Walser: stefan.walser@hslu.ch

HVAC design for swimming pools: potential for heat recovery?

Raul-Lucian Nistor, Lecturer Adam Marius, Ph.D, University "POLITEHNICA" Timișoara

• **Abstract—In the HVAC industry, many building types require both heating and cooling at the same time. This need brings with it the potential for increased energy efficiency using a heat recovery system that can transfer waste heat from spaces that need cooling to spaces that need heating. Traditionally, heat recovery systems are used in buildings such as office buildings, but the question is, are there other types of buildings that have the potential to drastically reduce energy consumption using a heat recovery system? Using a comparative case study, this paper explores the energy saving potential for an HVAC system for swimming pools using a 4 pipe multi-purpose chiller.**

• **Index Terms— 4 pipe multi-purpose chiller, heat recovery, HVAC swimming pool heat recovery.**

• **Introduction**

• There are several ways a heat recovery system can work. Traditionally, heat recovery systems are associated with VRF systems, but there is also the 4 pipe multi-purpose chiller used in applied systems.

• The first variable refrigerant flow air conditioning system, was introduced in the market for the first time by Daikin in 1982, known also as Variable Refrigerant Volume, VRV - trademark of Daikin Industries, Ltd. [1]

• The VRF with heat recovery system uses a 3 pipe system to provide heating to one space and cooling to another at the same time. These pipes consist of a suction gas pipe, discharge gas pipe, and a liquid pipe. The additional 3rd pipe enables the system to carry the waste thermal energy of an indoor unit to the rest of the system. [2]. In this way the energy extracted from a cooling zone is used to heat a heating zone. In theory, if the cooling and heating loads are equal, the system would not exchange thermal heat with the outside. This conservation and reuse of thermal waste is what gives this type of system a higher SCOP and SEER rating than other VRF systems.
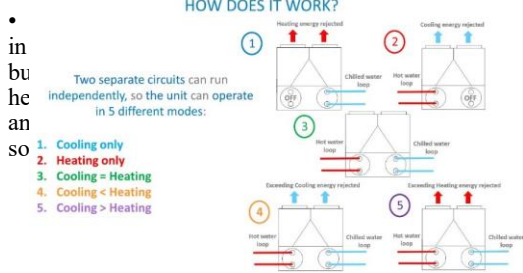
•
in
bu
he
an
so

Figure 1.   4-Pipe chiller operational modes

Using 2 independent refrigerant cycles, the 4 pipe multi-purpose chiller can work in 5 different modes: cooling only mode, heating only mode, cooling=heating, cooling<heating and cooling>heating. [2]

When in cooling only or heating only mode, the unit works like 2 traditional heat pump chillers. It is only when we have both heating and cooling needs does the heat recovery come into play, transferring waste heat extracted from cooling spaces and transferring it to heated spaces. Similar to a VRF heat recovery system, if the cooling and heating loads are equal, the system will not exchange thermal heat with the outside.

Office buildings are a good opportunity to implement these systems and make good economic sense.

Especially in glass curtain facade buildings, many times during spring and fall, the south side areas will require cooling where as the north side areas will require heating (in the northern hemisphere). Not to mention small meeting rooms where, in well insulated buildings, the heat generated by the users and equipment can be sufficient to require cooling, while the rest of the areas require heating.

And also, not to forget server rooms, that are notorious for requiring year round cooling. But what about other buildings that require nearly year round heating and cooling?

Why indoor swimming pools?

As part of my bachelor's degree, that on which this paper is based on, I researched the various specific challenges inherent to HVAC systems in swimming pools.

First of all, the set point temperature is higher than in other buildings. This is due to the fact that the usual temperature of water in swimming pools is 28°C. And also, the difference in temperature between water and indoor air has to be at least 2°C, so as to reduce the "cold draft" sensation when exiting the water. That means, that the minimal, year round temperature for an indoor swimming pool is 30°C, at least 6-10 degrees higher than other common indoor spaces during the winter. This means that an indoor swimming pool, due to it's designed conditions, will require a longer heating period when compared to other spaces. Also, humidity is an important factor when it comes to HVAC design. The large volume of water generates large quantities of water vapor that impacts the relative humidity. To keep the comfort level require, relative humidity in swimming polls must be kept to a maximum of 55-60%.

Usually, indoor swimming pools are part of a larger recreation center, that also have restaurants, coffee shops and, sport gyms and of course administrative office areas.

Fitness gyms tend to have very different design conditions. Due to the fact that sport activities generate higher levels of body heat by occupants, when compared to resting. A cooler environment is required to ensure

comfort. This means that usually, gyms and other spaces with sporting activities tend to require a longer cooling period when compared to other buildings.

In cases when we have spaces that require different cooling and heating periods, there is the potential to reuse waste heat extracted from cooling zones, to heat the heating zones and thus reduce energy load and CO_2 emissions.

The case study project.

The bachelor's degree project started from identifying the need, in the city of Timisoara Romania, for a public recreational and sports medicine complex. There are a lot of privately owned swimming pools, fitness gyms and physiotherapy clinics in Timisoara, but very few open to the general public. The selected site is situated in the south of Timisoara, near the county hospital and municipal stadium. It is on the edge of an existing park in close proximiy to high rise residential buildings with good public transportation connections. The site thus having the right balance of medicine, sport, recreational and civic character to it for the proposed function.

Figure 2. Project site map

The recreational center. Has a 885 m² swimming pool area, a 185 m² fitness gym, two 60 m² changing rooms with showers, a reception area , a cafe, and several small physiotherapy rooms and an administrative office.

Figure 3.   Outdoor and indoor renders

The building functions as sports medicine center in the first half of the day and a recreational center in the second half, for a total of 12 hours a day from 10am to 10pm, 6 days a week, with max. of 100 users at any given time.
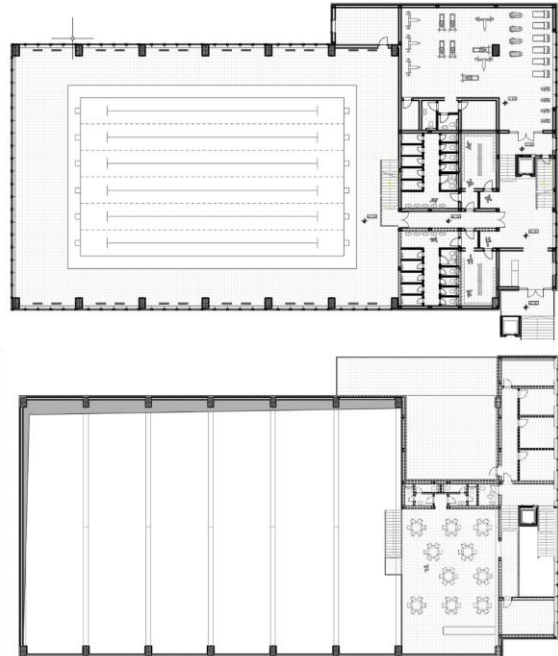

Figure 4.   Ground floor plan and upper level floor plan

Figure 5.   All heating and cooling loads where calculated using Vabi Elements, a software that can quickly create an accurate 3D model of a building and perform a Dynamic Simulation Modeling (DSM) calculation to assess the building's energy performance and the thermal comfort of the indoor environment. The calculation takes into account detailed information about the building fabric and services, as well as specific details regarding occupancy levels and time schedules. [3].
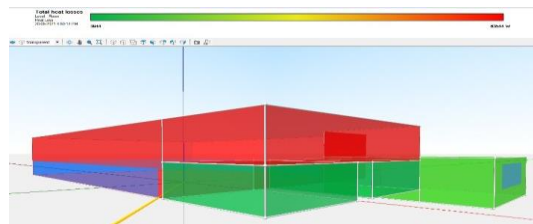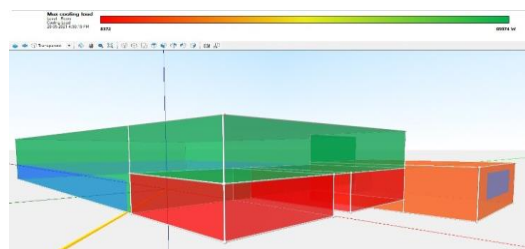

Figure 6.   Vabi elements cooling and heating load calculation.

After calculations, heat load, cooling load and quantity of water vapor for the main areas are as follows:

TABLE I.
HEAT LOAD, COOLING LOAD AND WATER VAPOR

nr	Area	Cooling load [kW]	Heating load [kW]	Water vapor [kg/h]
1	Swimming pool area	63.2	65.4	81.6
2	Fitness gym	19.2	18.0	8.8
3	Changing room (women)	11,5	5,2	11,1
4	Changing room (men)	11,5	5,8	11,1
5	Auxiliary spaces	37.7	26.9	7.8
6	Hot water preparation		43,6	
	TOTAL	143.1	164.9	120.4

The case study solutions.

In this case, an applied solution, with an AHU, chillers and fan coil units is most suitable. Although, in principal a VRF system with heat recovery would be ideal in such a scenario, the heating capability of VRF systems at high outdoor temperatures is limited.

Considering the high level of water vapor generated by the indoor swimming pool, an air handling unit AHU with a cube heat exchanger is required to maintain the relative humidity below a 55% threshold.
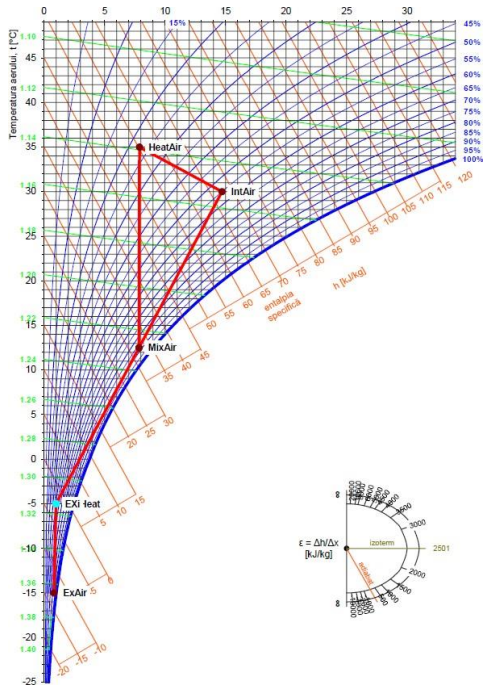

Figure 7.   AHU during winter

For the swimming pool, for heating, cooling and moisture control, the calculated flow of the AHU is 11,500 m³/h and would require a 45kW pre-heating coil, a 135kW cooling coil, and a 85kW heating coil, considering

-15°C outdoor air at 80% humidity in the winter, and 35°C outdoor air at 40% humidity in the summer.
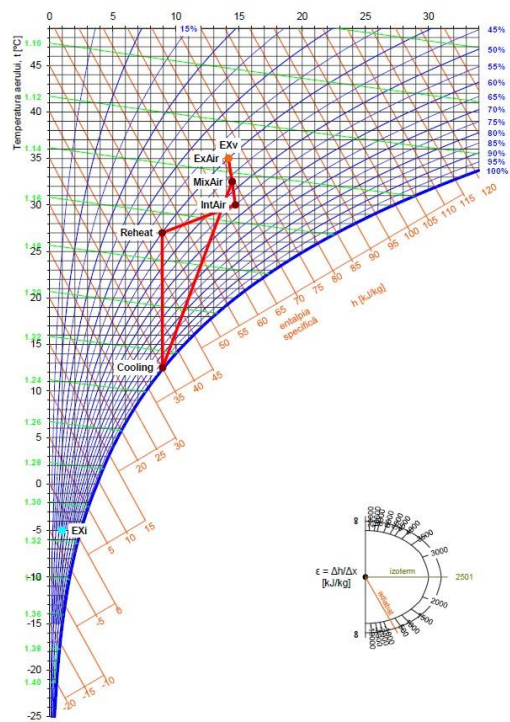

Figure 8.   AHU during summer

To reduce the heating and cooling loads, a air mixing unit with a 50% fresh air intake is used.

The Air handling unit was configured and selected using Daikin selection tool software.

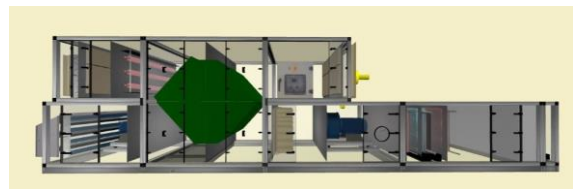The Swimming pool area will also have floor heating for and additional level of comfort.

Figure 9.   AHU configuration using Daikin selection tool software

The other spaces, the gym, the changing rooms and so on will be heated and cooled by 18 fan coil units FCU. Regarding ventilation, 3 heat recovery ventilation units are required in the fitness gym and the two changing rooms. Each heat recovery ventilation unit (VAM) has a nominal air flow of 2000 m³/h. They are a separate system and will not be covered in this paper.

The main focus of this paper is to compare two different chiller solutions in regards to efficiency and CO2 emissions to see what solution is best suited to this particular case and if there are any general conclusions that can be reached.

In total, considering the heating and cooling loads of the preheat, heating/reheating, cooling coils, hot water preparation, and pool water reheat the total heating load of

the building in the winter is 213,5kW at -15°C and the total cooling load is 207,9kW at 35°C in the summer.

Solution 1.

A 4 pipe multi-purpose chiller with two Inverter Driven Single Screw compressors, it uses R134a refrigerant and has a heating capacity of 238.93kW and a cooling capacity of 182.4kW when in balanced mixed heating and cooling mode and up to 399,6kW when in cooling only

For hot water production, air to water reversible heat pump will be used. It has a scroll compressor and uses R-32 refrigerant. It has a heating capacity of 215kW.

In this paper, gas furnace solutions for hot water production have been intentionally omitted, seeing as the energy strategy of the EU for the foreseeable future is to phase out natural gas consumption and to move towards more Eco-friendly solutions based on renewable electric energy solutions.

mode.

Figure 10. 4-pipe multi-purpose chiller selection

Figure 13. Heat pump selection

It has a operating range from -15°C up to +50°C, making it extremely versatile in use and suitable for this specific application. It's high heating capacity comes into use when the occasional full pool water change is needed, approximately once every couple of months, and the full reheating of the water can be done in approximately 48 hours.
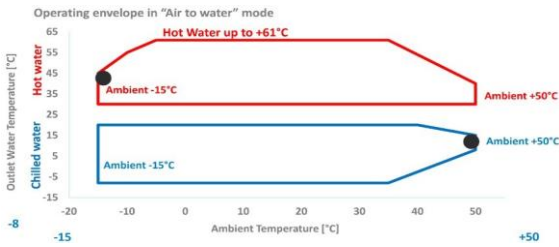

Figure 11. Operating range for 4-pipe chiler.

Solution 2.

Using an air cooled chiller, with 2 scroll compressors for chilled water. It has a cooling capacity 211kW. It uses R32 refrigerant.

Figure 12. Chiller selection.

What about SEER and SCOP?

The Seasonal Energy Efficiency Ratio also known as SEER and Seasonal Coefficient of Power, also known as SCOP are coefficients that are used to estimate the efficiency of any cooling or heating system over a seasonal cooling or heating period. They are derived from the Energy Efficiency Ratio (EER) and Coefficient of Power (COP).

The EER and COP represent the ratio between usable thermal energy, and electrical energy used to run the system. A EER or COP of 5, for example, means to get 5kWh of thermal energy, 1kWh of electrical energy is required. Therese coefficients are calculated at a certain outdoor temperatures, at the higher average outdoor temperature (for EER) and the lower average outdoor temperature for (for COP) for any given country or region.

The SEER and SCOP coefficients take into account the fact that very rarely, only around 3% of the time, a building is exposed to highest or lowest considered temperatures, therefore the cooling and heating loads are lower than the "worst case scenario" the HVAC system was designed to handle. The SEER and SCOP coefficients use the EER and COP of systems at different intermediate temperatures and used to estimate the seasonal costs for heating and cooling. The european ESEER, for example, is calculated using the formula:

$$ESEER = (EER_{100\%} \times 0.03) + (EER_{75\%} \times 0.33) + (EER_{50\%} \times 0.41) + (EER_{25\%} \times 0.23)$$

Figure 14. ESEER calculation formula

Aditionally, the 4-pipe multi-purpose chiller has a TER coefficient, that stands for total efficiency ratio. It is a combination of both COP and EER and describes the efficiency when both heating and cooling is required. [4]

Comparing the two solutions in regards to efficacy and energy consumption.

Solution 1. In regards to SCOP and SEER, the chiller performers as relative standard heap pump and chiller solutions with a SCOP=3.21 in heating only mode, and SEER=4.56 in cooling only mode. The real difference is the TER coefficient that comes into effect when both heating and cooling is required simultaneously TER=7.46.

Due to the fact that heating is required including in the summer for reheating purposes in the AHU and hot water production and pool water reheating, the chiller will never be in cooling only operation mode. It is estimated that 4-pipe chiller will work 1248 hours a year in heating only mode and 2764 hours in cooling+heating mode.

Solution 2. The air cooled chiller has a SEER=4.28 and the air cooled heat pump has a SCOP=3.37. The chiller will work 2764 hours a year, and the air cooled heat pump will function 4012 hours a year, but of course, not at full load. [5]

nr	Solution	SCOP	SEER	TER
1	4-Pipe Chiller	3.21	4.56	7.46
2	Chiller+H.P.	3.70	4.40	-

TABLE II.
SCOP, SEER AND TER COEFFICIENTS

In regards to energy consumption , domestic hot water and pool water reheating demands have been taken into account the full estimated 4012 hours of use in a year.

nr	Solution	Total elect.enegy [kWh/yr.]	Average elect. power load [kW]	Diff. [%]
1	4-Pipe Chiller	196,455.5	48.96	-
2	Chiller+H.P.	249,888.5	62.29	+21%

TABLE III.
ANNUAL ELECTRICAL ENERGY CONSUMPTION, AVERAGE ELECTRICAL POWER LOAD AND DIFFERENCE

As we can see, the second solution solution with an individual chiller and air cooled heat pump uses 21% more electrical energy to run compared to the 4-pipe solution. In regards to running costs, and CO_2 emissions, the average cost of electrical energy is estimated at 0.154 euros/ kWh , and a the average conversion factor of CO_2 emissions is 0.09 kg/kWh.

nr	Solution	Estimated Running costs [euro/year]	CO2 emission [kg /year]	Diff. [%]
1	4-Pipe Chiller	30,254	17,680	-
2	Chiller+H.P.	38,483	22,490	+21%

TABLE IV.
ANNUAL ELECTRICAL ENERGY COSTS, CO2 EMISSIONS

Conclusion.

In this particular case, regarding this swimming pool project a 4-pipe multi-purpose chiller solution would increase energy efficiency by 21%, lead to running cost savings of up to 8300 euros/year and reduce CO_2 emissions by 4810 $kgCO_2$/year, when compared to a traditional air cooled chiller plus an air cooled heat pump solution.

It is hard to generalize and say that the 4-pipe multi-purpose chiller is the optimal solution for all swimming pool projects. There are a lot of variables that go into correctly evaluating efficiency that are very sensitive to local and project specific conditions, but we can take away certain observations.

It is always important to understand the building's function and requirements, in the case of swimming pools, we have to take into account higher indoor temperatures and very high water vapor sources, not to mention heat required for domestic hot water and pool water reheating.

When certain buildings require heating and cooling simultaneously, and heating and cooling loads are relatively balanced, a 4-pipe multi-purpose chiller can be a good solution and work to provide hot water and chilled water in an all-in-one solution.

But maybe the bigger take away is the fact that whenever a building requires both heating and cooling at the same time there is always a good opportunity for heat recovery that can transfer waste heat from areas that need cooling, to areas that need cooling, limiting the transfer of heat energy to the outside. This can drastically increase energy efficiency, reduce running costs, and reduce CO_2 emissions.

REFERENCES

1   https://www.daikin.com/products/ac/lineup/vrv
2   https://www.daikin.com/products/
3   https://builddesk.co.uk/software/vabi-elements/
4   https://mitclima.ro/tehnologii/units-for-4-pipe-systems.html
5   https://www.daikin.ro/content/dam/dace-ro/literature/ Literatura2019/Lista%20de%20preturi%20Applied%20Systems %202019-2020.pdf

Design of Drainage Systems in The High-rise Building

Martin Sokol[1], and Taťjana Jánošková[2]

[1] Department of Building Services, Faculty of Civil Engineering, Slovak University of Technology in Bratislava, Slovakia, martin.sokol@stuba.sk

[2] Department of Building Services, Faculty of Civil Engineering, Slovak University of Technology in Bratislava, Slovakia, tatjana.janoskova@stuba.sk

Year of work: 2021

Abstract – **The drainage system design in a high-rise building is very specific compared to buildings with a lower number of floors. Foul water stacks must be designed to not create excessive negative pressure or overpressure in them. Exceeding the maximum values leads to the loss of the odor trap function, which causes the spread of unpleasant odors and viruses in the interior of the building from the drainage or sewer system. The final work of the study dealt with the complete design of the foul and rainwater drainage system for a 24-story apartment house with a polyfunction, including the site piping. The project documentation was prepared in the BIM environment using Autodesk Revit with geometric detail LOD 300. A secondary task of the final thesis was to propose several alternatives for foul water stacks with an evaluation of the functional and investment aspects. The work aimed to design a functional foul and rainwater system in a high-rise building, considering several alternatives for assessing hydraulic conditions in stacks based on foreign research and measurements.**

Index Terms – **foul water drainage, rainwater drainage, hydraulic conditions, high-rise building, odor traps.**

Introduction

High negative pressure and overpressure values are common problems of drainage systems in high-rise buildings [8]. Nowadays, due to the increasing number of floors, large and complex layouts, the design of stacks is becoming more complicated. Many factors influence pressure fluctuations in stacks. In addition to the correct design of dimensions, fittings, accessories, and ventilation, changes in the direction of the stacks must also be appropriately designed [12]. Overpressure occurs most often above changes in the direction of stacks. At lower overpressure, the bubbling of the water in the odor traps, and at higher pressure, the water is ejected out or knocked out of the sanitary appliances, Fig. 1d, e. Negative pressure occurs in the stack at the connection points of branch pipes

with the flow or under the change of direction of the stack [14]. When the maximum negative pressure is exceeded, water is sucked out of the odor trap, Fig. 1a. Loss of function of odor traps is defined as the bubbling, ejecting, flushing out, and complete suctioning of water from the trap, in which unpleasant odors and viruses are spread to the interior of the building from the drainage system [11]. Rainwater drainage from the facade is also a separate chapter.

I. WATER FLOW IN THE STACK

The water from the branch pipe hits the opposite wall of the stack and then falls downwards. It flows around the pipe's inner walls during the fall and forms a hollow cylinder with an air core in the center. The air core closes at the connection points of branch pipes with the flow, causing a piston effect, and negative pressure is created, Fig. 2a. When the piston effect occurs, a large amount of air is sucked in from the vent pipe. In case of incorrect design, the air is sucked also from the branch pipes, resulting in water being sucked out of the odor trap [8].

If the direction of the stack changes by more than 45°, the water stops flowing around the pipe's inner walls, and the cross-section starts to fill up, Fig. 2b. Overpressure occurs above the change of direction, and negative pressure occurs below the change of direction, Fig. 2c.

When is in the stack little or no flow, the air flows in the stack from bottom to top. The pressure loss that occurs in such a flow is one of the other causes of negative pressure in the stack [9].

A. Water flow velocity in the stack

Fig. 3 shows two states of water velocity in the stack. Curve 1 represents the theoretical flow velocity according to Torricelli's law, and curve 2 real flow velocity in the stack, which considers air resistance and friction against
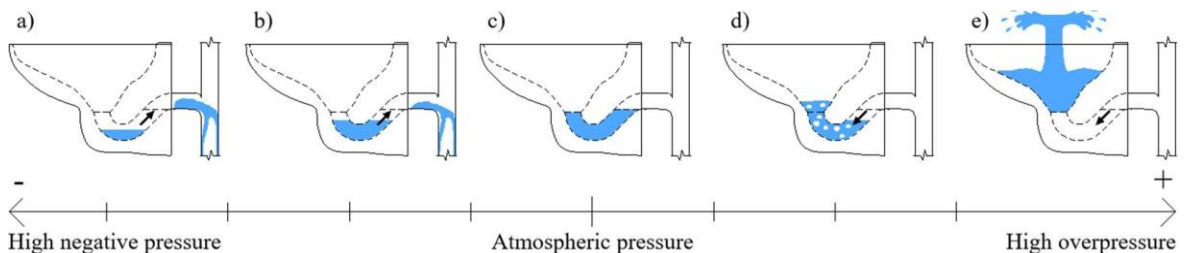

Figure 1. Effect of the pressure in the stack on the water level in the odor trap
a) complete draining of water from the odor trap, b) partial draining of water from the odor trap, c) no effect on the water level in the odor trap, d) bubbling of water in the odor trap, e) knocking out/pushing out of the water from the odor stopper
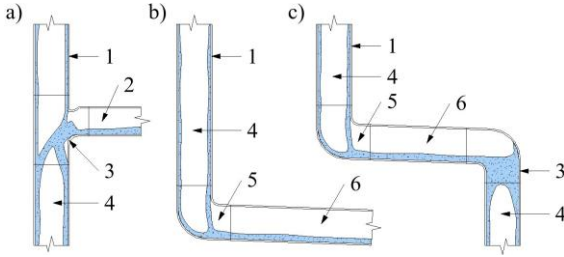
Figure 2. Water flow in the stack
a) at the point of connection of the branch pipe, b) at the point of transition of the stack to the drain, c) at the point of stack offset,
1 – flow around the inner walls of the stack, 2 - water flow from the branch pipe, 3 - formation of the piston effect, 4 - air core, 5 – water impact on the wall of the arc, 6 - steady-state mode of flow

the pipe inner walls. Curve 2 shows that the water reaches a velocity of 12 m/s after about 20 meters, the increase in velocity is minimal from this limit. After about 35 meters, it reaches its maximum speed of 13 m/s, which it does not exceed further due to air resistance and friction against the pipe's inner walls. From the graph, it can be concluded that it does not make sense to design offsets on the stack in order to reduce the velocity of water flow in the stack. The most significant increase in water velocity is the first 10 m.
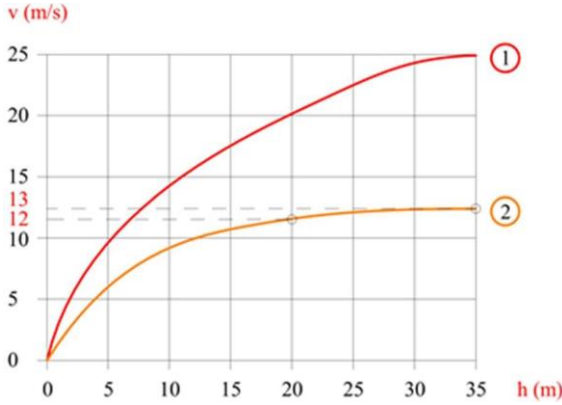

Figure 3. Water flow velocity in the stack [5]
1 - theoretical flow velocity, 2 - real flow velocity (effect of friction and air resistance), h – the height of fall (m), v - flow velocity (m/s)

II. HYDRAULIC CONDITIONS IN STACKS

Stacks with direct vents need to be assessed in high-rise buildings. This limit is usually 70 m, but the assessment should already be carried out at lower heights for stacks with higher flow rates. It is not necessary to carry out an assessment for stacks with additional vent, with Sovent fittings and active protection elements. There are several ways of assessing stacks that are based on the theory, according to Dobromyslov and Wyly-Eaton [6, 9].

The most frequently assessed quantities for stacks are as follows:

- maximum negative pressure Δp_{max} (Pa),
- the maximum pressure loss that occurs when air flows into the stack from the atmosphere Δp_{op} (Pa),
- critical length of the stack L_{cr} (m).

The most important variable in the assessment of stacks in high-rise buildings is the pressure resistance of the odor

traps, which influences the final design of the dimension and the system. One assessment alternative is described in more detail in the paper.

According to Dobromyslov [1], the maximum negative pressure in the stack Δp_{max} (Pa) is calculated according to the formula:

$$\Delta p_{max} = \frac{3590 \, x \, \left[\frac{Q_{tot}}{(1 + \cos \alpha) \, x \, d_{op}^2}\right]^{1,667}}{\left(\frac{d_{op}}{d_{pp}}\right)^{0,71}} \quad (Pa) \qquad (1)$$

where:
Q_{tot} - total foul water flow in the stack (m³/s),
d_{op} - internal diameter of the stack (m),
d_{pp} - internal diameter of the branch pipe (m),
α - the angle of connection of the branch pipe to the stack (°).

According to Wyly-Eaton [9], the air flow rate into the stack Q_a (m³/s) is calculated by the formula:

$$Q_a = 1,5 \, x \, Q_{tot} \, x \, \frac{1-f}{f} \quad (m^3/s) \qquad (2)$$

where:
Q_{tot} - total foul water flow in the stack (m³/s),
f - degree of filling of the stack (-).

We calculate the maximum pressure loss when air flows in the stack from atmosphere Δp_{op} (Pa) according to the formula:

$$\Delta p_{op} = 2240 \, x \, Q_a^{1,85} x \, \frac{L}{d_{op}^5 \, p_a} \quad (Pa) \qquad (3)$$

where:
Q_a - airflow into the stack from the atmosphere (m³/s),
L - the sum of the length of the stack and vent pipe (m),
d_{op} - internal diameter of the stack (m),
p_a - atmospheric pressure (Pa) [9].

The maximum pressure loss Δp_{op} is set to 250 Pa according to EN 12056-1 [15] in order to maintain the minimum airflow $Q_{a,min}$ into the vent pipe from the atmosphere. The maximum negative pressure Δp_{max} should not exceed 464 Pa for stacks from 70 - 100 m. For stacks over 100 m, the sum of the maximum negative pressure Δp_{max} and the maximum pressure loss Δp_{op} should not exceed 464 Pa [9].

A. Pressure resistance of odor traps

Odor traps are the only protection against the spread of unpleasant odors from the sewer and drainage system. According to EN 12056-2 [15] and STN 73 6760 [16], the minimum height of the water seal in the odor trap at the connection to the foul water pipe is 50 mm, and at the connection to the rainwater pipe is 80 mm. Nowadays, odor traps with 50, 60, and 70 mm water seal height are most commonly produced. When designing foul water stacks, the height of the water seal must be taken into account. The maximum pressure that the odor trap is able to withstand Δp_{cr} (Pa) is calculated according to the formula (4). When designing foul water stacks, it is also necessary to take into account the period of non-use of the sanitary appliance,

which greatly influences the height of the water level in the odor trap, therefore, the resistance to negative pressure and overpressure.

$$\Delta p_{cr} = 1{,}1 \times \rho \times g \times h_{tot} \text{ (Pa)} \quad (4)$$

where:

ρ - water density (kg/m^3),

g - gravitational acceleration (m/s^2),

h_{tot} - the height of the water seal in the odor trap (m) [7].

In the 1980s, foreign research was carried out, which confirmed that the daily average drop in water in the odor trap is 1 mm at a temperature of 20 °C. However, this value has not been fully accepted for two reasons. The first reason was that the condensation of water on the inner surface of the odor trap, which subsequently returns, was not taken into account. The second reason was the absence of consideration of gases from the branch pipe with a high water vapor content, which condenses near the odor trap and refills the water level. For this reason, a less verified value of 0.5 mm [7] water drop in the odor trap has been used. After modifying formula (4), we calculate the maximum pressure that the odor trap is able to withstand, taking into account evaporation $\Delta p_{cr,e}$ (Pa):

$$\Delta p_{cr} = 1{,}1 \times \rho \times g \times (h_{tot} - h_0) \quad \text{(Pa)} \quad (5)$$

where:

ρ - water density (kg/m^3),

g - gravitational acceleration (m/s^2),

h_{tot} - the height of the water seal in the odor trap (m),

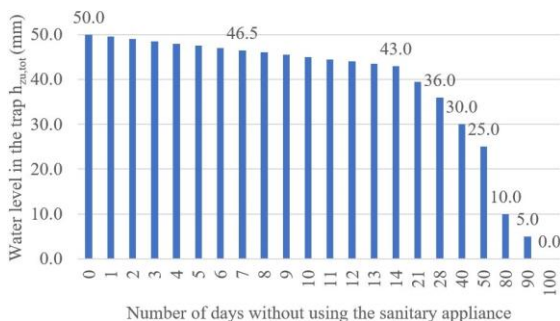h_0 - water level drop in the odor trap due to evaporation (m) [6].

Figure 4. Decrease of water in the odor trap due to evaporation

The water drop due to evaporation at 50 mm odor trap is shown in Fig. 4. The resistance of the odor trap to pressure due to evaporation is shown in Fig. 5. The most commonly used odor trap height is 43 mm, which occurs after 2 weeks of not using the sanitary appliance. After this period, the pressure resistance of the odor trap is around 464 Pa. If the premises are expected to be unused for more than 2 weeks, lower values should be used. In case there are odor traps on the foul water stack with a larger water seal height, larger pressure resistance values calculated according to formula (5) can be used. Figs. 4 and 5 show that the 50 mm water seal loses its ability to prevent odor sulfation after approximately 100 days of not using the sanitary appliance.
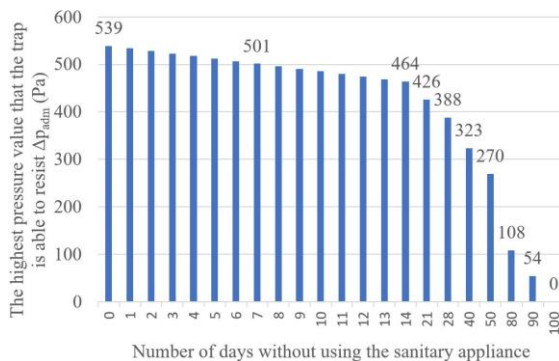

Figure 5. Resistance of the odor trap to pressure due to evaporation

III. FITTINGS USED ON STACKS

The fittings that are used to connect the branch pipes to the stack significantly affect the hydraulic conditions in the tack, Fig. 6. Experimental measurements have shown that when connecting the branch pipes to the stack by a 45° branch pipe, water can be sucked out of the odor trap Fig. 6a due to the negative pressure. It is not recommended to install such fittings on tacks.
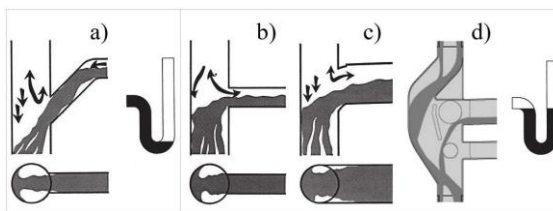

Figure 6. Most commonly fitting used on stacks [18]
a) simple Y-branch 45°, b) simple Y-branch 88,5°, c) simple Y-branch 88,5° with inner arc, d) Sovent fitting

More favorable flow occurs at:
- simple Y-branch 88.5°, if the dimension of the branch pipe is smaller than the dimension of the stack, Fig. 6b,
- simple Y-branch 88.5° with inner arc, if the dimension of the branch pipe is DN 90 or more, Fig. 6c,
- Sovent fitting, Fig. 6d.

With simple Y-branches 88.5°, odor traps are not sucked out with the correct design, and there is sufficient ventilation of the branch pipes, Figure 6b. Stacks with 88.5° branches with an internal arc can be designed for higher flow rates. The most favorable flow occurs in the Sovent fitting, which, together with the fittings from the Supertube class, provides an effective solution for changes in the direction of stacks.

A. Special fittings for stacks offsets

Special fittings designed to change the direction of stacks include the BottomTurn fitting and BackFlip. These fittings are only compatible with the Sovent fitting. The BottomTurn fitting is placed at the transition of the stack to the drain or offset. The BackFlip fitting is placed at the transition of the drain or the offset to the stack.

In the BottomTurn fitting, the flow divider changes from ring flow around the pipe's inner walls to layered flow without disrupting the continuous air column. Fig. 7.

There is no need to attach sanitary appliances above the offset using a bypass when using this fitting.
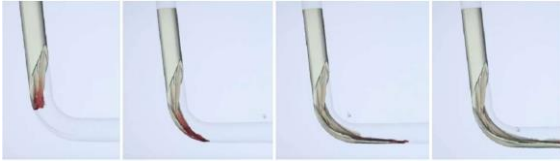

Figure 7. Water flow in the BottomTurn fitting [18]

In the BackFlip fitting, by twisting the shape of the fitting, there is a change from layered flow to ring flow of the pipe's inner walls without disturbing the continuous air column, Fig. 8.
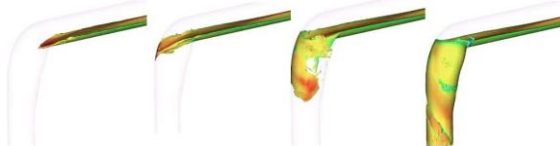

Figure 8. Water flow in the BackFlip fitting [18]

IV. DESIGN OF DRAINAGE SYSTEMS

The apartment house with polyfunction had 24 floors above ground and 3 underground floors. It consisted of 3 differently structured buildings with different heights, Fig.9. In the building, a split drainage system was proposed.
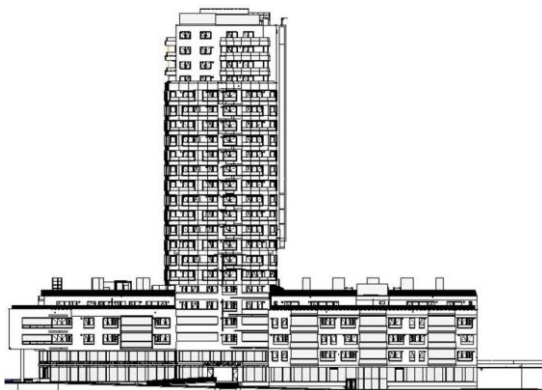

Figure 9. Apartment building with polyfunction

The following parts of the drainage system were designed for the apartment building:
- foul water pipes, including pumping equipment (area sewerage, building drainage),
- rainwater pipes, including safety overflows, leaching devices, a storage tank, an oil separator, water drainage from the facade - the high-rise building had a siphonic roof drainage system (area sewerage, building drainage),
- pipe anchoring, fire penetrations, thermal expansion dilation, thermal engineering assessment of selected critical piping detail located in the building façade.

A. Foul water stacks

The design of foul water stacks was the most important part of the thesis. There were approximately 40 foul water stacks throughout the building. The following stack systems were designed:
- stack with direct vent, Fig. 10a,
- stack with additional vent, Fig. 10b,
- stack with Sovent fitting, Fig. 10c,
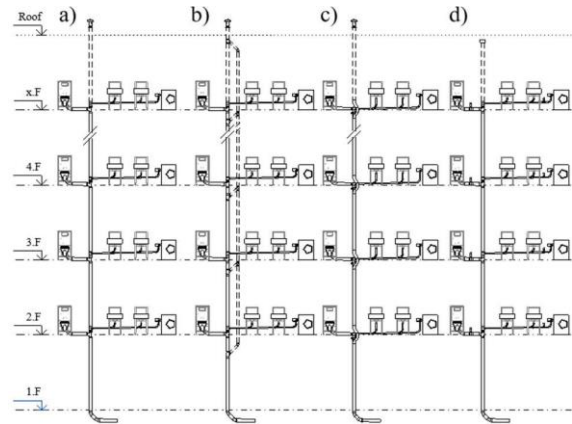- stack with air admittance valve, Fig. 10d.

Figure 10. Overview of designed technical solutions for stacks (illustrative picture)

a) stack with direct vent, b) stack with additional vent, c) stack with Sovent fitting, d) stack with air admittance valve (max. 4 floors)

According to EN 12056-2 [15], all stacks were designed as direct vented stacks in the first step. Stacks exceeding 70 m in length were then assessed in two alternatives for Δp_{max} (Pa), Δp_{op} (Pa), L_{cr} (m), Table I. No stack exceeded 100 mm in length.

TABLE I.
ASSESSMENT OF SELECTED STACKS WITH DIRECT VENT

Stack	Q_{ww} (l/s)	L (m)	EN 12056-2	After assessment	Δp_{max} (Pa)	Δp_{op} (Pa)	L_{cr} (m)
K1B	3,22	70	**DN100**	**DN125**	228	135	223
K2B	3,08	70	**DN100**	**DN100**	292	189	126
K3B	3,77	70	**DN125**	**DN125**	297	149	158
K8B	3,97	74	**DN100**	**DN125**	323	153	141
K9B	4,96	74	**DN125**	**DN150**	234	132	243
K10B	5,60	76	**DN125**	**DN150**	286	142	201

Q_{ww} – calculated foul water flow rate (l/s),

L – the actual length of the waste pipe (m),

Δp_{max} – maximum negative pressure in the stack (Pa),

Δp_{op} – the maximum pressure loss when air flows into the stack from the atmosphere (Pa),

L_{cr} – critical length of the pipe (m).

In the case of uneconomical stack dimensions larger than DN 125, other stack systems were designed and evaluated from a functional and investment point of view, Fig. 11 (piping material, anchoring, fire penetrations elements, etc.) [13]. Functional considerations meant that difficult changes in the direction of the stacks had to be resolved in some cases. The installation shafts were a single fire section across the entire height of the building, and in some cases, it was difficult to decide on the correct system. Stacks with an air admittance valve were only proposed in exceptional cases where it was not possible to bring ventilation above the roof.
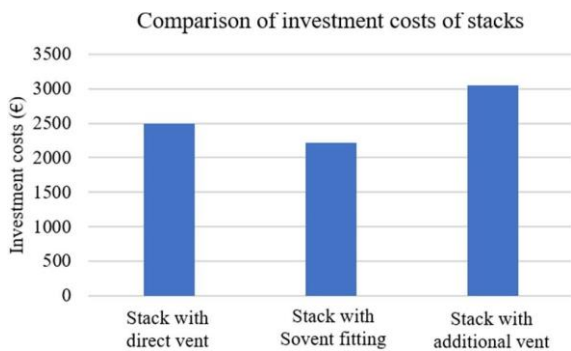
Figure 11. Comparison of the investment costs of the K10B stack in 3 alternatives

The most suitable stacks were then used to project documentation of the building. 20 sheets were prepared for the whole project of the building. In Fig. 12 we can see a part of the floor plan of the object with 3D view.
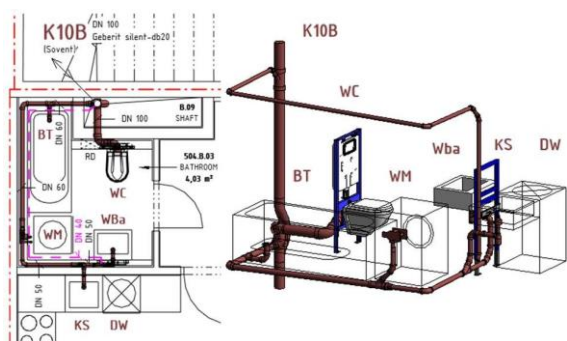

Figure 12. Floor plan and 3D view of part of the building
DW – dishwasher, KS – kitchen sink, Wba – washbasin, WM – wash machine, BT – bath tube, WC – water closet, RD – revision doors, K – the mark of the stack

B. Changes in the direction of stacks

Changes in the direction of stacks are another problem that arises in high-rise drainage. In case of improper design of the stack offset, water from fittings located above the offset can be ejected due to overpressure, Fig. 1e. Problems with high overpressure cannot be solved by calculation, only by correct technical solution. The commentary to DIN 1868-100 and EN 12056-4 [5] prescribes a number of traditional technical solutions, however, demanding space requirements and, in some cases, fire penetrations. The advantage of the stack with Sovent fittings is that this stack can be offset with the Supertube system, which is very efficient.
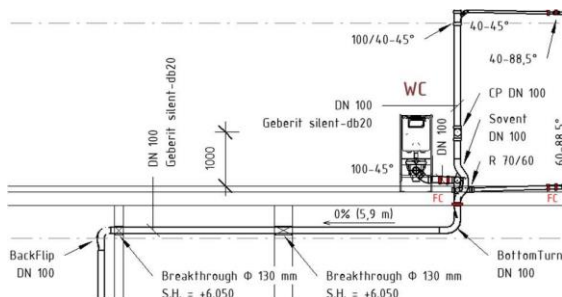

Figure 13. Supertube offset system change for stack
WC – water closet, FC – fire crossing, CP – cleaning piece

The layout of the apartment building with the polyfunction was very complex. The stacks of the high-rise building had to be offset above large office spaces. The very low ceiling spaces for pipes also greatly influenced the design of the stacks, as it was necessary to use the Supertube system, which is only compatible with the Sovent fitting, Fig. 13. In places where there was more space, bypasses were used, Fig. 14.
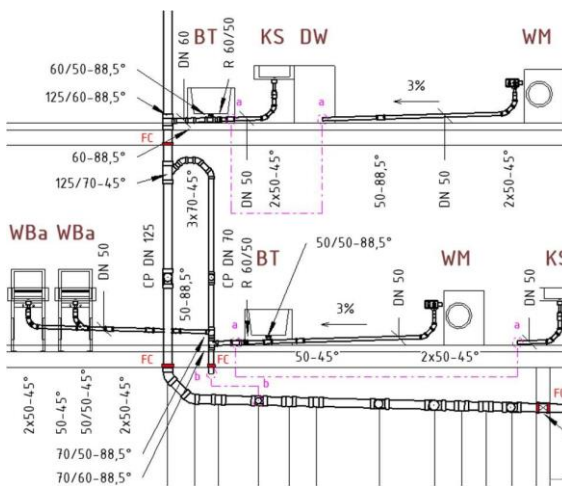

Figure 14. Change the direction of the stack through the bypass
DW – dishwasher, KS – kitchen sink, Wba – washbasin, WM – wash machine, BT – bath tube, FC – fire crossing, CP – cleaning piece

C. Rainwater drainage from the facade

In high-rise buildings, whose dominant size is height, a new problem arises concerning the drainage of rainwater from the facade. In Fig. 15 we can see a comparison of the building form shape factor to wind-driven rain. High-rise buildings with a dominant height catch rainfall over their entire height, while buildings of wider sizes have half of the façade almost dry.
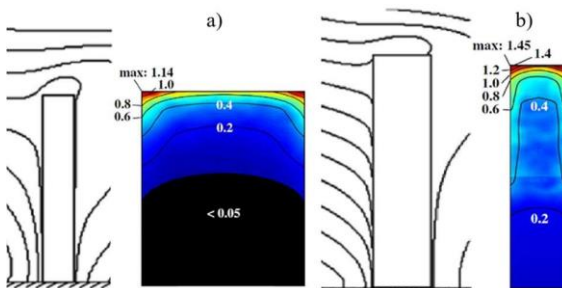

Figure 15 Influence of the shape of the building on the wind-driven rain [3]
a) high rise building 50 x 60 x 10 m (width x height x depth)
b) high rise building 20 x 80 x 20 m (width x height x depth)

A drainage system was designed to runoff rainwater from the facade for the entire building. Due to the lack of standards dealing with this issue, calculations were based on foreign designers' experience from Switzerland. In calculations of rainwater flows, 1/3 of the area for the silicate façade and 1/2 of the area for the glazed façade were considered. The water flowing from the facades was discharged into separate gutters or roof drains.

V. DISCUSSION

The issue of drainage in high-rise buildings is a relatively large and demanding topic due to the complicated hydraulic conditions of foul water flow in drainage pipes. Although this area is not new at all, many buildings have a problem with high values of negative pressure and overpressure in stacks.

Special stack systems for high-rise buildings are gradually replacing traditional stack systems. A significant problem arises with the investment costs, which are not always lower with special systems. Therefore, oftentimes the investor pushes the designers of sanitary installations into cheaper and more marketable systems, which mainly include stacks with direct vents. An integral part of the design of direct-vent stacks in high-rise buildings is the assessment, which is often neglected. In order to avoid undesirable negative pressure, it is recommended that stacks are assessed for at least one alternative. However, great care should also be taken with regard to changes of direction, which can greatly eliminate the danger of overpressure.

When designing the rainwater drainage system, it is necessary to consider the area of the façade. In high-rise buildings with a large façade area, water can accumulate at the connection point between the façade wall and the surrounding surface, which can cause water to overflow into the interior or endanger people.

VI. CONCLUSION

Due to the increasing number of floors in the buildings, more and more demands are being placed on the internal drainage systems in terms of hygiene and quality. When designing drainage systems in this type of building, strict compliance with legislation, standards, and technical regulations is very important. In order to avoid undesirable effects associated with pressure fluctuations and noise spreading, new material solutions will also be needed to improve the quality of these pipelines.

As a result of the thesis, an analysis of the hydraulic conditions in the waste pipes was carried out, and project documentation with a BIM model in detail LOD 300, Fig. 16. The designs of stacks met stringent criteria in terms of hydraulic condition.
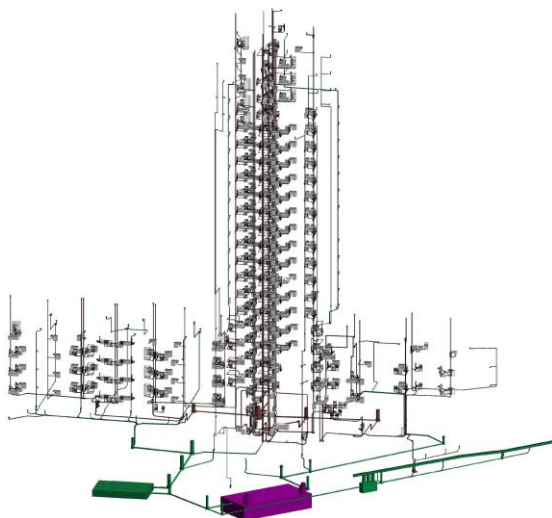

Figure 16. View of the designed drainage systems

ACKNOWLEDGMENT

REFERENCES

1   A. Dobromyslov, "Rasčet i konstruirovanije system kanalizacii zdanij (Calculation and construction of drainage in buildings)" *1 edition Strojizda*, Moscow 1978.

2   A. Öngören, R. Weiss, "Principles of a genuine high flow wastewater fitting with an in-pipe integrated ventilation" *CIB W062 Symposium,* 2018 pp. 17 – 24.

3   B. Blocken, D. Derome, J. Carameliet, "Rainwater runoff from building facades: a review" *Building and Environment,* vol. 60, 2013. https://doi.org/10.1016/j.buildenv.2012.10.008

4   E. Schillart, "Navrhování odvodnění plochých střech 2, podtlakové systémy "(Flat roof drainage design 2, siphonic systems)", Materiály pro stavbu, 2017, Available at: https://www.topwet.sk/upload/data/cz/files/navrhovani-odvodneni-plochych-strech-2.pdf

[5] F. Heinrichs, B. Rickmann, K. Störrlein, "Kommentar zum DIN 1986-100 and EN 12056-4. Gebäude und Grund stucksentwässerung (Commentary on DIN 1986-100 and EN 12056-4. Building and land drainage)" *DIN Deutsches Institut für Normung,* 2010. ISBN 978-3-410-20533-3.

6   J. Valášek, "Vodovody a kanalizácia vo vysokých budovách (Water supply and drainage in high-rise buildings)" Bratislava: *Alfa*, 1982. ISBN 63-021-82.

7   J. Valášek, "Komentár k ČSN 73 6760: Dimenzovanie potrubia vnútornej kanalizácie (Commentary on ČSN 73 6760: Design of drainage pipes)" *Vydavatelství úradú pro normalizaci a měrení*, 1986. ISBN 59-313-83.

8   J. Peráčková, "Dimenzovanie splaškových odpadových potrubí (Design of foul water stacks)", 2018, Available at: https://voda.tzb-info.cz/kanalizace-splaskova/17916-dimenzovanie-splaskovych-o dpadovych potrubi

[9] J. Vrána, "Vnitřní kanalizace ve vysokých budovách (Drainage in high-rise buildgins)", 2004, Available at: https://voda.tzb-info.cz/vyskove-budovy/2029-vnitrni-kanalizace-ve-vysokych-budovach

10   L. Jágerská, J. Peráčková, "Dimenzovanie podtlakového odvodnenia plochých striech (Dimensioning of siphonic drainage of flat roofs)" *TZB Haustechnik*, 2016, Bratislava, Jaga, ISSN 1210-356X, pp. 49 – 54.

11   M. Gormley, T. Aspray, D. Kelly, "COVID-19: mitigating transmission via wastewater plumbing systems" *Watermanagement* vol. 176 (6), pp. 271 – 273. https://doi.org/10.1016/S2214-109X(20)30112-1

12   S. Yabe, M. Otsuka, T. Kawaguchi, R. Sugimoto, "An Experimental Investigation of the Influence of Different Offset Piping Methods on the Drainage Performance of a Drainage Stack" *CIB W062 Symposium,* 2015 pp. 30 – 55.

13   T. Jánošková, "Protipožiarne opatrenia pri inštaláciách ZTI (Fire precautions for sanitary installations)" *TZB Haustechnik*, 2013, Bratislava, Jaga. ISSN 1210-356X, pp. 26 – 28.

14   V. Pomogaeva, L. Matechko, D. Prokofiev, T. Narezhnaya, "Investigation of the motion processes of wastewater in sewerage of high-rise buildings", 2018, pp. 1-9. https://doi.org/10.1051/e3sconf/20183302013

15   STN EN 12056 "Gravitačné kanalizačné systémy vnútri budov (Gravity drainage systems inside buildings)", 2002.

16   STN 73 6760 "Kanalizácia v budovách (Drainage in buildings)", 2009.

17   TNI CEN/TR 17426 "Sanitary appliances - Drainage systems for the application of sanitary appliances", 2020.

18   Geberit, "Company documents", Available at: https://catalog.geberit.sk/sk-SK/home

Trigeneration in hospital environment: energy modeling of a completely monitored plant and optimization of operational management

Gabriele Risoli*, Daniele Testi**

Department of Energy Engineering (DESTEC), University of Pisa, 2020
*gabrielerisoli@outlook.it, **daniele.testi@unipi.it*

Abstract — The high energy demand is one of the critical points of the budget items of hospital complexes. The demand for electricity, thermal energy, and cooling energy for climatization is a source of great economic expenses. A possible solution to this problem could be the installation of cogeneration plants or CHP (Combined Heat and Power) and trigeneration plants or CCHP (Combined Cooling, Heat and Power), for the simultaneous production of electricity, heat, and cooling energy.

In this paper we have shown how to achieve the optimal operational strategy that minimizes cost for the management of the trigeneration plant at the Versilia Hospital in Lido di Camaiore. The plant consists of two cogeneration units powered by natural gas; the heat recovery takes place in heat exchangers that allow the production of hot water and steam, which is also the thermal power supply for the absorption refrigeration unit. Through the monitoring data taken from the Building Management System, it has been possible to define the curves of energy needs; the implementation of a forecasting model to predict the actual energy demands has improved the results of the simulation.

Simply by implementing the proposed optimal operational strategy, without any intervention on the energy generation system, a reduction of CO_2 emissions as high as 200 tons per year can be achieved on the Hospital complex. Over 350,000 € per year of operational costs can be saved with an optimally controlled polygeneration system, compared to traditional separate production.

BMS	Building Management System
COP	Coefficient Of Performance
CHP	Combined Heat and Power
CCHP	Combined Cooling, Heat and Power
EEC	Energy Efficiency Certificates
E	Electric load
E_{PV}	Photovoltaic power generation
E_{CHP}	Cogenerator power generation
E_{chill}	Electrical chillers consumptions power
$E_{in/out}$	Electric power exchanged with grid
HVAC	Heating and Ventilating Air Conditioning
IOM	Ideal Optimal Management
RTOO	Real-time Operation Optimization
AM	Actual Management
FTL	Following Thermal Load
FEL	Following Electric Load
CFL	Continuous Full Load
SP	Separate Production

Index Terms — Building Management System, Cogeneration, Forecasting, Operational Management, Trigeneration.

I. INTRODUCTION

A. Trigeneration at Versilia Hospital

Hospitals are always active and highly energy-intensive systems, with massive consumption of electricity, heat, and cooling energy. According to ENEA [1], the specific energy demand of a hospital is about three times higher than the demand of a house in similar climatic conditions. The reason is to be found in the type of service, which must be constant and continuous 24/7 and must guarantee high levels of comfort, healthiness, and safety.

Cogeneration is one of the most effective ways to significantly reduce the consumption of a hospital. The continuous demand for electricity and heat, in most cases simultaneous, makes the installation of cogeneration plants an optimal solution, with a significant reduction in consumption and emissions, as well as ensuring the continuity of the energy resource.

The Versilia Hospital in Lido di Camaiore, Lucca, Italy, is a seven-floor building of about 70,000 square meters; it was inaugurated in 2002 and it is a renowned example of a health facility designed according to the principles of rational use of energy. The technological and electrical plants of the hospital are managed through a Building Management System, or BMS, integrated into a complex monitoring system with over 12,000 analysis and regulation points. The BMS allows the visualization in real time and with remote access of the performance of the machines, of the thermo-hygrometric conditions of locals and rooms, and helps to intervene promptly in case of failure or emergency, with visual and audible alarm signals.

The BMS system was the main tool for the acquisition of historical data on building energy request laying the ground for this work, which has the goal to search for the optimal operational management from an economic point of view of the trigeneration plant of the Versilia Hospital, aiming at minimizing the annual costs for energy due to the purchase of natural gas and electricity from the national electric grid. The evaluation of boundary layers such as cost of energy, local climate conditions and energy needs and the implementation of the energetic systems and the conduct of the simulations of different operational strategies were performed in the MATLAB workspace. To achieve a more realistic simulation of operative reality, for which some variables are unknown, we implemented a self-regression forecasting model based on previous input data.

Once the modeling of the machines has been carried out, and the algorithms of the management strategies have been defined, in addition to an economic comparison, an analysis will be proposed to evaluate energy waste and

environmental impact. Alternative plant solutions that can bring benefits in terms of savings and lead to an even more rational use of energy will therefore be evaluated.

B. Energy systems and machines

Versilia Hospital is a complex system in which passive elements that aim to reduce building energy request and active systems like renewable energy and combined production of heat and power coexists. The main energy systems considered are the following:

a. Photovoltaic plant of 200 kWp, divided into two sections of 100 kWp each, it consists of 864 polycrystalline silicon modules; the energy produced is converted into alternating current thanks to four 40 kW inverters;

b. Cogenerator: an internal combustion engine powered by natural gas, nominal power of 1,003 kW with heat recovery section to produce steam and hot water;

c. Microturbines: a group of three turbines of nominal 200 kW each for total 600 kW, fueled by natural gas with great modulation capacity for the pursuit of the electrical load;

d. Classical boilers: thermal power plant consisting of three traditional generators for about 8,000 kW, and two boilers for steam production with a nominal power of 460 kW and 2,093 kW;

e. Chillers: three electrical refrigeration units of 1,300 kW each operating in parallel, and a refrigeration absorption unit water/lithium bromide of 551 kW, which use saturated steam as supply; each chiller is equipped with a dedicated evaporative tower;

f. HVAC – Heating and Ventilation Air Conditioning: is the main system used for climatization and heating for the internal spaces of the hospital. There are over 50 HVAC machines divided in two sections between the second floor and the seventh floor of the building.

II. METHODS

A. Estimation of loads, microclimate and energy cost

The determination of the boundary conditions of the system, i.e. those input quantities that vary during the simulation, was carried out using multiple sources: in addition to the availability of climatic data and energy prices found via web, the data available from the historical recordings stored in the BMS and typical hourly trends from other works were used to recreate the energy demand.

The microclimate influences the behavior of machines and devices, and it is therefore essential to define the climatic conditions of the area. All climate variables were taken hourly using the European Commission's interactive tool PVGIS, the Photovoltaic Geographical Information System [2] [3] which contains a large database with records of climatic conditions of most European locations. Given the geographical coordinates of the hospital, the temperature and relative humidity were downloaded, necessary since the performance of the chillers are a function of the wet bulb temperature, solar radiation, and wind speed, which affect the performance of the photovoltaic generator that also depends on the ambient temperature, and the solar height, used for post-processing of the forecasting model for irradiance.

The two thermal loads for heating and domestic hot water, and the production of dry saturated steam at 8 bar,

were not determined by data available from BMS, as they were not sufficiently exhaustive and complete to have an accurate measurement. It was preferred to use a different approach, manipulating typical trends related to the summer, winter, and intermediate seasons, and adapting them to the case. Operations were carried out to make the thermal load dependent on the external temperature, a valid hypothesis since we observed hourly trends related to seasonality and climatic conditions, as well as a correlation with prevailing work intensity during the hours of light.

For the determination of the electrical load and the cooling energy needs, we used a series of "valid" data downloaded from BMS interface. The latter was calculated through the data downloaded via BMS related to the ignition status of the four chillers, the outlet temperature of the chillers, the outlet/inlet temperature to the batteries of HVAC, and the flow rate circulating in the cooling coils. Since data for the flow rate processed by each refrigeration unit were unavailable, the flow rate was obtained by dividing the total amount sent to the cooling batteries of the HVACs based on the number of machines active at a given time, and on the respective thermal jump between the outlet temperature and the inlet temperature to the chiller, also used to determine the hourly cooling capacity of each machine. This operation was also useful to estimate the electrical consumption of the three chillers equipped with a compressor, obtained by dividing the hourly cooling thermal power by the nominal coefficient of performance, or COP.

The electrical load was determined using (1), which considers the exchanges with the electricity grid $E_{in/out}$, the power produced by the cogeneration units E_{CHP}, the electric power produced by photovoltaics E_{PV}, and power consumed by electric chillers E_{chill}, as anticipated. Fig. 1 shows the loads obtained with the exposed methodology.

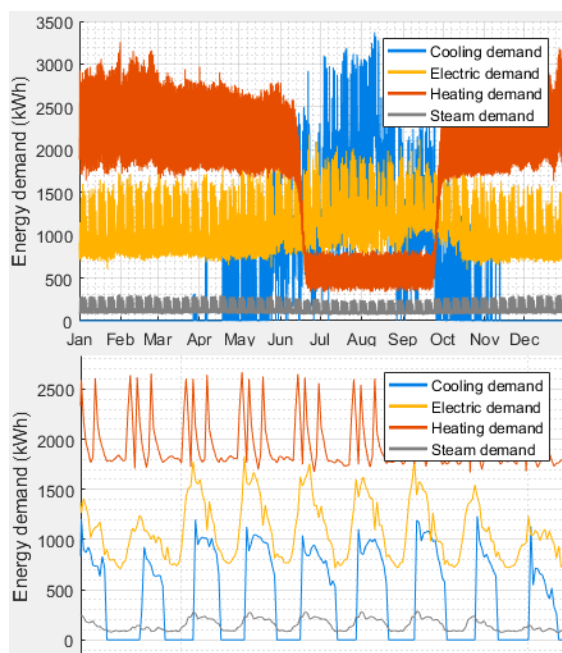$$E = E_{PV} + E_{CHP} - E_{chill} - E_{in/out} \qquad (1)$$

Figure 1. Energy requests and detail of a typical week of May

The prices of energy are necessary for the determination of the hourly operative cost. The purchase prices of natural gas (that is the only fuel supplying the thermal plants) and the purchase price of electricity were taken on daily and hourly basis respectively, both available on the GME website [4] [5] (Gestore dei Mercati Energetici). For the sale price of electricity, we used the parameter of Electricity Prices Ratio [6] for a typical day, which is defined as the ratio between the sale price and the purchase price of electric energy.

B. Forecasting

To run a more realistic simulation of operational strategies, a forecasting model has been implemented in the workspace of MATLAB to predict the quantities that change over time described above, assuming that at each time step it is not possible to know the exact value of energy demand, or energy prices, or climate condition. We created an autoregressive model that uses a limited number of previous k values of the variable y_{n-i} multiplied by coefficients a_i in a linear combination to predict the actual value $\tilde{y}_n$ at nth time step, as shown in (2):

$$\tilde{y}_n = \sum_{i=1}^{k} a_i \, y_{n-i} \qquad (2)$$

The coefficients, which represent the unknown terms of the equation, are determined by minimizing the error committed between the real value and the expected value, over a training period greater than k. The operation is repeated after a certain number of time steps called retraining period, which has the aim of looking for coefficients more suitable to describe the seasonal behavior of the variables. Both the period of self-regression, the period of training, and the period of retraining, have been manipulated for each of the variables to be predicted, trying to minimize the error over the year according to two statistical parameters, the mean absolute error MAE and the root mean square error RMSE.

Post-processing operations were then carried out to make the prediction of some variables more realistic. Fig. 2 shows the results obtained for the electrical load.

C. Model of devices and machines

To simulate the behavior of machines under variable operating conditions, we created and implemented models in MATLAB workspace as functions. Below follows a brief description for each of the functions created for the devices present at the Versilia Hospital:
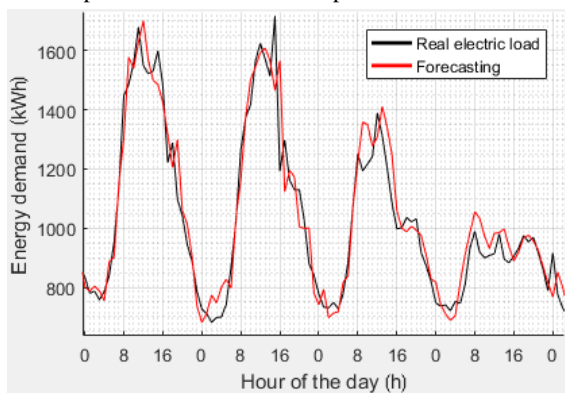

Figure 2.   Forecast of the electrical load for some days of March

a. Photovoltaic generator: the temperature of the photovoltaic module is a function of the external temperature, the incident radiation and the wind speed, a model also defined by PVGIS [7]; then the efficiency of the photovoltaic system is evaluated on the base of the temperature of the module and the incident radiation, from which we calculated the generated power [8] [9].

b. Cogenerator: based on the datasheets provided, we found the operating curve at partial loads by interpolating available data of output electrical power and recoverable thermal power. The engine was however used at 80% of nominal power or at nominal power, in addition to the OFF state. The function has the load factor as input and returns the electrical and thermal efficiency, from which recoverable heat, electrical power, and fuel consumption can be determined. The heat recovery takes place in two exchangers, the first of water/water type and nominal power of 602 kW, is fed with the water of the cooling circuit of the machine and is used to produce hot water; the second is a 504 kW gas/steam heat exchanger that allows recovery from exhaust gases.

c. Turbines: for the second cogeneration unit, the partial load curve is available from datasheet that reports efficiency under ISO standard conditions, both for the electrical efficiency and for the heat recoverable from the exhaust gases, converted into useful heat in two exchangers placed in series: the first is a gas/steam exchanger of 420 kW, the second is a gas/water exchanger of 400 kW. Also, for turbines, the function takes partial load factor as an input, and gives thermal and electrical efficiency as output: with this, we can evaluate fuel consumption and thermal and electric power produced.

d. Refrigeration units: the model adopted for the four chillers is based on the concept of exergetic efficiency [10], expressed as the ratio between the COP and the Carnot COP, or the theoretical maximum limit. This ratio is kept constant, and depends only on the nominal operating conditions indicated on the datasheets of the machines (condenser temperature, evaporator temperature, generator temperature for the absorption refrigeration unit), while the Carnot COP is considered variable with the temperature of the water at the cooling tower, sum of the wet bulb temperature and the approach temperature, set at 6°C. While the absorber can only take ON/OFF state, depending on the cooling demand and the availability of steam, the three electric chillers can modulate up to a minimum partial load, and a COP correction factor is provided as the partial load changes. A predefined electric consumption proportional to the thermal power to be dissipated at cooling towers of the refrigeration units was therefore fixed. While the output variables are common to all refrigeration units (cooling capacity and COP necessary to determine electricity consumption), the input variables to the functions are temperature at the cooling tower and steam available for the absorber unit, temperature at the cooling tower and load factor for the electric chillers. Refrigeration units start sequentially with priority to the absorber, then screw-compressor chiller and at last the two centrifugal-compressor chillers.

e. Traditional generators: for traditional boilers and steam generators, thermal efficiency trends have been defined as the partial load changes, which can be found in literature [11] [12] [13], and from which fuel consumption can be traced.

f. Steam/water exchangers: at last, two simple functions have been implemented for steam/water exchangers that allow the transfer of excess thermal energy from high-temperature recovery for the additional production of hot water if the request has not yet been met through the trigeneration plant.

D. Simulation of operational strategies

Once the boundary conditions and the models of the devices were defined, we run the simulations of 7 different operational strategies, over a period of one year with an hourly frequency simulated as a for-cycle of 8,760 time steps; these strategies, according to the imposed logic, search for the working point of the cogeneration plant from a pool of load factors characterized by two degrees of freedom: the engine (with three working point – Off state, 80% of nominal power and maximum power) and turbines (which light up in cascade).

There is also a post-strategy that allows to balance energy gaps due to the imperfect prediction of loads, which may deviate from real requests: the post-strategy consists in the adoption of traditional generators to meet thermal needs and in the purchase of electricity from the grid to meet the electrical load.

The strategies used for the simulation are the following:

a. Actual Management – AM: the current management provides for the coverage of electricity needs with only the cogeneration plant, following the electricity demand. Seasonal operating programs are planned for the internal combustion engine and for turbines, especially during the night hours and weekends.

b. Ideal Optimal Management – IOM: perfect load forecasting; among all the possible combinations of turbine and engine load factors, the one that guarantees the minimum operating cost is chosen.

c. Real-Time Operation Optimization – RTOO: similar to the previous strategy, however the incoming energy needs are evaluated by forecasting the loads and other boundary conditions, and post-strategy is adopted.

d. Following Thermal Load – FTL: tracking of the thermal load with the cogeneration plant.

e. Following Electric Load – FEL: tracking of the electrical load with the cogeneration plant.

f. Continuous Full-Load – CFL: the cogenerator and turbines always work at the nominal load throughout the considered period.

g. Separate Production – SP: finally, a scenario is also proposed in which there is no CHP/CCHP plant, to highlight its advantages. The thermal energy is supplied by traditional generators only, electricity is completely purchased from the grid (except for the small fraction provided by PV generator), and the cooling energy is produced only with electric chillers.

The cost of management at each time step and for each strategy is therefore expressed as the sum of the cost of electricity and gas purchased, minus the gaining from electricity sells to grid; we also evaluate and consider in total cost the economic return obtainable from the sale of

Energy Efficiency Certificates (EEC), which represent the main incentive mechanism for energy efficiency in the industrial sector. A single EEC is equal to a Ton of oil equivalent of pollutant saved, and they can be accumulated for plants which are considered as High Efficiency Cogeneration [14] and sold at price of 260 € each. For this specific case only the turbines, being of more recent conception, are considered High Efficiency Cogeneration.

III. DATA PRESENTATION AND DISCUSSION

A. Energy exchange, emission and operative cost

Fig. 3 shows the exchanges with the electrical grid obtained from the simulation. For each configuration, because of the high consumption due to the activation of the refrigeration units, it is inevitable to purchase electricity during summer. The best solution in terms of cost is given by the adoption of IOM and RTOO strategies, from which it is evident that the convenience lies in the limitation of electricity exchanges with the grid. The thermal tracking results in a continuous on/off regime for the cogenerator during the summer. This is not only far from the ideal condition but is also not contemplable in the operational reality of the hospital, which sees the cogenerator as the best system for combined production. Table 1 shows the total cost, while Table 2 shows emission and relative reduction of emitted pollutants achieved compared to separate production of heat and power.

During the summer, there is a greater use of the two cogeneration plants by adopting the IOM or RTOO strategy, compared to management such as the tracking of the thermal load; the latter has high load factors of the machines outside the summer period, like the CFL strategy, due to the high demand for thermal energy for heating, which requires an intense use of the cogeneration units to meet the thermal needs.
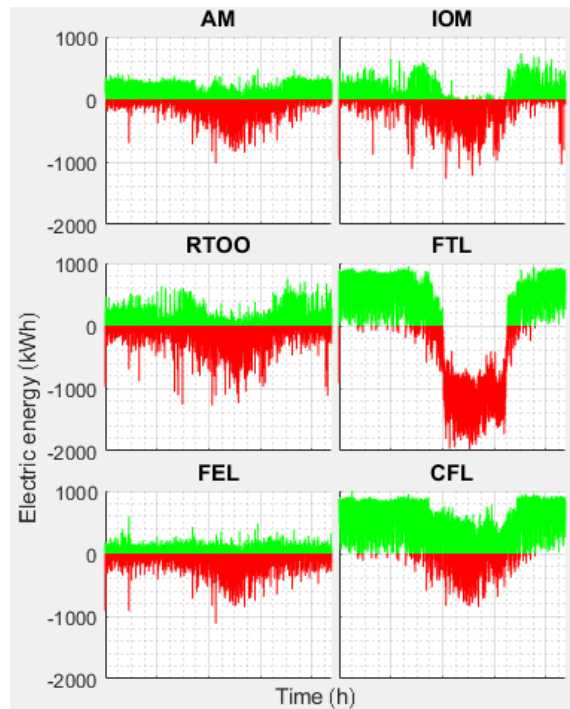

Figure 3. Electricity exchange with grid during the simulated year. In green the energy sold, in red the energy purchased

TABLE I.
OPERATING COSTS AND SAVINGS ACHIEVED THROUGH THE PROPOSED
STRATEGIES COMPARED TO SEPARATE PRODUCTION

Strategy	Operating cost	Savings
AM	524,900 €	− 46.0 %
IOM	483,500 €	− 50.3 %
RTOO	505,800 €	− 48.0 %
FTL	579,300 €	− 40.4 %
FEL	538,300 €	− 44.7 %
CFL	530,900 €	− 45.4 %
SP	972,700 €	/

TABLE II.
EMISSIONS OF CARBON DIOXIDE PER OPERATIVE STRATEGY

Strategy	Emission (Ton CO_2)			CO_2 saving
	$CO_{2,fuel}$	$CO_{2,grid}$	$CO_{2,TOT}$	
AM	7,423	285	7,708	− 26.7 %
IOM	6,924	328	7,252	− 31.1 %
RTOO	7,123	395	7,518	− 28.5 %
FTL	6,923	1,564	8,487	− 19.3 %
FEL	7,400	332	7,723	− 26.6 %
CFL	8,500	198	8,698	− 17.3 %
SP	4,751	5,948	10,519	/

It is interesting that strategies that seek the lowest cost led also to a substantial reduction of pollutants emitted. These are evaluated by breaking down the production of carbon dioxide into two contributions: the first contribution is linked to the actual consumption of fuel; the second contribution is instead linked to the emissions generated by the purchasing of electricity from the grid and is evaluated through the introduction of an average emission factor[1] [15].

While for separate production the emissions due to the massive purchase of electricity from the grid are prevalent, for all the proposed strategies they are an order of magnitude lower than "direct" emissions.

B. Operational reality

The operational reality can deviate from the models created and the hypothesized management choices, and there may be inconveniences that modify the real activity of the plant. It was therefore decided to evaluate the actual electrical efficiency of the turbines, which are the most monitored machines, and of the absorber chiller. The analysis is possible thanks to the data taken from the BMS and showed periods of malfunction and failure of the absorber, while for the turbines it was possible to find the "real" electrical efficiency, evaluated by the consumption of natural gas, electricity produced, and power delivered by the individual units.

The data were placed in correspondence between electrical efficiency and power delivered by turbines and considering only data in which a single turbine is turned on also allowed to more accurately correlate power and efficiency[2]. The result is illustrated in Fig. 4, which shows the Power-Efficiency diagram obtained: there is a particularly dense cloud of data for powers close to the nominal one, but below a limit value of 167 kW there is a very strong dispersion, which does not allow to define a reliable regression curve that describes the electrical efficiency for load factors less than 83%: therefore, only data for powers between 167 kW and 200 kW were considered acceptable. For these data, we defined a linear regression curve using the least squares method, while those below this value were not considered sufficiently valid and were discarded, estimating the trend in the rest of the field of application with another simple linear curve.

The simulations in this new set-up of the non-CCHP system have highlighted the importance of the absorption refrigeration unit: for the RTOO strategy, in fact, despite the higher cost due to less efficient turbines, the difference in summer is even more significant, with gap in hourly cost that even exceed 15 €/hour compared to the basic simulation, for about 26,000 € more per year. Obviously costs and emissions rise for each strategy.
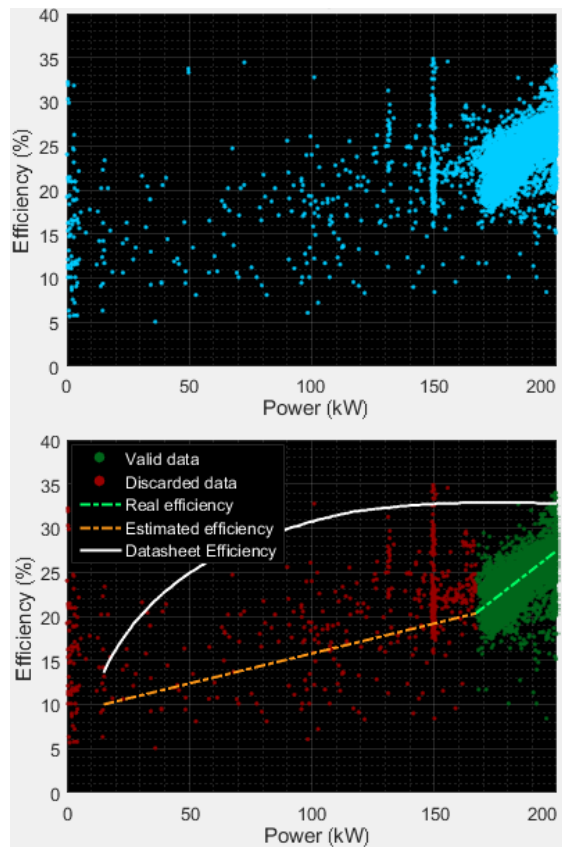

Figure 4. Experimental turbine efficiency obtained from data analysis performed

C. Different scenario with new machines

Finally, simulations were conducted proposing alternative machines, chosen after consultations of catalogues and technical data sheets found via web: the cogenerator taken into consideration is a model of the same manufacturer, larger in size (1,790 kW of nominal power) and with modulation capacity up to minimum loads of 50%, proposed as an alternative to the current cogeneration group. The installation allows to achieve a substantial saving, exceeding 15,700 € per year, and the benefits are particularly evident in summer, with a sharp reduction in the electricity purchased and savings ranging between 0 € and 12 € per time step. Different absorption chiller doesn't seem to bring evident economic advantages: the chillers taken into consideration had power ranging from 763 kW up to 1,420 kW, and the only benefit is a consistent reduction in the waste of thermal energy.

IV. CONCLUSIONS

We can therefore conclude that the simulation of different operational management, combined with the modeling of energy production plants and after careful evaluation of energy request of the building, allows to more accurately evaluate the optimal solution for the operative management of the plants of a complex structure. Our expectations are confirmed: the combined production of electricity, heat and cooling energy is a particularly advantageous solution to reduce costs related to energy expenditure, up to a maximum of 40%. The installation of polygeneration plants seems to be the right choice for a health facility, which have energetic demands with a repeated and low variable trend, and so well predictable, and for which there is simultaneous demand for steam, thermal and cooling energy, as well as a significant demand for electricity. That means that the forecasts would be very accurate, thanks to the repetitiveness of the hourly loads. In fact, despite a difference of 3.9% between the cost obtained with ideal load forecasting and real forecast, a net saving is achieved compared to other operational management, further reducible with monitoring data recorded at a higher frequency to guarantee a more accurate and punctual forecasting. Trigeneration also guarantees significant energy savings during summer, but an accurate sizing of the absorption refrigeration unit is necessary to obtain considerable advantages.

The study and analysis allow us to affirm that the actual management still has room for improvement: the implementation of a control system that aims at minimizing the cost, based on the forecast of loads and other variables that affect the overall system, leads to a saving of about 17,000 € per year, which in a business context means a considerable economic return compared to an irrelevant investment, especially where there is already a central monitoring and control system, with personnel already trained in its use as in this case study.

The paper highlighted the usefulness of technological modeling and the importance of simulation for a building and plant management system, particularly effective if integrated into an extensive monitoring network that allows a wide availability of historical data.

REFERENCES

1. ENEA, "Annual Energy Efficiency Report. Analysis and results of our country's energy efficiency policies", 2019.

2. European Commission – Photovoltaic Geographical Information System (PVGIS), JRC PVGIS Interactive Tool, *hiips://re.jrc.ec.europa.eu/pvg_tools/it/#DR*.

3. European Commission – Photovoltaic Geographical Information System (PVGIS), "Data sources and calculation method", *hiips://ec.europa.eu/jrc/en/PVGIS/docs/methods*.

4. GME, Electricity Markets – Historical data MGP, *hiips://www.mercatoelettrico.org/it/download/DatiStorici.aspx.*

5. GME, Gas Markets – Historical data gas markets, *hiips://www.mercatoelettrico.org/It/Download/DatiStoriciGas.aspx*.

6. L. Urbanucci, D. Testi, J.C. Bruno, "An Operational Optimization method for a Complex Polygeneration plant based on Real-time Measurements", *Energy Conversion and Management*, vol. 170, pp. 50-61, 2018.

7. D. Fairman, "Assessing the Outdoor Operating Temperature of Photovoltaic Modules", *Progress in Photovoltaics: Research and Applications*, vol. 16/4, pp. 307-315, 2008.

8. T. Huld, A.M. Gracia Amillo, "Estimating PV Module Performance over large Geographical Regions: The Role of Irradiance, Air Temperature, Wind Speed and Solar Spectrum", *Energies*, vol. 8/6, pp. 5159-5181, 2015.

9. T. Huld, R. Müller, A. Gambardella, "A new solar Radiation Database for Estimating PV Performance in Europe and Africa", *Solar Energy*, vol. 86, pp. 1803-1815, 2012.

10. European Committee for Standardization (CEN), "Heating Systems in Buildings – Method for Calculation of System energy Requirements and system Efficiencies – Part 4-2: Space Heating Generation Systems, heat pump systems", 2006.

11. M. Dvorák, P. Havel, "Combined heat and power Production Planning under Liberalized market Conditions", *Applied Thermal Engineering*, vol. 43, pp. 163-173, 2012.

12. Z. Zhou, P. Liu, Z. Li, E.N. Pistikopoulos, M.C. Georgiadis, "Impacts of Equipment off-design Characteristics on the Optimal design and Operation of Combined Cooling, Heating and Power Systems", *Computer Aided Chemical Engineering*, vol. 31, pp. 990-994, 2012.

13. H. Li, R. Nalim, P.A. Haldi, "Thermal-economic Optimization of a Distributed Multi-generation Energy System – A case study of Beijing", *Applied Thermal Engineering*, vol. 26/7, pp. 709-719, 2006.

14. GME, Environmental Markets – Energy Efficiency Certificates, *hiips://www.mercatoelettrico.org/It/Statistiche/TEE/StatisticheTEE.aspx*.

15. Istituto Superiore per la Protezione e la Ricerca Ambientale ISPRA, "Atmospheric Emission Factors of Greenhouse gases in the National Electricity sector and in the main European Countries", 2019.

Forecast Driven Building Energy Flexibility using Battery Electrical Storage System

First Author: Rick Cox[1],
Second Authors: Shalika Walker[1], Wim Zeiler[1] and Joep van der Velden[2]
[1] Department of the Built Environment, Eindhoven University of Technology, PO Box 513, 5600 MB Eindhoven, The Netherlands;
rick.j.g.cox@gmail.com (R.C.); S.W.Walker@tue.nl (S.W.); W.Zeiler@tue.nl (W.Z.)
[2] Kropman Installatietechniek, Lagelandseweg 84, 6545 CG Nijmegen, The Netherlands; Joep.van.der.velden@kropman.nl

Abstract—**In order to provide flexibility services for a future smart grid, the built environment has the potential to contribute through demand-side management. Such a demand-side management strategy is the stabilization or flattening of the demand profile with the operation of a Battery Energy Storage System (BESS). This can be achieved with the aid of proper electricity demand forecasting models. Considering these aspects, in this study, an office building is used to demonstrate forecast-driven building energy flexibility by operating a Battery Electric Storage System (BESS). The objective of flattening the building energy demand profile with the operation of a BESS is achieved through electricity demand forecasting models that are developed and assessed for each individual load group of the building. The prediction models showed acceptable results with the Coefficient of Variation of the Root Mean Square Error (CVRMSE) values below 30%. Both the simulation and experimental results show that the flattened load shape objective can be met more than 95% of the time for the evaluation period without compromising the thermal comfort of users. Accurate energy demand forecasting is shown to be pivotal for meeting the load shape objectives.**

Index Terms— **electricity, demand forecasting, flexibility, office building, Smart Grid**

I. INTRODUCTION

Even though the European Union agrees on drastically lowering CO_2 emissions [1,2], still in most of the European countries electricity generation is achieved by means of fossil fuels. In the Netherlands, to meet the associated targets, transition towards more sustainable energy generation is vital [3,4]. Transitioning towards a low-carbon society does not mean the targets should be achieved only with sustainable generation but also with energy saving on the demand side [5,6].

This transition on the generation side and also on the demand side is expected to bring about a variety of challenges. The foreseen large-scale deployment of Renewable Energy Sources (RESs) is planned to integrate into the built environment, which makes the buildings active 'prosumers' with the ability to consume and produce energy. This may seriously affect the stability of energy grids [7,8] while changing the power generation characteristics on the low- and medium-voltage grid levels [9]. Additionally, the continuing electrification of space heating by heat pumps and transport by electric vehicles, puts pressure on the transmission and distribution grids further, thereby, increasing the risk of congestion [10,11].

All the aforementioned problems call for more intelligent ways of consuming electricity and providing more flexibility. This study is focused on the power system flexibility that can be achieved at the demand-side or more specifically built-environment [12]. Gellings [13] describes demand-side management as: "*the planning and implementation of those electric utility activities designed to influence customer uses of electricity in ways that will produce desired changes in the utility's load shape*". Focusing on the load shape objectives, techniques such as peak shaving and valley filling could be used [14] with the use of storage systems. To provide the above-mentioned flexibility through load shape objectives, from the buildings to the grid, it is necessary to perform accurate short-term and subsystem level electricity load forecasting of individual buildings [15].

• Contributing to solving the mentioned problems, the objective of this research is to achieve energy flexibility opportunities using subsystem-level electricity demand predictions and a Battery Electric Storage System (BESS) while flattening the electricity demand profile.

II. METHODS

The case study office building used for this study is located in The Netherlands. It is a traditional office building which was built in 1993. The building has an approximate floor area of 1500 m^2 and a practical maximum occupancy count of 35 [16]. A detailed description of the subsystems of the building is as follows:

1. Air Handling Unit (AHU) and Heating, Ventilation, and Air-conditioning (HVAC)-control unit [17].
2. Chiller: The chiller is an electric, double-stage air-source compression cooling machine. It is an on-off operated machine.
3. Lighting: The building is equipped with fluorescent lighting.
4. Plug loads: all the remaining electricity consuming devices such as computers, printers, coffee machines, etc.
5. PV system: 65 Photovoltaic (PV) panels with a total capacity of 16.9 kWp [18].
6. Battery Electric Storage System: Nilar ECI-600V battery system with 48 kWh of storage capacity in combination with a SUNSYS-PCS2-33TR bi-directional inverter and transformer.

The method used consists of two steps.

A. Step 1: Establish prediction models

The total electricity consumption of the case study building consists of 5 major load groups and a BESS, which were extensively monitored. The behaviour of each load group differs from each other. Therefore, different prediction methodologies are proposed depending on the groups' characteristics. Total building's electricity demand predictions are formed by the sum of the individual load group predictions.

Building Management System (BMS) data from 1 January 2017 to 31 December 2018 are used in the establishment of the prediction models. For the solar PV yield and outdoor temperature Solargis® models were used. The Solargis® dataset contains data from 25 May 2018 to 4 April 2019 (~10 months).

The performance of the prediction models was calculated using various error metrics [19].

a. The Coefficient of Determination (R^2)

R^2 evaluates how much of the variability in the actual values is explained by the model [20], and it takes a value between 0 and 1. Closer to 1 represents the best performance R^2 is only used for the assessment of the chiller model in this research. More information can be found in [21]. The mathematical definition of R^2 is given by Equation 1.

$$R^2 = 1 - \frac{\sum_{i=1}^{N}(\hat{x} - x_i)^2}{\sum_{i=1}^{N}(x_i - \bar{x})^2} \quad [-] \tag{1}$$

Where,

$\hat{x}_i$	The predicted value for data point i (e.g., power demand)
x_i	The measured (observed) value for data point i
$\bar{x}$	The mean of all observed values in the dataset

b. The Weighted Average Percentage Error (WAPE)

The WAPE describes the average magnitude of error produced by the model, relative to the measured values and it is best when closer to 0. Equation 2 shows the mathematical definition of the WAPE [22].

$$WAPE = \frac{\sum_{i=1}^{N}|\frac{\hat{x}_i - x_i}{x_i}| x_i}{\sum_{i=1}^{N} x_i} [\%] = \frac{\sum_{i=1}^{N}|x_i - \hat{x}_i|}{\sum_{i=1}^{N} x_i} \tag{2}$$
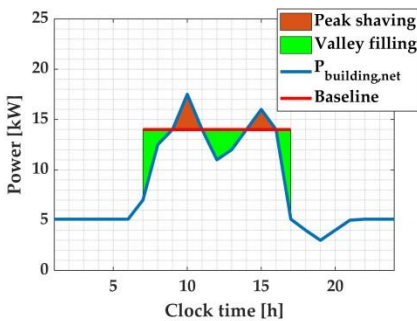
c. The Coefficient of Variation of the Root Mean Square Error (CVRMSE)

The American Society of Heating, Refrigerating, and Air Conditioning Engineers (ASHRAE) recommends CVRMSE values below 30% [23] for hourly predictions. The mathematical definition is provided in Equation 3 [24].

$$CVRMSE = \frac{\frac{\sqrt{\sum_{i=1}^{N}(x_i - \hat{x}_i)^2}}{N}}{\bar{x}} \quad [\%] \tag{3}$$

B. Step 2: Establish the Operational Strategy

The objective of this study is to stabilize/flatten a building energy demand profile using peak shaving and valley filling during office work hours with the aid of the BESS. A peak or valley can be identified in comparison to a 'desired flattened power demand profile'. A peak refers to a higher power demand than desired, and a valley to a lower power demand than desired. Instead of the term 'desired power demand', henceforth, the term 'baseline' (BL) is used. An illustrative example of a BL which is set between 07:00 and 17:00 (working hours of the building) is shown in Fig. 1. By charging and discharging the BESS, the peaks can be shaved and valleys can be filled allowing to meet the load shape objectives. The established BL heavily affects the operation of the BESS.

Another important parameter that is dependent on the baseline (and vice versa) is the initial State of Charge (SoC_{ini}) of the BESS before the load balancing period starts. Since the study considered the working hours of the building, the load balancing period starts at 07:00. The mutual dependence of BL and SoC_{ini} calls for a strategy to determine the best balance. For both workdays and weekend days, the predictions are calculated at 00:00 for the upcoming 24 hours and then used when determining the BL and SoC_{ini}. On the other hand, battery operation is constrained to work between a 0.8 SoC and 0.2 SoC margin, which means a capacity of ~28.8 kWh out of the total 48 kWh is available for operation throughout the day. The steps followed to determine the best balance between BL and SoC_{ini} are as follows:

- First, the algorithm starts at 00:00 by receiving the predicted energy demand profile for the next 24 hours.

- Secondly, based on the maximum predicted power demand of the prediction profile, a series of test baselines (BL_{test}) are generated (see Fig. 2a).
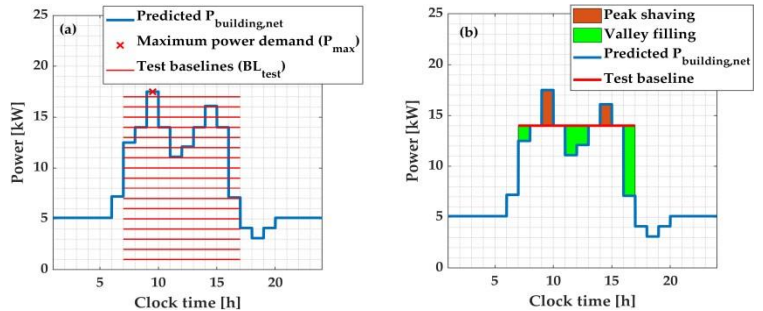

Fig. 1. Peak shaving and valley filling depending on the established baseline

Fig. 2. (a) Principle of defining test baselines based on the maximum predicted power demand. **(b)** Peak shaving and valley filling depending on the test baseline and building energy demand forecast.

- Next, for different SoC_{ini} values ranging from 20% to 80% (20%, 30%, …, 80%), the charging and discharging patterns of battery storage are evaluated for each BL_{test} profile as illustrated in Fig. 2b (charging efficiency - 85.5%, discharging efficiency - 95%).

For each of these evaluated cases two key variables are calculated which are the 'inability to discharge ($X_{discharge}$)' and the 'inability to charge (X_{charge})'. These two variables contain the cumulative energy which could not be delivered by the BESS to shave the peaks throughout the day, and the cumulative energy which could not be stored by the battery to fill the valleys throughout the day, respectively. This information forms the basis to decide which case is expected to perform best. Then, the most suitable BL and SoC_{ini} are chosen and used for the operation of the specific workday.

For a weekend or a holiday, the aim is to maximize PV self-consumption and prevent net power injection into the grid, meaning BL = 0 kW is chosen for weekends. In this case, by using these energy predictions performed at 00:00 and the assumed charging efficiency of the battery, the required SoC_{ini} is calculated to prevent net injection between 07:00 and 17:00.

The operational strategy is illustrated in Fig. 3. Between 7.00 and 8.00, the BESS is only allowed to discharge. This translates to a gradual increase of the building's load at the beginning of the day. Also, notice on weekdays the BESS is turned off at 16:33. At this time, the HVAC system is turned off and building loads are then allowed to decrease naturally before the office closes for that day.

The final results are presented in 15-minute resolution. This granularity is of interest, because national electricity grid balancing in the Netherlands is carried out in time blocks of 15 minutes (clock quarters), also known as the program time unit (PTU) [25].

Finally, to assess the performance of the flexibility efforts, several key performance indicators (KPIs) are chosen.

A. KPI 1: Total energy consumption (excluding PV power generation) [26]. In this paper, this is limited to electricity only;
B. KPI 2: Exported electricity (feed in from the building's PV system into the AC grid) [26];
C. KPI 3: Imported electricity (power from the grid) [26];
D. KPI 4: Battery Electric Storage System (BESS) losses;
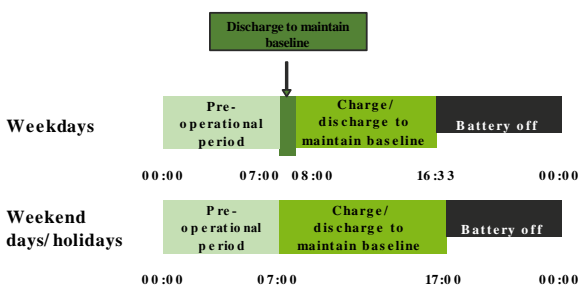E. KPI 5: Self-consumption [27];

F. KPI 6: Self-sufficiency [27];
G. KPI 7: Percentage indicating the proportion of working hours wherein the baseline is successfully maintained.

The prediction models are integrated with the proposed operational strategy and simulated in MATLAB before implementing it in the Building Management System (BMS).

Additional constraints of the BESS:

- Whenever the difference between the buildings net electricity demand ($P_{building,net}$), and the baseline is too small, the battery will not deliver or store power. A slight deviation from the baseline (BL) value cannot be prevented
- The minimum dis(charge) threshold is 3 kW DC due to the inverter efficiency greatly reducing for low powers. With a discharging efficiency of 95% [28] the 3 kW DC power requirement translates to a threshold of 2.81 kW AC power threshold for discharging. Similarly, with a charging efficiency of 85.5% [28] the DC power requirement translates to a threshold of 3.51 kW AC power threshold.

After the simulations, finally, the practical implementation of the prediction models, algorithms, and BESS control strategies in the InsiteView® Building Management System (BMS) is performed. After beta testing was carried out for ~4 weeks and an experimental phase was conducted for 13 days, from 7 August 2019 to 19 August 2019.

III. RESULTS AND DISCUSSION

A. Establish Prediction Models

AHU & controls

As shown in Fig. 4, the energy consumption of AHU & controls against outside temperature follows a characteristic S shape. Therefore, for the demand prediction of this subsystem, a parametric approach is chosen. The S shape characteristic of this load group can be described mathematically by combining a logistic function and a parabolic function. To better fit the model, a variance stabilizing transformation is performed using the natural logarithm of the dataset.
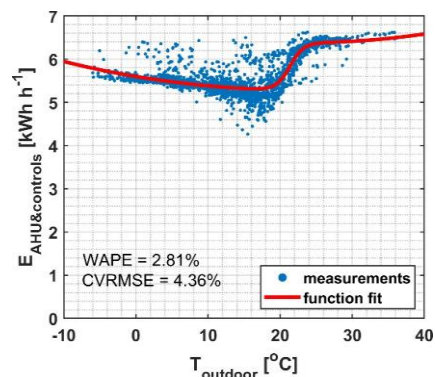
Fig. 4. Final function fit power demand for the AHU and HVAC control unit during office hours

Fig. 3. BESS operational schedule

Table 1. Fitted parameters for AHU & controls prediction model

Parameter	Value
A	0.0075
B	−0.3576
C	123.8934
α	0.0155
β	−0.0016
γ	−1.0342
δ	21.2692

Table 2. Fitted parameters for chiller prediction model

Parameter	Value
a_0	-10.9190
a_1	0.7902
a_2	-0.1223

Table 3. Summary of prediction performance for each load group

Load group	Model	R²	WAPE	CVRMS
AHU & controls	Parametric fitting	N/A	2.8%	
Chiller	Multi-variable linear regression			
Lighting	Rece			
Plugs				

The final equation to predict the AHU and HVAC control unit energy demand ($E_{AHU\&controls}$) as function of the ambient temperature ($T_{outdoor}$) is given by Equation 4, with numerical values for its parameters in Table 1.

$$E_{AHU\&controls,t=i} = \exp\left((A \cdot T_{outdoor}^2 + B \cdot T_{outdoor} + C) \cdot \left[\alpha + \frac{\beta}{1+\exp(-\gamma\cdot(T_{outdoor}-\delta))}\right]\right) [kWh.h^{-1}] \quad (4)$$

Chiller

The outdoor temperature has a direct impact on the chiller energy demand. Employing temperature variables, this prediction model was developed using multi-variable linear regression. The final equation for the prediction of the chiller is given by Equation 5. with corresponding parameters in Table 2.

$$E_{chiller,t=i} = a_0 + a_1 \cdot T_{t=i} + a_2 \cdot T_{t=i-1} [kW] \quad (5)$$

Plug loads and lighting

Occupancy has a direct impact on plug loads [29]. However, because the day-ahead occupancy cannot be predicted accurately, an approach is chosen wherein the future plug load and lighting demand are based on (recent) historic demands as shown in Equation 6.

$$E_{pred,t=i} = \frac{\sum_{k=1}^{N}(E_{t=i-24*k})}{N} [kW] \quad (6)$$

Where

$E_{pred,t=i}$	Represents the predicted electricity demand value for clock hour i
$E_{t=i-24*k}$	Represents the historic electricity demand, for the same clock hour as i, k days back
N	Number of historic workdays used in the forecast

Using a holistic approach, it was found that both the lighting and plug load predictions reach optimum performance when using five historic days (N = 5) in the forecast.

PV system & ambient temperature

The case study building uses services from Solargis® since May 2018. Solargis® provides both temperature and PV yield predictions on an hourly basis for every hour of the day and up to 48 hours ahead. For all the prediction models described above, these temperature predictions are used as an input for both the simulations and experimental phase.

Accuracies of the prediction models

A summary of the developed models and corresponding performance metrics for each load group is provided in Table 4. For the purpose of this research, the proposed model accuracies are considered sufficient.

B. Results from the operational strategy - simulations

Using the prediction models described in the previous section, the proposed operational strategy is simulated in MATLAB. Table 4 provides an overview of the assessed Key Performance Indicators (KPIs). The results show that:

- The total energy consumption (KPI 1) has increased by 2.2%. This increment is caused by the conversion loss in the BESS (KPI 4).

- The total exported electricity (KPI 2) has decreased by 60.9%. It follows that the operational strategy has significantly increased self-consumption (KPI 5) from 82.3% to 93.1%.

- The amount of imported electricity (KPI 3) is reduced by 0.4%, as the BESS was capable of providing (some of) the required energy.

- Self-sufficiency (KPI 6) has increased by 2%, which means that the ratio of self-consumed electricity from PV to total energy consumption (KPI 1) has improved.

- KPI 7, which describes the ability of the system to maintain the baseline, shows that the baseline was successfully maintained for 97.2% of the time on weekdays between 07:00 and 16:33.

Table 4. Key Performance indicator (KPI) assessment for simulation results

Key Performance Indicator	Without BESS	With BESS load balancing	Difference [%]
KPI 1: Total final energy use (excluding PV power generation) [26]. (In this paper, this is limited to electricity only)	55 538 kWh	56 781 kWh	2,2%
KPI 2: Exported electricity (feed-in from building's PV system into the AC grid) [26]	2 309 kWh	902 kWh	-60,9%
KPI 3: Imported electricity (power from the grid) [26]	44 769 kWh	44 604 kWh	-0,4%
KPI 4: Battery Electric Storage System (BESS) losses	0 kWh	1 245 kWh	N/A
KPI 5: Self-consumption [27]	82,3%	93,1%	10,8%
KPI 6: Self-sufficiency [27]	19,4%	21,4%	2%
KPI 7: Percentage indicating the proportion of the working hours wherein the baseline is successfully maintained.	N/A	97,2%	N/A

Table 5. KPI assessment for experimental results

Key Performance Indicator	Without BESS	With BESS load balancing	Difference [%]
KPI 1: Total final energy use (excluding PV power generation) [26]. (In this paper, this is limited to electricity only)	2190 kWh	2317 kWh	5,8%
KPI 2: Exported electricity (feed-in from building's PV system into the AC grid) [26]	115 kWh	70 kWh	-39,1%
KPI 3: Imported electricity (power from the grid) [26]	1500 kWh	1582 kWh	5,5%
KPI 4: Battery Electric Storage System (BESS) losses	0 kWh	127 kWh	-
KPI 5: Self-consumption [27]	85,8%	91,3%	5,5%
KPI 6: Self-sufficiency [27]	31,5%	31,7%	0,2%
KPI 7: Percentage indicating the proportion of the working hours wherein the baseline is successfully maintained.	N/A	96,2	-

Fig. 5a through Fig 5f shows the load duration curves for the analyzed period. From these Figures, the overall decrease of high positive powers (peaks shaved) can be identified. Other than that, an increase in the duration of lower positive powers can also be seen (valleys filled). This is the direct consequence of the load balancing strategies.

C. Results from operational strategy – Building Management System (BMS) implementation

This section shows the results after the strategy has been implemented in the office building. During this experimental period, KPI's of the building when operating the BESS can readily be calculated from the measurements that are extracted from the Building Management System (BMS). An overview of the resulting KPIs is shown in Table 5. The results show that:

- The total energy consumption increased due to BESS losses.

- The exported electricity to the national grid is reduced from 115 to 70 kWh, and imported electricity increased from 1500 to 1582 kWh.

- Self-sufficiency has increased from 31.5% to 31.7%

- Self-consumption from 85.8% to 91.3%.

- During 96.2% of the time, the BESS was able to successfully maintain the BL within the tolerance.

The load duration curves for the experimental period on the real building are shown in Fig. 6.
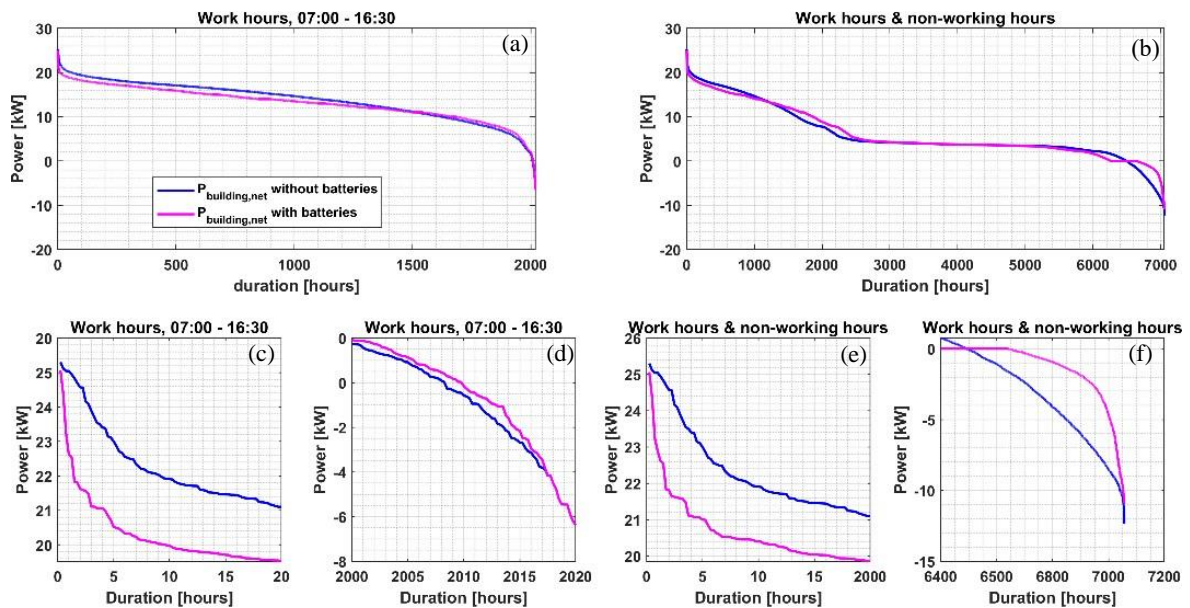
Fig 5. Load duration curves for simulation results. (a) Work hours only (b) All hours of the data set (c&d) Close-ups of (a) (e&f) Close-ups of (b)
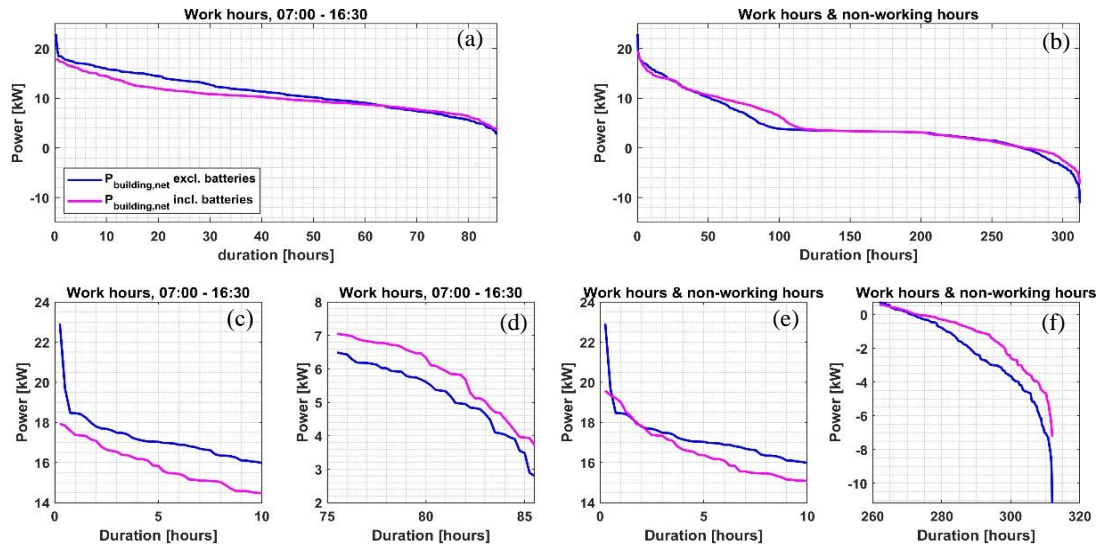
Fig. 6. Load duration curves for the experimental results. (a) Work hours only (b) All hours of the dataset (c&d) Close-ups of (a) (e&f) Close-ups of (b)

IV. CONCLUSIONS

This study performed a demand-side energy management strategy to provide flexibility from the build side towards the grid. The practical implementation was performed without compromising the thermal comfort of the building users, meaning that no changes in the normal operation of the buildings or the settings have been done. The operational strategy introduced was able to decrease the peak loads in magnitude and in duration. This helps in decreasing the risk of congestion in the grid. Due to BESS losses, total energy consumption is shown to have increased marginally.

Utilization of flexibility in the future Smart Grid will occur through information and communication technology (ICT) regardless of the exact market design. In the future, it is unknown whether a steady load profile as demonstrated in this paper will be the true load shape objective of a Smart Grid. However, because no operational Smart Grid exists that can be used to define the load shape objective in the Dutch context, and since the method introduced in this article has proven to be successful after implementing in the building, it is safe to conclude that the baseline approach is adequate for demonstrating load flexibility for a future electricity grid setting. In the future, the value of flexibility can be incorporated into the operation algorithms, if the relevant guidelines and regulations are provided by the energy markets.

ACKNOWLEDGEMENT

REFERENCES

[1] Mancini, F.; Nastasi, B. Energy Retrofitting Effects on the Energy Flexibility of Dwellings. Energies 2019, 12, 2788.

[2] Rijksoverheid. Energierapport, Transitie Naar Duurzaam. 2016. Available online: https://www.rijksoverheid.nl/documenten/rapporten/2016/01/18/energierapport-transitie- naar-duurzaam (accessed on 3 February 2018).

[3] PBL Energietransitie. Available online: https://themasites.pbl.nl/energietransitie/ (accessed on 28 March 2020).

[4] Koirala, B.; Chaves-Ávila, J.; Gómez, T.; Hakvoort, R.; Herder, P. Local Alternative for Energy Supply: Performance Assessment of Integrated Community Energy Systems. Energies 2016, 9, 981.

[5] Gvozdenovic, K.; Maassen, W.; Zeiler, W.; Besselink, H. Roadmap to nearly Zero Energy Buildings. REHVA 2015, 2, 6–10.

[6] Arteconi, A.; Polonara, F. Assessing the Demand Side Management Potential and the Energy Flexibility of Heat Pumps in Buildings. Energies 2018, 11, 1846.

[7] Jensen, S.Ø.; Marszal-Pomianowska, A.; Lollini, R.; Pasut, W.; Knotzer, A.; Engelmann, P.; Stafford, A.; Reynders, G. IEA EBC Annex 67 Energy Flexible Buildings. Energy Build. 2017, 155, 25–34.

[8] Kuiken, D.; Más, H.; Haji Ghasemi, M.; Blaauwbroek, N.; Vo, T.; van der Klauw, T.; Nguyen, P. Energy Flexibility from Large Prosumers to Support Distribution System Operation—A Technical and Legal Case Study on the Amsterdam ArenA Stadium. Energies 2018, 11, 122.

[9] Manditereza, P.T.; Bansal, R. Renewable distributed generation: The hidden challenges—A review from the protection perspective. Renew. Sustain. Energy Rev. 2016, 58, 1457–1465.

[10] Verzijlbergh, R.A.; Vries, L.J. De Renewable Energy Sources and Responsive Demand. Do We Need Congestion Management in the Distribution Grid? IEEE Trans. Power Syst. 2014, 29, 2119–2128.

[11] Protopapadaki, C.; Saelens, D. Heat pump and PV impact on residential low-voltage distribution grids as a function of building and district properties. Appl. Energy 2017, 192, 268–281.

[12] Aduda, K.O.; Labeodan, T.; Zeiler, W.; Boxem, G.; Zhao, Y. Demand side flexibility: Potentials and building performance implications. Sustain. Cities Soc. 2016, 22, 146–163.

[13] Gellings, C.W. The Concept of Demand-Side Management for Electric Utilities. Proc. IEEE 1985, 73, 1468–1470.

[14] Voerman, M. Grid Connected Active Office Building with Integrated Electrical Storage. Master's Thesis, Eindhoven University of Technology, Eindhoven, The Netherlands, 2017.

[15] Amarasinghe, K.; Marino, D.L.; Manic, M. Energy Load Forecasting Using Deep Neural Networks; IEEE: Piscataway, NJ, USA, 2016; pp. 7046–7051.

[16] Aduda, K.O. Smart Grid-Building Energy Interactions: Demand Side Power Flexibility in Office Buildings. Ph.D. Thesis, Technische Universiteit Eindhoven, Eindhoven, The Netherlands, 2018.

[17] Thomassen, T. Smart Grid Building Energy Management. Master's Thesis, Eindhoven University of Technology, Eindhoven, The Netherlands, 2014.

[18] de Bont, K. Developing a Photovoltaic- and Electrical Storage System for Investigation of Demand Side Management Strategies in Office buildings. Master's Thesis, Eindhoven University of Technology, Eindhoven, The Netherlands, 2016.

[19] Walker, S.; Khan, W.; Katic, K.; Maassen, W.; Zeiler, W. Accuracy of different machine learning algorithms and added-value of predicting aggregated-level energy performance of commercial buildings. Energy Build. 2019, 209, 109705.

[20] James, G.; Witten, D.; Hastie, T.; Tibshirani, R. An Introduction to Statistical Learning; Springer Texts in Statistics; Springer: New York, NY, USA, 2013; Volume 103, ISBN 978- 1-4614-7137-0.

[21] Cox, R.; Walker, S.; van der Velden, J.; Nguyen, P.; Zeiler, W. Flattening the Electricity Demand Profile of Office Buildings for Future-Proof Smart Grids. Energies 2020, 13, 2357. https://doi.org/10.3390/en13092357

[22] Louhichi, K.; Jacquet, F.; Butault, J.P. Estimating Input Allocation from Heterogeneous Data Sources: A Comparison of Alternative Estimation Approaches. Agric. Econ. Rev. 2012, 13, 83–102.

[23] Monfet, D.; Corsi, M.; Choinière, D.; Arkhipova, E. Development of an energy prediction tool for commercial buildings using case-based reasoning. Energy Build. 2014, 81, 152–160.

[24] Fan, C.; Xiao, F.; Zhao, Y. A short-term building cooling load prediction method using deep learning algorithms. Appl. Energy 2017, 195, 222–233.

[25] Tennet. The Imbalance Pricing System. 2016. Available online: https://www.tennet.eu/fileadmin/user_ upload/SO_NL/ALG_imbalance_pricing_system.doc.pdf (accessed on 5 April 2019).

[26] Finck, C.; Clauß, J.; Vogler-Finck, P.; Beagon, P.; Zhang, K.; Kazmi, H. Review of Applied and Tested Control Possibilities for Energy Flexibility in Buildings. 2018. Available online: http://www.annex67.org/media/1551/review-of-applied-and-tested-control-possibilities-for-energy- flexibility-in-buildings-technical-report-annex67.pdf (accessed on 3 December 2018).

[27] Luthander, R.; Widén, J.; Nilsson, D.; Palm, J. Photovoltaic self-consumption in buildings: A review. Appl. Energy 2015, 142, 80–94.

[28] J. J. Feenstra, "Optimizing electricity demand and supply with an office building connected battery and PV-system," Eindhoven University of Technology, 2019.

[29] Mahdavi, A.; Tahmasebi, F.; Kayalar, M. Prediction of plug loads in office buildings: Simplified and probabilistic methods. Energy Build. 2016, 129, 322–329.

nZEB (r)evolution. Simulations over the daily life applicability of EPB standards

Students: Bogdan Taralunga, Catalin Oprescu **Coordinators:** Tiberiu Catalina, Sebastian Stan

Technical University of Civil Engineering Bucharest, Faculty of Building Services ROMANIA
University of Arhitecture and Urbanism Ion Mincu Bucharest

Students' email adresses: catalin.oprescu96@gmail.com b.taralunga@gmail.com
Supervisors` email adresses: tiberiu.catalina@gmail.com sebastian.stan.arh@gmail.com

The year when the work has been accepted at the home univesity: 2021

Abstract— **This paper presents a study on the daily life applicability of EBP standards. The model used is a primary school belonging to the Brasov county, named Venetia de Sus. The simulation is intended to analyze the current state of the building as well as ways to improve it to the standards of NZEB.**

The simulations showed that the current state of the building lets much to be desired on the efficiency of the energy used, 284.8 kWh/sqm/year being the resulted primary energy consumption and 73.63 kCO2/sqm/year being the CO2 emissions. Much of the data was to be expected since the building is very old and besides some minor renovations along the years on the windows and exterior walls, nothing much was changed.

Bringing the building to the NZEB standard not only required some structural renovation of the walls, ground floor and ceiling but changes to the windows, heating system and lighting system as well as bringing a mechanical ventilation system to the building that it never had so far, all to reduce the primary energy consumption to 71 kWh/sqm/year and the CO2 emissions to 17.55 kCO2/sqm/year. Altogether this achieved a 75% economy.

Index terms – NZEB, EPB standards, PV/T, primary energy, CO2 emissions

I. INTRODUCTION

The current EU building stock is old and energy inefficient. The latest studies show that buildings are responsible for approximately 40% of the energy consumption and 36% of the CO2 emissions of the EU. Currently, about 35% of the EU buildings are over 50 years old and almost 75% of the building stock is energy inefficient.

Besides the intensive efforts put into energy renovation of existing buildings, the EU is also concentrating on the implementation of advanced energy efficiency requirements for all new buildings. Moreover, Directive 2010/31/EU on the energy performance of buildings (EPBD) requires that by the end of 2020 all new buildings are nearly zero-energy buildings.[1]

NZEBs are buildings with a very high energy performance. The low amount of energy that these buildings require comes mostly from renewable sources. In combination, existing technologies related to energy savings, energy efficiency and renewable energies are sufficient to reach the NZEB target. The slightly higher technology costs of early NZEBs have reduced since 2020 in reaction to more mature markets and larger volumes.[2]

Even though in recent years there has been great progress in the field of energy efficient buildings, people still tend to have different views and various concerns regarding NZEBs, very often connected to the investment and maintenance costs. In addition to that, early NZEBs are often associated with a lack of trust among end-users, due to the complexity of systems and end-users's beliefs about various constraints regarding living in NZEBs. Understanding the doubts and fears as well as the benefits for the end-users living in NZEBs may substantially contribute to a better acceptance of high-energy performance buildings in the future that we all step to.[3]

NZEB is accomplished by incorporating energy saving strategies with passive and active energy production designs and technologies. The site-specific design will respond to its location, regional climate and intended use. In order to realize savings in energy costs, time needs to be dedicated to analyzing the interactions of building systems and to life cycle cost analyses of potential efficiency upgrades.[4]

Effective NZEB projects require thinking about design in a different way. Maximizing the use of passive resources, such as natural daylight and ventilation, will aid in making buildings more efficient. Active renewable resources such as wind and solar energy can be captured and used to replace the energy used by the building. Make-up for the remaining energy consumption can be offset by reducing waste, maximizing efficiency, and by integrating energy management control systems. In turn, these spaces become healthier, more satisfying spaces in which to live, work, or play.[5]

There are many advantages to building or renovating a building to be a NZEB, but **THE KEY** advandages ar: 1) low energy demand for heating (and cooling), 2) high share of renewable energy sources, 3) low energy costs, 4) low CO2 emissions, 5) good thermal comfort and indoor air quality.

While these are all important advantages for the core concept, the **indoor air quality** might be the single most important aspect of NZEB, now more than ever given that for 3 years we have been battling with the **COVID-19 pandemic** and with no end in sight we must do all that we can to limit the spread and design a safe environment for every person, no matter the cost.[6]

So far we have only done the simulations but we are looking forward to seeing this changes being implemented and look at children going back to school without any worry of getting infected by COVID-19 or even the common flu.

II. DESGIN BUIDLER STUDY

A. Objectives of the Design Builder simulations

The aim of this approach is to have a precise estimation of the performances the building in its current and future state attains. This allows relevant comparisons in order to clarify the efficiency of the proposed intervention. Moreover, this analysis constitutes a solid starting point for the implementation of the renewable energies.

Fig. 1. The position of the school in the village

B. Description of the method used

The approach of this study begins initially with the current state in which the building can be found. Afterwards the analysis is gradually built with the knowledge regarding the ways in which the school works, the number of children, their schedule etc. The first major step is the annual analysis of the school. This highlights the weak points of the building, the periods of the year in which the most energy is lost, used. It is also important to note the periods in which the solar gains are most prevalent.
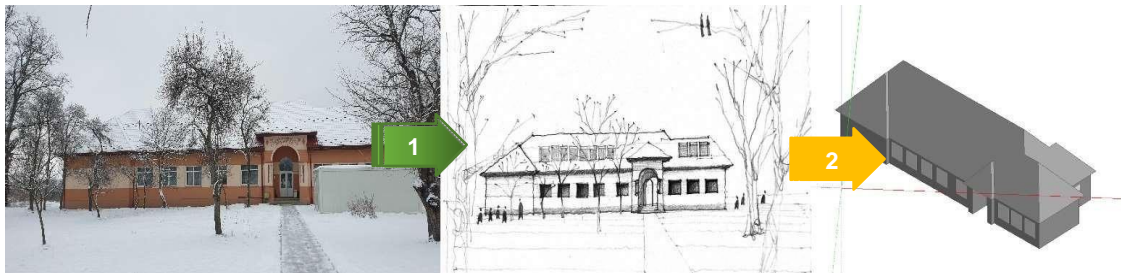

Fig. 2. From site visits to sketching ideas and implementing the 3D model

The second phase of the study means reconstructing the first analysis and integrating classic solutions which prove to make significant differences. Therefore, the second part of the study constitutes a second analysis of the upgraded version of the school. The second major step was comparing the results and focusing on the aspects that needed more attention and more efficient intervention.

This also allows for a better understanding of the ways in which renewable energies can be implemented in the project.

C. First scenario: Actual state of the building

The point of departure is visiting the site, taking the measurements of the building and consulting the documentation in order to better understand the layers of the envelope. The software necessitates a 3D model (fig.2) of the building and it allows the user to divide the surface into multiple zones (fig.3) in order to analyze them independently in accordance with their respective needs.
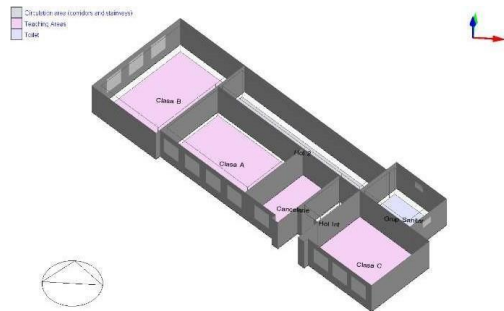

Fig. 3. Dividing the school in different thermic zones

One essential aspect, once the 3D model is done, is the accurate description of the envelope of the building (fig.4). It was at some points necessary to create new material templates inside the software in order to improve the accuracy of the study. For instance, the ceiling of the school is made with wood beams and the space left between them is occupied by a clay straws filling, a local material obtained with a traditional technique.

Once the construction details are implemented in the program, the next step is configuring the activity schedules (fig.5) in accordance with the actual schedules of the pupils, teachers and staff, the occupants of the building. These are later necessary for the development of functioning schedules of the different systems of the building. For example, the electrical system is especially needed when the building is occupied, therefore a decrease in consumption can be expected during holydays.
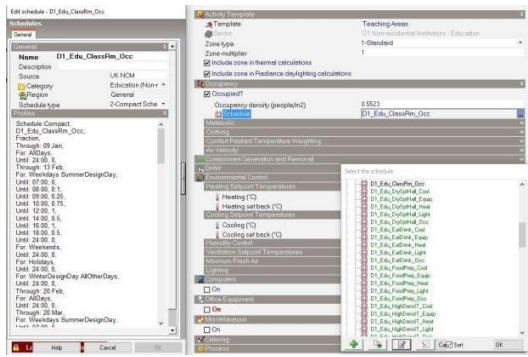
Fig. 5. Planning schedules for each zone of the building

Ultimately, the known number of occupants was spread across the different thermic zones (classrooms, hallways, bathroom, and teacher`s room). This allows the calculation of the metabollic activity contribution to the heat balance of the building. It is also mandatory to include information regarding the air infiltrations, the energy sources for the building equipments (e.g. natural gas for the heating system, electricity from grid for the DHW system), their efficiency as well as their consumption rates.

D. Second scenario: Classic improvements

The first step in bringing the school to the nZEB standards is treating the envelope. In this sense, the new 3D model was modified by adding 15cm of insulation to the walls, 30cm to the ceiling and 10cm to the ground floor. Furthermore, the windows are replaced in this new scenario with more efficient ones. Values like occupation density, schedules remain unchanged. However significant improvements were noticed in the analysis results after implementing heat recovery with an effectiveness of 0.85, a new heating system (heat pump) fueled by electricity and with a seasonal CoP of at least 2.0.

Once the second model is finished, the possible comparisons between the two can lead to relevant conclusions in multiple aspects. First and foremost, the impact of the intervention has to be checked in the Heating Design tab, where the software displays the energy lost through the different parts of the building, as well as through ventilation and heating. It is important to note the difference between the two tables displayed in figure 6.

One elementary condition was the delivery temperature of the domestic hot water system. The temperature is supposed to be above 60 degrees Celsius so as to prevent the apparition of bacteria such as Legionella. The healthcare aspect of public institutions proves to be more important than ever given the current pandemic.
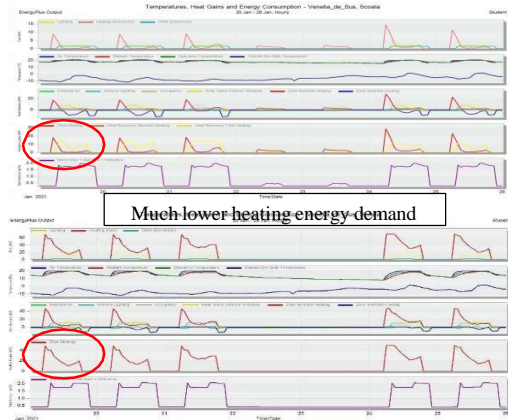

Fig.6 Comparison between the initial and the upgraded building

E. COVID-19 and air freshness

One final observation worth to be mentioned is that regarding the potential of the ventilation system implemented to prevent the spread of viruses such as SARS-CoV-2. By increasing the airflow from 15 m3/person (as it is suggested in the current legislation) to 36 m3/h/person with an increase in energy consumption of only 1.16, as the analysis in Design Builder suggests (From 13865.5 kWh to 16103.15 kWh).

The potential of such changes goes to show that the adaptive character of buildings can easily be built upon their energy efficiency. It is therefore essential to take into

consideration the capability of the building to integrate and adapt to new conditions such as the ones imposed by the Covid-19 pandemic.

III. RENEWABLE ENERGY SIMULATION STUDY

A. Objectives of the Simulation Study

The scope of the simulation study is to assess whether the implementation of solar panels, PV panels and of a wind turbine are viable renewable energy sources for the primary school renovated using the EPB standards.

B. Reference building

Primary school Venetia de Sus is an old building, founded in 1937 in the village of Venetia de Sus of the Brasov county. The building is situated in a rural area in a sheltered environment with only a ground floor.

Fig. 7. Reference building - Venetia de Sus

The exterior walls of the building are made of 32 cm solid brick. The floor slab is made of concrete and has no thermal insulation. The roof is made out of tile and both the windows and the doors have double glazing.

The building is located at 468m above sea level with a latitude of 45.859° and a longitude of 25.242°, in climate zone IV with an exterior temperature of -21°C and in eolian zone II denoting a wind speed of 0.2m/s.
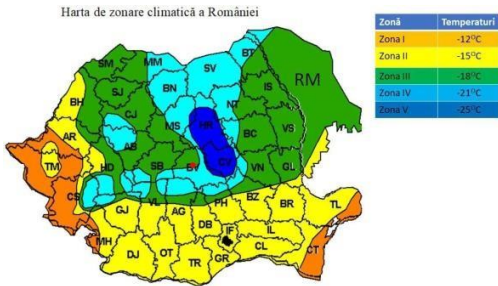
Fig.8 Climate map of Romania

C. Simulation Methodology

Case study 1 – Solar panels

For simulating the solar energy yield of the zone we have used Sonnenkraft's solar simulation tool with the desired usage of the solar energy being primarily for heating and hot water.

With a need for hot water of 265 liters/day and a heated building area of close to 300 m2 we would need a collector area of 12.9 m2 meaning a number of 5 collectors with a tilt angle of 45° and orientated south.
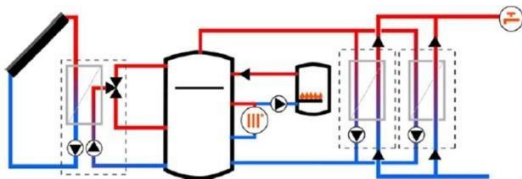

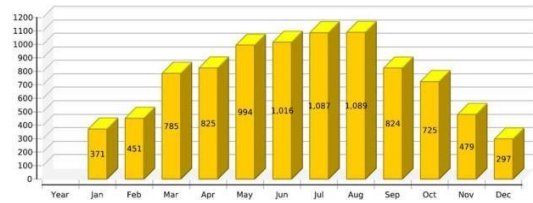Fig.9 Schematic view of the system

Fig.10 Solar thermal energy to the system – [kWh]

Total annual field yield would reach 8944 kWh. The summer month will bring the largest yield but the system will still work to bring a bit of energy even in the harsh days of winter, not dropping under 300 kWh besides December.

Case study 2 – Grid connected PV

For this study we used the JRC Photovoltaic Geographical Information System to simulate the performance of grid-connected PV in the zone of the building.

Using 5 kWp of installed PV power with a PV technology of mono crystalline silicon and a slope of 45°, the yearly PV energy production would reach 5854 kWh.
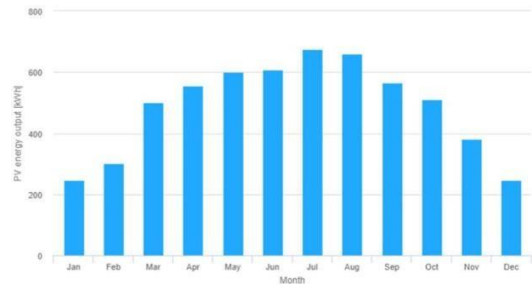

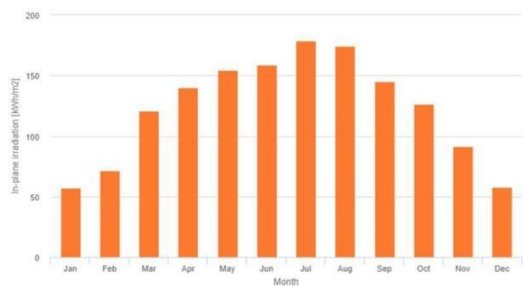Fig.11 Monthly energy output from fix-angle PV system

Fig.12 Monthly in-plane irradiation for fixed-angle

The year-to-year variability of 359 kWh being 26 % less than the monthly average output, makes us look forward to

the stability of the energy generation over time. (Fig.11, Fig.12)

Case study 3 – Wind energy

The last study we've done is on the usage of wind turbines to capture the wind energy for everyday usage.

To make a simulation as close as we can to the parameters of the zone we checked the meteorological data of the zone over the years and we have remarked that on average the wind speed is 1.92m/s with slight deviations of 2-5% depending on the month.(Fig.13)

Given the low wind speed, we next had to find a wind turbine that can make the most out of it at a reasonable cost.

After much research we have decided to use a VAWT-a vertical axis wind turbine-, model 0752 of company ROLIX.

This new type of vertical axis wind turbine is specifically designed for efficient collection of low intensity wind, inconstant, or in existing gusts at low altitudes above the ground.(Fig.14)

With the vertical positioning of the rotor, the wind turbine produced by Rolix has the same power performance as a classic wind turbine, but has a much smaller overall composition, and does not produce noise or annoying shadows.
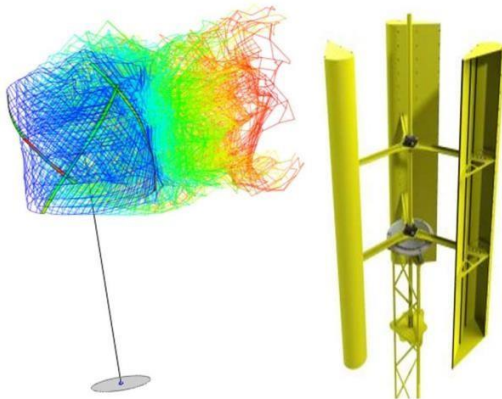

Fig.13 Wind speed simulation of 1.92m/s with color by age

Wind energy is a clean and renewable energy but it is intermittent, with variations during the day and season, and even from one year to another. Wind turbines operate about 60% of the year in windy regions.

Most turbines produce energy over 25% of the time, this percentage increasing in winter, when the winds are stronger.

In the situation where the current produced by the wind turbine cannot be introduced in the electrical network, there is the option of storing the additional current in the batteries for later use. The batteries (12V, 24V, 48V etc) are connected to an inverter that converts the current to the voltage of the appliances in the house, ie 220V. Based on

the annual estimates of wind speed we simulated that using this type of vertical turbine will yield 4842 kWh/year.

While this yield might not be the highest compared to the other options we still need to remember that this system works best in the winter compared to the solar and PV systems that shine in the summer.

D. Results and Discussion

Based on the result of all 3 case studies we would very much want to recommend the implementation of the solar thermal energy system to reduce the burden of the pre-existing heating and hot water systems in combination with the vertical turbine to take advantage of the wind energy that can be generated as well as a backup energy source in case of a blackout generated by the national power supply failure or natural disasters.

IV.   CONCLUSIONS

The most obvious lesson to be learned from this analysis is the amazing capacity of technology to help us in the development of our buildings. Integrating the abilities of such software as Design Builder in the matter of bringing up to date old buildings, even historic ones, is of great importance, as it allows us to find precise estimations and build solid arguments for our decisions.

By doing the 3 case studies on renewable sources of energy we managed to compile that the total annual field yield of an integrated solar thermal energy system would be 8944 kWh, for a PV system made out of the PV technology of mono crystalline silicon, the yearly PV energy production would reach 5854 kWh and for a Vertical Axis Wind Turbine, though lower than the other renewable energy systems would still yield a 4842 kWh per year and provide energy most noticeably in the winter.

From an economic point of view, the improvements studied in this paper can bring significance in annual costs of resources. For instance, given the natural gas price for 150RON/ MWh, the price would reduce from 7633.5 RON to 2514 RON for a whole year.

REFERENCES

1   https://ec.europa.eu/energy/content/nzeb_en
2   https://www.researchgate.net/publication/314280467_The_importance_of_the_solar_systems_to_achieve_the_nZEB_level_in_the_energy_renovation_of_southern_Europe's_buildings
3   https://www.sciencedirect.com/topics/engineering/nearly-zero-energy-building
4   https://thermohouse.ie/blog/nzeb/
5   https://www.millionacres.com/real-estate-investing/commercial-real-estate/pros-and-cons-net-zero-energy-building/
6   https://ec.europa.eu/cefdigital/wiki/display/CEFDIGITAL/Fighting+COVID-19

Event Pictures

The REHVA Community of Young Professionals brings together participants from past editions of the student competitions to share knowledge and best-practices .

This Book of Papers aims at concentrating the knowledge of each edition of the competition and serve as a way to commemorate the occasion.

REHVA warmly thanks all the people involved in the organisation and participation to the event.

Join the discussion on the
@RCYP Linkedin group!